Friedrich-Alexander-Universität
Faculty of Sciences

Dissertation

2026

Mohit Agarwal

Light-Controlled Polyelectrolyte-Dye Nano-Objects: A Small-Angle Neutron Scattering Study

Light-Controlled Polyelectrolyte-Dye Nano-Objects: A Small-Angle Neutron Scattering Study

Der Naturwissenschaftlichen Fakultät
der Friedrich-Alexander-Universität Erlangen-Nürnberg
zur
Erlangung des Doktorgrades Dr. rer. nat.

vorgelegt von:

Mohit AGARWAL

aus Uttar Pradesh/Indien

Als Dissertation genehmigt von der Naturwissenschaftlichen Fakultät der Friedrich-Alexander-Universität Erlangen-Nürnberg

Tag der mündlichen Prüfung: 26.10.2026

Gutachter:

Prof. Dr. Franziska Gröhn

Prof. Dr. Carolin Müller

Prof. Dr. Karl Mandel

Die vorliegende Arbeit entstand im Zeitraum von September 2019 bis März 2023 im Department für Chemie und Pharmazie (Interdisciplinary Center for Molecular Materials) der Friedrich-Alexander-Universität Erlangen-Nürnberg im Arbeitskreis von Frau Prof. Dr. Franziska Gröhn. Ein Teil der vorliegenden Arbeit entstand am Institut Laue-Langevin (Grenoble, Frankreich) unter Co-Betreuung von Dr. Ralf Schweins.

Acknowledgements

First and foremost, I would like to express my sincere gratitude to my supervisor, Prof. Dr. Franziska Gröhn, for her continuous support, guidance, and patience throughout this work. Thank you for trusting me with a fascinating research topic, for the freedom to explore my own ideas, and for always encouraging me to sharpen both the science and the story behind it.

I am also deeply grateful to my second supervisor, Dr. Ralf Schweins, for his valuable input, critical questions, and practical expertise, especially when the discussion moved from “nice data” to “what does it really mean?”. Your feedback helped me strengthen both the experimental approach and the interpretation, and I greatly appreciated your support throughout the project.

I am deeply grateful to all members of the Gröhn Group, including Anja, Max, Sarah, Nina, and Krishna, for the supportive and friendly working atmosphere, for countless discussions (scientific and otherwise), and for the small everyday things that make research survivable, including good advice and shared troubleshooting. In particular, I would like to thank Alex and Müge for their help, honesty, and encouragement when experiments (or my confidence) refused to cooperate. Thank you also to everyone who contributed through discussions, shared protocols, instrument training, and the general art of keeping a lab running. My special thanks go to Leonore Steinbauer for her help with administrative matters at FAU.

I gratefully acknowledge the Partnership for Soft Condensed Matter (PSCM). This work benefited from SasView 4.2.2, originally developed by the DANSE project under NSF award DMR-0520547. I would like to acknowledge Dr. Joachim Kohlbrecher for providing all the help in measuring SANS at PSI on such short notice. Many thanks to Dr. Martina Sandroni for ensuring an unlimited supply of essentials in the chemistry labs at ILL and for all her help with my experiments. I would also like to thank Dr. Leonardo Chiappisi for the many discussions and for his help whenever the DLS and UV–Vis instruments had problems. I am also thankful to Benoit Laurent for helping me build the SANS under in-situ UV irradiation setup. My heartfelt thanks go to Nicole Rupin Triplett for all the administrative work at ILL, and to Christelle for processing all my travel claims so quickly.

I would also like to thank my colleagues at ILL, who became friends over time, whether through scientific discussions or an occasional, much-needed coffee break. Although they were not directly involved in my projects, they were always available whenever I needed help in the lab or outside.

I would like to thank Wenke for all the fun discussions, for introducing me to German culture, for joining the SAS conference in Brazil, and for so much more. Without you, it would not have been possible to manage the SANS beamtime at PSI. Thank you for bearing with me throughout these three years. You are the most talented PhD student I have met at ILL. I will also never forget serving as PhD representative together with you and my other dear friend Fernanda. That was one of the best times of my PhD.

My acknowledgements would be incomplete without mentioning Larissa. I still remember our first interaction just after the COVID lockdown, when we resumed working at ILL. I was very

impressed by your football skills, to be honest, and by your commitment to running. Thank you for being at ILL at the same time.

As we all know, a PhD also comes with many challenges, and to get through them, you need friends who are always there for you, whether it is a Wednesday evening or a weekend. Thank you Fernanda, Sam, and Himanshu for being my family away from home. Also, thank you, Sam for teaching me how not to drown.

I would also like to mention my office mates, Serena and Erik, for all the scientific and fun talks during coffee breaks and in the labs. I really enjoyed sharing an office with you. Thank you, Serena, for teaching me how to make tiramisu. Although I may never be an expert like you, I am definitely getting better. I am also grateful to have met Tong at ILL and to have shared so many fun activities with her.

Thank you, Miloš, for encouraging me to go on hikes around Grenoble and for introducing me to some of the world's best beers. I would also like to thank my other colleagues, Xaver, Peter, Martha, Giacomo, and Kamal, for all the fun conversations.

I am thankful to Friedrich-Alexander Universität Erlangen-Nürnberg and the Institut Laue–Langevin for providing the infrastructure and environment necessary to complete this work.

I would also like to thank my dearest friend Abhinav for our discussions on scientific, philosophical, and many other topics. Thank you, Aditya, Kriti, Ankita, and Deeksha, for being such kind friends.

Finally, I owe my deepest thanks to my family, especially my parents, for their constant encouragement, trust, and patience, particularly during the phases when I was physically present but mentally still inside a scattering curve. To my siblings, Deeksha, and friends, thank you for keeping me grounded and for reminding me that there is a world outside the lab. And to Charu, thank you for your love, support, and for being the calm in the chaos. This thesis would not have been possible without you.

Table of Contents

Table of Contents VIII
List of Abbreviations.....X
Abstract XI
Kurzzusammenfassung XII
Thesis Publications and Author Contributions XIII
1. Introduction 1
1.1 Interactions and Forces Involved in Macromolecular Self-Assembly.....2
1.1.1 Electrostatic Interaction.....5
1.2 State of Knowledge.....6
1.2.1 General Principles of Electrostatic Self-Assembly in Charged Soft-Matter Systems.....6
1.2.2 Established Electrostatic Self-Assembly Platforms.....7
1.2.3 Motivation for Solution-Phase Macroion–Multivalent Counterion Assemblies.....7
1.3 Stimuli-Responsive and Light-Switchable Self-Assembly.....8
1.3.1 Molecular Approaches to Light-Responsiveness.....8
1.3.2 Polyamidoamine (PAMAM) Dendrimers in Light-Responsive Electrostatic Self-Assembly.....9
1.3.3 Acid Yellow 38 as a Light-Switchable Model Counterion.....11
1.4 Characterization Techniques.....13
2 Objective.....16
3 Own Contributions.....18
3.1 Morphology Control in Light-Responsive Electrostatic Nanoassemblies.....18
3.2 How Macroion Architecture Sets the Switching Response.....19
3.3 SANS Under In-Situ UV Irradiation: Pathways, Kinetics, and Intermediates.....21
3.4 Photoacid-Based Assemblies and Multi-Addressable Switching in Water.....23
3.5 Coupling Photoacidity and Photoisomerization in One Assembly Platform.....25
4 Conclusion.....27
5 Outlook.....30
6 References.....32
7 Appendix.....40
7.1 Full Publication List.....40
7.2 Publications with Contribution on this Thesis.....41
7.2.1 Controlling the Morphology in Electrostatic Self-Assembly via Light.....41

7.2.2 The Role of Light Irradiation and Dendrimer Generation in Directing Electrostatic Self-Assembly.....73
7.2.3 Light-Induced Structural Evolutions in Electrostatic Nanoassemblies.....113
7.2.4 Double-Wavelength-Switchable Molecular Self-Assembly of a Photoacid and Spirooxazine in an Aqueous Solution.....151
7.2.5 Photoacid-Macroion Assemblies: How Photo-Excitation Switches the Size of Nano-Objects.....158
7.2.6 Joining Two Switches in One Nano-Object: Photoacidity and Photoisomerization in Electrostatic Self-Assembly.....177
8 Conference Contributions.....185
9 Methods.....186
9.1 Light Scattering.....186
9.1.1 Dynamic Light Scattering.....187
9.1.2 Static Light Scattering (SLS).....189
9.1.3 Combined SLS/DLS Interpretation.....190
9.2 Small-Angle Neutron Scattering.....191
9.3 UV-Vis Spectroscopy.....197
9.4 Isothermal Titration Calorimetry (ITC).....198
9.5 ζ-potential.....199
9.6 References.....200

List of Abbreviations

AY38	Acid Yellow 38
PAMAM	Poly(amidoamine)
G4	4^{th} generation dendrimer
DLS	Dynamic light scattering
SANS	Small-angle neutron scattering
SLS	Static light scattering
ITC	Isothermal titration calorimetry
UV-Vis	UV- and visible light
R_G	Radius of gyration
R_H	Hydrodynamic radius
ΔG	Gibbs free energy
ΔH	Enthalpy
ΔS	Entropy
µm	Micrometer
nm	Nanometer

Abstract

Light-tunable self-assembly in aqueous media offers a direct route to adaptive soft nanomaterials, yet predictive control has remained challenging because irradiation alters molecular state, intermolecular interactions, and assembly pathways simultaneously. The objective of this thesis is to understand the structural changes and mechanisms underlying light-switchable electrostatic self-assembly and to validate them using small-angle neutron scattering (SANS) under in-situ UV irradiation, supported by complementary spectroscopy, light scattering, electrokinetic measurements, and thermodynamic analysis. The thesis connects molecular photoswitching to interaction balance and, ultimately, to mesoscale structure and kinetics.

The thesis establishes a multistimulus control in water using photoactive molecular components capable of *cis*–*trans* isomerization, demonstrating that stable nanoassemblies can be reversibly switched by wavelength-selective irradiation, pH variation, and thermal recovery. The focus lies on dendrimer–azo dye assemblies, in which the interplay between a defined macroion architecture and photoswitchable counterions enables a systematic investigation of structure formation. Subsequently, photoacid-driven electrostatic assemblies are introduced to elucidate how light-induced changes in protonation state and effective charge are translated into controlled modulation of supramolecular dimensions. Variations in the charge ratio, concentration, and dendrimer generation reveal how effective surface charge density, photoisomer-dependent binding, and secondary interactions govern monodispersity, anisotropy, and irradiation-induced morphological transitions.

The thesis culminates in time-resolved structural measurements using in-situ UV-SANS, enabling direct observation of irradiation-driven pathways rather than only final structures. By comparing distinct preparation routes and irradiation protocols, the work demonstrates that photoisomerization and binding kinetics can control the rate of structural reorganization, thereby selecting transient intermediate states and determining final morphologies. Overall, this thesis establishes experimentally grounded principles for designing light-tunable self-assembled structures in water and positions SANS under in-situ irradiation as a quantitative bridge between molecular switching, interaction balance, and the emergence of nanoscale structure and dynamics.

Kurzzusammenfassung

Lichtsteuerbare Selbstassemblierung in wässrigen Medien bietet einen direkten Zugang zu adaptiven weichen Nanomaterialien. Eine vorhersagbare Kontrolle ist jedoch weiterhin herausfordernd, da Bestrahlung den molekularen Zustand, intermolekulare Wechselwirkungen und Assemblierungspfade gleichzeitig verändert. Ziel dieser Arbeit ist es, die strukturellen Änderungen und Mechanismen der lichtschaltbaren elektrostatischen Selbstassemblierung zu verstehen und diese mithilfe von Kleinwinkel-Neutronenstreuung (SANS) unter in-situ-UV-Bestrahlung zu validieren, unterstützt durch komplementäre Spektroskopie, Lichtstreuung, elektrokinetische Messungen und thermodynamische Analyse. Die Arbeit verknüpft molekulares Photoschalten mit dem Wechselwirkungsgleichgewicht und schließlich mit mesoskaliger Struktur und Kinetik.

Die vorliegende Arbeit etabliert eine Multistimulus-Kontrolle in wässriger Lösung unter Verwendung photoaktiver molekularer Komponenten, die zur *cis*–*trans*-Isomerisierung befähigt sind, und zeigt, dass stabile Nanoassemblies durch wellenlängenselektive Bestrahlung, pH-Variation und thermische Rückisomerisierung reversibel geschaltet werden können. Der Fokus liegt auf Dendrimer–Azofarbstoff-Assemblies, bei denen das Zusammenspiel aus definierter Makroionenarchitektur und photoschaltbaren Gegenionen eine systematische Untersuchung der Strukturbildung ermöglicht. Anschließend werden photosäuregetriebene elektrostatische Assemblies eingeführt, um aufzuklären, wie lichtinduzierte Änderungen des Protonierungszustands und der effektiven Ladung in eine kontrollierte Modulation supramolekularer Dimensionen übersetzt werden. Die Variation von Ladungsverhältnis, Konzentration und Dendrimergeneration zeigt, wie effektive Oberflächenladungsdichte, photoisomerabhängige Bindung und sekundäre Wechselwirkungen Monodispersität, Anisotropie und bestrahlungsinduzierte morphologische Übergänge bestimmen.

Die Arbeit endet mit zeitaufgelösten Strukturmessungen mittels in-situ-UV-SANS, wodurch bestrahlungsgetriebene Pfade direkt beobachtet werden können, anstatt nur Endstrukturen zu erfassen. Durch den Vergleich unterschiedlicher Präparationswege und Bestrahlungsprotokolle zeigt die Arbeit, dass Photoisomerisierung und Bindungskinetik die Kinetik der strukturellen Reorganisation kontrollieren können und dadurch transiente Zwischenzustände auswählen sowie finale Morphologien bestimmen. Insgesamt etabliert diese Arbeit experimentell fundierte Prinzipien für das Design lichtsteuerbarer selbstassemblierter Strukturen in Wasser und positioniert SANS unter in-situ-Bestrahlung als quantitative Brücke zwischen molekularem Schalten, Wechselwirkungsgleichgewicht und der Entstehung nanoskaliger Struktur und Dynamik.

Thesis Publications and Author Contributions

In this section, the publications are presented, which will be discussed in this cumulative PhD thesis.

I **Mohit Agarwal**, Alexander Zika, Ralf Schweins, Franziska Gröhn; Controlling the Morphology in Electrostatic Self-Assembly via Light, *Polymers,* **2024***, 16(1),* 50. **Contributions:** Planning and performance of the sample preparation and light scattering experiments; major contribution to size and shape characterization; major contribution to data analysis, understanding and manuscript writing.

II **Mohit Agarwal**, Alexander Zika, Müge Yücel, Joachim Kohlbrecher, Ralf Schweins, Franziska Gröhn; The Role of Light Irradiation and Dendrimer Generation in Directing Electrostatic Self-Assembly, *Polymers, **2025**, 17(2), 170,* **Contribution**: Planning and performance of the sample preparation and light scattering experiments; major contribution to size and shape characterization; major contribution to data analysis, interpretation and manuscript writing.

III **Mohit Agarwal**, Ralf Schweins, Franziska Gröhn; Light-Induced Structural Evolutions in Electrostatic Nanoassemblies, *Polymers, **2026**, 18(2), 190,* **Contribution**: Planning and performance of the sample preparation and light scattering experiments; including the build-up of a novel SANS in-situ irradiation setup; major contribution to size and shape characterization; major contribution to data analysis, elucidating general principles and manuscript writing.

IV Alexander Zika, **Mohit Agarwal**, Ralf Schweins, Franziska Gröhn; Joining Two Switches in One Nano-Object: Photoacidity and Photoisomerization in Electrostatic Self-Assembly, *Chem. Eur. J.,* **2022**, e202203373. **Contributions:** Performance of the sample preparation and small-angle neutron scattering experiments; major contribution to size and shape characterization and data analysis.

V Alexander Zika, **Mohit Agarwal**, Ralf Schweins, Franziska Gröhn; Double-Wavelength-Switchable Molecular Self-Assembly of a Photoacid and Spirooxazine in an Aqueous Solution, *J. Phys. Chem. Lett.,* **2023**, *14*, 9563-9568. **Contributions:** Performance of the sample preparation and small-angle neutron scattering experiments; major contribution to size and shape characterization and data analysis.

VI Alexander Zika, **Mohit Agarwal**, Wiebke Zika, Dirk Guldi, Ralf Schweins, Franziska Gröhn; Photoacid-Macroion Assemblies: How Photo-Excitation Switches the Size of Nano-Objects, *Nanoscale,* **2024,** *16*, 923-940 **Contributions:** Performance of the sample preparation and small-angle neutron scattering experiments; major contribution to size and shape characterization and data analysis.

1. Introduction

Self-assembly describes the spontaneous organization of molecular or colloidal building blocks into ordered structures through local interactions, without direct external construction [1–4]. This principle is especially important at the nanoscale, where conventional top-down fabrication becomes limited, and structure formation instead emerges from the intrinsic properties of the components and their environment. Because self-assembly can generate well-defined architectures from relatively simple building blocks, it provides a fundamental basis for understanding and designing complex soft-matter systems.

Self-assembly is a fundamental organizing principle in nature, where non-covalent interactions give rise to complex architectures such as lipid membranes, protein complexes, and nucleic acid assemblies. Inspired by these natural examples, self-assembly has long been an important concept for the design of synthetic soft materials, including micelles, colloids, and supramolecular structures. Nevertheless, predictive control over self-assembled structures remains challenging, because the same weak and reversible interactions that enable adaptive organization can also result in uncontrolled aggregation, precipitation, or gelation. As the underlying mechanisms have become better understood, these processes are increasingly being reinterpreted not only as limitations, but also as opportunities for controlled structure formation. Colloidal self-assembly exemplifies this development: interaction-driven processes that may be detrimental under uncontrolled conditions can be deliberately tuned to produce materials with tailored properties for applications such as inks, ceramics, and pharmaceutical formulations [5,6].

The scientific understanding of self-assembly has evolved progressively across multiple disciplines. It was first studied scientifically in the early 20th century, with Langmuir and Debye's observations on colloidal behavior, followed by Turnbull and Pauling's groundbreaking studies on protein folding in the mid-20th century. Material scientists in the 1970s and 80s, notably Feynman and Drexler, began exploring self-assembly for fabricating nanoscale structures. In the past three decades, significant strides have been made in developing self-assembling materials across various domains, including metals, semiconductors, polymers, and smart materials [7–9].

From a technological standpoint, self-assembly is not just advantageous; it is highly enabling. Its spontaneous and reversible nature minimizes waste, making it a sustainable solution. It boasts a wide range of applications, from the nucleation of inorganic materials to the creation of monolayers, micelles, vesicles, and beyond. Moreover, the future of self-assembly holds even more promise. Researchers are exploring novel techniques, such as electric fields and chemical reactions, to regulate self-assembly. Controlled self-assembly is poised to produce innovative materials and devices such as transistors, solar cells, 3D structures, tissue engineering scaffolds, and advanced optical systems. Moreover, ongoing

research aims to enable self-assembling materials to adapt shape or form in response to specific triggers like temperature, concentration, or pH fluctuations, opening up a world of possibilities [9].

Self-assembly relies on various non-covalent interactions, including electrostatic interactions, to form directional assemblies. In colloidal systems, electrostatic self-assembly is particularly significant, as electric charges control particle behavior, enabling the formation of colloids with controllable shapes and sizes. By adjusting electrostatic interactions, the stability of colloidal suspensions can be manipulated for applications like inks, ceramics, and pharmaceuticals. Electrostatic self-assembly also contributes to the fabrication of complex structures and devices, such as photonic crystals, electronic devices, and sensing systems, through precise control of particle position and orientation using electric fields and charges.

1.1. Interactions and Forces Involved in Macromolecular Self-Assembly

Self-assembly can be a hierarchical process that spans different levels of organization, beginning with molecular or macromolecular association and extending to supramolecular structures. Macromolecular self-assembly is a topic of interest as it is ubiquitous in various fields such as biotechnology, medicine, polymer, nanotechnology, and recently in pharmaceutical formulation, particularly drug delivery. Macromolecular self-assembly under thermodynamic equilibrium conditions forms stable structures or patterns by the association or inclusion of weak noncovalent interactions.[3,10] Non-covalent interactions are fundamental to self-assembly, as they provide the driving forces and stabilization required for molecules and particles to organize into ordered structures [1]. These interactions include hydrogen bonding, van der Waals forces, electrostatic interactions, hydrophobic interactions, π-π interactions, and metal coordination. Here is an in-depth look at how secondary interactions drive and stabilize self-assembly:

Hydrogen bonds provide specific and directional interactions that guide the precise arrangement of molecules. This is critical for the formation of highly ordered structures [11,12]. Multiple hydrogen bonds can significantly stabilize the resulting assembly, ensuring the structure remains intact under various conditions. Major examples of hydrogen bonding include the DNA double helix and protein folding. In DNA, complementary base pairs are held together by hydrogen bonds, ensuring stable and specific pairing for genetic information storage. In proteins, hydrogen bonds between amino acid residues help define and stabilize three-dimensional structures [13–15]. Moreover, when hydrogen bonds are organized into double, triple, quadruple, or even larger arrays, their cooperative action significantly enhances binding strength and recognition selectivity. In such systems, overall stability depends not only on the number of hydrogen bonds but also on their spatial arrangement and on secondary electrostatic interactions between adjacent donor and acceptor sites, which can further strengthen or weaken the assembly as shown by Liu et al. [16].

Hydrophobic effects cause nonpolar molecules to aggregate in an aqueous environment, minimizing their exposure to water and lowering the system's free energy by increasing the entropy of the surrounding water. These interactions drive the formation of core-shell structures in amphiphilic molecules and stabilize biological membranes. For example, amphiphilic molecules self-assemble into micelles or vesicles, with hydrophobic cores sequestered inside [7,17]. Additionally, in protein folding, hydrophobic residues cluster in the interior, driving folding and stabilizing the structure [18]. Furthermore, hydrophobic effects in amphiphilic systems can lead to the formation of diverse self-assembled morphologies, including micelles, vesicles, and other ordered structures, depending on molecular architecture and solvent conditions [19]. This same driving force also enables the creation of hydrophobic compartments capable of solubilizing or encapsulating otherwise poorly water-soluble compounds, which is particularly important in nanomaterials and drug-delivery applications [20,21].

Van der Waals forces are weak, short-range noncovalent interactions that become decisive when molecules approach closely, helping to stabilize dense supramolecular and nanoscale assemblies alongside other interactions such as electrostatics, π–π stacking, hydrogen bonding, and hydrophobic effects [12,22]. These forces are particularly significant in nanoscale assemblies where surface interactions dominate [11]. In lipid bilayers, for example, self-assembly is driven primarily by the hydrophobic effect [23]. Likewise, in nanoparticle assemblies, van der Waals forces help stabilize closely packed arrangements that are important for the formation of functional nanomaterials. Representative examples are found in the work of the George M. Whitesides group, which identified van der Waals forces as part of the weak interactions underlying self-assembly [24], and in the work of the Steven De Feyter group, which showed that cooperative van der Waals interactions between alkyl chains and with surfaces can strongly influence two-dimensional packing and molecular organization [25,26]. In addition, Barratt and co-workers showed that in a poorly solvated hydrophobic binding pocket, favorable solute–solute dispersion interactions can make van der Waals forces a major enthalpic contributor to molecular association [27].

π-π interactions between aromatic rings facilitate the stacking and alignment of molecules, crucial for forming ordered and stable structures. These interactions help maintain the planarity and conjugation of aromatic systems, important for electronic and optical properties [28,29]. They also play a key role in the self-assembly of conductive polymers and organic semiconductors. For example, the E. W. Meijer group showed that π-conjugated oligomers can assemble hierarchically into stacked and helical supramolecular polymers [30–33], whereas the F. Würthner group demonstrated with perylene bisimide chromophores that subtle structural variations can control H- or J-type aggregation and thereby strongly influence the optical properties of the resulting assemblies [34,35].

Dipole–dipole interactions arise between molecules (or molecular segments) that possess permanent electric dipole moments and therefore interact through the electrostatic coupling of their partial charges. In contrast to purely isotropic dispersion forces, dipole–dipole interactions are directional: the interaction energy depends strongly on the relative orientation of the dipoles as well as on their separation [36–40]. Favorable "head-to-tail" arrangements lower the electrostatic energy, whereas side-by-side alignments can be repulsive, which makes these interactions particularly relevant for molecular ordering and anisotropic structuring in condensed phases [4,41]. The strength of dipole–dipole interactions typically decays with distance more rapidly than Coulomb interactions between full charges (often approximated as $\propto r^{-3}$ for fixed orientations and $\propto r^{-6}$ for orientation-averaged thermal motion), and it is strongly reduced in high-permittivity media such as water due to dielectric screening. Nevertheless, in aqueous soft-matter systems they can contribute measurably when dipole moments are large, when local environments reduce effective screening (e.g., in confined or low-dielectric regions), or when dipoles are constrained by binding, packing, or macromolecular architectures, thereby influencing association equilibria, preferred morphologies, and transition pathways [4,42]. Representative examples are found in the Lei Jiang group, who showed that small variations in the symmetry of intramolecular charge-transfer molecules led to distinct dipole-driven self-assembly pathways and markedly different supramolecular morphologies, including spheres, tubes, and belts [43]. Similarly, the Mingjun Huang group demonstrated that strong dipole–dipole interactions in side-chain liquid-crystalline polymers can induce polar nematic ordering and measurable macroscopic polarity when the dipole moment and mesogen geometry are suitably matched [44]. On a larger length scale, Leon Abelmann and co-workers further showed that dipolar interactions can even direct the formation of three-dimensional assemblies when the particle shape is designed so that parallel and antiparallel dipolar states are energetically balanced [45].

Metal ions can act as nodes and organic ligands as linkers, forming extended networks or frameworks through coordinate covalent bonds. Metal coordination contributes significantly to the stability and functionality of the assembled structures [46]. In the field of metal-organic frameworks (MOFs), porous structures formed by metal ions and organic ligands are used for gas storage and separation [47]. Metal coordination is also observed in coordination polymers, where extended networks are formed by metal-ligand coordination, and they could be applied in sensors and catalysis.

Recently, electrostatic interactions have emerged as an important concept in self-assembly, as they can bring oppositely charged building blocks into close proximity, while additional non-covalent interactions subsequently stabilize and direct the final structure.

1.1.1. Electrostatic Interaction

Electrostatic interactions arise from the attraction between opposite charges and the repulsion between like charges. In media with low dielectric constant and in the absence of free ions, these interactions are described by Coulomb's law, according to which the interaction strength decreases with increasing distance. Because of their comparatively long range, electrostatic interactions can influence the motion and arrangement of charged species before direct contact occurs.

In polar media such as water, the situation becomes more complex because dissolved ions screen electrostatic forces. Charged surfaces are surrounded by an electrical double layer, in which counterions accumulate near the surface and partially compensate the surface charge. Owing to thermal motion, this ion distribution remains diffuse, and its characteristic thickness is described by the Debye length, which depends on temperature and ionic strength. For an ionic concentration of 0.001 M, the Debye length in water at room temperature is approximately 9.6 nm [48]. With increasing ionic strength, the Debye length decreases, and electrostatic interactions become increasingly screened and short-ranged.

This screening has important consequences for charged soft-matter systems. In aqueous solution, the effective range and strength of electrostatic interactions are not determined by charge alone, but also by the concentration of dissolved ions, the charge density of the interacting species, and the dielectric environment. Thus, changes in ionic strength, pH, solvent composition, or temperature can strongly influence the interaction between charged molecules, macromolecules, particles, and interfaces. For weak acids, weak bases, polyelectrolytes, proteins, or pH-responsive macromolecules, changes in pH can additionally alter the degree of ionization and therefore the effective charge.

Despite screening in water, electrostatic interactions remain highly relevant because they can guide the association of oppositely charged species and influence their organization in solution. This is particularly important in soft-matter systems containing charged macromolecules, polyelectrolytes, proteins, nanoparticles, surfactants, or molecular ions. In such systems, electrostatic interactions provide a general and versatile driving force whose strength and range can be tuned through environmental conditions. The interplay between charge attraction, charge repulsion, counterion distribution, and screening is therefore central to understanding the behavior of charged species in aqueous media.

These principles form the physical basis for electrostatic self-assembly, where oppositely charged components associate into larger organized structures. In the following sections, this concept is discussed in the context of charged soft-matter systems, established assembly

platforms, and solution-phase nano-objects formed from charged macroions and multivalent counterions.

1.2. State of Knowledge

1.2.1. General Principles of Electrostatic Self-Assembly in Charged Soft-Matter Systems

Electrostatic self-assembly refers to the spontaneous association of oppositely charged components into larger, organized structures through Coulombic attraction. The general principle is schematically illustrated in Figure 1, where charged macromolecular or colloidal building blocks associate with oppositely charged molecular species to form organized assemblies in solution. In aqueous soft-matter systems, this principle is widely encountered in complexes formed from polyelectrolytes, surfactants, proteins, nanoparticles, and other charged molecular or colloidal building blocks. Compared with many other non-covalent interactions, electrostatic attraction can act over relatively large distances and therefore often provides the initial driving force for association between dispersed species in solution [48–50].

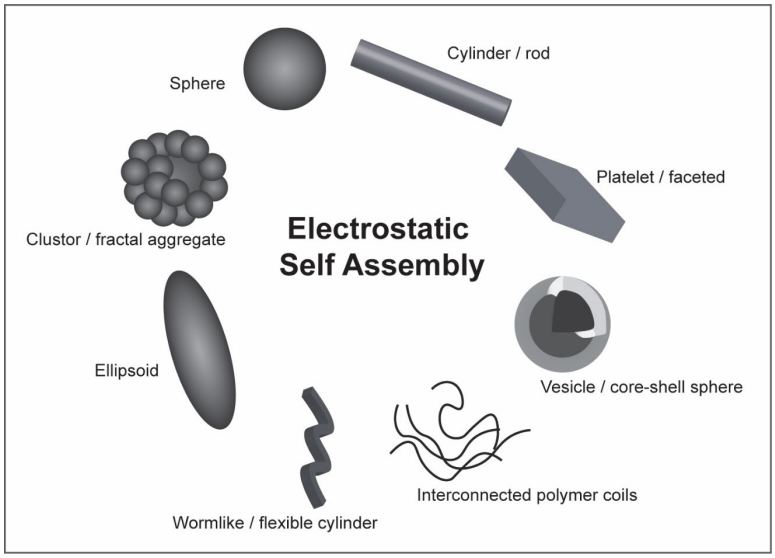


Figure 1 Schematic representation of electrostatic self-assembly in solution. Oppositely charged components, such as charged macromolecules, colloidal particles, surfactants, or multivalent molecular counterions, associate through electrostatic interaction to form organized supramolecular structures or nano-objects. The final morphology depends on charge ratio, ionic strength, molecular architecture, and additional secondary interactions.

The resulting assemblies are governed not only by charge attraction, but also by the balance of counterion release, chain or particle architecture, charge density, stoichiometry, ionic strength, pH, and solvation [15,51–58]. In many cases, electrostatic attraction first brings oppositely charged components into close proximity, while additional interactions such as hydrogen bonding, aromatic interactions, hydrophobic effects, or dipolar contributions influence local packing and final morphology. As a result, electrostatic self-assembly can generate a

wide range of structures, from dense complexes and coacervate phases to discrete nano-objects and ordered hierarchical architectures[59,60].

1.2.2. Established Electrostatic Self-Assembly Platforms

Electrostatic self-assembly has been extensively explored as a route to functional materials and organized soft-matter systems. One of the most established examples is the layer-by-layer assembly of oppositely charged polyelectrolytes, in which alternating adsorption produces multilayer films with tunable thickness, composition, and functionality [61–68]. Related approaches have been used to prepare coatings, capsules, membranes, and surface-supported architectures for applications in sensing, controlled release, catalysis, and biomedical materials [50,69–72].

Beyond thin films and interfaces, electrostatic association has also been used to generate interpolyelectrolyte complexes, complex coacervates, and colloidal aggregates in bulk solution [73,74]. These systems have demonstrated that electrostatic attraction between oppositely charged species can produce rich phase behavior and a broad range of morphologies [54,75]. At the same time, much of the established work focused either on macroscopic materials, bulk condensed phases, or surface-directed assembly [76]. Compared with these areas, the controlled formation of structurally defined and stimulus-responsive nano-objects in dilute aqueous solution remained less systematically understood, especially for systems in which morphology emerged from the interplay of electrostatics with more specific secondary interactions.

1.2.3. Motivation for Solution-Phase Macroion–Multivalent Counterion Assemblies

Solution-phase assemblies formed from charged macroions and oppositely charged multivalent molecular species are particularly attractive because they combine structural simplicity with a high degree of tunability [9,55,77]. Macroions provide defined size, shape, and charge density, while multivalent counterions can contribute not only charge compensation but also molecular anisotropy, aromaticity, dipolar character, or specific short-range interactions [18,39,61]. In such systems, long-range electrostatic attraction drives the association of oppositely charged components, while molecular architecture and additional non-covalent interactions influence the resulting morphology [49,71]. This combination makes macroion–multivalent counterion assemblies especially suitable for investigating how molecular-level interactions are translated into mesoscopic structure in aqueous solution.

In contrast to electrostatically assembled films or bulk complexes, solution-phase nano-objects can remain dynamic and structurally responsive under mild conditions. Their morphology may be tuned by charge ratio, ionic strength, pH, concentration, and molecular design, making them highly relevant as model systems for responsive self-

assembly [52,78–80]. At the same time, these assemblies provide mechanistic insight into a central question of soft-matter science: how long-range electrostatic attraction and local structure-directing interactions cooperate to generate spheres, rods, ellipsoids, networks, or other morphologies in aqueous solution [55,81–83].

This solution-phase approach is particularly relevant for the systems discussed in this thesis, where charged macromolecular building blocks are interconnected by oppositely charged multivalent molecular counterions to form discrete and structurally tunable nano-objects in water. Here, electrostatic interactions provide the initial driving force for association, while secondary interactions and molecular design enable control over size, shape, and responsiveness.

1.3. Stimuli-Responsive and Light-Switchable Self-Assembly

Self-assembled nano-objects are especially attractive when their structure and properties can be altered in a controlled and reversible manner by external stimuli [9,55,84–86]. Because these systems are governed by non-covalent interactions, relatively small changes in the environment can shift the balance of attractive and repulsive forces, thereby inducing assembly, disassembly, or structural reorganization [88,89]. This responsiveness is highly relevant for adaptive soft materials, controlled delivery systems, sensing, and functional nanostructures whose behavior can be regulated on demand [50,89].

A variety of external triggers have been used to control self-assembled systems, including changes in pH, temperature, ionic strength, redox conditions, solvent composition, and the application of electric or magnetic fields [4,90–92]. Among these triggers, light is particularly attractive because it can be applied remotely and with high spatial and temporal precision, while avoiding direct chemical perturbation of the system. In addition, light-triggered processes can often be switched reversibly, which makes them especially useful for studying dynamic structural changes in soft-matter systems [9,51–53,59,93–99].

1.3.1. Molecular Approaches to Light-Responsiveness

Different molecular approaches have been developed to introduce light-responsiveness into self-assembled systems [89,100,101]. One widely used strategy is based on photoisomerization, in which irradiation induces a reversible change in molecular geometry and often also in polarity, dipole moment, or packing behavior [52,102,103]. Typical examples include azobenzenes, spiropyrans, and diarylethenes, which have been widely used to control supramolecular organization and materials properties [9]. Other approaches rely on photoacids or photobases, which modulate protonation equilibria, or on photolabile groups, which undergo bond cleavage upon irradiation [17,96,104]. More advanced concepts include light-driven molecular motors, which convert light energy into directional molecular motion and thereby enable dynamic control beyond simple equilibrium switching [105–107].

When such light-responsive units are incorporated into self-assembled systems, irradiation can alter intermolecular interactions and thereby influence the formation, stability, and morphology of the resulting nano-objects [87,108,109]. In aqueous environments, this effect is especially interesting because light-induced changes in molecular structure may shift not only local packing but also solvation behavior, dipolar interactions, and electrostatic balance [52,110]. Light-responsive self-assembly therefore provides an effective strategy for connecting molecular-scale switching processes to mesoscopic structural transformations.

1.3.2. Polyamidoamine (PAMAM) Dendrimers in Light-Responsive Electrostatic Self-Assembly

This concept becomes particularly powerful when combined with electrostatic self-assembly. In such systems, oppositely charged building blocks are first brought together by Coulombic attraction, while additional interactions determine how the components pack and what morphology is ultimately formed. Because electrostatic interactions are largely non-directional, the selection of suitable counterions is particularly important. Counterions that additionally provide directional or structure-directing interactions can reduce uncontrolled aggregation and promote the formation of defined nanostructures. Light-responsive electrostatic self-assembly is therefore a promising route to switchable nano-objects in aqueous solution, in which molecular switching can be translated into structural reorganization of the assembled state.

Polyelectrolytes are macromolecules that contain ionizable groups and therefore carry charge in aqueous solution. Because of their charged character, they interact strongly with oppositely charged species and are widely used as building blocks in electrostatic self-assembly [58]. Their behavior depends on factors such as charge type, charge density, chemical composition, molecular weight, and conformation in solution [111]. In particular, polyelectrolyte-based assemblies are attractive because their structure and stability can be tuned by pH, ionic strength, stoichiometry, and molecular architecture.

In the present work, **the positively charged macroionic component is based on poly(amidoamine) (PAMAM) dendrimers**. PAMAM dendrimers are synthetic, highly branched polyelectrolytes with a well-defined and monodisperse architecture. They consist of a central core from which branches containing amide and amine groups grow in a regular stepwise manner, leading to precise molecular weights, sizes, and surface functionalities. Owing to their defined structure, tunable surface chemistry, and compatibility with aqueous environments, PAMAM dendrimers have been widely investigated in biomedical and soft-matter contexts [112].

A key feature of PAMAM dendrimers is their pronounced pH-dependent charge behavior, which arises from the presence of ionizable primary, secondary, and tertiary amine groups. The protonation state of these groups affects the overall charge, conformation, solubility, and

intermolecular interactions of the dendrimer. Figure 2 shows the molecular structure of a G5 PAMAM dendrimer under basic, neutral, and acidic conditions. The G5 dendrimer contains 128 primary amine groups at the periphery and 126 tertiary amine groups within the interior. Because the charge state of these amines changes with pH, PAMAM dendrimers provide a versatile platform for studying how electrostatic interactions govern association with oppositely charged molecular species [99].

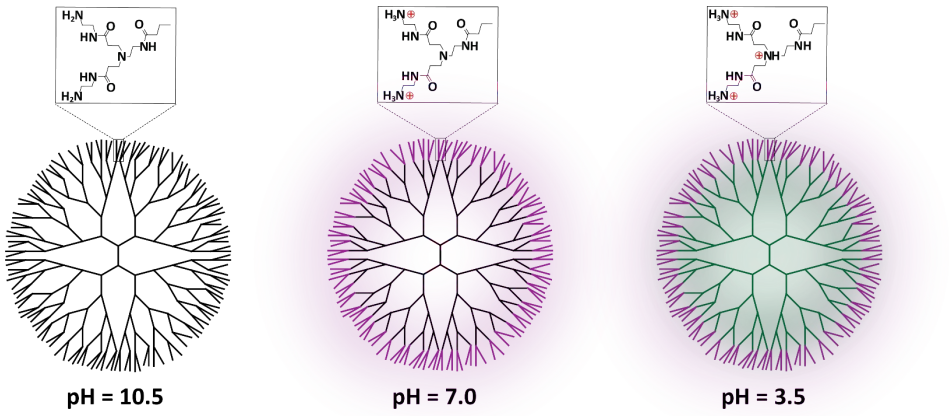


Figure 2 Molecular structure of G5 PAMAM dendrimer in basic, neutral, and acidic medium. Green color lines represent the tertiary positively charged amine groups, and violet represents the primary positively charged amines (the chemical structure of the outer layers is shown in the boxes on top).

For electrostatic self-assembly to occur, positively charged polyelectrolytes require oppositely charged counterions. In the context of solution-phase nanostructure formation, these counterions are not merely charge-compensating species, but can also act as functional molecular building blocks that influence the morphology and stability of the resulting assemblies. Suitable counterions therefore play a central role in determining the morphology and stability of electrostatically assembled structures. In addition to charge compensation, they may contribute further interactions such as hydrogen bonding, aromatic π–π interactions, dipole–dipole interactions, van der Waals forces, and hydrophobic or hydrophilic effects, which can influence packing and structural organization [9,52,78,96,99,113].

This combination of long-range electrostatic attraction with more specific secondary interactions is especially promising when multivalent organic counterions are used. Among these, azo dyes are particularly interesting because they combine anionic charge with aromatic and photoresponsive character. Many azo dyes contain sulfonate groups, which provide strong electrostatic attraction toward positively charged dendrimers, especially at neutral or acidic pH where PAMAM dendrimers are protonated. At the same time, their aromatic backbones can participate in π–π interactions, dipolar interactions, and hydrophobic association, thereby contributing to structural stabilization and directional organization within the assembly [52,98,114].

1.3.3. Acid Yellow 38 as a Light-switchable Model Counterion

Azo dyes are particularly suitable molecular building blocks for light-responsive self-assembly because their molecular geometry and polarity can be altered by photoisomerization. Upon irradiation with light of an appropriate wavelength, azo groups can undergo reversible *trans–cis* isomerization. The *trans* form is usually thermodynamically more stable, whereas the *cis* form is bent, less stable, and can thermally relax back to the *trans* state. This change in molecular geometry can influence packing, dipole moment, binding strength, and secondary interactions within self-assembled structures. Therefore, azo dyes are useful candidates for translating molecular photoswitching into structural changes at the nanoscale.

In this thesis, **particular attention is given to Acid Yellow 38 (AY38) as a multivalent photoresponsive counterion**. AY38 contains two azo bonds and two sulfonate groups. The sulfonate groups enable electrostatic complexation with positively charged PAMAM dendrimers, whereas the azo groups provide photosensitivity through reversible *trans–cis* isomerization upon irradiation with light of an appropriate wavelength. The *cis* isomer is less stable and relaxes thermally back to the *trans* state, with a half-life of approximately 12 h for AY38 under the relevant conditions [52,96]. This photoisomerization can be followed conveniently by UV-visible spectroscopy, as shown in Figure 3.

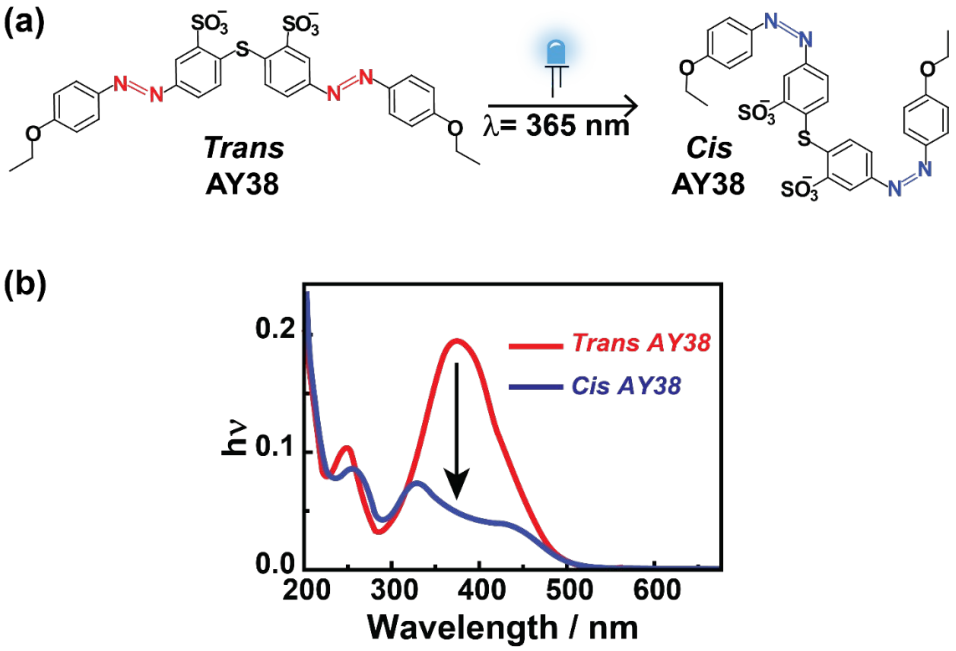


Figure 3 The effect of light-irradiation on Acid Yellow 38 azo dye is shown by (a) the molecular structures of different isomerization states, and (b) the UV-visible absorption studies of 1.0×10^{-4} molL^{-1}AY38 in H_2O.

The combination of PAMAM dendrimers and AY38, therefore, provides a well-defined model system for investigating light-responsive electrostatic self-assembly in aqueous solution. This system builds on earlier work from the Gröhn group, where electrostatic self-assembly of charged macroions and multivalent molecular counterions was

introduced as a route to defined nano-objects in water [52,55,115]. In such assemblies, charged macromolecules are interconnected by oppositely charged molecular species, rather than merely neutralized by small counterions. Previous studies further showed that molecular features, charge ratio, secondary interactions, and association thermodynamics can determine the size and shape of the resulting nano-objects [59,95].

Stimuli-responsive electrostatic self-assembly expands this concept by using building blocks whose interactions can be altered by external triggers. Changes in pH, temperature, redox conditions, light irradiation, or combinations of several stimuli have been shown to affect the size, shape, stability, and function of electrostatically assembled nano-objects [52,96,114]. Among these triggers, light is particularly attractive because it can be applied non-invasively and with temporal control, making it suitable for inducing structural changes directly in aqueous solution [9,93,116]. Earlier studies had already demonstrated light-responsive micellar systems [117], light-responsive electrostatically self-assembled nanostructures based on azobenzene-peptide assemblies [118], and interactions of azo dyes with cationic surfactants [119].

For azo-dye-based electrostatic self-assembly, a decisive step was the demonstration by the Gröhn group that photoirradiation can directly control nano-object size in aqueous systems composed of azo-switchable anionic dyes and cationic dendrimer macroions [52,58,114]. In these systems, electrostatic attraction brings the oppositely charged components together, while the molecular structure and photoisomerization behavior of the dye influence the interaction balance, assembly pathway, and final morphology. Thus, the PAMAM–AY38 platform is especially suitable for studying how molecular switching is translated into changes in nanostructure formation and stability. Later, this concept was extended to the first light-switchable particle shape change of an electrostatically self-assembled nano-object [96]. Related work further broadened the responsive landscape toward multistimuli systems and other responsive architectures, including azobenzene-functionalized peptides, light-, pH-, and metal-ion-responsive assemblies, and pH-triggered porphyrin-silica release systems [120–122].

While these studies established light as a powerful trigger for responsive electrostatic self-assembly, several structure-directing principles of AY38/PAMAM assemblies were still not fully resolved before the work presented in this thesis. In particular, it remained unclear how charge ratio, concentration, dendrimer generation, effective surface charge, secondary interactions, and photoisomerization jointly determine particle size, shape, monodispersity, and multimodality. Moreover, previous studies mainly compared structures before and after irradiation, whereas the actual light-induced restructuring pathway, including possible intermediate states, kinetic effects, and preparation-route dependence, had not been directly followed for electrostatic macroion–azo dye assemblies.

First advances toward real-time analysis of responsive self-assembly had been achieved in other systems using fluorescence spectroscopy, synchrotron SAXS, and combined in-situ UV-Vis/SANS methods to follow dynamic self-assembly and micellar restructuring [123–127]. However, such approaches had not yet been systematically transferred to electrostatic macroion–dye assemblies. Consequently, a detailed understanding of how molecular photoisomerization, charge evolution, and kinetic effects translate into the time-dependent structural evolution of electrostatic nanoassemblies was still missing.

Based on these considerations, PAMAM dendrimers of different generations and Acid Yellow 38 were selected as the central components of this thesis. Their assemblies in aqueous solution were characterized by small-angle neutron scattering (SANS), dynamic and static light scattering (DLS and SLS), UV-visible spectroscopy, isothermal titration calorimetry (ITC), ζ-potential measurements, and ultracentrifugation. Together, these techniques provide complementary insight into the size, shape, interaction mechanisms, and stability of the resulting self-assembled complexes.

1.4. Characterization Techniques

The electrostatically self-assembled systems investigated in this thesis were characterized by a combination of complementary experimental techniques. Detailed methodological descriptions, instrument settings, evaluation procedures, and theoretical background are provided in Chapter 10; in the main text, only a concise overview is given to explain the role of each method and how the different techniques work together to provide a coherent structural and physicochemical picture. This combined approach is essential because no single technique alone is sufficient to resolve the complexity of responsive nanoassemblies in solution. Instead, size, shape, internal structure, molecular interactions, thermodynamics, optical response, and colloidal stability must be assessed in parallel to understand both the formation and the light-induced reorganization of the assemblies.

Small-angle neutron scattering (SANS) is the central structural method in this thesis because it provides direct information on the size, shape, and internal organization of the self-assembled nano-objects on the nanometer length scale. In particular, SANS allows one to distinguish between spherical, ellipsoidal, cylindrical, and more complex particle morphologies and is therefore indispensable for identifying structural transformations in solution. All SANS experiments discussed in this thesis were carried out at the D11 instrument at the Institut Laue-Langevin (ILL), Grenoble, France, and at the SANS-I instrument at the Paul Scherrer Institute (PSI), Villigen, Switzerland.

Dynamic and static light scattering (DLS/SLS) complement SANS by providing rapid, non-invasive access to particle dimensions and overall size behavior. DLS yields the hydrodynamic radius and size distribution of the assemblies and is therefore particularly useful for monitoring particle growth, polydispersity, and aggregation phenomena over a broad size

range. SLS provides additional information on the radius of gyration of the scattering objects, which helps to assess particle topology in solution. In combination, DLS and SLS establish whether the assemblies are monodisperse or multimodal, whether they remain colloidally stable, and how their overall dimensions compare to the structural parameters obtained from SANS. In this way, light scattering offers a fast overview of solution-state behavior, whereas SANS provides the detailed nanoscale structural assignment. Measurements were carried out using an ALV CGS3 goniometer with an ALV 5004 correlator (ALV GmbH, Langen, Germany) equipped with a HeNe laser (λ = 632.8 nm, 23 mW).

UV-visible spectrophotometry provides the molecular-level optical information required to relate nanoscale structure to the state of the photoresponsive building blocks. In the systems studied here, UV-Vis spectroscopy is used primarily to follow the absorption behavior of Acid Yellow 38 in the presence of PAMAM dendrimers, to evaluate photoisomerization, and to identify spectral changes associated with aggregation and intermolecular interactions in solution. In addition, the method is used to estimate the relative fractions of *cis* and *trans* isomers, which is crucial for understanding how light-induced molecular changes translate into variations in particle size and morphology. Thus, while SANS and light scattering describe the nano-object as a whole, UV-Vis spectroscopy reveals the molecular switching processes that drive its restructuring. Absorption spectra were recorded with a JASCO V-630 spectrometer using 1 mm quartz cuvettes.

Isothermal titration calorimetry (ITC) provides the thermodynamic framework for interpreting the assembly process. By measuring the heat released or absorbed during the interaction of Acid Yellow 38 with PAMAM dendrimers, ITC yields binding enthalpy, entropy contributions, and stoichiometric information. These parameters make it possible to assess the energetic balance underlying self-assembly and to distinguish whether association is predominantly driven by electrostatic attraction, hydrophobic contributions, dipole-dipole interactions, or other secondary non-covalent effects. ITC therefore links the structural information obtained from scattering methods with the molecular interaction picture and helps explain why specific particle sizes and morphologies are favored under particular conditions. ITC experiments were performed using a VP-ITC microcalorimeter from MicroCal Inc. (Northampton, MA, USA).

ζ-potential measurements are used to characterize the surface charge and electrostatic stabilization of the assemblies in solution. Since the present systems are formed by electrostatic self-assembly, the effective surface charge is a key parameter governing colloidal stability, interparticle interactions, and the tendency toward further aggregation or restructuring. ζ-potential measurements, therefore, provide important information on the electrostatic balance of the nano-objects and help rationalize differences in particle stability and morphology under varying composition or irradiation conditions. In combination with DLS, SLS, and SANS, they connect charge characteristics with nanoscale

size and shape; together with UV-Vis and ITC, they further help relate optical switching and binding energetics to the colloidal behavior of the assemblies. Measurements were conducted using a Zetasizer Nano ZS analyzer with an integrated 4 mW HeNe laser (λ = 633 nm, Malvern Instruments Ltd., Malvern, UK).

Taken together, these techniques provide a multi-level characterization strategy: UV-Vis spectroscopy probes the molecular photoresponse, ITC quantifies the interaction thermodynamics, ζ-potential reports on electrostatic stabilization, DLS and SLS describe the overall particle dimensions and solution behavior, and SANS resolves the detailed nanoscale morphology and internal structure. These combined methodologies allow the responsive electrostatic self-assembly processes discussed in this thesis to be understood in a comprehensive and internally consistent manner.

2. Objective

Despite the considerable progress made in electrostatic self-assembly, important questions remain open concerning how light-responsive molecular changes are translated into structural changes of nanoassemblies in aqueous solution. In particular, the coupling between molecular switching, intermolecular interactions, structure formation, and structural evolution under irradiation is still not sufficiently understood. This thesis, therefore, aims to investigate light-tunable electrostatic self-assembly in water using photoresponsive molecular building blocks and to clarify which parameters govern the formation, stability, and reorganization of the resulting nano-objects.

One focus of this thesis is to examine how photoacids can be used as building blocks for switchable electrostatic self-assembly in aqueous solution. Photoacids exhibit a higher degree of deprotonation in the excited state and therefore undergo proton dissociation upon light excitation, leading to an irradiation-induced increase in anionic charge. This charge change makes them suitable molecular switches for controlling electrostatic interactions, assembly formation, particle stability, and structural response. For this purpose, model systems based on PAMAM dendrimers and naphthol-based photoacids are investigated in order to study how differences in molecular structure, acidity, and irradiation-induced charge changes influence association behavior, particle stability, and structural response. In this way, the thesis seeks to establish how molecular properties of the photoacid affect both the initial assembly formation and the behavior upon irradiation.

Another key aspect is to improve the understanding of which interactions determine the direction and extent of the light response in these systems. Particular attention is given to the interplay of electrostatic interactions with secondary interactions such as π-π interactions and dipole-dipole interactions. The aim is to clarify how this interaction balance influences whether assemblies grow or shrink, change shape, remain monodisperse, or develop broader structural distributions under different conditions.

A further objective is to characterize the nanoscale structures and morphologies of the assemblies in a systematic and detailed way over a broad range of conditions. This includes variations in molecular building-block structure, component ratio, concentration, dendrimer generation, and irradiation conditions. A central aim here is to relate these control parameters to particle size, shape, internal organization, dispersity, and colloidal stability, and thereby to identify the main factors that govern structural control in light-responsive electrostatic self-assembly.

In addition, the thesis aims to investigate multistimulus-responsive systems in which photoacids are combined with further switchable molecules. The goal is to examine whether different external triggers,

such as light of different wavelengths, pH, and thermal recovery, can be translated into reversible and distinguishable structural responses without inducing uncontrolled aggregation. This part of the thesis is intended to broaden the scope of the systems studied and to test how multiple switching mechanisms can act together within one self-assembled nano-object.

Beyond the characterization of final assembled states, this thesis aims to understand how responsive electrostatic nanoassemblies form and reorganize. Previous work has shown that light can control the size and shape of electrostatically assembled nano-objects, but the underlying structural pathways leading from the initial state to the final switched state have remained much less understood. Therefore, this work focuses not only on the endpoint morphologies before and after irradiation, but also on the processes by which these structures are reached. A central objective is to clarify how molecular switching events are translated into nanoscale structural evolution. In particular, the thesis investigates how azo dye *trans–cis* isomerization and photoacid deprotonation influence charge characteristics, interaction strength, particle stability, size, shape, and internal structure. Special attention is given to the role of charge ratio, concentration, dendrimer generation, and preparation pathway in determining whether assemblies remain well-defined, become multimodal, or undergo light-induced restructuring.

To address these questions, this thesis combines established scattering and spectroscopic methods with time-resolved structural analysis. In particular, an irradiation setup for SANS under in-situ UV irradiation is developed and applied in order to follow light-induced reorganization directly in solution. This approach is used to distinguish restructuring pathways from endpoint morphologies, identify kinetic effects and possible intermediate states, and determine how preparation route and irradiation conditions influence the final nanoscale architecture. In this way, the thesis seeks to establish a mechanistic understanding of switchable electrostatic self-assembly in aqueous solution. The goal is to connect molecular properties of the photoresponsive building blocks with both the final nanoassembly structure and the pathway by which this structure is formed, thereby providing design principles for responsive nano-objects with controllable structural evolution. By combining DLS, SLS, SANS, UV-Vis spectroscopy, ζ-potential measurements, and isothermal titration calorimetry, this thesis seeks to obtain a coherent picture of how molecular switching, interaction balance, nanoscale structure, and structural evolution are connected in light-responsive electrostatic self-assembly. On this basis, broader structure-directing relationships and key control parameters are discussed, while open questions and limitations are identified as a basis for future work.

3. Own Contributions

In the following chapters, the thesis investigates light-tunable electrostatic self-assembly in aqueous solution, emphasizing structural control and mechanistic insight from scattering methods. Photoswitchable azo dyes and well-defined macroions form nanoassemblies whose size, dispersity, and morphology are programmed by irradiation, charge ratio, concentration, and preparation route, ranging from a few nanometers to colloidal-sized assemblies. Light-driven molecular state changes are linked to effective surface charge density and interaction balance, showing how macroion architecture, including dendrimer generation, controls the switching response and accessible structures. SANS under in-situ UV irradiation resolves restructuring pathways and kinetics. Supporting chapters cover photoacid assemblies enabling reversible proton transfer switching and multi-stimulus addressability.

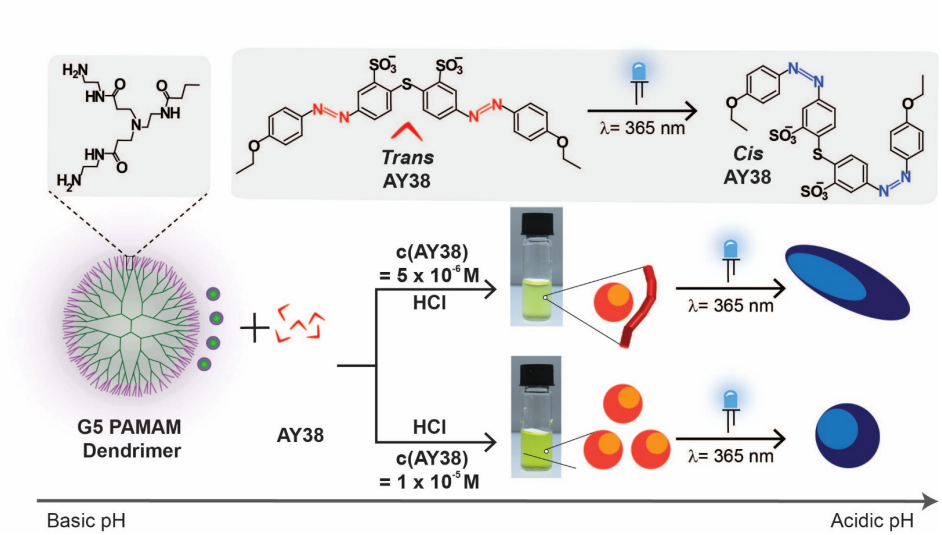
3.1. Morphology Control in Light-Responsive Electrostatic Nanoassemblies

Mohit Agarwal, Alexander Zika, Ralf Schweins, Franziska Gröhn; Controlling the Morphology in Electrostatic Self-Assembly via Light, *Polymers,* **2024***, 16(1),* 50.

This study establishes the central model platform used to develop light-tunable structures by electrostatic self-assembly in water and introduces the key experimental logic of the thesis. The guiding scheme 1 places a well-defined cationic macroion, a generation 5 PAMAM dendrimer, in controlled electrostatic contact with a multivalent anionic photoswitch, the azo dye Acid Yellow 38 (AY38). Assembly formation is gated by pH. At basic conditions (pH about 10.5), the dendrimer amines are largely uncharged, and complexation is suppressed. Upon acidification to a pH of about 3.5, the dendrimer becomes fully protonated (254 amine groups), enabling strong electrostatic association with the sulfonated azo dye. This preparation strategy is essential for the thesis because it separates a reproducible starting state from the subsequent light-driven perturbation, allowing structural changes under irradiation to be interpreted mechanistically rather than as preparation specifics.

A central control parameter is the charge ratio, l_c, defined as the ratio of anionic to cationic charge contributions, accounting for both the number of charges and the concentrations of dye anions and dendrimer cations. By systematically varying l_c and the absolute building block concentrations, the work maps a broad structural landscape and demonstrates that assemblies can be tuned from approximately 10 nm up to the colloidal regime, with morphologies including spheres, ellipsoids, cylinders, and flexible cylinders. The light trigger is UV

irradiation at 365 nm, which drives *trans* to *cis* isomerization of AY38 (with a long *cis* lifetime under acidic conditions). This molecular change modifies secondary interactions, particularly dipole-dipole interactions, within assemblies that are already held together by electrostatic attraction.



Scheme 1. Preparation of electrostatic self-assembly of AY38 azo dye and G5 PAMAM dendrimer, and the effect of building blocks concentrations on the nanoparticle structures in aqueous solution. Polymers, **2024**, 16(1), 50.

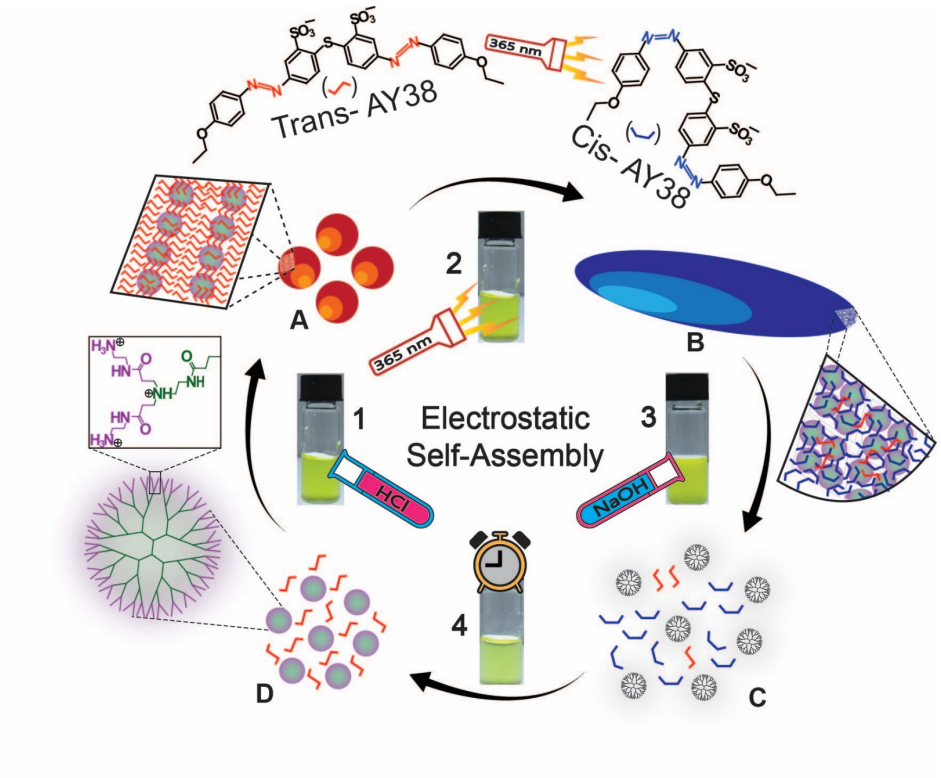
Scattering-based characterization provides the decisive link between molecular switching and mesoscale structure. In SANS, the measured scattering profile *I(q)* encodes morphology through the form factor, i.e., the characteristic *q*-dependence associated with particle shape and internal structure, while inter-particle correlations contribute via the structure factor. As a consequence, distinct morphologies (e.g., spherical, ellipsoidal, or rod-like objects) yield diagnostic features in *I(q)*, enabling shape changes to be separated from simple size growth. In contrast, dynamic and static light scattering quantify size distributions and dispersity and are therefore not uniquely assignable to a specific structural transition without additional constraints. The results show clear regime dependent behavior: at strong excess of positive charges, structures remain stable and largely unchanged under irradiation due to limited dye content; at moderate dye excess, irradiation induces pronounced size and shape transformations, for example converting small spheres into ellipsoidal assemblies; at higher dye excess, bimodal mixtures of small spheres and highly elongated objects emerge, yet irradiation can collapse these multimodal populations into highly monodisperse spherical particles, consistent with disassembly of surplus dye associated through secondary interactions. Collectively, this section provides the design map that motivates the thesis focus on in SANS under in-situ UV irradiation as the most direct route to connect switching, interaction balance, and structural evolution.

3.2. How Macroion Architecture Sets the Switching Response

Mohit Agarwal, Alexander Zika, Müge Yücel, Joachim Kohlbrecher, Ralf Schweins, Franziska Gröhn; The Role of Light Irradiation and Dendrimer

Generation in Directing Electrostatic Self-Assembly, *Polymers,* ***2025,*** *17(2), 170.*

This work extends the design logic established in Section 3.1 by introducing macroion architecture as an independent and systematic control parameter. The central scheme 2 frames the assemblies as a light addressable system: dendrimer and azo dye form electrostatic complexes under acidic conditions, irradiation induces dye isomerization and structural reorganization, and subsequent adjustment of solution conditions enables the system to be reset and probed reproducibly. Within this framework, the dendrimer generation is varied to modulate the size, valency, and charge density of the macroion scaffold while keeping the photoswitch chemistry constant. This strategy is crucial for the thesis objective because it enables the separation of two commonly entangled effects: changes caused by the molecular photoswitch itself and changes caused by the electrostatic environment in which switching occurs.



Scheme 2. Simplified sketch of the recurring assembly formation at the nanoscale. The molecular structures of dendrimers and the AY38 are shown. Red objects represent simplified *trans*, and blue objects indicate *cis*-dye molecules. The glass vials carry the same sample solution at different steps of the cycle. A UV lamp with a 365 nm wavelength is used in the experiment. Polymers, **2025**, 17(2), 170

A key outcome is that dendrimer generation controls not only assembly morphology but also the extent of photoswitching within the assembled state. Under irradiation, the azo dye undergoes *trans* to *cis* isomerization; however, the effective conversion is dendrimer generation dependent because dye molecules located within or near the

dendrimer rich environment can be partially shielded, leading to a photoprotective effect. Consequently, the ensemble *cis* fraction becomes an emergent structural variable: it reflects both photochemistry and confinement, and it directly affects binding asymmetry between isomers. Since *trans* and *cis* dyes differ in geometry and interaction propensity, differences in *cis* fraction feed back into charge neutralization, effective surface charge density, and colloidal stabilization.

Experimentally, this subsection establishes how generation dependent architecture maps onto measurable structural responses. In the absence of irradiation, assemblies formed across the studied generations remain relatively well-defined, reflecting robust electrostatic complexation. Upon irradiation, the restructuring amplitude and the resulting size range increase markedly and can differ strongly between generations, including the appearance of secondary populations at higher generations. These trends are quantified by multi-angle dynamic and static light scattering and validated structurally by SANS, which provides model-based evidence for generation-dependent form factor changes rather than relying on hydrodynamic size alone. Electrokinetic measurements link these structural differences to effective surface charge density, and complementary spectroscopic and thermodynamic analyses provide the molecular and energetic basis for the observed restructuring.

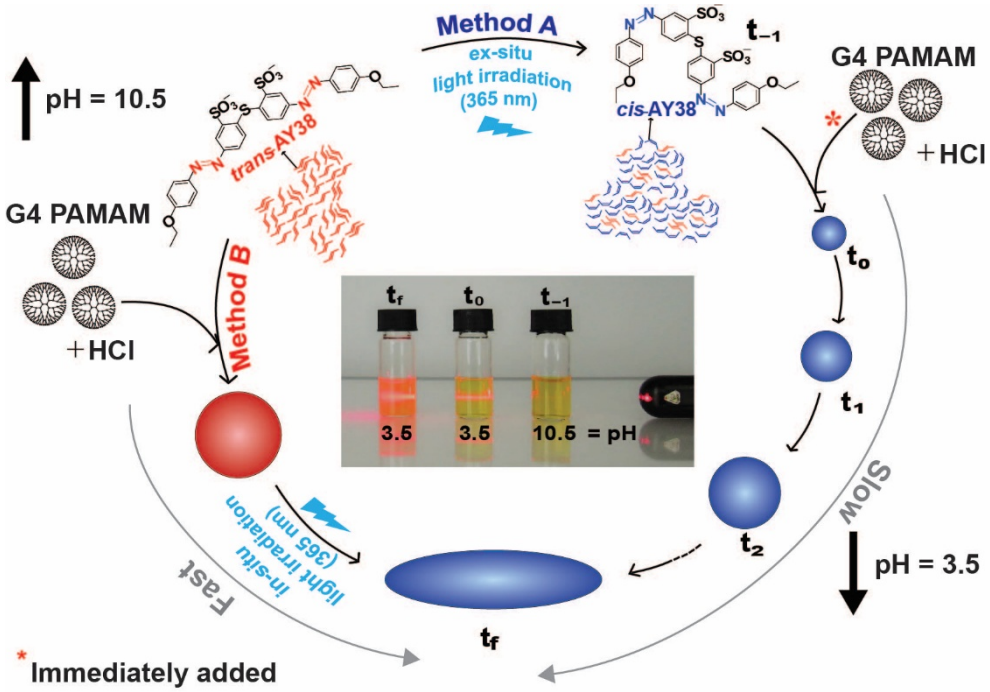
In the context of the thesis, this subsection establishes a transferable principle: macroion architecture is an active design element that governs how effectively light-induced molecular switching is expressed at the nanoscale. By controlling charge density, shielding, and binding site availability, dendrimer generation defines the range of accessible assembly states and determines whether irradiation produces subtle adjustment, strong morphological transitions, or multimodal restructuring. This architecture dependent perspective sets the stage for the in-situ irradiation experiments, where pathway and kinetic control can only be interpreted correctly when the generation dependent switching constraints are understood.

3.3. SANS Under In-Situ UV Irradiation: Pathways, Kinetics, and Intermediates

Mohit Agarwal, Ralf Schweins, Franziska Gröhn; Light-Induced Structural Evolutions in Electrostatic Nanoassemblies, *Polymers, **2026**, 18(2), 190.*

Light-responsive electrostatic assemblies are usually discussed in terms of “before” and “after” irradiation structures; however, for charged assemblies this perspective is often insufficient because the observed morphology can depend strongly on whether the system relaxes to an equilibrium state or becomes trapped in a metastable configuration. This work, therefore, formalizes the pathway question

that motivates the in-situ perspective of the thesis: under which conditions are the assemblies thermodynamically controlled, and when can the preparation route, including the irradiation protocol, lead to a different final structure (Scheme 3).



Scheme 3. Representation of the two different pathways to prepare electrostatic assemblies of anionic azo dye molecules and cationic dendrimer macroions (Acid Yellow 38 and G4 PAMAM dendrimer). Method A (pre-irradiation) slows down the formation of assemblies by a factor of 10 compared to method B (post-irradiation). The light irradiation occurs at λ = 365 nm for 20 min in both methods. The picture in the middle represents the scattering of samples in method A at different times (t_{-1} = before the addition of acid, t_0 = immediately after mixing the acid, t_f = after 3 h). Polymers, **2026**, 18(2), 190.

The analysis builds on the distinction between thermodynamically controlled assemblies, which represent equilibrium structures, and kinetically controlled assemblies, which may be trapped due to high activation barriers and therefore exhibit preparation dependence. Within the dendrimer–azo dye platform, this is addressed experimentally by probing how sensitively the nanoassemblies respond to controlled changes in composition and processing. In thermodynamically controlled regimes, the assemblies adjust reproducibly to the state favored at a given charge ratio and concentration, indicating that building blocks remain in exchange and that morphology is largely independent of the detailed route used to reach that state. In contrast, kinetically controlled regimes are identified by broader size distributions, bimodal populations, and pronounced sensitivity to mixing conditions and concentration, consistent with the presence of structural intermediates and long-lived non-equilibrium species.

Irradiation is treated in the same framework, not as a simple external trigger but as an additional route parameter that can shift the system between structural basins. UV exposure at a 365 nm wavelength is used to drive *trans* to *cis* isomerization of the azo dye, and the structural response is quantified by scattering methods. Dynamic and static light scattering capture changes in hydrodynamic size and polydispersity, while SANS provides the decisive form factor-based discrimination between genuine shape transitions and mere size growth. Supporting analyses further group samples into thermodynamically and kinetically controlled categories based on charge ratio, concentration, and the effect of irradiation, highlighting that irradiation can either induce modest, near-equilibrium adjustments or reorganize kinetically complex mixtures into more uniform populations.

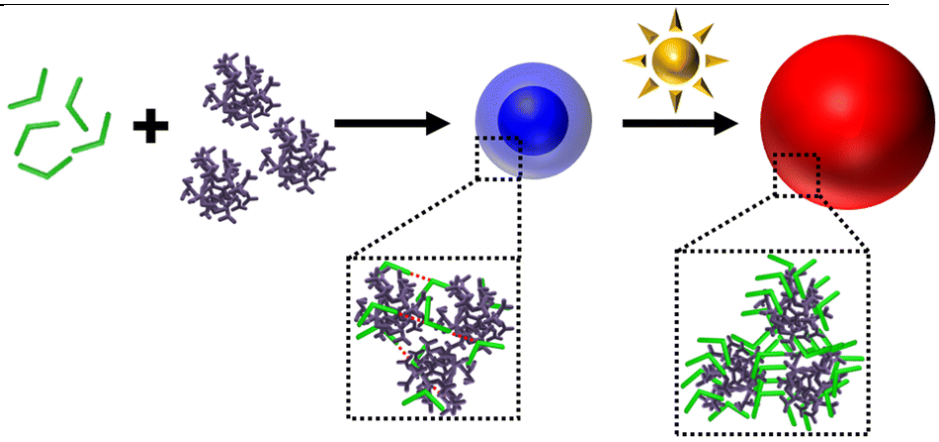
Overall, this study establishes why time and protocol must be treated as first-class design variables in light-tunable self-assembly. Defining when structures are pathway-independent and when they are not provides the direct rationale for using SANS under in-situ UV irradiation in the thesis as the most rigorous route to resolve restructuring pathways, identify intermediates, and connect molecular switching kinetics to mesoscale structural evolution.

3.4. Photoacid-Based Assemblies and Multi-Addressable Switching in Water

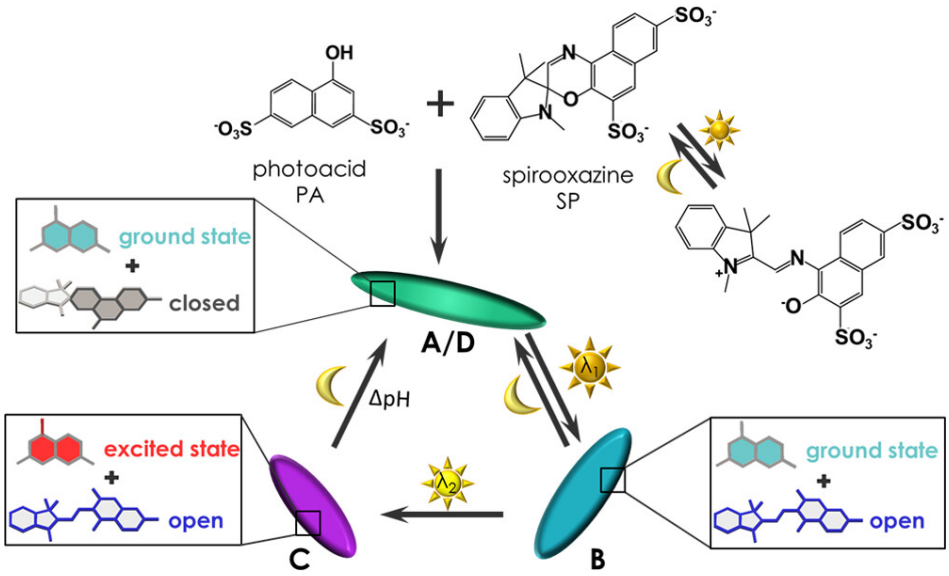
Alexander Zika, **Mohit Agarwal**, Ralf Schweins, Franziska Gröhn; Double-Wavelength-Switchable Molecular Self-Assembly of a Photoacid and Spirooxazine in an Aqueous Solution, *J. Phys. Chem. Lett.,* **2023**, *14*, 9563-9568.

Alexander Zika, **Mohit Agarwal**, Wiebke Zika, Dirk Guldi, Ralf Schweins, Franziska Gröhn; Photoacid-Macroion Assemblies: How Photo-Excitation Switches the Size of Nano-Objects, *Nanoscale,* **2024,** *16*, 923-940.

These studies extend the thesis framework beyond azo isomerization and emphasize how excited state proton transfer can be translated into a controllable nanoscale structure. In both studies, Schemes 4 and 5 provide the conceptual center: they explicitly map a molecular photoreaction onto a structural response and, by doing so, define design rules that align with the thesis focus on light-tunable assemblies validated by scattering.



Scheme 4. Scheme of photoacid-macroion nano-objects and their internal structure before and after irradiation. Before irradiation, free photoacid molecules are also present, but all photoacid molecules are bound in the assembly after irradiation. Nanoscale, **2024**, 16, 923-940.



Scheme 5. Schematic overview of the molecular self-assembly of photoacid and spirooxazine. J. Phys. Chem. Lett., **2023**, 14, 9563-9568.

In the photoacid–spirooxazine system, the scheme illustrates how two water soluble photoswitches are integrated into a single nanoscale object with multiple orthogonal control inputs. Photoexcitation of the photoacid triggers wavelength specific proton dissociation, while independent irradiation of the spirooxazine drives ring opening. The scheme further emphasizes that the resulting assemblies can be addressed not only by two wavelengths, but also by pH and dark or thermal relaxation, enabling a reset pathway and making switching sequences experimentally meaningful. Structurally, this work establishes that multi-addressability can be achieved even when both components are anionic, because assembly is stabilized by noncovalent interactions that become stronger or weaker upon switching. Within the thesis narrative, this provides a clear molecular level demonstration of

"programmable addressability" and motivates the need for scattering based structural validation when several stimuli act simultaneously.

The photoacid–macroion study translates this idea into a more classical electrostatic self-assembly framework. The scheme highlights electrostatic complexation between photoacids and oppositely charged macroions to form well-defined nano-objects whose size is reversibly switched by photoexcitation. Rather than treating the photoacid as a single case, this work systematically connects switching behavior to molecular descriptors by combining acidity in ground and excited states with structural readouts from light scattering and SANS, supported by electrokinetic and thermodynamic analysis. The key contribution to the thesis is that photoexcitation-induced charge modulation is shown to act as a quantitative handle on nano-

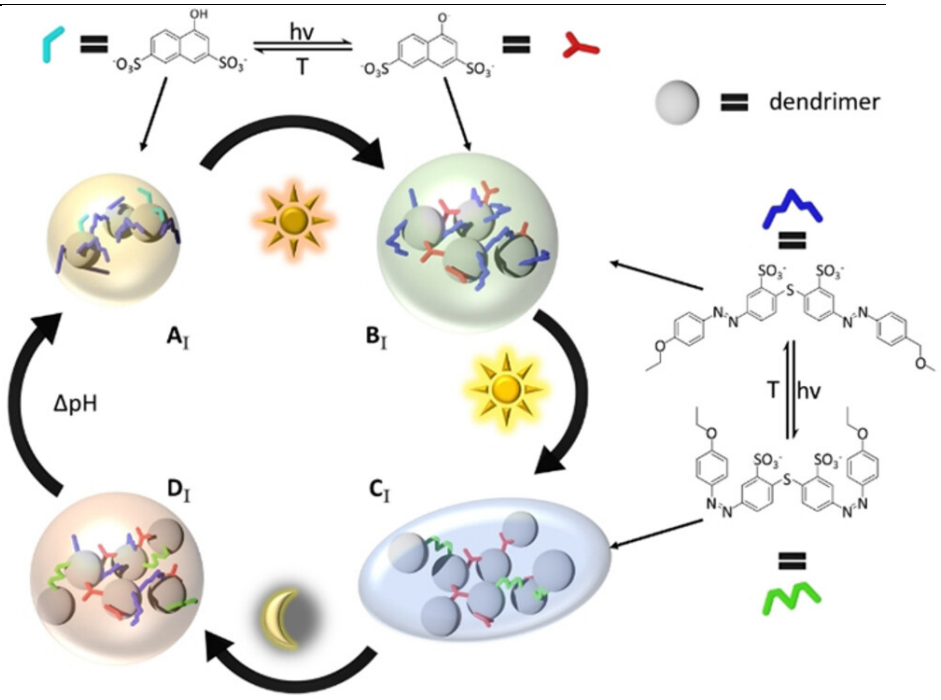
object dimensions, while secondary interactions, including hydrogen bonding and entropic contributions, shape the final structures.

Together, these publications reinforce the thesis main focus by demonstrating that photoacid chemistry offers a robust route to light-tunable structures, both as a multi-switchable molecular platform and as a predictable size-switching strategy in electrostatic macroion assemblies.

3.5. Coupling Photoacidity and Photoisomerization in One Assembly Platform

Alexander Zika, **Mohit Agarwal**, Ralf Schweins, Franziska Gröhn; Joining Two Switches in One Nano-Object: Photoacidity and Photoisomerization in Electrostatic Self-Assembly, *Chem. Eur. J.,* **2022**, e202203373.

This work presents an electrostatic co-assembly approach in which a cationic macroion scaffold is combined with two anionic photoresponsive components, a photoacid and an azo dye, to generate light-responsive nano-objects in aqueous solution. The scheme of the study organizes the system into defined stimulus steps, illustrating how irradiation can be used to access different molecular states within the same assembled object and how these changes translate into measurable structural responses (Scheme 6).



Scheme 6. Schematic overview of the multiswitchable system consisting of AY38, 1N36S, and G4 dendrimer. Chem. Eur. J., **2022**, e202203373.

In this platform, assembly is formed under conditions where electrostatic attraction drives co-localization of the components. Irradiation targeting the photoacid induces a light-driven proton transfer and modifies the charge conditions experienced by the complex. A second irradiation step at a different wavelength addresses the azo dye and induces photoisomerization, thereby changing its molecular geometry and polarity and, consequently, modulating the secondary interactions within the assembly. The experimental cycle and reset elements in the scheme emphasize reproducibility and enable direct comparison of states reached under different irradiation sequences.

Structurally, the study demonstrates that the two photoresponses lead to distinguishable changes in the nano-objects. Scattering-based measurements are used to quantify variations in size and polydispersity and to confirm that irradiation can induce not only size modulation but also changes in particle morphology. Importantly, the results show that the sequence of irradiation steps can influence the outcome, indicating that the response is pathway dependent under certain conditions and that intermediate states can contribute to the final structure.

In the broader context of this thesis, this subsection provides a compact example of how combining different photoresponsive mechanisms can expand the accessible response space of electrostatic nanoassemblies. It also reinforces a central methodological point of the thesis: when multiple switching processes and sequence effects are involved, structural conclusions require direct scattering-based validation, and pathway-dependent restructuring is most effectively

addressed by probing structures under irradiation rather than only at endpoint states.

4. Conclusion

The main objective of the thesis was to establish a coherent framework for designing light-tunable structures by electrostatic self-assembly in water, and to show that structural control is achievable only when molecular switching, interaction balance, and mesoscale structure are treated as a single connected problem. Across the studies collected in Chapter 3, the conceptual progression moves from a controllable model system to architecture-dependent design rules, to explicit pathway awareness, and finally to photoacid-based strategies that broaden the chemical scope of light-tunability. Together, these results define the conceptual and experimental foundation of the thesis main focus: SANS under in-situ UV irradiation as a quantitative bridge between molecular photochemistry and nanoscale structure formation.

The thesis first established the basic structural framework using electrostatic assembly of a well-defined cationic macroion and a multivalent anionic azo photoswitch. It turned out that the charge ratio is a decisive structure-directing parameter. In dendrimer excess, elongated and comparatively stable assemblies were obtained that changed little upon irradiation, whereas at moderate and high dye excess, irradiation induced pronounced restructuring, often converting bimodal or polydisperse systems into larger and more monodisperse nano-objects. The concentration was found to act as a second control parameter: lower concentrations favored larger aggregates, while higher concentrations led to smaller and more compact assemblies because the number of competing dye-loaded macroions increased and growth of individual particles became more limited. Also, the preparation route proved to be structurally relevant, showing that identical building blocks can access different morphologies depending on how the system is brought into the assembled state, in particular, it played a role whether a thermodynamically or kinetically controlled pathway was chosen. These results demonstrate that structural outcomes cannot be inferred from molecular switching alone and that scattering-based analysis is required to distinguish true shape changes from apparent size changes and to quantify polydispersity, multimodality, and structural heterogeneity in a physically meaningful way.

The framework was then strengthened by showing that macroion architecture is an active design element rather than a passive scaffold. Varying dendrimer generation revealed that generation controls not only particle size and shape, but also the aggregation number, extent of bimodality, and the magnitude of the light response. Lower generations behaved as more flexible and accessible building blocks, whereas higher generations introduced stronger steric crowding and reduced accessibility of binding sites. As a result, the largest and most extended light-induced aggregates were not obtained monotonically with increasing generation, but at an intermediate generation where

flexibility and confinement were balanced most favorably. At higher generations, steric hindrance limited dye accessibility and promoted the appearance of additional large aggregates before irradiation. A further key result is that the amount of isomerized *cis* dye depends on dendrimer generation because the nanoenvironment modifies the photochemical response. Thus, the observed switching response is not determined by the molecular properties of the dye alone, but by the assembled state as a whole. In this way, macroion architecture controls both the range of structures that can form and the extent to which these structures can be reorganized by light.

A further step of the thesis was to make the role of time and preparation pathway explicit. The results showed that responsive electrostatic assemblies must often be treated as pathway-sensitive systems and that thermodynamically controlled and kinetically controlled regimes can be distinguished experimentally. At low charge ratio, similar particles were obtained irrespective of preparation route, indicating thermodynamic control. In contrast, under excess dye conditions, different mixing protocols led to markedly different large aggregates, demonstrating kinetic trapping and pathway dependence. This means that irradiation protocol and preparation route are not merely practical details, but genuine structure-directing parameters. A direct consequence is that endpoint measurements alone are insufficient to determine how assemblies restructure, whether intermediate states are involved, or which kinetic bottlenecks govern the response. These insights justify the central role of scattering experiments under in-situ UV irradiation, where the restructuring pathway itself becomes measurable rather than inferred.

The thesis also demonstrates that multi-stimulus responsiveness can be realized within electrostatically assembled nano-objects by combining different photoresponsive mechanisms. In systems containing both photoacidity and photoisomerization, distinct switching modes provided different handles on the same assembly, and the order of activation influenced the final state even at identical composition. This shows that multi-addressability expands the accessible response space beyond what can be achieved with a single photoswitching mechanism alone. At the same time, these studies confirm that spectroscopic readout by itself is not sufficient to assign structural consequences, because identical or similar molecular switching signatures can correspond to different population states or morphologies at the nanoscale.

Finally, the framework was extended beyond classical azo isomerization by demonstrating that photoacid chemistry provides an additional and general route to light-tunability in water. Photoacid-based systems showed that light can modulate charge directly and thereby alter electrostatic association and nano-object dimensions. These studies also revealed that the structural response is not governed by electrostatics alone: dipole-dipole interactions, and entropic contributions can decisively influence the final structure. In this way,

electrostatic attraction provides the assembly scaffold, while the specific photochemistry determines how the hierarchy of interactions is shifted under irradiation. This broadens the concept of light-tunable electrostatic self-assembly from one based only on isomerization to one that also includes light-induced changes in acidity and charge state.

Overall, the thesis establishes several concrete structure-directing relationships. First, the charge ratio governs whether systems remain stable, become bimodal, or reorganize into monodisperse particles under irradiation. Second, concentration controls aggregate growth, with lower concentrations favoring larger aggregates and higher concentrations favoring smaller, more compact ones. Third, dendrimer generation influences accessibility, confinement, and switching amplitude, showing that macroion architecture actively shapes the light response. Fourth, the preparation route and irradiation protocol determine whether the system follows thermodynamic or kinetic pathways and can therefore bias the final morphology. Fifth, the light response is linked to changes in effective surface charge density and secondary interactions, meaning that particle growth, compaction, or shape change arises from a shifted interaction balance rather than from molecular switching alone.

Taken together, these results show that light-tunability becomes programmable only when irradiation, composition, macroion architecture, and preparation pathway are treated as coupled design variables. They further demonstrate that nanoscale response cannot be inferred from endpoint structures alone, since restructuring pathways and assembly conditions decisively shape the translation of molecular switching into supramolecular form. In this way, SANS under in-situ UV irradiation serves not simply as a characterization method, but as a central tool for establishing quantitative and transferable design principles for light-tunable electrostatic self-assembly in aqueous systems. The thesis thus provides a basis for future studies directed toward more robust switching, broader chemical scope, and application-oriented design.

5. Outlook

The results of this thesis show that light-tunable electrostatic self-assembly in water is a promising route toward responsive nano-object design. At the same time, the systems are highly sensitive to their environment, and future work should therefore further define the conditions under which switching remains stable and reversible. Parameters such as ionic strength, ion type, concentration, temperature, and repeated cycling will be particularly important. These factors influence electrostatic screening, interaction strength, molecular switching rates, and assembly kinetics, and will therefore determine whether a system remains reversible or becomes kinetically trapped, merged, or partially irreversible. Long-term cycling experiments will also be essential to assess fatigue, slow side reactions, and practical robustness.

A second important direction is the targeted use of intermediate states in pathway-controlled self-assembly. Transient open or loosely packed structures may offer properties that are not accessible in the final, more compact assemblies, such as temporary accessibility or altered interaction sites. Thus, future systems could be designed not only with a defined final morphology, but also with a programmed sequence and lifetime of structural states. Depending on the intended function, rapid responses may be desirable for sensing, whereas slower and more persistent adaptation may be advantageous for adaptive materials.

The framework developed here should also be extended to a broader range of components while preserving mechanistic clarity. Beyond PAMAM dendrimers, other macroion architectures such as linear polyelectrolytes, block copolymers, proteins, or charged nanoparticles could be used to test the general role of charge distribution, stiffness, confinement, and binding-site accessibility. Likewise, additional photoswitches and combinations of multiple triggers, such as wavelength, pH, and thermal recovery, could expand the accessible range of responsive behavior. In the longer term, this may lead to a broader component toolbox in which structural responses can be anticipated from molecular and supramolecular design parameters.

Time-resolved SANS under in-situ UV irradiation has proven to be a particularly powerful method because it follows structural evolution during switching rather than only before and after it. Future studies could combine this approach with synchronized UV-Vis spectroscopy and light scattering, allowing molecular state, particle populations, and structural evolution to be tracked on the same time axis. Such combined experiments, supported by simple kinetic models, could further translate time-resolved data into transferable structure-directing principles.

The longer-term outlook of this field is especially promising. Responsive electrostatic nanoassemblies offer a route to systems in which light serves not only to trigger molecular change, but also to direct

nanoscale organization, accessibility, and function through the resulting structural response. This opens perspectives for switchable uptake and release, adaptive soft materials, and responsive catalytic environments. In a broader sense, such systems may become relevant for drug delivery, where reversible structural transitions could regulate loading and release; for sensors, where structure-dependent optical or mechanical responses could serve as readout; and for nanoscale systems that integrate more complex photochemical functions, including molecular motors or hierarchical multistimulus switching. Of particular interest is also light-to-chemical energy conversion, where electrostatic self-assembly could provide a dynamic platform for organizing photoactive and catalytic components in water. In this way, the concepts developed in this thesis may contribute not only to a better understanding of responsive self-assembly, but also to the future design of adaptive nanoscale systems with functional relevance.

6. References

1. Lehn, J.M. Supramolecular Chemistry-Scope and Perspectives Molecules, Supermolecules, and Molecular Devices (Nobel Lecture). *Angew. Chemie Int. Ed. English.* **1988**, *27*, 89–112, doi:10.1002/anie.198800891.

2. Whitesides, G.M.; Mathias, J.P.; Seto, C.T. Molecular Self-Assembly and Nanochemistry: A Chemical Strategy for the Synthesis of Nanostructures. *Science* **1991**, *254*, 1312–1319, doi:10.1126/science.1962191.

3. George, W.; Bartosz, G. Self-Assembly at All Scales. *Sci.* **2002**, *295*, 2418–2421, doi:10.1126/science.1070821.

4. Chidambaram, S.; Nehru, K.; Sivakumar, M. Self-Assembling of Nanostructures. *Nanostructure, Nanosyst. Nanostructured Mater. Theory, Prod. Dev.* **2013**, 437–460, doi:10.1201/b15487-16.

5. Vogel, N.; Retsch, M.; Fustin, C.; Campo, A.; Jonas, U. Advances in Colloidal Assembly : The Design of Structure and Hierarchy in Two and Three Dimensions. *Chem. Phys.* **2015**, *115*, 6265–6311, doi:10.1021/cr400081d.

6. Sola, A.; Trinchi, A.; Hill, A.J. Self-Assembly Meets Additive Manufacturing: Bridging the Gap between Nanoscale Arrangement of Matter and Macroscale Fabrication. *Smart Mater. Manuf.* **2023**, *1*, doi:10.1016/j.smmf.2022.100013.

7. Liu, X.; Abbott, N.L. Spatial and Temporal Control of Surfactant Systems. *J. Colloid Interface Sci.* **2009**, *339*, 1–18, doi:10.1016/j.jcis.2009.07.006.

8. Bian, T.; Chu, Z.; Klajn, R. The Many Ways to Assemble Nanoparticles Using Light. *Adv. Mater.* **2019**, *1905866*, 1–17, doi:10.1002/adma.201905866.

9. Krieger, A.; Zika, A.; Gröhn, F. Functional Nano-Objects by Electrostatic Self-Assembly: Structure, Switching, and Photocatalysis. *Front. Chem.* **2022**, *9*, 1–46, doi:10.3389/fchem.2021.779360.

10. Ball, P. Polymers Made to Measure. *Nature* **1994**, *367*, 323–324, doi:10.1038/367323a0.

11. Srebnik, S.; Douglas, J.F. Self-Assembly of Charged Particles on Nanotubes and the Emergence of Particle Rings, Chains, Ribbons and Chiral Sheets. *Soft Matter* **2011**, *7*, 6897–6905, doi:10.1039/c1sm05168g.

12. Wang, J.; Liu, K.; Xing, R.; Yan, X. Peptide Self-Assembly: Thermodynamics and Kinetics. *Chem. Soc. Rev.* **2016**, *45*, 5589–5604, doi:10.1039/c6cs00176a.

13. Ghosh, A.; Haverick, M.; Stump, K.; Yang, X.; Tweedle, M.F.; Goldberger, J.E. Fine-Tuning the PH Trigger of Self-Assembly. *J. Am. Chem. Soc.* **2012**, *134*, 3647–3650, doi:10.1021/ja211113n.

14. Li, L.; Wu, R.; Guang, S.; Su, X.; Xu, H. The Investigation of the Hydrogen Bond Saturation Effect during the Dipole-Dipole Induced Azobenzene Supramolecular Self-Assembly. *Phys. Chem. Chem. Phys.* **2013**, *15*, 20753–20763, doi:10.1039/c3cp52864b.

15. Müller, W.; Schweins, R.; Nöcker, B.; Egold, H.; Huber, K. Comparative Study of the Self-Assembly Behaviour of 3-Chloro-4-Hydroxy-Phenylazo Dyes. *Soft Matter* **2023**, *19*, 4579–4587, doi:10.1039/d3sm00500c.

16. Liu, Y.; Wang, L.; Zhao, L.; Zhang, Y.; Li, Z.; Huang, F. Multiple Hydrogen Bonding Driven Supramolecular Architectures and Their Biomedical Applications. *Chem. Soc. Rev.* **2024**, *53*, 1592–1623, doi:10.1039/d3cs00705g.

17. Zhang, H.; Muhammad, J.; Liu, K.; Ras, R.H.A.; Ikkala, O. Light-Induced Reversible Hydrophobization of Cationic Gold Nanoparticles: Via Electrostatic Adsorption of a Photoacid. *Nanoscale* **2019**, *11*, 14118–14122, doi:10.1039/c9nr05416b.

18. Fu, I.W.; Markegard, C.B.; Nguyen, H.D. Solvent Effects on Kinetic Mechanisms of Self-Assembly by Peptide Amphiphiles via Molecular Dynamics Simulations. *Langmuir* **2015**, *31*, 315–324, doi:10.1021/la503399x.

19. Förster, B.S.; Antonietti, M. Amphiphilic Block Copolymers in Structure- Controlled Nanomaterial Hybrids. *Adv. Mater.* **1998**, *10*, 195–217. doi:10.1002/(SICI)1521-4095(199802)10:3<195:AID-ADMA195>3.0.CO;2-V.

20. Klein, S.; Luchs, T.; Leng, A.; Distel, L.V.R.; Neuhuber, W.; Hirsch, A. Encapsulation of Hydrophobic Drugs in Shell-by-Shell Coated Nanoparticles for Radio- and Chemotherapy — An In Vitro Study. *Bioengineering* **2020**, *7*, 126; 1–21. doi:10.3390/bioengineering7040126.

21. Schulze, E.J.; Wu, M.; Hofmann, C.; Spiecker, E.; Hirsch, A. Synthesis and Self-Assembly of a Discotic Oligo-Carboxylate Tetra- Porphyrin-Perylenebisimide Amphiphile. **2025**, *02093*, 1–7, doi:10.1002/chem.202502093.

22. Bishop, K.J.M.; Wilmer, C.E.; Soh, S.; Grzybowski, B.A. Nanoscale Forces and Their Uses in Self-Assembly. *Small* **2009**, *5*, 1600–1630, doi:10.1002/smll.200900358.

23. Schmuck, C.; Rehm, T.; Klein, K.; Gröhn, F. Formation of Vesicular Structures through the Self-Assembly of a Flexible Bis-Zwitterion in Dimethyl Sulfoxide. *Angew. Chemie - Int. Ed.* **2007**, *46*, 1693–1697, doi:10.1002/anie.200603629.

24. Whitesides, G.M.; Boncheva, M. Beyond Molecules : Self-Assembly of Mesoscopic and Macroscopic Components. **2002**, *99*, 4769–4774, doi:10.1073/pnas.082065899.

25. Lava, K.; Binnemans, K.; Feyter, S. De Hydrogen Bonding Versus van Der Waals Interactions : Competitive Influence of Noncovalent Interactions on 2D Self-Assembly at the Liquid – Solid Interface. **2010**, 14447–14458, doi:10.1002/chem.201001653.

26. Cao, L.; Xu, L.; Zhao, D.; Tahara, K.; Tobe, Y.; Feyter, S. De; Lei, S. Van Der Waals Interaction at the Solid / Liquid. **2014**, 11946–11949, doi:10.1039/c4cc03658a.

27. Barratt, E.; Bingham, R.J.; Warner, D.J.; Laughton, C.A.; Phillips, S.E. V; Homans, S.W. Van Der Waals Interactions Dominate Ligand - Protein Association in a Protein Binding Site Occluded from Solvent Water. *J Am Chem Soc.* **2005**, *127*, 11827–11834, doi: 10.1021/ja0527525.

28. Caputo, G.; Pinna, N. Nanoparticle Self-Assembly Using π-π Interactions. *J. Mater. Chem. A* **2013**, *1*, 2370–2378, doi:10.1039/c2ta00534d.

29. Harding, P.; Harding, D.J. Driving Molecular Self-Assembly with π–π Interactions. *Trends Chem.* **2024**, *6*, 575–576, doi:10.1016/j.trechm.2024.07.002.

30. Hoeben, F.J.M.; Jonkheijm, P.; Meijer, E.W.; Schenning, A.P.H.J. About Supramolecular Assemblies of π -Conjugated Systems. *Chemical Reviews* **2005**, *105*. 1491-1546, doi:10.1021/cr030070z.

31. De Greef, T.F.A.; Meijer, E.W. Supramolecular Polymers. *Nature* **2008**, *453*, 171–173, doi:10.1038/453171a.

32. Besenius, P.; Portale, G.; Bomans, P.H.H.; Janssen, H.M.; Palmans, A.R.A.; Meijer, E.W. Controlling the Growth and Shape of Chiral Supramolecular Polymers in Water. **2010**, *107*, 17888–17893, doi:10.1073/pnas.1009592107.

33. Aida, T.; Meijer, E.W.; Stupp, S.I. Functional Supramolecular Polymers. *Science* **2012**, *335*, 813–817, doi:10.1126/science.1205962.

34. Würthner, F.; Kaiser, T.E.; Saha-möller, C.R. J-Aggregates : From Serendipitous Discovery to Supra- Molecular Engineering of Functional Dye Materials. *Angew. Chem. Int. Ed.* **2011**, 3376–3410, doi:10.1002/anie.201002307.

35. Ernst, L.; Song, H.; Kim, D.; Würthner, F. Photoinduced Stepwise Charge Hopping in π-Stacked

Perylene Bisimide Donor – Bridge – Acceptor Arrays. *Nat. Chem.* **2025**, *17*, doi:10.1038/s41557-025-01770-7.

36. Naumov, P.; Sakurai, K.; Ishikawa, T.; Takahashi, J.; Koshihara, S.Y.; Ohashi, Y. Intramolecular Nitro-Assisted Proton Transfer in Photoirradiated 2-(2′,4′-Dinitrobenzyl)Pyridine: Polarized Optical Spectroscopic Study and Electronic Structure Calculations. *J. Phys. Chem. A* **2005**, *109*, 7264–7275, doi:10.1021/jp0520392.

37. Klajn, R.; Bishop, K.J.M.; Grzybowski, B.A. Light-Controlled Self-Assembly of Reversible and Irreversible Nanoparticle Suprastructures. *Proc. Natl. Acad. Sci. U. S. A.* **2007**, *104*, 10305–10309, doi:10.1073/pnas.0611371104.

38. Shashikala, H.B.M.; Nicolas, C.I.; Wang, X.Q. Tunable Doping in Graphene by Light-Switchable Molecules. *J. Phys. Chem. C* **2012**, *116*, 26102–26105, doi:10.1021/jp311269c.

39. Glotzer, S.C.; Solomon, M.J. Anisotropy of Building Blocks and Their Assembly into Complex Structures. *Nat. Mater.* **2007**, *6*, 557–562, doi:10.1038/nmat1949.

40. Yamagishi, H.; Sato, H.; Hori, A.; Sato, Y.; Matsuda, R.; Kato, K.; Aida, T. Self-Assembly of Lattices with High Structural Complexity from a Geometrically Simple Molecule, *Science* **2018**, *361*, 1242–1246. doi: 10.1126/science.aat6394.

41. Li, F.; Liu, D.; Wang, T.; Hu, J.; Meng, F.; Sun, H.; Shang, Z.; Li, P.; Feng, W.; Li, W.; et al. J-Aggregation in Porphyrin Nanoparticles Induced by Diphenylalanine. *J. Solid State Chem.* **2017**, *252*, 86–92, doi:10.1016/j.jssc.2017.04.035.

42. Sun, P.; Li, L.; Guang, S.; Xu, H. The Investigation of the Dipole-Dipole Action Direction and Molecular Space Configuration Effect during the Dipole–Dipole Induced Azobenzene Supramolecular Self-Assembly. *Colloids Surfaces A Physicochem. Eng. Asp.* **2019**, *580*, 123742, doi:10.1016/j.colsurfa.2019.123742.

43. Xu, J.; Wen, L.; Zhou, W.; Lv, J.; Guo, Y.; Zhu, M.; Liu, H.; Li, Y.; Jiang, L. Asymmetric and Symmetric Dipole - Dipole Interactions Drive Distinct Aggregation and Emission Behavior of Intramolecular Charge-Transfer Molecules. *J. Phys. Chem. C* **2009**, *113*, 5924–5932, doi:10.1021/jp809258h.

44. Dai, S.; Li, J.; Kougo, J.; Lei, H.; Aya, S.; Huang, M. Polar Liquid Crystalline Polymers Bearing Mesogenic Side Chains with Large Dipole Moment. *Macromolecules* **2021**, doi:10.1021/acs.macromol.1c00864.

45. Abelmann, L.; Hageman, T.A.G.; Löthman, P.A.; Mastrangeli, M.; Elwenspoek, M.C. Three-Dimensional Self-Assembly Using Dipolar Interaction. *Sci. Adv.* **2020**, *6*, doi:10.1126/sciadv.aba2007.

46. Cook, T.R.; Zheng, Y.R.; Stang, P.J. Metal-Organic Frameworks and Self-Assembled Supramolecular Coordination Complexes: Comparing and Contrasting the Design, Synthesis, and Functionality of Metal-Organic Materials. *Chem. Rev.* **2013**, *113*, 734–777, doi:10.1021/cr3002824.

47. Dong, L.; Gao, Z.A.; Lin, N. Self-Assembly of Metal–Organic Coordination Structures on Surfaces. *Prog. Surf. Sci.* **2016**, *91*, 101–135, doi:10.1016/j.progsurf.2016.08.001.

48. Smith, A.M.; Lee, A.A.; Perkin, S. The Electrostatic Screening Length in Concentrated Electrolytes Increases with Concentration. *J. Phys. Chem. Lett.* **2016**, *7*, 2157–2163, doi:10.1021/acs.jpclett.6b00867.

49. Moreno-Villoslada, I.; Torres-Gallegos, C.; Araya-Hermosilla, R.; Nishide, H. Influence of the Linear Aromatic Density on Methylene Blue Aggregation around Polyanions Containing Sulfonate Groups. *J. Phys. Chem. B* **2010**, *114*, 4151–4158, doi:10.1021/jp909105r.

50. Bian, T.; Gardin, A.; Gemen, J.; Houben, L.; Perego, C.; Lee, B.; Elad, N.; Chu, Z.; Pavan, G.M.;

Klajn, R. Electrostatic Co-Assembly of Nanoparticles with Oppositely Charged Small Molecules into Static and Dynamic Superstructures. *Nat. Chem.* **2021**, *13*, 940–949, doi:10.1038/s41557-021-00752-9.

51. Willerich, I.; Ritter, H.; Gröhn, F. Structure and Thermodynamics of Ionic Dendrimer-Dye Assemblies. *J. Phys. Chem. B* **2009**, *113*, 3339–3354, doi:10.1021/jp8096605.

52. Willerich, I.; Gröhn, F. Photoswitchable Nanoassemblies by Electrostatic Self-Assembly. *Angew. Chemie - Int. Ed.* **2010**, *49*, 8104–8108, doi:10.1002/anie.201003271.

53. Zika, A.; Bernhardt, S.; Gröhn, F. Photoresponsive Photoacid-Macroion. *Polymers (Basel).* **2020**, *12*, 1–17, doi:10.3390/polym12081746.

54. Berret, J.F. Stoichiometry of Electrostatic Complexes Determined by Light Scattering. *Macromolecules* **2007**, *40*, 4260–4266, doi:10.1021/ma062887a.

55. Gröhn, F. Soft Matter Nanoparticles with Various Shapes and Functionalities Can Form through Electrostatic Self-Assembly. *Soft Matter* **2010**, *6*, 4296–4302, doi:10.1039/c0sm00411a.

56. Willerich, I.; Li, Y.; Gröhn, F. Influencing Particle Size and Stability of Ionic Dendrimer-Dye Assemblies. *J. Phys. Chem. B* **2010**, *114*, 15466–15476, doi:10.1021/jp107358q.

57. Ruthard, C.; Schmidt, M.; Gröhn, F. Porphyrin-Polymer Networks, Worms, and Nanorods: PH-Triggerable Hierarchical Self-Assembly. *Macromol. Rapid Commun.* **2011**, *32*, 706–711, doi:10.1002/marc.201100097.

58. Willerich, I.; Schindler, T.; Ritter, H.; Gröhn, F. Controlling the Size of Electrostatically Self-Assembled Nanoparticles with Cyclodextrin as External Trigger. *Soft Matter* **2011**, *7*, 5444–5450, doi:10.1039/c1sm05405h.

59. Mariani, G.; Moldenhauer, D.; Schweins, R.; Gröhn, F. Elucidating Electrostatic Self-Assembly: Molecular Parameters as Key to Thermodynamics and Nanoparticle Shape. *J. Am. Chem. Soc.* **2016**, *138*, 1280–1293, doi:10.1021/jacs.5b11497.

60. Kutz, A.; Mariani, G.; Gröhn, F. Ionic Dye–Surfactant Nanoassemblies: Interplay of Electrostatics, Hydrophobic Effect, and π–π Stacking. *Colloid Polym. Sci.* **2016**, *294*, 591–606, doi:10.1007/s00396-015-3814-2.

61. Guan, Y.; Antonietti, M.; Faul, C.F.J. Ionic Self-Assembly of Dye-Surfactant Complexes: Influence of Tail Lengths and Dye Architecture on the Phase Morphology. *Langmuir* **2002**, *18*, 5939–5945, doi:10.1021/la0257182.

62. Faul, C.F.J.; Antonietti, M. Ionic Self-Assembly: Facile Synthesis of Supramolecular Materials. *Adv. Mater.* **2003**, *15*, 673–683, doi:10.1002/adma.200300379.

63. Gröhn, F.; Klein, K.; Brand, S. Facile Route to Supramolecular Structures: Self-Assembly of Dendrimers and Naphthalene Dicarboxylic Acids. *Chem. - A Eur. J.* **2008**, *14*, 6866–6869, doi:10.1002/chem.200800650.

64. Trubetskoy, V.S.; Loomis, A.; Hagstrom, J.E.; Budker, V.G.; Wolff, J.A. Layer-by-Layer Deposition of Oppositely Charged Polyelectrolytes on the Surface of Condensed DNA Particles. *Nucleic Acids Research* **1999**, *27*, 3090–3095, doi:10.1093/nar/27.15.3090.

65. Wang, Q. Modelling Layer-by-Layer Assembly of Flexible Polyelectrolytes. *J. Phys. Chem. B* **2006**, *12*, 5825–5828, doi:10.1021/jp0604387.

66. Liu, Q.; Yao, L.; Shen, Q.; Nie, Z.; Guo, M.; Yao, S. Layer-by-Layer Assembly of Polyelectrolyte and Nanoparticles, Monitored by Capillary Electrophoresis. *Chem. - A Eur. J.* **2009**, *15*, 12828–12836, doi:10.1002/chem.200901998.

67. Tettey, K.E.; Ho, J.W.C.; Lee, D. Modulating Layer-by-Layer Assembly of Oppositely Charged Nanoparticles Using a Short Amphiphilic Molecule. *J. Phys. Chem. C* **2011**, *115*, 6297–6304.

68. Zhang, Z.; Zeng, J.; Matsusaki, M. Fabrication of Fully Positively Charged Layer-by-Layer Polyelectrolyte Nanofilms with PH-Dependent Swelling Properties. *Langmuir* **2024**, *40*, 15588–15596, doi:10.1021/acs.langmuir.4c01327.

69. Wang, Y.; Han, P.; Xu, H.; Wang, Z.; Zhang, X.; Kabanov, A. V. Photocontrolled Self-Assembly and Disassembly of Block Ionomer Complex Vesicles: A Facile Approach toward Supramolecular Polymer Nanocontainers. *Langmuir* **2010**, *26*, 709–715, doi:10.1021/la9023844.

70. Frühbeißer, S.; Mariani, G.; Gröhn, F. Porphyrin Diacid-Polyelectrolyte Assemblies: Effective Photocatalysts in Solution. *Polymers (Basel).* **2016**, *8*, 40–46, doi:10.3390/polym8050180.

71. Wang, J.; Liu, K.; Xing, R.; Yan, X. Peptide Self-Assembly: Thermodynamics and Kinetics. *Chem. Soc. Rev.* **2016**, *45*, 5589–5604, doi:10.1039/c6cs00176a.

72. Piao, Y.; Wu, T.; Chen, B. One-Step Synthesis of Graphene Oxide-Polyamidoamine Dendrimer Nanocomposite Hydrogels by Self-Assembly. *Ind. Eng. Chem. Res.* **2016**, *55*, 6113–6121, doi:10.1021/acs.iecr.6b00947.

73. Fan, Y.; Wang, Y. Applications of Small-Angle X-Ray Scattering/Small-Angle Neutron Scattering and Cryogenic Transmission Electron Microscopy to Understand Self-Assembly of Surfactants. *Curr. Opin. Colloid Interface Sci.* **2019**, *42*, 1–16, doi:10.1016/j.cocis.2019.02.011.

74. Agrawal, A.; Douglas, J.F.; Tirrell, M.; Karim, A. Manipulation of Coacervate Droplets with an Electric Field. *Proc. Natl. Acad. Sci. U. S. A.* **2022**, *119*, 1–10, doi:10.1073/pnas.2203483119.

75. Mansfield, M.L.; Douglas, J.F. Shape Characteristics of Equilibrium and Non-Equilibrium Fractal Clusters. *J. Chem. Phys.* **2013**, *139*, doi:10.1063/1.4813020.

76. Grzybowski, B.A.; Winkleman, A.; Wiles, J.A.; Brumer, Y.; Whitesides, G.M. Electrostatic Self-Assembly of Macroscopic Crystals Using Contact Electrification. *Nat. Mater.* **2003**, *2*, 241–245, doi:10.1038/nmat860.

77. Willerich, I.; Gröhn, F. Switchable Nanoassemblies from Macroions and Multivalent Dye Counterions. *Chem. - A Eur. J.* **2008**, *14*, 9112–9116, doi:10.1002/chem.200801167.

78. Moldenhauer, D.; Gröhn, F. Nanoassemblies with Light-Responsive Size and Density from Linear Flexible Polyelectrolytes. *J. Polym. Sci. Part B Polym. Phys.* **2013**, *51*, 802–816, doi:10.1002/polb.23276.

79. Mariani, G.; Schweins, R.; Gröhn, F. Structure Tuning of Electrostatically Self-Assembled Nanoparticles through PH: The Role of Charge Ratio. *Macromol. Chem. Phys.* **2017**, *218*, 1–9, doi:10.1002/macp.201700191.

80. Moldenhauer, D.; Gröhn, F. Water-Soluble Spiropyrans with Inverse Photochromism and Their Photoresponsive Electrostatic Self-Assembly. *Chem. - A Eur. J.* **2017**, *23*, 3966–3978, doi:10.1002/chem.201605621.

81. Ainalem, M.L.; Carnerup, A.M.; Janiak, J.; Alfredsson, V.; Nylander, T.; Schillén, K. Condensing DNA with Poly(Amido Amine) Dendrimers of Different Generations: Means of Controlling Aggregate Morphology. *Soft Matter* **2009**, *5*, 2310–2320, doi:10.1039/b821629k.

82. Akamatsu, M.; Kobayashi, K.; Iwase, H.; Sakaguchi, Y.; Tanaka, R.; Sakai, K.; Sakai, H. Rapid Controlled Release by Photo-Irradiation Using Morphological Changes in Micelles Formed by Amphiphilic Lophine Dimers. *Sci. Rep.* **2021**, *11*, 1–10, doi:10.1038/s41598-021-90097-7.

83. Carl, N.; Prévost, S.; Fitzgerald, J.P.S.; Karg, M. Salt-Induced Cluster Formation of Gold Nanoparticles Followed by Stopped-Flow SAXS, DLS and Extinction Spectroscopy. *Phys. Chem. Chem. Phys.* **2017**, *19*, 16348–16357, doi:10.1039/c7cp01807j.

84. Brown, P.; Butts, C.P.; Eastoe, J. Stimuli-Responsive Surfactants. *Soft Matter* **2013**, *9*, 2365–2374, doi:10.1039/c3sm27716j.

85. Dutta, R.; Sil, S.; Kundu, S.; Nandi, S.; Sarkar, N. Multi-Stimuli Responsive Fabrication of Supramolecular Assemblies Using Ionic Self-Assembly Approach. *J. Mol. Liq.* **2019**, *286*, 110861, doi:10.1016/j.molliq.2019.04.138.

86. Xia, D.; Wang, P.; Ji, X.; Khashab, N.M.; Sessler, J.L.; Huang, F. Functional Supramolecular Polymeric Networks: The Marriage of Covalent Polymers and Macrocycle-Based Host-Guest Interactions. *Chem. Rev.* **2020**, *120*, 6070–6123, doi:10.1021/acs.chemrev.9b00839.

87. Martin, N.; Sharma, K.P.; Harniman, R.L.; Richardson, R.M.; Hutchings, R.J.; Alibhai, D.; Li, M.; Mann, S. Light-Induced Dynamic Shaping and Self-Division of Multipodal Polyelectrolyte-Surfactant Microarchitectures via Azobenzene Photomechanics. *Sci. Rep.* **2017**, *7*, 1–12, doi:10.1038/srep41327.

88. Engel, S.; Möller, N.; Stricker, L.; Peterlechner, M.; Ravoo, B.J. A Modular System for the Design of Stimuli-Responsive Multifunctional Nanoparticle Aggregates by Use of Host–Guest Chemistry. *Small* **2018**, *14*, 1–8, doi:10.1002/smll.201704287.

89. Xia, H.; Xie, K.; Zou, G. Advances in Spiropyrans/Spirooxazines and Applications Based on Fluorescence Resonance Energy Transfer (FRET) with Fluorescent Materials. *Molecules* **2017**, *22*, doi:10.3390/molecules22122236.

90. Browne, W.R.; Feringa, B.L. Light Switching of Molecules on Surfaces. *Annu. Rev. Phys. Chem.* **2009**, *60*, 407–428, doi:10.1146/annurev.physchem.040808.090423.

91. Dai, S.; Ravi, P.; Tam, K.C. Thermo- and Photo-Responsive Polymeric Systems. *Soft Matter* **2009**, *5*, 2513–2533, doi:10.1039/b820044k.

92. Liu, K.; Xing, R.; Zou, Q.; Ma, G.; Möhwald, H.; Yan, X. Simple Peptide-Tuned Self-Assembly of Photosensitizers towards Anticancer Photodynamic Therapy. *Angew. Chemie - Int. Ed.* **2016**, *55*, 3036–3039, doi:10.1002/anie.201509810.

93. Kundu, P.K.; Samanta, D.; Leizrowice, R.; Margulis, B.; Zhao, H.; Börner, M.; Udayabhaskararao, T.; Manna, D.; Klajn, R. Light-Controlled Self-Assembly of Non-Photoresponsive Nanoparticles. *Nat. Chem.* **2015**, *7*, 646–652, doi:10.1038/nchem.2303.

94. Kumar, K.; Knie, C.; Bléger, D.; Peletier, M.A.; Friedrich, H.; Hecht, S.; Broer, D.J.; Debije, M.G.; Schenning, A.P.H.J. A Chaotic Self-Oscillating Sunlight-Driven Polymer Actuator. *Nat. Commun.* **2016**, *7*, 1–8, doi:10.1038/ncomms11975.

95. Willerich, I.; Gröhn, F. Molecular Structure Encodes Nanoscale Assemblies: Understanding Driving Forces in Electrostatic Self-Assembly. *J. Am. Chem. Soc.* **2011**, *133*, 20341–20356, doi:10.1021/ja207565m.

96. Mariani, G.; Krieger, A.; Moldenhauer, D.; Schweins, R.; Gröhn, F. Light-Responsive Shape: From Micrometer-Long Nanocylinders to Compact Particles in Electrostatic Self-Assembly. *Macromol. Rapid Commun.* **2018**, *39*, 1–5, doi:10.1002/marc.201700860.

97. Zika, A.; Agarwal, M.; Schweins, R.; Gröhn, F. Joining Two Switches in One Nano-object: Photoacidity and Photoisomerization in Electrostatic Self-assembly. *Chem. – A Eur. J.* **2022**, *29*, 1–7, doi:10.1002/chem.202203373.

98. Zika, A.; Agarwal, M.; Schweins, R.; Gröhn, F. Double-Wavelength-Switchable Molecular Self-Assembly of a Photoacid and Spirooxazine in an Aqueous Solution. *J. Phys. Chem. Lett.* **2023**, *14*, 9563–9568, doi:10.1021/acs.jpclett.3c02392.

99. Agarwal, M.; Zika, A.; Schweins, R.; Gröhn, F. Controlling the Morphology in Electrostatic Self-Assembly via Light. *Polymers (Basel).* **2024**, *16*, 50, doi:10.3390/polym16010050.

100. Klajn, R. Immobilized Azobenzenes for the Construction of Photoresponsive Materials. *Pure Appl. Chem.* **2010**, *82*, 2247–2276, doi:10.1351/PAC-CON-10-09-04.

101. Wani, O.M.; Zeng, H.; Priimagi, A. A Light-Driven Artificial Flytrap. *Nat. Commun.* **2017**, *8*, 1–7, doi:10.1038/ncomms15546.

102. Xu, J.F.; Chen, Y.Z.; Wu, D.; Wu, L.Z.; Tung, C.H.; Yang, Q.Z. Photoresponsive Hydrogen-Bonded Supramolecular Polymers Based on a Stiff Stilbene Unit. *Angew. Chemie - Int. Ed.* **2013**, *52*, 9738–9742, doi:10.1002/anie.201303496.

103. Zheng, Y.B.; Pathem, B.K.; Hohman, J.N.; Thomas, J.C.; Kim, M.; Weiss, P.S. Photoresponsive Molecules in Well-Defined Nanoscale Environments. *Adv. Mater.* **2013**, *25*, 302–312, doi:10.1002/adma.201201532.

104. Zika, A.; Gröhn, F. Multiswitchable Photoacid-Hydroxyflavylium-Polyelectrolyte Nano-Assemblies. *Beilstein J. Org. Chem.* **2021**, *17*, 166–185, doi:10.3762/BJOC.17.17.

105. Koumura, N.; Zijistra, R.W.J.; Van Delden, R.A.; Harada, N.; Feringa, B.L. Light-Driven Monodirectional Molecular Rotor. *Nature* **1999**, *401*, 152–155, doi:10.1038/43646.

106. Katsonis, N.; Lubomska, M.; Pollard, M.M.; Feringa, B.L.; Rudolf, P. Synthetic Light-Activated Molecular Switches and Motors on Surfaces. *Prog. Surf. Sci.* **2007**, *82*, 407–434, doi:10.1016/j.progsurf.2007.03.011.

107. London, G.; Carroll, G.T.; Fernández Landaluce, T.; Pollard, M.M.; Rudolf, P.; Feringa, B.L. Light-Driven Altitudinal Molecular Motors on Surfaces. *Chem. Commun.* **2009**, 1712–1714, doi:10.1039/b821755f.

108. Guo, Y.; Gong, Y.; Gao, Y.; Xiao, J.; Wang, T.; Yu, L. Multi-Stimuli Responsive Supramolecular Structures Based on Azobenzene Surfactant-Encapsulated Polyoxometalate. *Langmuir* **2016**, *32*, 9293–9300, doi:10.1021/acs.langmuir.6b02539.

109. Yuan, W.; Gao, X.; Pei, E.; Li, Z. Light- and PH-Dually Responsive Dendrimer-Star Copolymer Containing Spiropyran Groups: Synthesis, Self-Assembly and Controlled Drug Release. *Polym. Chem.* **2018**, *9*, 3651–3661, doi:10.1039/c8py00721g.

110. Raimondo, C.; Reinders, F.; Soydaner, U.; Mayor, M.; Samorì, P. Light-Responsive Reversible Solvation and Precipitation of Gold Nanoparticles. *Chem. Commun.* **2010**, *46*, 1147–1149, doi:10.1039/b915491d.

111. Fu, J.; Schlenoff, J.B. Driving Forces for Oppositely Charged Polyion Association in Aqueous Solutions: Enthalpic, Entropic, but Not Electrostatic. *J. Am. Chem. Soc.* **2016**, *138*, 980–990, doi:10.1021/jacs.5b11878.

112. Laskar, P.; Dufès, C. Emergence of Cationic Polyamine Dendrimersomes: Design, Stimuli Sensitivity and Potential Biomedical Applications. *Nanoscale Adv.* **2021**, *3*, 6007–6026, doi:10.1039/d1na00536g.

113. Mariani, G.; Kutz, A.; Di, Z.; Schweins, R.; Gröhn, F. Inducing Hetero-Aggregation of Different Azo Dyes through Electrostatic Self-Assembly. *Chem. - A Eur. J.* **2017**, *23*, 6249–6254, doi:10.1002/chem.201605194.

114. Willerich, I.; Gröhn, F. Thermodynamics of Photoresponsive Polyelectrolyte-Dye Assemblies with Irradiation Wavelength Triggered Particle Size. *Macromolecules* **2011**, *44*, 4452–4461, doi:10.1021/ma200538e.

115. Willerich, I.; Gröhn, F. Switchable Nanoassemblies from Macroions and Multivalent Dye Counterions. *Chem. - A Eur. J.* **2008**, *14*, 9112–9116, doi:10.1002/chem.200801167.

116. Wang, L.; Li, Q. Photochromism into Nanosystems: Towards Lighting up the Future Nanoworld. *Chem. Soc. Rev.* **2018**, *47*, 1044–1097, doi:10.1039/c7cs00630f.

117. Ikeda, T.; Mamiya, J.I.; Yu, Y. Photomechanics of Liquid-Crystalline Elastomers and Other Polymers. *Angew. Chemie - Int. Ed.* **2007**, *46*, 506–528, doi:10.1002/anie.200602372.

118. Koga, T.; Ushirogochi, M.; Higashi, N. Regulation of Self-Assembling Process of a Cationic β-Sheet Peptide by Photoisomerization of an Anionic Azobenzene Derivative. *Polym. J.* **2007**, *39*, 16–17, doi:10.1295/polymj.PJ2006110.

119. Ghoreishi, S.M.; Behpour, M.; Shabani-Nooshabadi, M. Interaction of Anionic Azo Dye and TTAB - Cationic Surfactant. *J. Braz. Chem. Soc.* **2009**, *20*, 460–465, doi:10.1590/S0103-50532009000300008.

120. Fischer, W.; Quadir, M.A.; Barnard, A.; Smith, D.K.; Haag, R. Controlled Release of DNA from Photoresponsive Hyperbranched Polyglycerols with Oligoamine Shells. *Macromol. Biosci.* **2011**, *11*, 1736–1746, doi:10.1002/mabi.201100248.

121. Xie, X.; Wang, L.; Liu, X.; Du, Z.; Li, Y.; Li, B.; Wu, L.; Li, W. Light-Powered and Transient Peptide Two-Dimensional Assembly Driven by: Trans -to- Cis Isomerization of Azobenzene Side Chains. *Chem. Commun.* **2020**, *56*, 1867–1870, doi:10.1039/c9cc09448b.

122. Fathalla, M.; Sinatra, L. PH-Responsive Porphyrin-Silica Nanoparticles Conjugate via Ionic Self-Assembly. *J. Porous Mater.* **2021**, *28*, 183–189, doi:10.1007/s10934-020-00976-z.

123. Jensen, G.V.; Lund, R.; Gummel, J.; Monkenbusch, M.; Narayanan, T.; Pedersen, J.S. Direct Observation of the Formation of Surfactant Micelles under Nonisothermal Conditions by Synchrotron SAXS. *J. Am. Chem. Soc.* **2013**, *135*, 7214–7222, doi:10.1021/ja312469n.

124. Jensen, G.V.; Lund, R.; Gummel, J.; Narayanan, T.; Pedersen, J.S. Monitoring the Transition from Spherical to Polymer-like Surfactant Micelles Using Small-Angle X-Ray Scattering. *Angew. Chemie - Int. Ed.* **2014**, *53*, 11524–11528, doi:10.1002/anie.201406489.

125. Lund, R.; Brun, G.; Chevallier, E.; Narayanan, T.; Tribet, C. Kinetics of Photocontrollable Micelles: Light-Induced Self-Assembly and Disassembly of Azobenzene-Based Surfactants Revealed by TR-SAXS. *Langmuir* **2016**, *32*, 2539–2548, doi:10.1021/acs.langmuir.5b04711.

126. Kelly, E.A.; Houston, J.E.; Evans, R.C. Probing the Dynamic Self-Assembly Behaviour of Photoswitchable Wormlike Micelles in Real-Time. *Soft Matter* **2019**, *15*, 1253–1259, doi:10.1039/c8sm01948g.

127. Huang, Z.; Jiang, T.; Wang, J.; Ma, X.; Tian, H. Angew Chem Int Ed - 2020 - Huang - Real-Time Visual Monitoring of Kinetically Controlled Self-Assembly. *Angew. Chem. Int. Ed.* **2021**, *60*, 2855–2860, doi:10.1002/anie.202011740.

7. Appendix

7.1. Full Publication List

I. **Mohit Agarwal**, Alexander Zika, Ralf Schweins, Franziska Gröhn; Controlling the Morphology in Electrostatic Self-Assembly via Light, *Polymers,* **2024***, 16(1),* 50.

II. **Mohit Agarwal**, Alexander Zika, Müge Yücel, Joachim Kohlbrecher, Ralf Schweins, Franziska Gröhn; The Role of Light Irradiation and Dendrimer Generation in Directing Electrostatic Self-Assembly, *Polymers, **2025**, 17(2), 170.*

III. **Mohit Agarwal**, Ralf Schweins, Franziska Gröhn; Light-Induced Structural Evolutions in Electrostatic Nanoassemblies, *Polymers, **2026**, 18(2), 190.*

IV. Alexander Zika, **Mohit Agarwal**, Ralf Schweins, Franziska Gröhn; Joining Two Switches in One Nano-Object: Photoacidity and Photoisomerization in Electrostatic Self-Assembly, *Chem. Eur. J..,* **2022**, e202203373.

V. Alexander Zika, **Mohit Agarwal**, Ralf Schweins, Franziska Gröhn; Double-Wavelength-Switchable Molecular Self-Assembly of a Photoacid and Spirooxazine in an Aqueous Solution, *J. Phys. Chem. Lett.,* **2023**, *14*, 9563-9568.

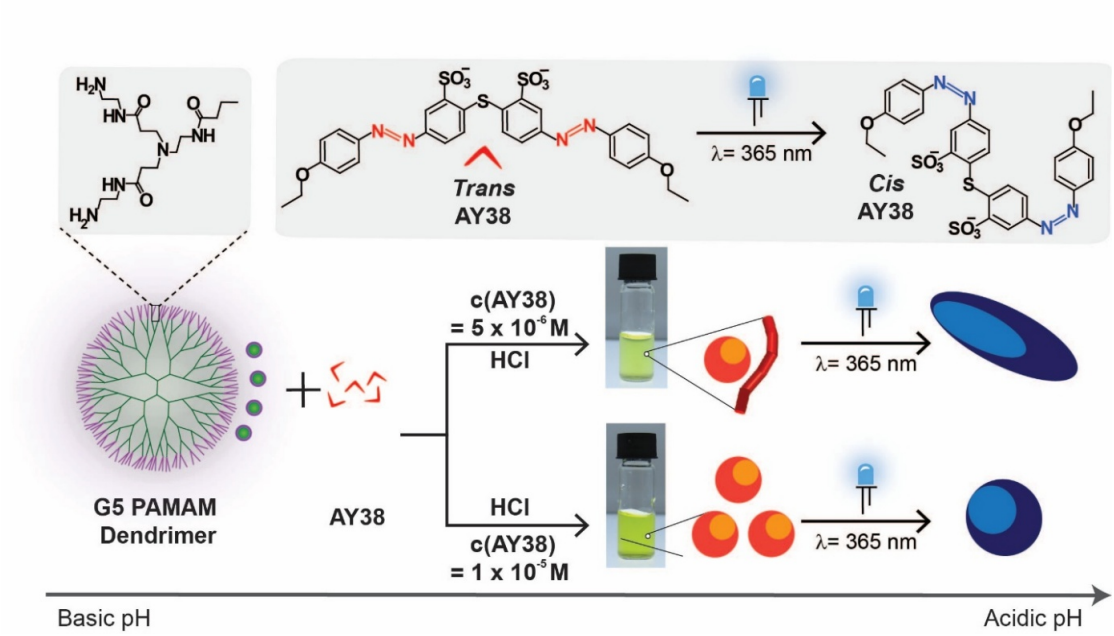
VI. Alexander Zika, **Mohit Agarwal**, Wiebke Zika, Dirk Guldi, Ralf Schweins, Franziska Gröhn; Photoacid-Macroion Assemblies: How Photo-Excitation Switches the Size of Nano-Objects, *Nanoscale,* **2024,** *16*, 923-940.

VII. Arthur Turkin, Dr. Marco Holzapfel, **Mohit Agarwal**, David Fischermeier, Prof. Dr. Roland Mitric, Dr. Ralf Schweins, Prof. Dr. Franziska Gröhn, Prof. Dr. Christoph Lambert; Solvent Induced Helix Folding of Defined Indolenine Squaraine Oligomers, *Chem. Eur. J.* **2021**, *27*, 8380 – 8389.

7.2. Publications with Contribution on this Thesis

7.2.1. Controlling the Morphology in Electrostatic Self-Assembly via Light

Mohit Agarwal, Alexander Zika, Ralf Schweins, Franziska Gröhn; *Polymers,* **2024,** *16(1)*, 50.



polymers

MDPI

Article

Controlling the Morphology in Electrostatic Self-Assembly via Light

Mohit Agarwal [1,2], Alexander Zika [1], Ralf Schweins [2] and Franziska Gröhn [1,*]

[1] Department of Chemistry and Pharmacy, Interdisciplinary Center for Molecular Materials, Friedrich-Alexander Universität Erlangen-Nürnberg, Egerlandstr. 3, D-91058 Erlangen, Germany
[2] Institut Laue-Langevin, DS/LSS, 71 Avenue des Martyrs, F-38000 Grenoble, France; schweins@ill.eu
* Correspondence: franziska.groehn@fau.de; Tel.: +49-913-185-20731

Abstract: Electrostatic self-assembly of macroions is an emerging area with great potential in the development of nanoscale functional objects, where photo-irradiation responsiveness can either elevate or suppress the self-assembly. The ability to control the size and shape of macroion assemblies would greatly facilitate the fabrication of desired nano-objects that can be harnessed in various applications such as catalysis, drug delivery, bio-sensors, and actuators. Here, we demonstrate that a polyelectrolyte with a size of 5 nm and multivalent counterions with a size of 1 nm can produce well-defined nanostructures ranging in size from 10–1000 nm in an aqueous environment by utilizing the concept of electrostatic self-assembly and other intermolecular non-covalent interactions including dipole–dipole interactions. The *pH*- and photoresponsiveness of polyelectrolytes and azo dyes provide diverse parameters to tune the nanostructures. Our findings demonstrate a facile approach to fabricating and manipulating self-assembled nanoparticles using light and neutron scattering techniques.

Keywords: electrostatic assembly; light irradiation; nanostructures; polyelectrolyte; thermodynamically controlled; kinetically controlled

check for updates

Citation: Agarwal, M.; Zika, A.; Schweins, R.; Gröhn, F. Controlling the Morphology in Electrostatic Self-Assembly via Light. *Polymers* **2024**, *16*, 50. https://doi.org/10.3390/polym16010050

Academic Editor: Ivan Gitsov

Received: 16 November 2023
Revised: 13 December 2023
Accepted: 18 December 2023
Published: 22 December 2023

Copyright: © 2023 by the authors. Licensee MDPI, Basel, Switzerland. This article is an open access article distributed under the terms and conditions of the Creative Commons Attribution (CC BY) license (https://creativecommons.org/licenses/by/4.0/).

1. Introduction

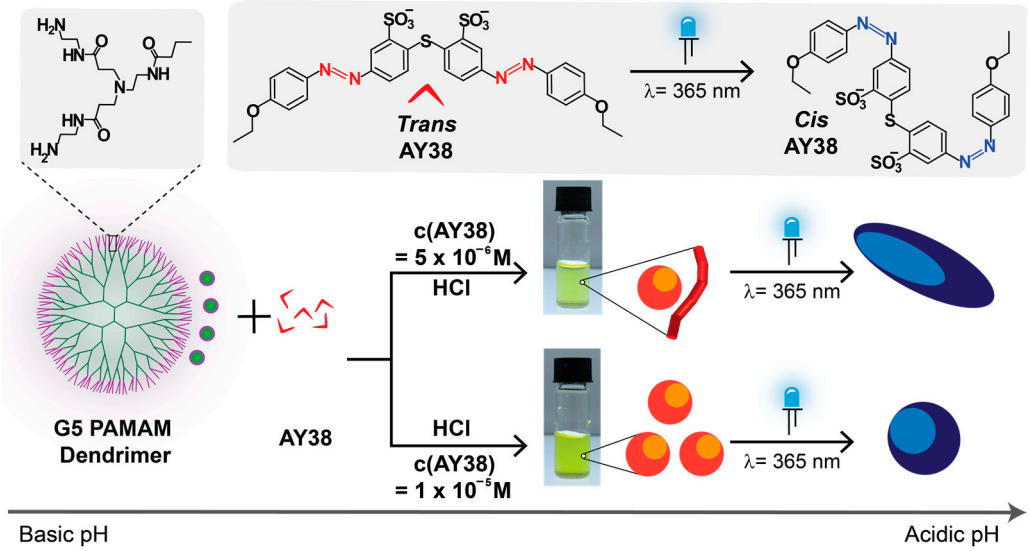
Self-assembly generates complex structures with a variety of functional properties over a range of length scales. Diverse structures such as cell membranes [1,2], supramolecules [3–5], and protein complexes [6–10] are formed via multiple non-covalent interactions between adjacent molecules that occur due to their chemical nature. Recently, electrostatic self-assembly has emerged as one of the most facile approaches for fabricating such synthetic particles in aqueous solution [11–14]. This process is mainly driven by thermodynamics [15,16]; however, kinetics is also found to be an essential factor in structural manipulation [17]. Non-covalent interactions determine the lowest energy state that provides thermodynamic control and eventually stabilized nanostructures. Due to their relatively weak nature, these non-covalent interactions can be altered using various parameters, including pH, concentration, preparation method, charge ratio, and counterions. The precise manipulation of the nano-objects with external stimuli is critical to multiple applications ranging from nanoelectronics [11,13,18–21] to controlled drug delivery [22–24]. Light responsiveness as a non-invasive trigger attracted the most attention in this respect [14,25,26]. An additional advantage of this external stimulus is that it can be applied and switched back 'on demand' because of the excellent reversibility of the interactions. For example, light irradiation has been used to control a nanoparticle's size and shape [11,14,25–27], giving rise to diverse functions and applications, including therapy [28–30] and sensors [31–33].

In electrostatic self-assembly, nanoparticle formations are fundamentally based on the nature of charges involved within the structure [11]. These charges arrange themselves to form assembled structures [34]. Generally, the electrostatic interactions are non-directional, and thus are best combined with a second kind of interactions such as dipole–dipole, π–π bonding, hydrogen bonding, hydrophobic effects, and van der Waals forces that

provide the directionality for the structural formation [16,17,35–38]. Often, short-range secondary interactions are induced when long-range electrostatic forces bring building blocks together. Recent studies have been performed to understand the role of charges using different parameters such as concentration and charge ratio, l_c (the ratio of the number of anionic charges to the number of cationic charges multiplied by the concentration of their anions and cations, respectively) [13,14,39]. Mariani et al. used a cationic polyamidoamine (PAMAM) dendrimer of different generations (2–8) for well-defined cationic macroions and mono-, di-, and trivalent azo dyes as anionic molecular counterions as a model system, where they observed the effect of generation dependency on the shape of the assemblies. The nano-assemblies transformed from isotropic to anisotropic structures when increasing the dendrimer generations [17].

Moreover, divalent azo dyes such as Acid Yellow 38 (AY38) and Direct Yellow 12 (DY12) have also been used recently in electrostatic assemblies to introduce photosensitivity in the system [14,25,26]. The negatively charged azo dyes bind with the dendrimer molecules in neutral and acidic mediums. These azo dyes can then isomerize from *trans* state (thermodynamically favored) to *cis* form (less favored) upon UV irradiation. In the case of AY38, the half-life ($t_{1/2}$) of the *cis* state is approximately 12 h at pH = 3.5 ($t_{1/2} \approx 5$ h for DY12) [25,40,41]. Moldenhauer et al. used the photoresponsive behavior of AY38 with linear polyelectrolytes to study the electrostatic assemblies [42]. Previously, electrostatic assemblies have been formed using AY38 dye and G4 PAMAM dendrimer by Willerich et al. [14], where the pH control and light irradiation caused reproducible nano assemblies. Later, Zika et al. [13] introduced the effect of photoacids in this type of system and created multi-switchable electrostatic assemblies with defined sizes and shapes.

In the present work (Scheme 1), we used the G5 PAMAM dendrimer, which has almost twice the positive charges of G4 and is more rigid than lower generations. Generation 5 PAMAM dendrimer comprises 128 primary and 126 tertiary amines that do not show any charges in the basic medium (at pH = 10.5). However, on decreasing the pH, primary amines become protonated and cationic, and finally, at pH = 3.5, all the amine groups (254) become positively charged. Generation 5 is also slightly larger in size (5.4 nm) as compared to G4 PAMAM dendrimer (4.5 nm) [43].



Scheme 1. Preparation of electrostatic self-assembly of AY38 azo dye and G5 PAMAM dendrimer and effect of building blocks concentrations on the nanoparticle structures in aqueous solution.

Herein, we aim to investigate the shape of the assemblies before and after irradiation, understand the kinetic and thermodynamic aspects of electrostatic assemblies as well as factors that lead to monodisperse versus multimodal assemblies, and attempt to provide an understanding that allows controlling these factors. Combining the effects of the charge

ratio and photoswitchability on shape transformation has not yet been explored, to our knowledge. Here, we used these two parameters to tune the size of nanoparticles over a vast range of length scales (10 nm to 3 μm) with various configurations such as spheres, cylinders, flexible cylinders, and ellipsoids. To gain a more insightful understanding of the mentioned prospects, the thorough characterization of the nanoparticles will be demonstrated and discussed in the following.

2. Materials and Methods

2.1. Chemicals

Generation 5 PAMAM dendrimer was purchased from Aldrich, Darmstadt, Germany, and dynamic light scattering (DLS) in D_2O and H_2O confirmed the size (5.4 nm) given by the manufacturer Dendritech, Midland, MI, USA. AY38 (>40% purity) was purchased from Merck, Darmstadt, Germany, and purified to > 98% by multiple recrystallizations from water and ethanol, as described previously [42,44]. D_2O, NaOD, and DCl were purchased from Merck, Darmstadt, Germany, and NaOD and DCl were used to adjust the *pD* of the solution.

2.2. Sample Preparation

As small-angle neutron scattering (SANS) is central to this study, we used D_2O as a solvent and all regents in the deuterated form except for the assembly components throughout the complete study. All samples were prepared using D_2O as a solvent in the basic medium at *pD* = 10.5. The azo dye stock solution (1.4×10^{-3} mol L^{-1}) was diluted with D_2O depending on the charge ratio. The appropriate amount of dendrimer stock solution (4.0×10^{-5} mol L^{-1}) was added under continuous stirring for ideal mixing. Later, a reasonable amount of standard 0.1 mol L^{-1} DCl solution (until *pD* = 3.5) was added in one shot while stirring to induce the assembly formation. The *pH* measurements were performed using a glass electrode on a Mettler Toledo *pH* meter. The *pH* obtained from the *pH* meter was converted into *pD* values according to [45–47]:

$$pD = pH + 0.41 \tag{1}$$

The sample was irradiated in a vial while stirring using a UV lamp at 365 nm wavelength for 20 min. A longer irradiation time did not influence the results, suggesting that the azo dye's photostationary state was reached. Measurements were performed shortly after irradiation.

2.3. Light Scattering

Static and dynamic light scattering (SLS, DLS) are highly suitable techniques for characterizing polyelectrolytes in solution. The DLS, also known as photon correlation spectroscopy (PCS), investigates the fluctuation in the scattered intensity with time (Brownian motion of the scattering particles). This technique exploits quasi-elastic scattering and probes temporal fluctuations of the scattered intensity by using coherent laser light. Instead of using the scattering angle θ, the scattering vector $\vec{q}$ (also known as momentum transfer) is defined as $\vec{q} = \vec{K_s} - \vec{K_i}$, where $\vec{K_s}$ and $\vec{K_i}$ are the propagation vectors of scattering and incident light, respectively. The magnitude of q can be given by:

$$q = \left|\vec{q}\right| = \frac{4\pi n_D}{\lambda} sin\left(\frac{\theta}{2}\right) \tag{2}$$

with λ being the wavelength of incident light in solution.

The intensity–time autocorrelation function, $g_2(q,\tau)$ in DLS is measured by:

$$g_2(q,\tau) = \frac{\langle I(q,t)I(q,t+\tau)\rangle}{\langle I(q,t)\rangle^2} \tag{3}$$

The above function describes the correlation between the scattering intensity at time t = 0 to time t + τ, where q is the momentum transfer and τ is the shift in time. The Siegert relation can convert the intensity–time autocorrelation function into field–time autocorrelation function $g_1(q, \tau)$:

$$g_2(q, \tau) = 1 + [g_1(q, \tau)]^2 \quad (4)$$

The $g_1(\tau)$ was analyzed by a regularized inverse Laplace transformation using the CONTIN algorithm by S. Provencher [48,49] to obtain the intensity-weighted relaxation times distribution. Mean relaxation times were then transferred into apparent diffusion coefficient D_{app} using the relation:

$$D_{app} = q^{-2}\tau^{-1} \quad (5)$$

Measurements covered a broad range of q by measuring a scattering angle of $20^\circ \leq \theta \leq 150^\circ$ with a 5-degree step. To measure the hydrodynamic radius (R_H), D_{app} extrapolated to q = 0. From this, the R_H can be calculated using the Stokes-Einstein relationship:

$$D(q^2 = 0) = \frac{kT}{6\pi\eta R_H} \quad (6)$$

where k is the Boltzmann constant, T is the absolute temperature in Kelvin, and η is the solvent viscosity.

The macroscopic scattering cross-section $\frac{d\sum}{d\Omega}(q)$ for light scattering is commonly denoted as the Rayleigh ratio ΔR_θ:

$$\frac{d\sum}{d\Omega}(q) = \Delta R_\theta = KcM_wP(q) \quad (7)$$

where K is the optical constant, c is the mass concentration, M_w is the weight-averaged molecular weight, and $P(q)$ is the form factor. K is given by:

$$K = \frac{4\pi^2}{\lambda_0^4 N_A}\left(n_{D,0}\frac{dn}{dc}\right)^2 \quad (8)$$

with λ_0 being the wavelength of the incoming light, N_A the Avogadro constant, $n_{D,0}$ the refractive index of the standard solution used to calibrate absolute intensity, and dn/dc the refractive index increment. Either Guinier approximation can be used to determine the size via R_G at low q:

$$P(q) \approx exp\left(\frac{-q^2R_G^2}{3}\right) \quad (9)$$

or the Zimm equation:

$$\frac{Kc}{\Delta R_\theta} = \frac{1}{M_w}\left(1 + \frac{1}{3}q^2\langle R_G^2\rangle\right) + 2A_2c \quad (10)$$

where R_G is the radius of gyration, A_2 is the second osmotic virial coefficient, and c is the mass concentration.

The ratio of R_G/R_H, also known as the ρ ratio, provides essential information on the scattering particle topology, especially in the small range of particles (size = 10–100 nm) due to the limited length scale of light scattering [50]. SLS data have also been combined with small-angle neutron scattering (SANS) data to extend the low q-range for large aggregates. Combined light scattering techniques give primary hints on the particle shape, while small-angle scattering is needed for a thorough structural analysis.

Measurements were carried out using an ALV CGS3 goniometer with an ALV 5004 correlator (ALV GmbH, Langen, Germany) equipped with a HeNe laser with a wavelength of λ = 632.8 nm and a maximum output power of 23 mW.

2.4. ζ-Potential

The particle and its microenvironment determine the electrostatic properties of nanostructures in a solution. Such properties of nanostructures can be characterized by their ζ-potential measurements. This technique measures the difference in electrostatic potential between the medium and the fluid layer of dispersed nanostructures. The ζ-potential was calculated from the electrophoretic mobility using the Helmholtz–Smoluchowski equation below [51,52]:

$$\zeta = (\mu * \eta)/\varepsilon \tag{11}$$

where μ is the electrophoretic mobility of charged particles, η is the viscosity of the solution, and ε is the dielectric constant of the dispersive medium.

The ζ-potential measurements were conducted on a Zetasizer Nano ZS analyzer with an integrated 4 mW HeNe laser, λ = 633 nm (Malvern Instruments Ltd., Malvern, UK).

2.5. UV-Vis Spectroscopy

Absorption spectra were recorded on a JASCO V-630 spectrometer using 1 mm path-length quartz cuvettes. Room temperature was used for each measurement. For the reference measurements, D_2O was used as a solvent. UV-Vis measurements were also performed to calculate the amount of *trans* and *cis* isomers in the solution and in the assemblies. The fraction of the bound dye molecules was calculated by the following formula:

$$Fraction\ of\ bound\ Cis\ dye = \frac{quantity\ of\ Cis\ dye\ in\ the\ assemblies}{total\ quantity\ of\ dye\ in\ the\ assemblies} \tag{12}$$

$$= \frac{Cis\ area(before\ centr.) - Cis\ area(supernat.)}{(Cis\ area(before\ centr.) - Cis\ area(supernat.)) + (Trans\ area(before\ centr.) - Trans\ area(supernat.))} \tag{13}$$

The value obtained from the above formula was multiplied by 100 to find the bound *cis* % in the assemblies. The area of the isomers was calculated using the Gaussian model in Origin 9.0 software as follows:

$$y = y_0 + (A/(w\sqrt{\pi/2}))e^{(-2((x-xc)/w^2))} \tag{14}$$

where y is the Gaussian function, y_0 is the offset, xc is the center of the peak, w is the width, and A is the area of the peak.

2.6. Small-Angle Neutron Scattering

As the scattering length of neutrons (b) depends on the isotope and is significantly different for hydrogen and deuterium, using deuterated compounds or solvents to get higher contrast using neutrons is advantageous to analyzing organic material in solution. SANS measurements were performed at beamline D11 at the Institut Laue–Langevin (ILL), Grenoble, France. The proposal numbers of the beamtimes were 9-12-662 [doi:10.5291/ILL-DATA.9-12-662], and 9-12-624 [doi:10.5291/ILL-DATA.9-12-624].

SANS samples were prepared in D_2O with mainly two different azo dye concentrations of c_{AY38} = 0.5 × 10^{-4} mol L^{-1} and 1.0 × 10^{-4} mol L^{-1} and transferred into Hellma 404-QX quartz cells with a 2 mm path length. The employed neutron beam was 15 mm in diameter. At neutron wavelength λ = 6.0 Å (FWHM 10%), three different sample–detector distances (1.7, 8.0, and 38 m) were used with a collimation distance of 4.0, 8.0, and 40.5 m to cover the whole particle. A total scattering vector range of 0.016 $nm^{-1} \leq q \leq$ 4.9 nm^{-1} was investigated. Scattered neutrons were detected using a multitube ^{3}He gas detector consisting of three detector panels: a central one with 192 horizontally oriented tubes, and a left- and right-side panel of 32 vertically oriented tubes. Each tube was 1 m long with a

pixel size of 4 mm along the tube, with the inner tube diameter being 8 mm. The detector was, therefore, composed of 256 × 256 pixels. Two-dimensional data were corrected for empty cell scattering, electronic background, detector uniformity via measuring 1 mm H_2O scattering, and transmissions using the Mantid 6.0 software package [53]. Data were put on an absolute scale via the attenuated direct beam intensity, measured per instrument configuration. Azimuthally averaged scattering curves were then used to subtract the solvent scattering and incoherent background.

The SANS intensity after data correction is:

$$I(q) = \varnothing V_{NP} (\Delta\rho_{SLD})^2 P(q) S(q) \tag{15}$$

where ∅ is the volume fraction, V_{NP} is the particle volume, $\Delta\rho_{SLD}$ is the difference in scattering length densities between the solute and the solvent, and $P(q)$, the particle form factor, corresponds to the particle shape. The structure factor $S(q)$ represents the interparticle correlations considered equal to 1, as the samples were diluted.

For example, for a sphere with radius R, the form factor $P(q)$ is [54]

$$P(q,\alpha) = \frac{scale}{V}\left(3\frac{sinqR - qRcosqR}{(qR)^3}\right)^2 + background \tag{16}$$

while for a cylinder with length L and radius R, $P(q)$ is [55,56]

$$P(q,\alpha) = \frac{scale}{V}\left(2(\Delta\rho)V\frac{sin\left(\frac{1}{2}qLcos\alpha\right)}{\frac{1}{2}qLcos\alpha}\frac{J_1(qRsin\alpha)}{qRsin\alpha}\right)^2 + background \tag{17}$$

where α is the angle between the cylinder's axes, $V = \pi R^2 L$ is the volume of the cylinder, $\Delta\rho$ (contrast) is the scattering length density difference between the scatterer and the solvent, and J_1 is the first-order Bessel function.

For an ellipsoid, the form factor $P(q)$ is:

$$P(q,\alpha) = \frac{scale}{V}\left(\Delta\rho V\frac{3(\sin qr - qr\ cos\ qr)}{(qr)^3}\right)^2 + background \tag{18}$$

with

$$r = \left[R_e^2 sin^2\alpha + R_p^2 cos\alpha\right]^{1/2} \tag{19}$$

where α is the angle between the ellipsoidal axes and $V = (4/3)\pi R_p R_e^2$ is the volume of the ellipsoid, R_p is the polar radius along the rotational axis, and R_e is the equatorial radius perpendicular to the rotational axis of the ellipsoid.

As explained above in SLS, the Guinier radius can also be used for low-q SANS data, where ln(q) is plotted against q^2 [54]. Guinier radius is usually restricted to small-q ranges only until the Guinier law follows ($q^2 \times R_g \leq 1.2$). Therefore, it is applied only for small-sized nanoparticles (1–100 nm).

SasView 4.2.2 was employed to fit the scattering data using various model form factors. The reduced χ^2 value can assess the SANS data's fitting quality. The polydispersity index (PDI) is also provided using this software.

2.7. Isothermal Titration Calorimetry

ITC experiments were performed at the VP-ITC microcalorimeter from MicroCal Inc. (Northampton, MA, USA).

ITC is a technique that measures the heat changes (released or absorbed) upon mixing two solutions. Two identical reference and sample cells with a volume of 1.442 mL each are enclosed in an adiabatic jacket. In this study, the reference cell was filled with the

solvent (D_2O), and the working cell contained the sample solution. A volume of 288 µL of titrant from the syringe was injected stepwise into the sample cell under constant stirring. For the presented experiments, the stirring rate was 351 rpm. All the measurements were performed at RT (25 °C). Small aliquots of titrant (typically 2 µL) were injected in 50–60 steps to achieve the charge ratio range of $0.2 \leq I_c \leq 4.4$. The duration of each injection was 300 s with a total measurement time of 4–4.5 h (including equilibration time). Due to the absorption or release of heat, each injection produces a distinctive peak. A separate measurement was performed with the titrant and the solvent for the data subtraction. The data analysis and fitting were performed using the Origin 7.0 software provided by MicroCal. The data were fitted with the two-site model. Gibbs free energy (ΔG) was calculated using a formula:

$$\Delta G = \Delta H - T\Delta S = -RTlnK \quad (20)$$

3. Results

The present study focuses on the physical–chemical aspects of the formation of nanoparticles in solution with defined sizes and varying shapes formed by electrostatic self-assembly of acid yellow 38 azo dye (AY38) and generation 5 PAMAM dendrimers. Here, the effect of irradiation has been studied while varying the charge ratio and concentration of these assemblies. In this study, the charge ratio, l_c, is represented as the ratio of the number of anionic dye sulfonates groups (originating from AY38) to the number of cationic amine groups (primary and tertiary amines originating from PAMAM dendrimer). Due to the different number of ions in both building blocks (AY38 has two anions, and G5 dendrimer has 254 cations), a higher dye concentration was used to balance the charge ratio.

Due to the pH responsiveness of PAMAM dendrimers, stock solutions of dye and dendrimer were mixed in water in a basic medium (pD = 10.5) to prevent assembly formation. Later, to initiate the self-assembly process, a small amount of DCl was added until the pD of the solution declined to pD = 3.5. These nanoparticles were characterized by various methods, as will be discussed in the following:

3.1. Light and Small-Angle Neutron Scattering

Light scattering experiments were performed for the nanoparticle size evaluation, where the hydrodynamic radii R_H were received from DLS, and SLS was performed to obtain information on scattered particle topology. The ratio of the radius of gyration, R_G (obtained from SLS) to R_H, gives an indication of the nanoparticles' shape before analyzing it in detail by SANS. For AY38/G5 assemblies with two charge ratios, l_c = 0.5 and l_c = 2.0, the electric field autocorrelation functions g_1 (τ) are plotted together with the corresponding relaxation time distributions in Figure 1. DLS indicated stable assemblies of different sizes at different charge ratios. A bimodal distribution with hydrodynamic radius, R_H = (5.8 ± 2.4) nm and R_H = (89 ± 4.5) nm, was observed (red color) at l_c = 0.5 (Figure 1a). The small-size peak (intensity weight % = 5%) originates from excess free dendrimers in the solution. Irradiation does not have any major effect on the aggregates in this case. At l_c = 2.0, again two different types of aggregates form, with R_H = (18 ± 4) nm and R_H = (350 ± 140) nm. According to DLS, the primary peak (intensity-weighted) contributes to the smaller particles (≈ 95%) prior to irradiation, which shows that the majority of particles are small particles in the solution compared to large aggregates. An enormous change in particle size (up to five-fold) was noticed upon irradiation, with a significant decrease in distribution width (σ ≈ 0.24 to 0.02), as can be seen in Figure 1b. The results agree with the previous studies, where, however, polydispersity and bimodal distributions were not explored in detail [42,57].

The charge ratio has been one of the critical factors in altering the electrostatic assemblies in our recent studies [14,16]. However, photoswitchability and its effects on particle morphology have yet to be fundamentally understood in detail.

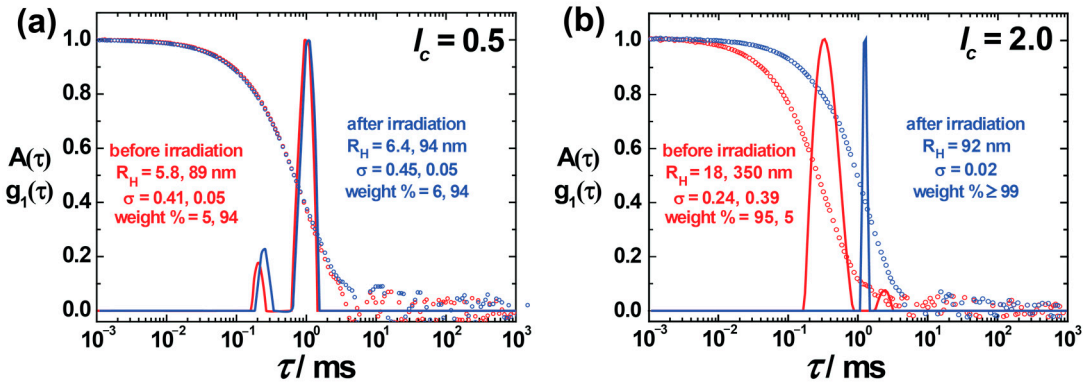


Figure 1. Dynamic light scattering on AY38/G5 assemblies at charge ratio (**a**) l_c = 0.5 and (**b**) l_c = 2.0: Electric field autocorrelation function $g_1(\tau)$ and distribution of relaxation times A(τ) at a scattering angle of θ = 90 show the increase in assembly size. R_H = hydrodynamic radius; σ = standard deviation (peak width) of the distribution.

The DLS results are displayed in Figure 2a, where the hydrodynamic radius, R_H, is plotted against l_c. The red and blue colors in Figure 2 represent assemblies before and after irradiation, respectively. In excess of the dendrimer (l_c = 0.5 and 0.75), nearly monomodal particles with some free G5 PAMAM dendrimers were observed in the solution. At l_c = 1.0, the building blocks form highly aggregated and large nanostructures (up to 1 μm diameter) and will be discussed later in conjunction with the ζ-potential studies.

Upon increasing the l_c to moderate excess of dye (l_c = 1.5), nearly monodisperse particles form with the size of R_H = 19 nm, and the previously unbound dendrimer molecules now associate with the assemblies. On further increasing the dye content ($l_c \geq 2.0$), a bimodal distribution (a mixture of 10–20 nm nanoparticles and large aggregates up to micrometer sizes) with increased polydispersity appears. These sizes are represented by the open symbols along with their charge ratios. Only the 5% intensity weight contribution comes from the larger aggregates at l_c = 2.0, which increases to 30% and 40% at l_c = 3.0 and 4.0, respectively (Figure S1). Upon expanding the l_c to a very high excess of dye (l_c = 30.0), only 5% of the intensity-weighted particles were found to be small particles (R_H = 12 nm); otherwise, the rest of them form large aggregates up to 200 nm radius as shown in Figure S2. This suggests that the smaller assemblies are similar to the ones observed at l_c = 1.5. With increasing amounts of dye, the interaction increases between these assemblies, and larger aggregates are formed. These large aggregates could be the result of a kinetic process. Irradiating these assemblies using λ = 365 nm significantly modulates them depending on their charge ratios. No notable changes in size have been observed at $l_c \leq 1.0$, where the cationic charges from dendrimers stabilize the charged nanostructures. Thus, the isomerization of the dye from *trans* to *cis* does not influence the stability of the nano-assemblies, and the size remains the same [14].

On increasing the charge ratio, i.e., where the anionic charges dominate, the polydispersity decreases sharply upon irradiation, and the light restructures these bimodal aggregates to produce well-defined monodisperse nanoparticles with a size between R_H = 47 nm and R_H = 181 nm depending on their charge ratio. The most substantial difference in size occurred at a moderate excess of dye (l_c =1.5), whereas for larger charge ratios, the size increment is not as immense as in l_c = 1.5. In addition, at higher l_c, the larger and smaller aggregates (bimodal system) dissolve to fabricate monomodal nanoparticles upon irradiation.

Along with the charge ratio, the concentration effects were also observed in the case of a high excess of dendrimer (l_c < 1.0) and a moderate excess of dye charges ($1.0 \leq l_c \leq 2.0$). The DLS result of these charge ratios in Figure S3 shows the effect of concentration and irradiation on the assembly sizes. The size decreases with the increase in concentration. It must be due to the absolute amount of excess charges (anionic or cationic) in the assemblies that help stabilize the assemblies and inhibit the growth of aggregates.

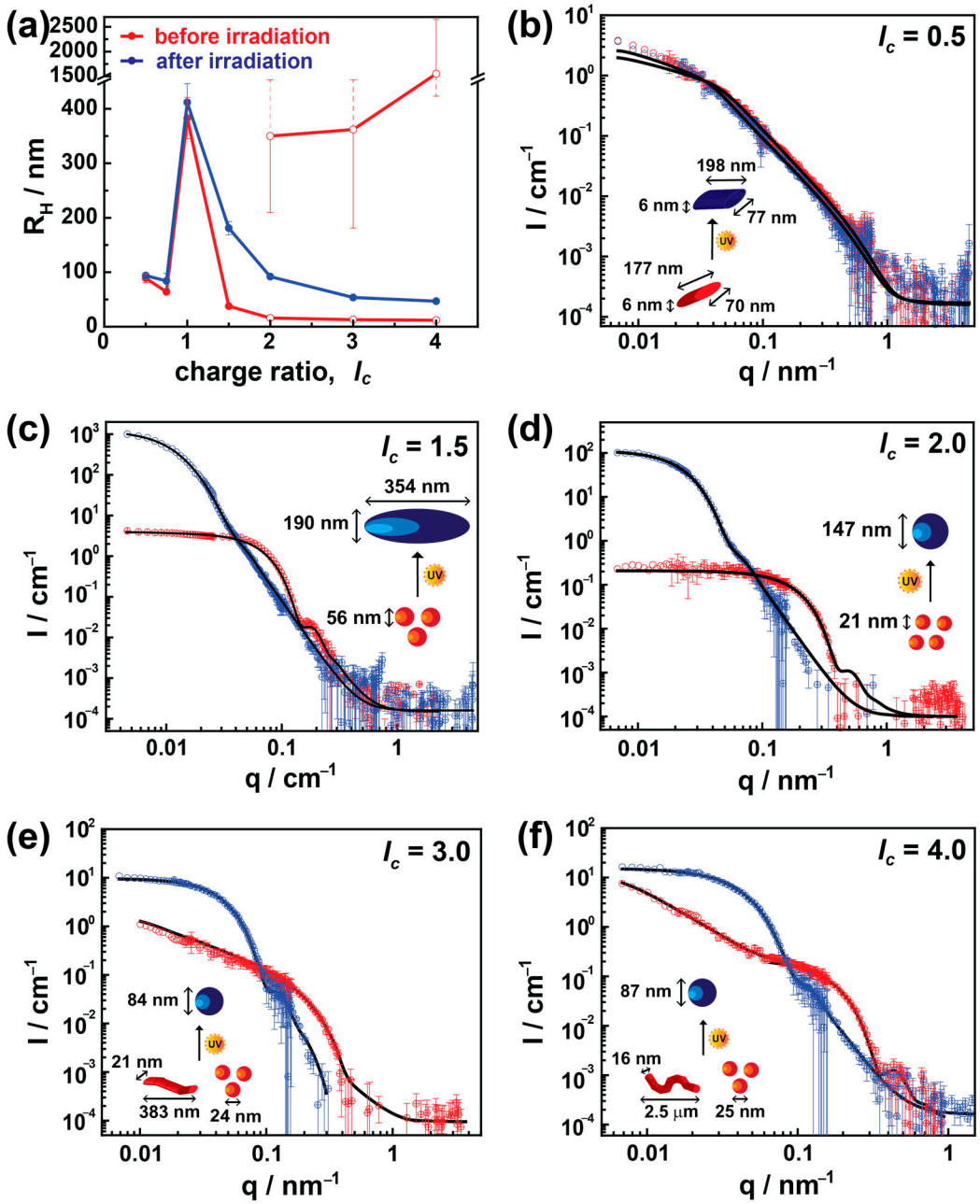


Figure 2. The effect of charge ratio and irradiation on AY38/G5 photosensitive assembly: (**a**) hydrodynamic radius, R_H, obtained by multiangle DLS (open red symbols for I_c = 2.0, 3.0, and 4.0 indicate a bimodal distribution); (**b**–**f**) SLS-SANS. Red and blue color represent the nanoparticles before and after irradiation. Black lines represent the best structural model fit. The inset sketches also indicate corresponding shapes.

To sum up the results from light scattering, it was observed that highly monodispersed assemblies form upon irradiation, and the largest change in size is observed in the case of moderate excess dyes. With increasing the charge ratio and concentration, the surplus dye ions tend to stabilize the assemblies, which might be a reason for small changes in size due to irradiation, as previously explained by Willerich et al. [14]. Moreover, in the excess of dye ions, secondary dye–dye interactions take place, which could be the reason for polydispersity in the samples. The role of charged species regarding stability and shape modifications are further investigated in detail in ζ-potential and UV-Vis studies mentioned below.

After characterizing these nanoparticles in detail using light scattering, it is highly interesting to investigate the detailed shape of the particles. Therefore, the photo and charge ratio effects on the nanoparticle structures, particularly the shape, have been addressed by combining results from static light scattering and small-angle neutron scattering measurements, as shown in Figure 2b–f. SLS data merged with SANS data very well in all cases. The Guinier radii corresponding to the structural model fits are well in agreement with the Guinier radii obtained from Guinier plots, which again confirms the model's accuracy (Table S1).

Figure 2b shows data for l_c = 0.5. Data are fitted using an elliptically elongated cylinder model with a length of (177 ± 22) nm and an elliptical cross-section of an axial radius of 3 nm, that is, well-defined elongated particles with a remarkable axis ratio of 13. No significant structural changes occur after irradiation; the shape remained with a similar radius and axis ratio, exhibiting a length of (198 ± 35) nm after irradiation. The results are in agreement with DLS. The excess of positive charges from dendrimer molecules provides stability to the assemblies, and due to the decreased amount of azo dye, no changes are observed upon irradiation.

Contrarily, a substantial difference in size and shape has been observed in the case of a moderate excess of dye (l_c = 1.5). Here, small spherically shaped nanoparticles of diameter (56 ± 10) nm convert to ellipsoidal assemblies with an axial length of (190 ± 16) nm and equatorial length of (395 ± 40) nm with a low polydispersity ($\sigma \leq 0.10$) due to irradiation, as shown in Figure 2c. In the case of l_c = 2.0, again, a considerable difference in size has been observed after irradiation, where 21 nm nanoparticles are converted into 147 nm spherical particles. However, prior to irradiation, a few data points (obtained from SLS measurements) at low-q do not fall within the range of a quality fit. This is possibly due to a small number of large aggregates observed in DLS (R_H = 350 ± 140 nm) and the limited length scale of SANS.

On further increasing the charge ratio (l_c > 2), bimodal particle distributions with different particle shapes and large polydispersity are observed. These coexisting shapes were small spherical objects (20–40 nm) along with exceedingly elongated flexible or elliptical cylinders with a length of up to µm sizes, where the small aggregates are in excess (>80%). Again, this agrees with the light scattering results. As the bimodal assemblies begin to be seen at an excess of dye ($l_c \geq 2.0$), this may indicate that secondary interactions between dye molecules must play a pivotal role in inducing the polydispersity. Interestingly, upon irradiation, even though there are two highly different structural nano-assemblies, these bimodal assemblies transform into highly monodisperse spherical particles. This can be understood with the isomerization of the azo dye to the *cis* state. Due thereto, the surplus dye ions associated with secondary non-covalent interactions start to disassemble. Thus, monodispersed nano-assemblies are formed, similar to the previous study by Willerich et al. [14]. More details will be given in ζ-potential and UV-Vis studies below.

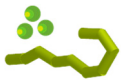
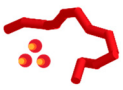
After observing the concentration effect on the assembly size using light scattering, it is further explored in SANS (Figure S4) using various charge ratios and 0.5×10^{-4} mol L^{-1} concentration (in terms of AY38). Before irradiation, charge ratios l_c = 2.0, 3.0, and 4.0 show a similar bimodal distribution with small spherical aggregates and elongated micrometer-sized structures. In this case, the smaller aggregates were larger (≈36 nm) than those observed at higher concentrations (≤25 nm) for the same charge ratios. Various factors could be involved in controlling the size of the assemblies by varying the concentrations. At lower concentrations, the number of dye-loaded dendrimers formed in the beginning during the self-assembly process decreases, leading to a higher number of building blocks being available for the nano-assembly growth, resulting in large aggregates [58]. As the concentration increases, more dye-loaded dendrimers form, competing for the free building blocks. This restricts the growth of each particle, leading to smaller aggregates. The saturation level of dye–dendrimer and dye–dye interactions is achieved at higher concentrations, so further concentration increases do not significantly affect the size [59–61]. Moreover, at lower concentrations, the electrostatic repulsion between the dye-loaded

dendrimers decreases due to large interparticle distances, which allows them to interact and form larger assemblies, whereas in higher concentrations, due to high electrostatic repulsion, compact assemblies form. At lower concentrations, due to the decreased amount of dye and dendrimer molecules, the particles likely have a longer diffusion time before encountering other molecules. This extended diffusion time can result in a lower amount of dye–dye interactions, which leads to less stabilized nano-assemblies and the particles growing in size.

After irradiation, highly monodisperse (PDI $\leq$ 0.2) spherical structures are formed from the bimodal distribution. Compared to the higher concentration, the size of the nano-assemblies is larger, similar to before irradiation. This can be understood with the larger size of the nano-assemblies before irradiation.

All the structures obtained from SANS before and after irradiation, including concentration and charge ratio effects, are summarized in Table 1. The size is not up to the scale in the table. For low concentration, the data are not available for l_c = 0.5 and 1.5. Upon irradiation, the shape of the assemblies becomes more isotropic when the charge ratio increases, irrespective of their concentrations. Thus, evidently, a decreased dye–dye interaction causes the formation of more isotropic aggregates, as found previously for non-switchable systems [39]. This is also accompanied by a lower surface charge density (charged dye molecules detach), for which the smaller surface to be stabilized of the more isotropic structure likely is favored.

Table 1. Nanoparticle shapes of AY38/G5 nanoparticles at different charge ratios obtained by SLS-SANS experiments (size is not up to the scale). The green and magenta colors represent samples at C_{AY38} = 0.5 × 10^{-4} mol L^{-1} before and after irradiation. The red and blue color show the samples at C_{AY38} = 1.0 × 10^{-4} mol L^{-1} before and after irradiation.

l_c	C_{AY38} = 0.5 × 10^{-4} mol L^{-1}		C_{AY38} = 1.0 × 10^{-4} mol L^{-1}	
	Before Irradiation	**After Irradiation**	**Before Irradiation**	**After Irradiation**
0.5	Shape Variation in AY38/G5 Assemblies			
1.5				
2.0				
3.0				
4.0				

3.2. Kinetic and Thermodynamic Assemblies

Well-defined self-assembled structures can be thermodynamically controlled, i.e., represent equilibrium structures, or kinetically controlled, i.e., be kinetically trapped, as due to a high activation energy, the thermodynamic minimum is not reached [17,62,63]. The preparation route can thus affect the outcome of a kinetically controlled particle design, i.e., by various reaction conditions, including temperature, order of mixing, and stirring velocity. In contrast, more stable assemblies and the lowest free energy, thus independent of the preparation route, favor the thermodynamically controlled structure. According to the

previous studies, assemblies dissolve again upon adding excess dendrimer, for example, when changing the charge ratio from l_c = 0.75 to l_c = 0.5, which suggests that the nanostructures are not kinetically trapped but adjust to the respective thermodynamically favored state for each composition ratio [39]. From this, it can be deduced that the nanoparticles and building blocks are in equilibrium.

As the above experiment was qualitative, a detailed study of different mixing procedures is needed to gain a deeper insight into the assembly formation in solution. Since the assembly formation upon mixing the charged components takes place on a fast time scale, separating the mixing steps of building blocks would be essential to understanding the mechanics of assembly formation. In the standard sample preparation method I (developed from previous studies), both the components are first mixed at *pD* = 10.5, and subsequent adjustment to *pD* = 3.5 follows, which offers the advantage of a complete mixing prior to assembly formation due to deprotonated dendrimer being uncharged [14,25,39]. In contrast, in methods II and III, the stock solutions were prepared in acidic medium (*pD* = 3.5). The dendrimer molecules were entirely charged when mixed with an acidic dye solution (the dendrimer solution was incorporated into the dye solution in method II and in the opposite way in method III).

Figure 3a shows the size distribution of l_c = 0.5, prepared using methods I, II, and III. All the assemblies show bimodal distributions, where the small aggregates must originate from the excess of dendrimer molecules, and the large aggregates are the product of dye–dendrimer interactions. Irrespective of preparation routes, all the assemblies are similar in size, which suggests that these assemblies are thermodynamically controlled. At l_c = 2.0, diverse structures are formed based on their methods of preparation (Figure 3b), whereas at l_c = 2.0, larger aggregates result (along with the small assemblies) with a significant standard deviation and a large quantity of the assemblies. The hydrodynamic radius of the small aggregates is in the range of 18–30 nm. However, the larger aggregates vary, and methods II and III form aggregates with R_H > 500 nm. Thus, the nano-assemblies—to be more exact, the larger nanoparticles—are kinetically controlled when there is an excess of anionic charges.

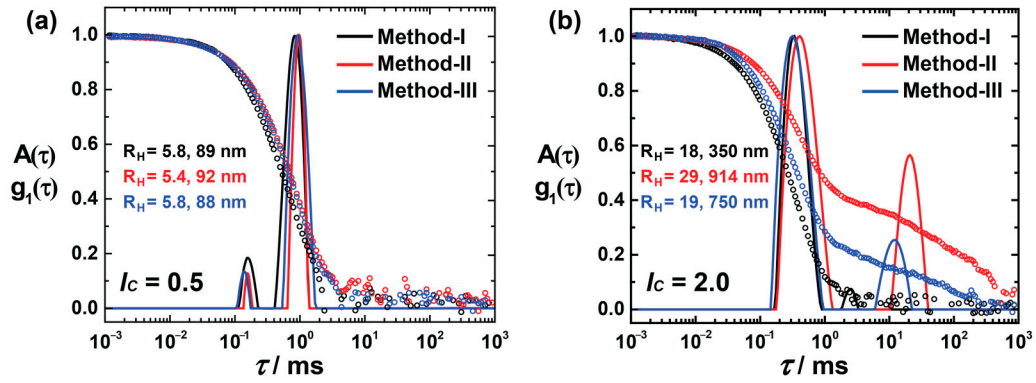


Figure 3. DLS for different preparation routes: Electric field autocorrelation function $g_1(\tau)$ and distribution of relaxation times $A(\tau)$ (scattering angle $\theta = 90^\circ$) of AY38/G5 assemblies before irradiation: (**a**) at l_c = 0.5 and (**b**) at l_c = 2.0, where method I is the preparation way used throughout this study. In methods II and III, stock solutions were prepared and mixed in acidic medium (*pD* = 3.5). In method II, the dendrimer solution was added to the dye solution, while in method III, it was the other way around.

After irradiation, light-scattering results were observed, as given in Figure S5, for both charge ratios. No significant changes in size occur at l_c = 0.5, but larger particles are observed using methods II and III in a higher charge ratio. All the large aggregates detected before irradiation disassemble and fabricate more monodispersed assemblies with small particles. Using SANS, Figure S6 reveals the structure variation (size and shape) by changing the preparation route for l_c = 2.0. SANS reveals the elongated structures prior

to irradiation. These elongated particles and smaller spheres reassemble to form highly monodispersed spheres upon irradiation, as addressed above.

In general, this kinetic influence appears only in high charge ratio (l_c > 1.5) and before irradiation. Until $l_c \leq 1.5$ and after irradiation, all the samples follow a thermodynamically controlled process where they exhibit the same size, irrespective of the preparation methods, as shown in Table S2. This again suggests that the reason for the kinetically controlled step lies with the dye–dye interaction.

The size difference in different preparation methods could possibly be due to an inhomogeneous distribution of dye molecules and oppositely charged polyelectrolytes when mixed. A cooperative binding process propagates directly simultaneously with the mixing, i.e., starts before complete mixing is reached. Thus, not the equilibrium structure but a kinetically driven structure forms, which in some cases may be kinetically stabilized in its initial form. Therefore, the method of preparation influences the formation of nano-assemblies to some extent, and assemblies of desired sizes can be achieved by the corresponding choice of preparation route. The same preparation method must be followed throughout the present work to be able to understand the G5/AY38 assemblies at different charge ratios and concentrations quantitatively. Here, method I provides the most ideal mixing conditions as it leads to a thermodynamically controlled equilibrium structure; based on the above experiments, this preparation route will not be influenced by kinetic effects, as compared to methods II and III, and yield comparatively small sizes and highly stable assemblies.

3.3. ζ-Potential Studies

The charges from dye and dendrimer play a critical role in stabilizing these electrostatic assemblies. Therefore, it is crucial to understand the diversity in particle charges due to charge ratio and irradiation and how it affects particle stability. ζ-potential studies can provide this information by measuring the electrostatic potential between the shear plane of the nanoparticles and the liquid medium, as shown in Figure 4a. In the case of dendrimer excess, the assemblies exhibit highly positive ζ-potential values of ζ > 40 mV that do not indicate any substantial changes upon irradiation in the case of TC nanostructures. In comparison, at l_c > 1.0, the number of sulfonate charges increases, providing highly negative ζ-potentials of ζ < −20 mV, which electrostatically stabilizes the assemblies very well. On irradiating these particles, the ζ-potential values weaken abruptly and become less negative or close to 0 mV.

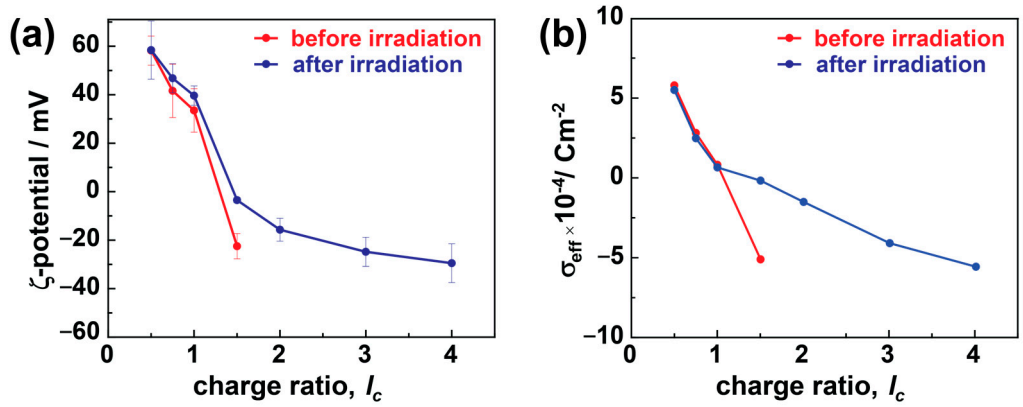


Figure 4. Charge characteristics of dendrimer-dye assemblies: (**a**) ζ-potential, and (**b**) effective charge density, σ_{eff}. Red: before irradiation, blue: after irradiation.

In the case of excess dendrimers (l_c < 1.0), the free positive amine charges from dendrimers stabilize the assemblies, and only minimal changes in ζ-potential have been noticed upon irradiation. The nanostructures are slightly positive at a stoichiometric ratio (l_c = 1.0), and the dye molecules partially redistribute to the excess dendrimer molecules

and form larger aggregates than the monomers (as in host–guest assemblies), and the ζ-potential shows a positive value [39]. A similar phenomenon applies in the case of polymer brushes, where even the slight excess of polyelectrolyte charges ensures stability and forms thermodynamically controlled products. More details on the formation mechanism will be discussed in conjunction with the UV-Vis results below.

Conversely, in the case of excess dye molecules, the free sulfonate charges provide the negative ζ-potential, stabilizing the electrostatic assemblies at higher charge ratios ($l_c > 1$). The surplus dye molecules are either present as free dye ions or bound over-stoichiometrically by dye–dye interactions with the electrostatically bound dye ions in the assembly. The surplus dye ions help stabilize the particles by providing sufficient charges to the dye–dendrimer assemblies (also the cause of negative ζ-potential, Figure 2a). At the same time, the dye–dye interactions lead to large-size aggregates and high polydispersity in the assemblies. A higher negative ζ-potential results in more densely charged and small stable assemblies along with micrometer-sized aggregates, which increase the number of large assemblies upon increasing the charge ratio. In the case of bimodal distribution (before irradiation at $l_c \geq 2.0$), the ζ-potential values represent the average of the different species; therefore, they cannot be interpreted much further [64]. The ζ-potential values change significantly upon irradiation in these cases due to the over-stoichiometric dye ions bound by dipole–dipole interactions. These loosely bound dye ions partially dissociate from the (bimodal) assemblies and reduce the stability of charged stabilized particles. Therefore, the weakening of the ζ-potential (increase to 0 mV) was observed upon irradiation. At the same time, these partially dissociated aggregates recombine to overcome the stability threshold and form more monodisperse and large particles that require a certain charge density for stabilization.

Considering the effective surface charge density (σ_{eff}) is a more efficient way to understand the effects of size and charges on the particle stability. σ_{eff} is calculated by combining the values of ζ-potential and R_H together by using the given formula:

$$\sigma_{eff} = \frac{Q_{eff}}{S_{assembly}} = \frac{4\pi\varepsilon\zeta R_{eff}}{4\pi R_{eff}^2} = \frac{\varepsilon\zeta}{R_{eff}} \approx \frac{\varepsilon\zeta}{R_H} \quad (21)$$

where Q_{eff} is the effective charge, $S_{assembly}$ is the assembly surface, ε is the permittivity constant, and R_{eff} is the effective radius approximated to be the R_H. Figure 4b plots the change in σ_{eff} as a function of charge ratio. Prior to irradiation, the charge density decreases (from positive to negative) as the l_c value increases. This is due to the increasing amount of dye compared to dendrimer, which increases the charge density of the aggregates, as discussed for the ζ-potential. σ_{eff} is calculated only for monomodal aggregate samples. Upon irradiation, the charge density of the dendrimer excess particles nearly stays constant, further elucidating that the isomerization from *trans* to *cis* does not influence the stability as there are no dye–dye interactions present, and the assemblies are stabilized by the positive charges provided by the polyelectrolytes. In the case of moderate dye excess ($l_c = 1.5$), the dipole–dipole bound excess dye ions (partly) dissociate upon irradiation. Thus, the small nano-assemblies are not electrostatically stabilized anymore, and larger aggregates form. Upon increasing the l_c further ($l_c > 1.5$), the previous polydispersed assemblies become monodisperse and are stabilized by their high charge density.

In summary, both the excess polyelectrolyte and dye charges can stabilize the assemblies. The nanostructures do not change upon irradiation at an excess of dendrimer charges, as the isomerization does not influence the overall charge density [39]. The dye–dye interaction between the smaller assemblies leads to larger aggregates and polydispersity in excess of anionic charges. Upon irradiation, the dye–dye interaction is interrupted, and monodisperse assemblies are formed, which are stabilized by the anionic charges.

3.4. UV-Vis Spectroscopy

To understand the origin of the secondary dye–dye interaction, which is responsible for stabilization as well as the bimodality observed in DLS/SANS, UV-Vis measurements were performed. To compare all results, a concentration of c_{AY38} =1.0 × 10^{-4} mol L^{-} was used throughout the experiments. As shown in Figure 5a, no difference is observed in UV-Vis spectra of AY38 dye only and the solutions with dendrimer. Similar absorptions were observed before irradiation for different charge ratios, suggesting that the dendrimer addition does not affect the azo dye spectrum. This leads to the conclusion that the dye–dye interaction cannot be π–π interaction. The occurrence of hydrogen bonding can be excluded, as the dye AY38 cannot form hydrogen bonds with itself. Lastly, the hydrophobic effect can also be excluded, as the building blocks are polar molecules. Thus, it must be dipole–dipole interactions that bind multiple dye molecules to the electrostatically attached dye–dendrimer assemblies and create large aggregates. Upon irradiation, these surplus dye molecules disconnect due to *cis* isomer conformation, which is unsuitable for adjacent dipole–dipole interactions and has less than half of the dipole moment value (12.96 Debye) compared to *trans* dye molecules (27.96 Debye), as shown in Figure 5c.

To gain more information regarding stabilization and nanostructure, the amount of both *trans* and *cis* isomers was calculated prior to irradiation using the UV-Vis data fitted with Gaussian plots in Origin 9.0 software, as shown in Figure S7a. As the thermodynamically preferred molecular form, *trans* isomers remain in the majority (>90%) and do not vary upon changing the l_c. However, upon irradiation, the dye isomerizes to different extents depending on the charge ratios. In dendrimer excess (l_c = 0.5), only 25% of the dye converts into *cis* molecules upon irradiation, and the slightest change in size is observed. In this case, the photoprotective effect limits the dye isomerization to the *cis* state: when the dye is electrostatically bound with both sulfonate groups to the dendrimer, isomerization is hindered. With an increasing charge ratio, the degree of isomerization increases to a maximum of 75% at a moderate excess of dye (l_c = 1.5), where the most noticeable difference in size is observed (Figure 2a). This increase is due to the increasing amount of dye. Due to that, likely, a lower number of dye molecules bind with both sulfonate groups to the dendrimer and are hindered from isomerizing. Upon increasing the charge ratio further, the *cis* isomer amount decreases again (Table S3). Due to the combination of electrostatic and dipole–dipole interaction, the molecule is again hindered from isomerizing. With an increasing charge ratio, the dye–dye interaction also increases, and thus the isomerization decreases.

To understand the role of both isomers in influencing the nanostructures, centrifugation was applied to the dye–dendrimer samples to quantify the *trans* and *cis* amounts in assemblies and the solution. The nanoparticles were separated from the solution using the centrifuge at the speed of 10,000 rpm for 15 min. This way, the assemblies were separated at the bottom, and only the free dye molecules remained in the supernatant (also checked by DLS, as shown in Figure S8). UV-Vis spectroscopy was then used to determine the concentration of free dye molecules in the solution after centrifugation, as shown in Figure 5b. In the case of low l_c < 1, no free dye was observed in the solution as expected. The dye ions are preferably available for electrostatic interactions. Due to the strength of electrostatic interactions, the photoprotective effect occurs, limiting the dye to isomerizing in abundance (Figure 5f). The dye binds electrostatically to most dendrimer charges at a balanced l_c (≈1.0). Due to the steric hindrance, a few dye molecules (≈5%) do not interact with the polyelectrolyte dendrimer but are present in the solution as a free dye (Figure S9). Due to the surplus dye ions in the solution, the calculated l_c (≈0.95) is smaller than the original l_c (≈1.0). Therefore, only a few charges remain in the assembly, leading to less stabilized particles and less densely charged large aggregates (up to 1 µm). After irradiation, the bound dye only isomerizes to a limited extent due to the photoprotective effect, and no significant change in the assemblies was observed.

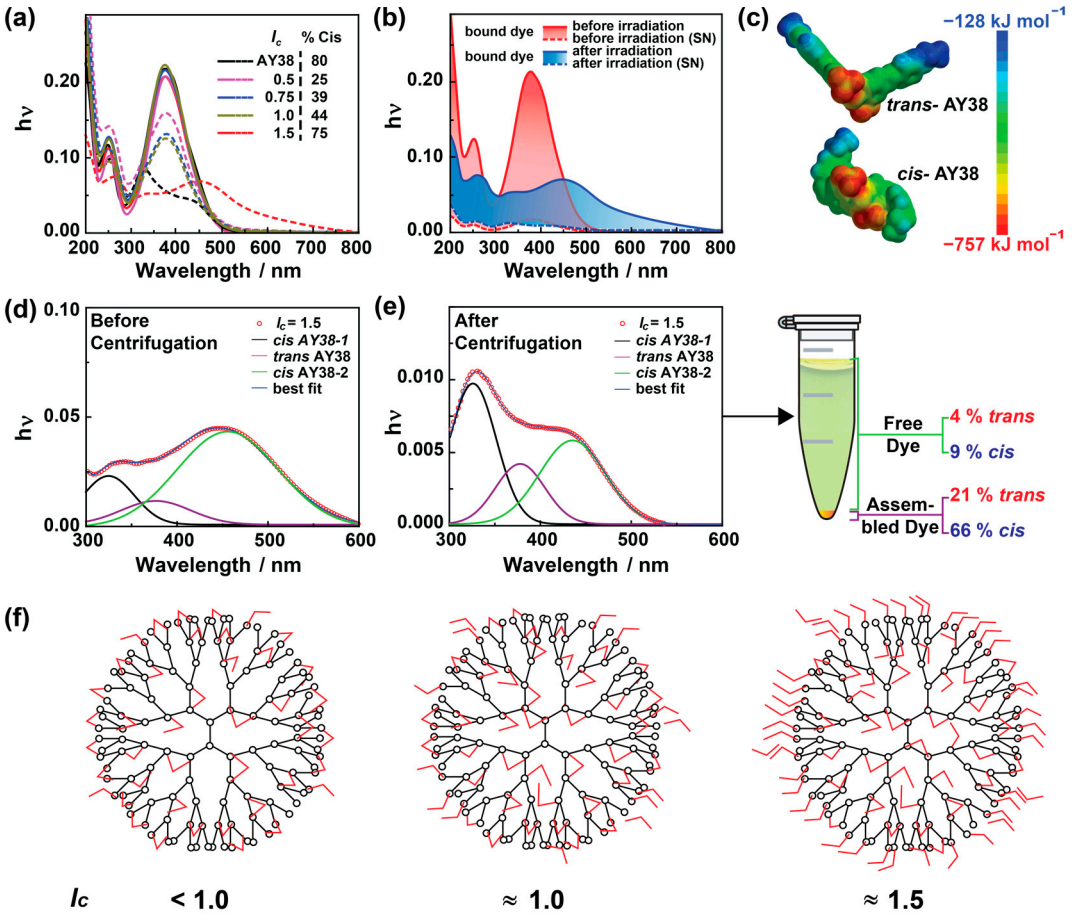


Figure 5. (**a**) UV-Vis spectroscopy of AY38/G5 assemblies at various charge ratios (straight lines represent the samples before irradiation, and short-dashed lines the samples after the irradiation). (**b**) The effect of centrifugation before and after irradiation (straight lines represent the samples before centrifugation and short-dashed lines the supernatant after the centrifugation. The colored area represents the dye–dendrimer assemblies). (**c**) Dipole moment of *trans* and *cis* AY38 at the molecular surface. (**d**) Analysis of UV spectra before and after irradiation, and (**e**) the supernatant after centrifugation (data are fitted using the Gauss model for multiple peaks from *cis* and *trans* AY38). The centrifuge tube represents the irradiated sample after centrifugation. (**f**) The schematic diagram represents the effect of charge ratio (l_c < 1.0, $l_c \approx 1.0$, $l_c \approx 1.5$) on dye–dendrimer bindings. G4 PAMAM dendrimer is displayed as an example. Red objects designate *trans* AY38 dye molecules.

UV-Vis absorption before and after irradiation (solid lines) is shown in Figure 5b for l_c = 1.5 (concentration of AY38 = 1.0 × 10^{-4} mol L^{-1}) and compares the results with the supernatant after centrifugation (short-dashed lines). The area covered by the red and blue colors represents the area occupied by dye–dendrimer assemblies; the rest belongs to the individual building blocks (free azo dye, in this case). As seen in the centrifuge tube shown in Figure 5e, the total free dye contributes approximately 13% of the total solution (a similar amount is observed before and after irradiation). As already known, the *trans* state is a more stable form of Acid Yellow 38, and the major part of the dye exists in its *trans* form (>90%) in solution before irradiation (Figure S7). After irradiation, approximately 75% of the dye isomerizes to the *cis* state, of which 9% are present as the free dye molecules. The remaining (66%) are bound in dye–dendrimer assemblies after irradiation. From 25% of the *trans* amount, 4% is present as free dye, whereas 21% contributes to the assemblies (Figure 5c–d). This suggests that due to the photoprotective effect, a portion of the *trans* molecules (25%) does not isomerize, and primarily, the free and over stoichiometric *trans* dye molecules isomerize to a *cis* state. To understand the origin of this behavior, one

may consider the difference in polarity. Both isomers have different polarities due to their geometry (Figure 5c), which may cause the *cis* form to interact less strongly with other azo molecules through secondary dipole–dipole interactions.

At l_c = 1.5, a high degree of isomerization is possible due to the difference in binding behavior of the two azo dye isomers. Approximately 87% of the dye is bound to the dendrimer molecules (the calculated value of $l_c \approx 1.3$). This must be a combination of electrostatic and dipole–dipole interactions, as shown in Figure 5f. The majority of dye ions are bound by only one site and could easily be isomerized without being influenced via the photoprotective effect.

To conclude the results from UV-Vis studies, dipole–dipole interactions are evidently involved in the structure determination and also cause the formation of polydispersed assemblies if present in excess. The photoprotective effect limits the isomerization of dye molecules and controls the size of the assemblies before and after the irradiation.

3.5. Isothermal Titration Calorimetry (ITC)

ITC is an excellent pathway to develop a fundamental understanding of thermodynamic parameters involved in assembly formation. Figure 6 shows the titration of different concentrations of AY38 ((0.5 and 1.0) $\times$ 10^{-4} mol L^{-1}) into (1.0 and 2.0) $\times$ 10^{-8} mol L^{-1} G5 dendrimer solution. Both sets of raw data can be fitted with a two-set-of-site binding model. The fitted values are given in Table 2.

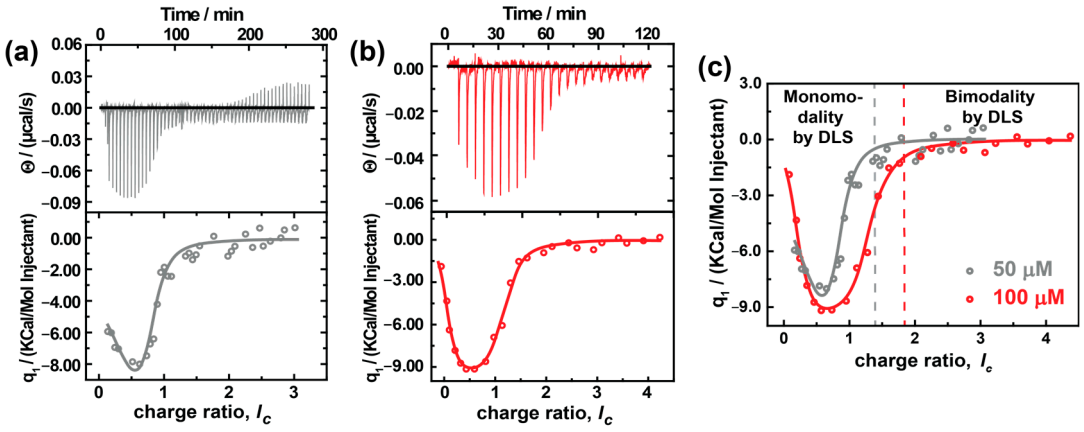


Figure 6. ITC analysis of AY38/G5 system using two different concentrations of AY38; (**a**) 0.5 $\times$ 10^{-4} mol L^{-1}, (**b**) 1.0 $\times$ 10^{-4} mol L^{-1}, and (**c**) ITC data fit comparison of two concentrations (AY38 is titrated into G5). Fits to the data according to a two-site model are shown as grey and red lines.

Table 2. ITC results of AY38/G5 system. AY38 is titrated into G5. Two-site model: (a) ΔH: 3–5%; (b) K: 20–60%; (c) Dye ions/den: 5–10%.

C_{AY38} /($\times 10^{-4}$) mol L^{-1}	Dye Ions/Den	K_1/M^{-1}	ΔH_1 per Site /kJ mol^{-1}	ΔS_1 per Site /J $mol^{-1}K^{-1}$	ΔG_1 per Site /kJ mol^{-1}	Dye Ions/Den	K_2/M^{-1}	ΔH_2 per Site /kJ mol^{-1}	ΔS_2 per Site /J $mol^{-1}K^{-1}$	ΔG_2 per Site /kJ mol^{-1}
0.5	70	2.2×10^{10}	19.9	5.4	−0.86	222	1.0×10^{13}	−136	−101	−0.33
1.0	51	4.5×10^{9}	6.7	1.3	−1.1	216	1.1×10^{13}	−34.6	−24.9	−0.34

It becomes evident that the first binding step is endothermic and entropically driven with a binding enthalpy of $\Delta H_{1,50}$ = 19.9 kJ/mol and $\Delta H_{1,100}$ = 5.4 kJ/mol, respectively, and an entropy of $\Delta S_{1,50}$ = 1.3 kJ/mol and $\Delta S_{1,100}$ = 6.7 kJ/mol, respectively. This corresponds to the electrostatic interaction between the dye and the dendrimer: First, the Cl^- counterions (from DCl) are exchanged with the -$SO3^-$ ions (from the azo dye), i.e., chloride ions and the hydration shell are separated from the cationic macroion charges, which are endothermic and accompanied by an increase in entropy. Contrary to the simple anticipations (where electrostatic interaction is exothermic), the enthalpy here increases. In electrostatic inter-

actions, it may seem evident that dye ions binding to macroions will liberate energy due to the Screened Coulomb attraction between macroions and counterions. However, the exchange of counterions with its entropic effects carries the association forward, as was described for linear polyelectrolytes by Antonietti et al. [65], since dendrimers are strongly hydrophilic molecules. At the beginning of the titration, the dye ions break the hydration shell surrounding the dendrimer building blocks and remove the initial counterions. The absorption of Ca^{2+} and La^{3+} to bilayer membranes and a few colloidal objects (such as cationic micelles and liposomes) follows a similar behavior [66,67]. The difference in the enthalpy and entropy between both experiments can be understood with the concentration. At higher concentrations, the change in entropy is lower compared to lower concentrations due to the high ionic strength. Subsequently, less energy is needed to break the hydration shell. Moreover, in dilute solutions, the assemblies have more freedom of motion, which would increase the randomness and, therefore, the entropy of the solution.

Further comparing both experiments, the binding stoichiometry differs strongly. In the first step, 70 dendrimer sites become attached to dye ions electrostatically at lower concentration, but only 51 sites at higher concentration. This decrease is possibly due to the presence of a higher number of monomeric dendrimers at higher concentrations that compete for the same amount of dye-loaded dendrimers and result in a limited growth of the aggregates, as explained earlier in context with the SANS results.

As mentioned above, a two-set-of-site process is observed. The second binding step is enthalpically driven with a binding enthalpy of $\Delta H_{2,50} = -136$ kJ/mol and $\Delta H_{2,100} = -34.6$ kJ/mol and an entropy of $\Delta S_{2,50} = -101$ kJ/mol and $\Delta S_{2,100} = -24.9$ kJ/mol. The second step ranges from $0.65 \leq l_c \leq 4.0$, corresponding to the combination of electrostatic and secondary interactions. This is further evident from the binding stoichiometry, which has a value of around 220 doubly-charged dye molecules per dendrimer, while the dendrimer has only 254 charges in total. No further heat release can be observed in the ITC from $l_c = 1.5$ onwards and $l_c = 2.0$ onwards in the cases of $c_{AY38} = 0.5 \times 10^{-4}$ mol L^{-1} and $c_{AY38} = 1.0 \times 10^{-4}$ mol L^{-1}, respectively. This is where the dipole–dipole interactions dominate over electrostatic interactions, leading to a second type of aggregation (bimodal distribution) in both concentrations, also observed in light and neutron scattering techniques. Interestingly, comparing both concentrations, the binding stoichiometry and the free energy are both the same, while the enthalpy and entropy differ. This behavior may again be due to the presence of fewer monomers at lower concentrations. As a result, the secondary interaction is stronger, and thus the enthalpy is more negative. At the same time, the entropy decreases as we observe fewer assemblies with a larger size.

Previous studies have already established that *trans* dye molecules have a higher ability to bind over-stoichiometrically to the electrostatic self-assemblies than the *cis* molecules since *cis* isomers show almost no dye–dye interaction compared to the *trans* isomers, explained by steric hindrance or geometric constraints of the *cis* dye molecules, as outlined above [13]. As shown herein, the difference in dipole moment is also an essential factor. In that study, only one binding site was observed, as Willerich et al. titrated PAMAM dendrimer into the AY38 dye solution. The only step is a combination of dye–dendrimer electrostatic interactions and dye–dye secondary interactions [14,25]. While the value for enthalpy and entropy differs from the sum observed with our system, the dye was also bound over-stoichiometrically. The reason for the differences in values is the different dendrimer generations and concentrations. In particular, the difference in generation influences (i) the electrostatic interaction, i.e., the equilibrium thermodynamics, (ii) steric effects, and (iii) the kinetics of the assembly formation. Additionally, in equilibrium, the assembly sizes increased with increasing the dendrimer generations in the previous system where the dye undergoes dye–dye interactions [68]. This is in accordance with the study of Willerich et al., where they observed a more negative ΔG of the association while forming larger assemblies [15]. However, the overall results of the two studies are consistent with a more detailed study and the interpretation provided herein. A detailed study of the

generation dependency and its effects on electrostatic assemblies will be addressed in a future study.

Overall, ITC confirms that the dipole–dipole interaction causes the polydispersity of the nano-assemblies. The changes observed in DLS and SANS regarding the different concentrations can also be observed and understood with ITC. At the same time, while it is clear that the concentration influences the size, the overall thermodynamic behavior is the same for both concentrations.

3.6. General Discussion

From the above experiments, it is confirmed that the secondary interactions that come into effect once the ionic building blocks approach each other ultimately affect the assembly formation processes. To further understand the role of secondary interactions in detail on kinetically and thermodynamically controlled assemblies, the irradiation-caused change in particle volume in % and the total amount of *cis* dye in % are plotted against the l_c of the sample (Figure 7). The change in volume % and the degree of isomerization due to irradiation share a similar dependency on the charge ratio. Due to the majority of small aggregates in bimodal systems, only the small particles are considered in the plot above. The values in Figure 6 are taken from $0.5 \leq l_c \leq 4.0$ with multiple concentrations (c_{AY38} = (0.5, 1.0, 1.5, and 2.0) $\times$ 10^{-4} mol L^{-1}). The volume % and the *cis* % increase up to the TC process ($\leq$1.5) and start declining when KC assemblies form.

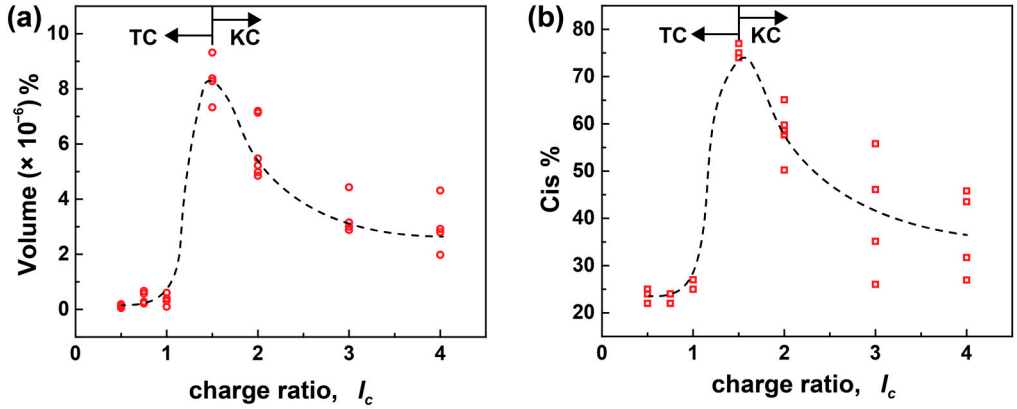


Figure 7. The influence of the charge ratio on (**a**) change in the volume % and (**b**) total *Cis* % for the AY38/G5 system upon irradiation using multiple concentrations (c_{AY38} = 0.5 $\times$ 10^{-4} mol L^{-1}, c_{AY38} = 1.0 $\times$ 10^{-4} mol L^{-1}, c_{AY38} = 1.5$\times$ 10^{-4} mol L^{-1}, c_{AY38} = 2.0 $\times$ 10^{-4} mol L^{-1}). R_H values were obtained from multiangle DLS and converted into the volume using the formula of a sphere volume ($V = \frac{4}{3}\pi R_H^3$), and the *cis* % was calculated using UV-Vis spectroscopy (see experimental pasrt). The arrows represent the starting point of the TC and KC processes. The open symbols represent samples from different concentrations at the same charge ratio.

At an excess of dendrimer charges, no significant changes in the volume and isomerization upon irradiation take place. Due to the photoprotective effect, nearly no isomerization occurs. Therefore, no change is observed upon irradiation and the particles are stabilized by the surplus dendrimer charges. Nevertheless, the samples containing a moderate excess of dye (l_c = 1.5) show a sharp increase in size and *cis* % due to their unique combination of electrostatic and secondary interactions, as discussed above. On further increasing the dye amount, the excess of dye ions assists in stabilizing the assemblies, leading to smaller percentage changes in particle volume and amount of *cis* dye, as compared to the moderate excess of dye. Moreover, the secondary interactions dominate at high l_c and cause the formation of (kinetically controlled) bimodal aggregates. Consequently, the *cis* amount directly affects the size of the aggregates. Hence, the combination of charge ratio and concentration allows control of the degree of isomerization and, ultimately, the size and structure of the nano-assemblies.

4. Conclusions

Insight has been gained in controllably fabricating functional nanostructures using electrostatic self-assembly in an aqueous environment. This study presented the facile route to regulate the aggregation of small building blocks and create nanoscale structures with diverse shapes and sizes. The electrostatic assemblies of generation 5 PAMAM dendrimer and AY38 azo dye have been investigated, where the effects of charge ratio and concentration have been observed, including the quantitative analysis of kinetically and thermodynamically controlled assemblies. Monodispersed particles with narrow size distributions and varying shapes are primarily achieved in either samples with dendrimer excess or samples with a moderate excess of dye ($l_c \leq 1.5$). The surplus charges (positive and negative) help in stabilizing the assemblies in the solution. In contrast, bimodal and multimodal distributions were found in the samples of higher l_c (>1.5). Remarkably, upon irradiation, the structure of the nano-assemblies changes to well-defined monodispersed assemblies and also to polydispersed nano-assemblies.

Further, the changes in size upon irradiation have been directly correlated with the percentage of *cis* dye, since the *cis* isomer cannot undergo dipole–dipole interactions. The concentration was further used to manipulate the size and shape of the assemblies. The size decreased with increasing the concentrations of building blocks while keeping the charge ratio constant. This type of secondary interaction has been defined as dipole–dipole interaction. In the future, varying the dendrimer generation could be valuable here as other generations provide different numbers of charges and additional flexibility in the molecule, which may influence the polydispersity. The generation dependency will be addressed in a future publication.

Supplementary Materials: The following supporting information can be downloaded at: https://www.mdpi.com/article/10.3390/polym16010050/s1. Figure S1: Dynamic light scattering of AY38/G5 assemblies; Figure S2: Dynamic light scattering of AY38/G5 assemblies at charge ratio lc = 30.0 before irradiation; Figure S3: Thermodynamically and kinetically controlled assemblies; Figure S4: SLS-SANS of AY38/G5 assemblies at different charge; Figure S5: Electric-field autocorrelation function g1(τ) and distribution of relaxation times A(τ) (scattering angle θ = 90°) of AY38/G5 assemblies after irradiation at lc = 0.5 (thermodynamically controlled), and 2.0 (kinetically controlled; Figure S6: SLS-SANS of AY38/G5 at lc = 2.0 using two preparation routes and the effect of irradiation on assemblies; Figure S7: Centrifugation: Analysis of UV-Vis spectra before irradiation for AY38/G5 at lc = 1.5; Figure S8: Electric field autocorrelation function g1(τ) for the supernatant received after centrifugation of lc = 1.5; Figure S9: The effect of centrifugation on the absorbance of AY38/G5 at lc = 1.0 is recorded by UV-Vis studies; Table S1: Radius of gyration for multiple charge ratios at different concentrations using SANS models and the Guinier; Table S2: DLS table for AY38/G5 using different methods of preparation; Table S3: Bound cis% in the assemblies after irradiation by varying the concentration and charge ratio of AY38/G5 assemblies.

Author Contributions: Conceptualization, R.S. and F.G.; Methodology, M.A., A.Z. and R.S.; Software, M.A.; Validation, R.S. and F.G.; Formal analysis, M.A.; Investigation, M.A.; Resources, R.S. and F.G.; Writing—original draft, M.A. and A.Z.; Writing—review & editing, A.Z., R.S. and F.G.; Visualization, M.A.; Supervision, R.S. and F.G.; Funding acquisition, R.S. and F.G. All authors have read and agreed to the published version of the manuscript.

Funding: Funding of the Institut Laue Langevin (ILL), Grenoble, France (ILL PhD student program), and of the German Science Foundation (DFG, GR 2701/3-2) and the and the Interdisciplinary Center for Molecular Materials (ICMM, Friedrich-Alexander -Universität Erlangen-Nürnberg) is gratefully acknowledged.

Data Availability Statement: The data presented are inclided in this study. SANS-data will be available at doi:10.5291/ILL-DATA.9-12-662 and doi:10.5291/ILL-DATA.9-12-624].

Acknowledgments: The partnership of Soft Condensed Matter (PSCM) is thankfully acknowledged. This work benefited from the SasView application, initially developed by the DANSE project under NSF award DMR-0520547. We would also like to thank Juliette Devos, Life Sciences group, ILL, for helping with centrifugation.

Conflicts of Interest: The authors declare no conflict of interest.

References

1. Discher, D.E.; Eisenberg, A. Polymer Vesicles. *Science* **2002**, *297*, 967–973. [CrossRef] [PubMed]
2. Liu, H.Y.; Pappa, A.M.; Pavia, A.; Pitsalidis, C.; Thiburce, Q.; Salleo, A.; Owens, R.M.; Daniel, S. Self-Assembly of Mammalian-Cell Membranes on Bioelectronic Devices with Functional Transmembrane Proteins. *Langmuir* **2020**, *36*, 7325–7331. [CrossRef] [PubMed]
3. De Greef, T.F.A.; Meijer, E.W. Supramolecular Polymers. *Nature* **2008**, *453*, 171–173. [CrossRef] [PubMed]
4. Aida, T.; Meijer, E.W.; Stupp, S.I. Functional Supramolecular Polymers. *Science* **2012**, *335*, 813–817. [CrossRef]
5. Xia, D.; Wang, P.; Ji, X.; Khashab, N.M.; Sessler, J.L.; Huang, F. Functional Supramolecular Polymeric Networks: The Marriage of Covalent Polymers and Macrocycle-Based Host-Guest Interactions. *Chem. Rev.* **2020**, *120*, 6070–6123. [CrossRef]
6. Percec, V.; Dulcey, A.E.; Balagurusamy, V.S.K.; Miura, Y.; Smidrkal, J.; Peterca, M.; Hummelin, S.; Edlund, U.; Hudson, S.D.; Heiney, P.A.; et al. Self-Assembly of Amphiphilic Dendritic Dipeptides into Helical Pores. *Nature* **2004**, *430*, 764–768. [CrossRef]
7. Kostiainen, M.A.; Hiekkataipale, P.; Laiho, A.; Lemieux, V.; Seitsonen, J.; Ruokolainen, J.; Ceci, P. Electrostatic Assembly of Binary Nanoparticle Superlattices Using Protein Cages. *Nat. Nanotechnol.* **2013**, *8*, 52–56. [CrossRef]
8. Sartori, P.; Leibler, S. Lessons from Equilibrium Statistical Physics Regarding the Assembly of Protein Complexes. *Proc. Natl. Acad. Sci. USA* **2020**, *117*, 114–120. [CrossRef]
9. Lapenta, F.; Aupič, J.; Vezzoli, M.; Strmšek, Ž.; Da Vela, S.; Svergun, D.I.; Carazo, J.M.; Melero, R.; Jerala, R. Self-Assembly and Regulation of Protein Cages from Pre-Organised Coiled-Coil Modules. *Nat. Commun.* **2021**, *12*, 939. [CrossRef]
10. Qiu, X.; Chiechi, R.C. Printable Logic Circuits Comprising Self-Assembled Protein Complexes. *Nat. Commun.* **2022**, *13*, 2312. [CrossRef]
11. Krieger, A.; Zika, A.; Gröhn, F. Functional Nano-Objects by Electrostatic Self-Assembly: Structure, Switching, and Photocatalysis. *Front. Chem.* **2022**, *9*, 779360. [CrossRef] [PubMed]
12. Faul, C.F.J.; Antonietti, M. Ionic Self-Assembly: Facile Synthesis of Supramolecular Materials. *Adv. Mater.* **2003**, *15*, 673–683. [CrossRef]
13. Zika, A.; Agarwal, M.; Schweins, R.; Gröhn, F. Joining Two Switches in One Nano-object: Photoacidity and Photoisomerization in Electrostatic Self-assembly. *Chem. A Eur. J.* **2022**, *29*, e202203373. [CrossRef] [PubMed]
14. Willerich, I.; Gröhn, F. Photoswitchable Nanoassemblies by Electrostatic Self-Assembly. *Angew. Chem. Int. Ed.* **2010**, *49*, 8104–8108. [CrossRef] [PubMed]
15. Willerich, I.; Gröhn, F. Molecular Structure Encodes Nanoscale Assemblies: Understanding Driving Forces in Electrostatic Self-Assembly. *J. Am. Chem. Soc.* **2011**, *133*, 20341–20356. [CrossRef] [PubMed]
16. Mariani, G.; Moldenhauer, D.; Schweins, R.; Gröhn, F. Elucidating Electrostatic Self-Assembly: Molecular Parameters as Key to Thermodynamics and Nanoparticle Shape. *J. Am. Chem. Soc.* **2016**, *138*, 1280–1293. [CrossRef] [PubMed]
17. Wang, J.; Liu, K.; Xing, R.; Yan, X. Peptide Self-Assembly: Thermodynamics and Kinetics. *Chem. Soc. Rev.* **2016**, *45*, 5589–5604. [CrossRef] [PubMed]
18. Chau, R.; Doyle, B.; Datta, S.; Kavalieros, J.; Zhang, K. Integrated Nanoelectronics for the Future. *Nat. Mater.* **2007**, *6*, 810–812. [CrossRef]
19. Lu, W.; Lieber, C.M. Nanoelectronics from the Bottom Up. *J. Nanosci. Nanotechnol.* **2009**, *6*, 137–146. [CrossRef]
20. Cohen-Karni, T.; Langer, R.; Kohane, D.S. The Smartest Materials: The Future of Nanoelectronics in Medicine. *ACS Nano* **2012**, *6*, 6541–6545. [CrossRef]
21. Rosso, K.M.; Zarzycki, P. The Steady March toward Biomimetic Nanoelectronics. *ACS Nano* **2021**, *15*, 7844–7847. [CrossRef] [PubMed]
22. Criscione, J.M.; Le, B.L.; Stern, E.; Brennan, M.; Rahner, C.; Papademetris, X.; Fahmy, T.M. Self-Assembly of PH-Responsive Fluorinated Dendrimer-Based Particulates for Drug Delivery and Noninvasive Imaging. *Biomaterials* **2009**, *30*, 3946–3955. [CrossRef] [PubMed]
23. Bolu, B.S.; Sanyal, R.; Sanyal, A. Drug Delivery Systems from Self-Assembly of Dendron-Polymer Conjugates. *Molecules* **2018**, *23*, 1570. [CrossRef] [PubMed]
24. Webber, M.J.; Pashuck, E.T. (Macro)Molecular Self-Assembly for Hydrogel Drug Delivery. *Adv. Drug Deliv. Rev.* **2021**, *172*, 275–295. [CrossRef] [PubMed]
25. Willerich, I.; Gröhn, F. Thermodynamics of Photoresponsive Polyelectrolyte-Dye Assemblies with Irradiation Wavelength Triggered Particle Size. *Macromolecules* **2011**, *44*, 4452–4461. [CrossRef]
26. Mariani, G.; Krieger, A.; Moldenhauer, D.; Schweins, R.; Gröhn, F. Light-Responsive Shape: From Micrometer-Long Nanocylinders to Compact Particles in Electrostatic Self-Assembly. *Macromol. Rapid Commun.* **2018**, *39*, e1700860. [CrossRef] [PubMed]
27. Markiewicz, G.; Pakulski, D.; Galanti, A.; Patroniak, V.; Ciesielski, A.; Stefankiewicz, A.R.; Samorì, P. Photoisomerisation and Light-Induced Morphological Switching of a Polyoxometalate-Azobenzene Hybrid. *Chem. Commun.* **2017**, *53*, 7278–7281. [CrossRef] [PubMed]
28. Tian, J.; Cheng, N.; Liu, Q.; Xing, W.; Sun, X. Cobalt Phosphide Nanowires: Efficient Nanostructures for Fluorescence Sensing of Biomolecules and Photocatalytic Evolution of Dihydrogen from Water under Visible Light. *Angew. Chem. Int. Ed.* **2015**, *54*, 5493–5497. [CrossRef]

29. Wani, O.M.; Zeng, H.; Priimagi, A. A Light-Driven Artificial Flytrap. *Nat. Commun.* **2017**, *8*, 15546. [CrossRef]
30. Yan, P.; Jiang, D.; Tian, Y.; Xu, L.; Qian, J.; Li, H.; Xia, J.; Li, H. A Sensitive Signal-on Photoelectrochemical Sensor for Tetracycline Determination Using Visible-Light-Driven Flower-like CN/BiOBr Composites. *Biosens. Bioelectron.* **2018**, *111*, 74–81. [CrossRef]
31. Yin, F.; Yang, C.; Wang, Q.; Zeng, S.; Hu, R.; Lin, G.; Tian, J.; Hu, S.; Lan, R.F.; Yoon, H.S.; et al. A Light-Driven Therapy of Pancreatic Adenocarcinoma Using Gold Nanorods-Based Nanocarriers for Co-Delivery of Doxorubicin and SiRNA. *Theranostics* **2015**, *5*, 818–833. [CrossRef] [PubMed]
32. Liu, K.; Xing, R.; Zou, Q.; Ma, G.; Möhwald, H.; Yan, X. Simple Peptide-Tuned Self-Assembly of Photosensitizers towards Anticancer Photodynamic Therapy. *Angew. Chem. Int. Ed.* **2016**, *55*, 3036–3039. [CrossRef] [PubMed]
33. Cheng, X.; Sun, R.; Yin, L.; Chai, Z.; Shi, H.; Gao, M. Light-Triggered Assembly of Gold Nanoparticles for Photothermal Therapy and Photoacoustic Imaging of Tumors In Vivo. *Adv. Mater.* **2017**, *29*, 1–6. [CrossRef] [PubMed]
34. Kalsin, A.M.; Fialkowski, M.; Paszewski, M.; Smoukov, S.K.; Bishop, K.J.M.; Grzybowski, B.A. Electrostatic Self-Assembly of Binary Nanoparticle Crystals with a Diamond-like Lattice. *Science* **2006**, *312*, 420–424. [CrossRef] [PubMed]
35. Srebnik, S.; Douglas, J.F. Self-Assembly of Charged Particles on Nanotubes and the Emergence of Particle Rings, Chains, Ribbons and Chiral Sheets. *Soft Matter* **2011**, *7*, 6897–6905. [CrossRef]
36. Li, L.; Wu, R.; Guang, S.; Su, X.; Xu, H. The Investigation of the Hydrogen Bond Saturation Effect during the Dipole-Dipole Induced Azobenzene Supramolecular Self-Assembly. *Phys. Chem. Chem. Phys.* **2013**, *15*, 20753–20763. [CrossRef] [PubMed]
37. Bishop, K.J.M.; Wilmer, C.E.; Soh, S.; Grzybowski, B.A. Nanoscale Forces and Their Uses in Self-Assembly. *Small* **2009**, *5*, 1600–1630. [CrossRef] [PubMed]
38. Li, F.; Liu, D.; Wang, T.; Hu, J.; Meng, F.; Sun, H.; Shang, Z.; Li, P.; Feng, W.; Li, W.; et al. J-Aggregation in Porphyrin Nanoparticles Induced by Diphenylalanine. *J. Solid State Chem.* **2017**, *252*, 86–92. [CrossRef]
39. Willerich, I.; Li, Y.; Gröhn, F. Influencing Particle Size and Stability of Ionic Dendrimer-Dye Assemblies. *J. Phys. Chem. B* **2010**, *114*, 15466–15476. [CrossRef]
40. Negishi, N.; Ishihara, K.; Shinohara, I. Adsorption of Photochromic Azo Dye onto Styrene-Divinylbenzene Copolymer. *J. Polym. Sci. Polym. Lett. Ed.* **1981**, *19*, 593–597. [CrossRef]
41. Petrak, K.; Douglas, P.; Leyshon, L.L. Photoregulated Sorption of Dyes to Polymers I. The Effect of Polymers on Some Photochemical Properties of Acid Yellow 38. *J. Appl. Polym. Sci.* **1986**, *31*, 553–565. [CrossRef]
42. Moldenhauer, D.; Gröhn, F. Nanoassemblies with Light-Responsive Size and Density from Linear Flexible Polyelectrolytes. *J. Polym. Sci. Part B Polym. Phys.* **2013**, *51*, 802–816. [CrossRef]
43. Müller, R.; Laschober, C.; Szymanski, W.W.; Allmaier, G. Determination of Molecular Weight, Particle Size, and Density of High Number Generation PAMAM Dendrimers Using MALDI-TOF-MS and NES-GEMMA. *Macromolecules* **2007**, *40*, 5599–5605. [CrossRef]
44. Robinson, C.; Mills, H.A.T. The Colloid Chemistry of Dyes: The Aqueous Solutions of Benzopurpurine 4B and Its Isomer Prepared from m-Tolidine—Part I. *Proc. R. Soc. Lond. Ser. A* **1931**, *131*, 576–595.
45. Glasoe, P.K.; Long, F.A. Use of Glass Electrodes to Measure Acidities in Deuterium Oxide. *J. Phys. Chem.* **1960**, *64*, 188–190. [CrossRef]
46. Covington, A.K.; Paabo, M.; Robinson, R.A.; Bates, R.G. Use of the Glass Electrode in Deuterium Oxide and the Relation between the Standardized pD (pa_D) Scale and the Operational pH in Heavy Water. *Anal. Chem.* **1968**, *40*, 700–706. [CrossRef]
47. Krężel, A.; Bal, W. A Formula for Correlating pK_a Values Determined in D_2O and H_2O. *J. Inorg. Biochem.* **2004**, *98*, 161–166. [CrossRef] [PubMed]
48. Provencher, S.W. A Constrained Regularization Method for Inverting Data Represented by Linear Algebraic or Integral Equations. *Comput. Phys. Commun.* **1982**, *27*, 213–227. [CrossRef]
49. Provencher, S.W. Contin: A General Purpose Constrained Regularization Program for Inverting Noisy Linear Algebraic and Integral Equations. *Comput. Phys. Commun.* **1982**, *27*, 229–242. [CrossRef]
50. Schärtl, W. Fundamental Concepts. In *Light Scattering from Polymer Solutions and Nanoparticle Dispersions*; Springer: Berlin/Heidelberg, Germany, 2007; pp. 1–24. [CrossRef]
51. Smoluchowski, M.V. Molekular-kinetische Theorie der Opaleszenz von Gasen im kritischen Zustande, sowie einiger verwandter Erscheinungen. *Ann. Phys.* **1908**, *330*, 205–226. [CrossRef]
52. Polaczyk, A.L.; Amburgey, J.E.; Alansari, A.; Poler, J.C.; Propato, M.; Hill, V.R. Calculation and Uncertainty of Zeta Potentials of Microorganisms in a 1:1 Electrolyte with a Conductivity Similar to Surface Water. *Colloids Surfaces A Physicochem. Eng. Asp.* **2020**, *586*, 124097. [CrossRef]
53. Arnold, O.; Bilheux, J.C.; Borreguero, J.M.; Buts, A.; Campbell, S.I.; Chapon, L.; Doucet, M.; Draper, N.; Ferraz Leal, R.; Gigg, M.A.; et al. Mantid—Data Analysis and Visualization Package for Neutron Scattering and μ SR Experiments. *Nucl. Instrum. Methods Phys. Res. Sect. A Accel. Spectrometers Detect. Assoc. Equip.* **2014**, *764*, 156–166. [CrossRef]
54. Guinier, A.; Fouret, G. General Theory. In *Small-Angle Scattering of X-rays*; John Wiley and Sons, Inc.: New York, NY, USA, 1955; Volume 18, pp. 5–78. [CrossRef]
55. Pedersen, J.S. Analysis of Small-Angle Scattering Data from Colloids and Polymer Solutions: Modeling and Least-Squares Fitting. *Adv. Colloid Interface Sci.* **1997**, *70*, 171–210. [CrossRef]
56. Onsager, L. The Effects of Shape on the Interaction of Colloidal Particles. *Ann. N. Y. Acad. Sci.* **1949**, *51*, 627–659. [CrossRef]

57. Ainalem, M.L.; Carnerup, A.M.; Janiak, J.; Alfredsson, V.; Nylander, T.; Schillén, K. Condensing DNA with Poly(Amido Amine) Dendrimers of Different Generations: Means of Controlling Aggregate Morphology. *Soft Matter* **2009**, *5*, 2310–2320. [CrossRef]
58. Bian, T.; Gardin, A.; Gemen, J.; Houben, L.; Perego, C.; Lee, B.; Elad, N.; Chu, Z.; Pavan, G.M.; Klajn, R. Electrostatic Co-Assembly of Nanoparticles with Oppositely Charged Small Molecules into Static and Dynamic Superstructures. *Nat. Chem.* **2021**, *13*, 940–949. [CrossRef] [PubMed]
59. Li, Y.; Liu, J.; Wang, Y.; Wang, Z.L. Preparation of Monodispersed Fe-Mo Nanoparticles as the Catalyst for CVD Synthesis of Carbon Nanotubes. *Chem. Mater.* **2001**, *13*, 1008–1014. [CrossRef]
60. Hufschmid, R.; Arami, H.; Ferguson, R.M.; Gonzales, M.; Teeman, E.; Brush, L.N.; Browning, N.D.; Krishnan, K.M. Synthesis of Phase-Pure and Monodisperse Iron Oxide Nanoparticles by Thermal Decomposition. *Nanoscale* **2015**, *7*, 11142–11154. [CrossRef]
61. Sharifi Dehsari, H.; Halda Ribeiro, A.; Ersöz, B.; Tremel, W.; Jakob, G.; Asadi, K. Effect of Precursor Concentration on Size Evolution of Iron Oxide Nanoparticles. *CrystEngComm* **2017**, *19*, 6694–6702. [CrossRef]
62. Zangoli, M.; Gazzano, M.; Monti, F.; Maini, L.; Gentili, D.; Liscio, A.; Zanelli, A.; Salatelli, E.; Gigli, G.; Baroncini, M.; et al. Thermodynamically versus Kinetically Controlled Self-Assembly of a Naphthalenediimide-Thiophene Derivative: From Crystalline, Fluorescent, n-Type Semiconducting 1D Needles to Nanofibers. *ACS Appl. Mater. Interfaces* **2019**, *11*, 16864–16871. [CrossRef]
63. Huang, Z.; Jiang, T.; Wang, J.; Ma, X.; Tian, H. Real-Time Visual Monitoring of Kinetically Controlled Self-Assembly. *Angew. Chem.* **2021**, *133*, 2891–2896. [CrossRef]
64. Derman, S.; Akdeste, Z.M. Particle Size and Zeta Potential Investigation of Synthetic Peptide-Protein Conjugates. *Turk. J. Biochem.* **2015**, *40*, 282–289. [CrossRef]
65. Sinn, C.G.; Dimova, R.; Antonietti, M. Isothermal Titration Calorimetry of the Polyelectrolyte/Water Interaction and Binding of Ca^{2+}: Effects Determining the Quality of Polymeric Scale Inhibitors. *Macromolecules* **2004**, *37*, 3444–3450. [CrossRef]
66. Garidel, P.; Blume, A. Interaction of Alkaline Earth Cations with the Negatively Charged Phospholipid 1,2-Dimyristoyl-Sn-Glycero-3-Phosphoglycerol: A Differential Scanning and Isothermal Titration Calorimetric Study. *Langmuir* **1999**, *15*, 5526–5534. [CrossRef]
67. Lehrmann, R.; Seelig, J. Adsorption of Ca^{2+} and La^{3+} to Bilayer Membranes: Measurement of the Adsorption Enthalpy and Binding Constant with Titration Calorimetry. *Biochim. Biophys. Acta—Biomembr.* **1994**, *1189*, 89–95. [CrossRef]
68. Willerich, I.; Schindler, T.; Gröhn, F. Effect of Polyelectrolyte Architecture and Size on Macroion-Dye Assemblies. *J. Phys. Chem. B* **2011**, *115*, 9710–9719. [CrossRef]

Disclaimer/Publisher's Note: The statements, opinions and data contained in all publications are solely those of the individual author(s) and contributor(s) and not of MDPI and/or the editor(s). MDPI and/or the editor(s) disclaim responsibility for any injury to people or property resulting from any ideas, methods, instructions or products referred to in the content.

Supporting Information

Results:

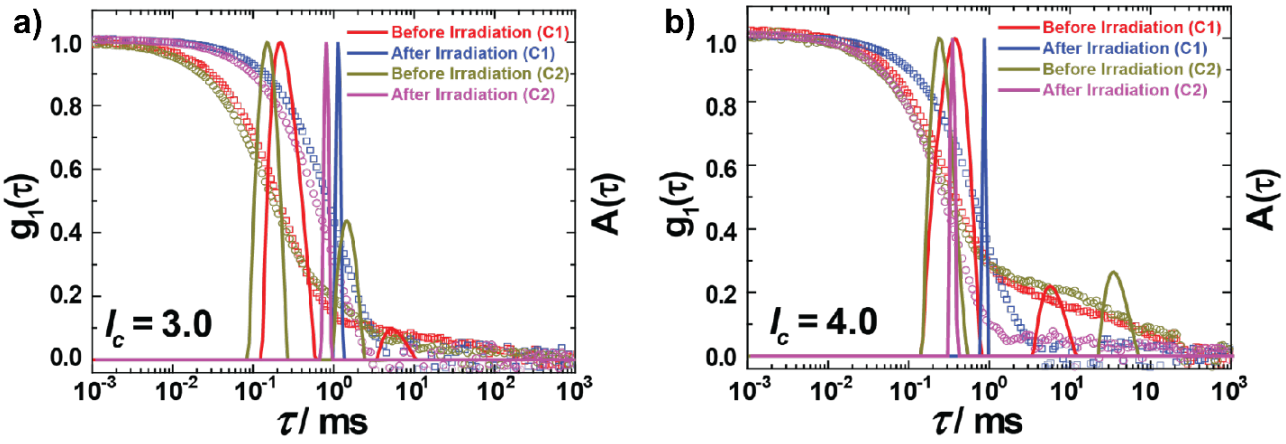


Figure S1 Dynamic light scattering of AY38/G5 assemblies at charge ratio l_c =3.0 **(a)** and 4.0 **(b)** before and after UV irradiation for concentration C1 = 0.5 × 10^{-4} mol L^{-1} AY38 and C2 = 1.0 × 10^{-4} mol L^{-1} AY38: Electric field autocorrelation function $g_1(\tau)$ and distribution of relaxation times A(τ) at a scattering angle of θ = 90 show the increase in assembly size. R_H = hydrodynamic radius; σ = standard deviation of the distribution.

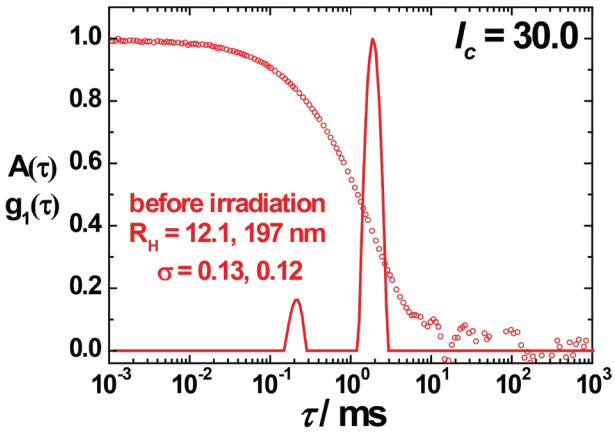


Figure S2 Dynamic light scattering of AY38/G5 assemblies at charge ratio l_c = 30.0 before irradiation at C_{AY38} = 1.0 × 10^{-4} mol L^{-1}.T

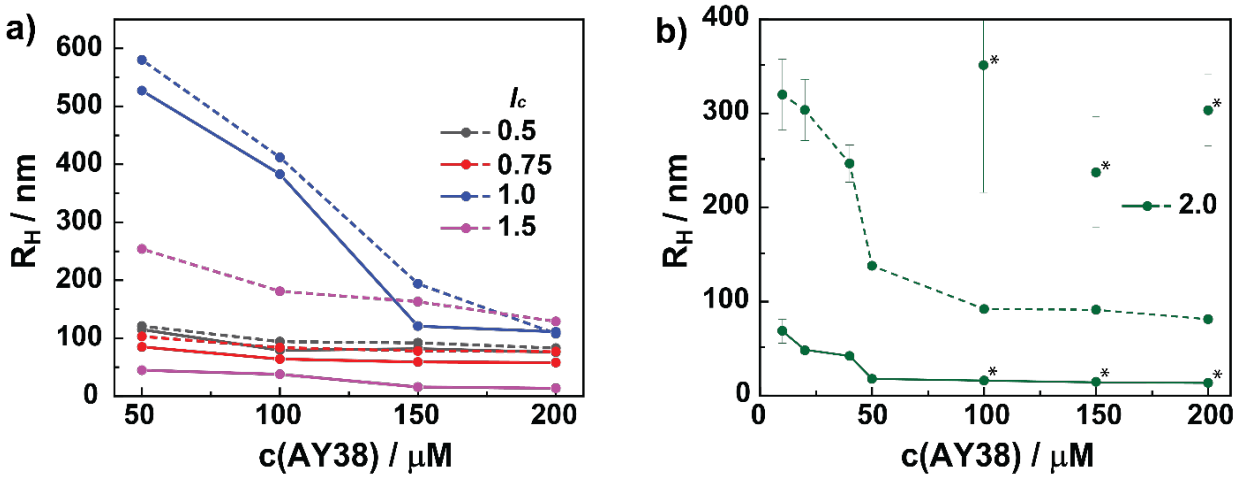


Figure S3 Various samples are divided into **(a)** Thermodynamically controlled and **(b)** Kinetically controlled assemblies based on their charge ratios, concentration, and the effect of irradiation. The straight line represents samples prior to irradiation, and the dashed lines after irradiation. Stars in **(b)** are used for samples with a bimodal distribution **1** Radius of gyration for multiple charge ratios at different concentrations using SANS models and the Guinier approximation. The error is < 10% in all the cases (Concentration is given in terms of AY38).

Table S1 Radius of gyration for multiple charge ratios at different concentrations using SANS structural models and the Guinier approximation to check the correctness of the fitted model. The error is < 10% in all the cases (Concentration is given in terms of AY38).

Charge Ratio	**1.5**	**2.0**	**2.0**	**3.0**	**3.0**	**4.0**	**4.0**
AY38 Concentration / μM	**100**	**50**	**100**	**50**	**100**	**50**	**100**
	R_G / nm						
Before irradiation(exp)	35.9		7.6				
Before Irradiation(Calc)	21.6		7.9				
After Irradiation(exp)	107.8	81.2	54.1	61	32.4	77	36.5
After Irradiation(Calc)	99.3	77	56.7	62.3	32.6	76	33.9

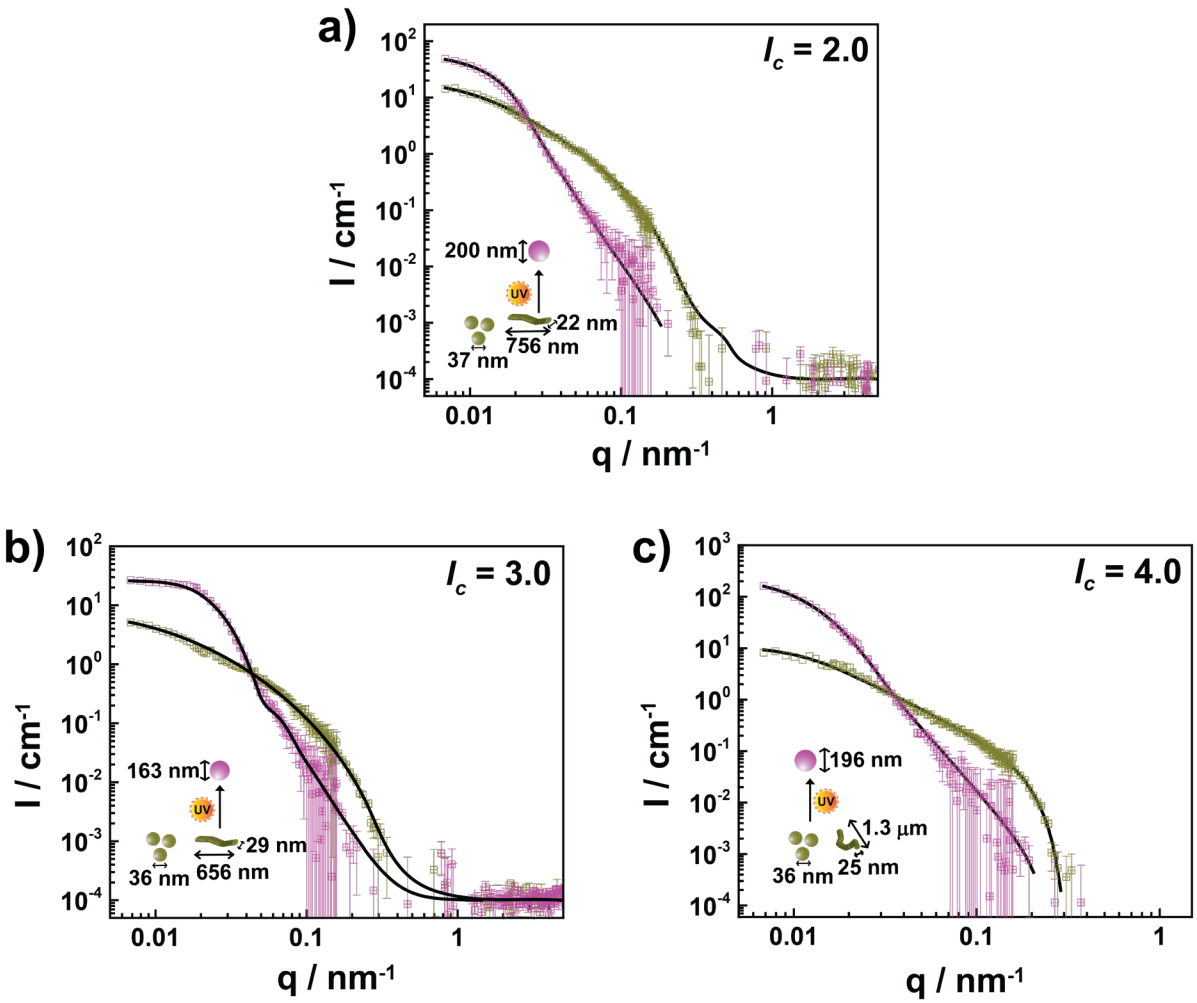


Figure S4 SLS-SANS of AY38/G5 assemblies at charge ratios I_c: **(a)** 2.0; **(b)** 3.0; and **(c)** 4.0. Dark yellow and magenta color represent the nanoparticles before and after irradiation, black straight lines represent the best fit. (C_{AY38} = 0.5 × 10^{-4} mol L^{-1}). The shapes shown in the figures are obtained by fitting the SLS-SANS data using SasView 4.2.2 software. The sizes of the figures are not up to the scale.

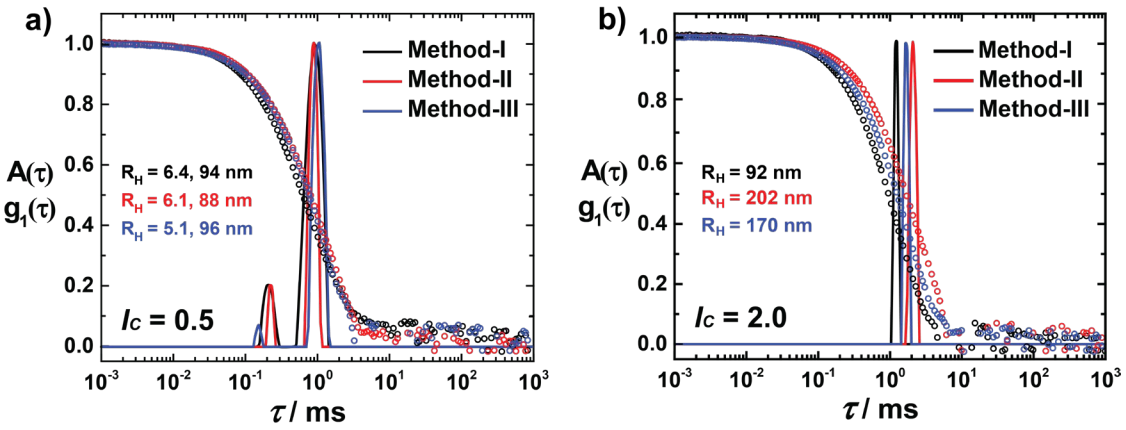


Figure S5 Electric-field autocorrelation function $g_1(\tau)$ and distribution of relaxation times $A(\tau)$ (scattering angle θ = 90°) of AY38/G5 assemblies after irradiation at I_c = **(a)** 0.5 (Thermodynamically controlled), and **(b)** 2.0 (Kinetically controlled), where, method-I is the preparation way used throughout this study. In method-II and III, stock solutions were prepared and mixed in acidic medium (pD = 3.5). In method II, dendrimer solution was added to the dye solution, while in method III, it was the other way around.

Different preparation routes distinguish the thermodynamic and kinetic controlled samples based on their charge ratios [1]. In method-I, the stock solutions of AY38 and G5 PAMAM dendrimer were mixed in basic (pD = 10.5) deuterated solution while continuously stirring, and 2-3 μL of 1 M DCl was added into it to change the pD to 3.5 where electrostatic assemblies started forming. Whereas, in the case of method-II and III, both the stock solutions were mixed in an acidic solution while stirring, in which AY38 dye was added first in method II and G5 was added first in method III. The dynamic light scattering results of I_c = 0.5 and 2.0 are given below, with the R_H values prepared by all three methods mentioned above in Figure S5.

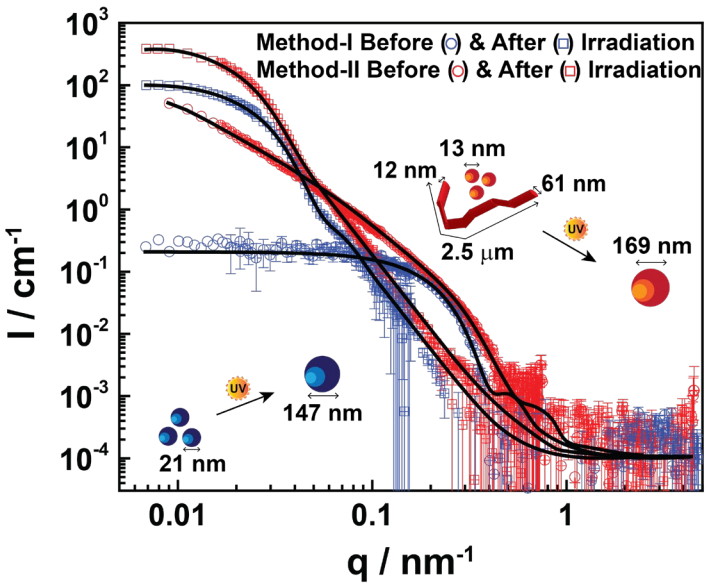


Figure S6 SLS-SANS of AY38/G5 assemblies at I_c = 2.0 using two preparation routes and the effect of irradiation on assemblies. Blue and red color represents method I and II, where open circles show the samples before irradiation and open squares after irradiation. The black line shows the best fit for the data displayed.

Figure S6 shows the SLS-SANS result of AY38/G5 at I_c = 2.0, where two preparation routes are used to formulate the assemblies. Both methods result in different structures before irradiation. Using method-I, we obtain monomodal particles with spherical form factor whereas, in method-II, similar small spheres form along with elongated flexible cylindrical structures up to 2.5 μm in size, which, upon irradiation, converts into large and highly monodisperse spherical particles in both cases.

Table S2 DLS for AY38/G5 system using different methods of preparation. In method-I, all the building blocks were prepared and mixed in acidic medium. In method II, the stock solutions were prepared at *pD* = 10.5, and later, DCl was added to initiate the assemblies. R_{H1} and R_{H2} represent the bimodality.

AY38/G5	Before Irradiation				After Irradiation	
I_c	Method-I		Method-II		Method-I	Method-II
	R_{H1} / nm	R_{H2} / nm	R_{H1} / nm	R_{H2} / nm	R_H / nm	R_H / nm
0.5	89 ± 8		86 ± 11		94 ± 5	93 ± 6
0.75	64 ± 4		60 ± 9		84 ± 14	86 ± 9
1	383 ± 38		366 ± 43		412 ± 34	440 ± 29
1.5	38 ± 3		19 ± 5	147 ± 23	181 ± 12	205 ± 16
2	18 ± 2	350 ± 140	29 ± 3	914 ± 324	92 ± 3	224 ± 11
3	13 ± 1	362 ± 181	10 ± 1	242 ± 103	54 ± 1	280 ± 15
4	12 ± 1	1550 ± 1100	12 ± 1	552 ± 215	47 ± 1	145 ± 7

Table S3 shows the percentage of isomerization upon irradiation at different charge ratios and concentrations. The dye concentration does not seem to affect the *cis* % in low to moderate I_c (≤ 1.5), but it starts to decrease by increasing the concentration in case of dye excess.

AY38/μM	0.5	0.75	1.0	1.5	2.0	3.0	4.0
	Cis%	Cis%	Cis%	Cis%	Cis%	Cis%	Cis%
20					65		
40					60		
50	22	22	27	77	58	56	46
100	25	24	27	75	58	46	44
150	24	22	27	74	57	35	32
200	25	24	25	74	50	26	27

In Figure S7, the amount of dye isomers was calculated before and after centrifugation at I_c = 1.5 in AY38/G5 assemblies. Prior to irradiation, the more stable *trans* molecules were

present in the majority (> 90%), leaving < 10% of cis dye molecules. The data shown in Figure S7 is fitted by multiple peak fit using the Gaussian model in Origin software. The change of isomers amount can be noticed in Figure 5(d-e), where, after irradiation, the *cis* molecules are in the majority.

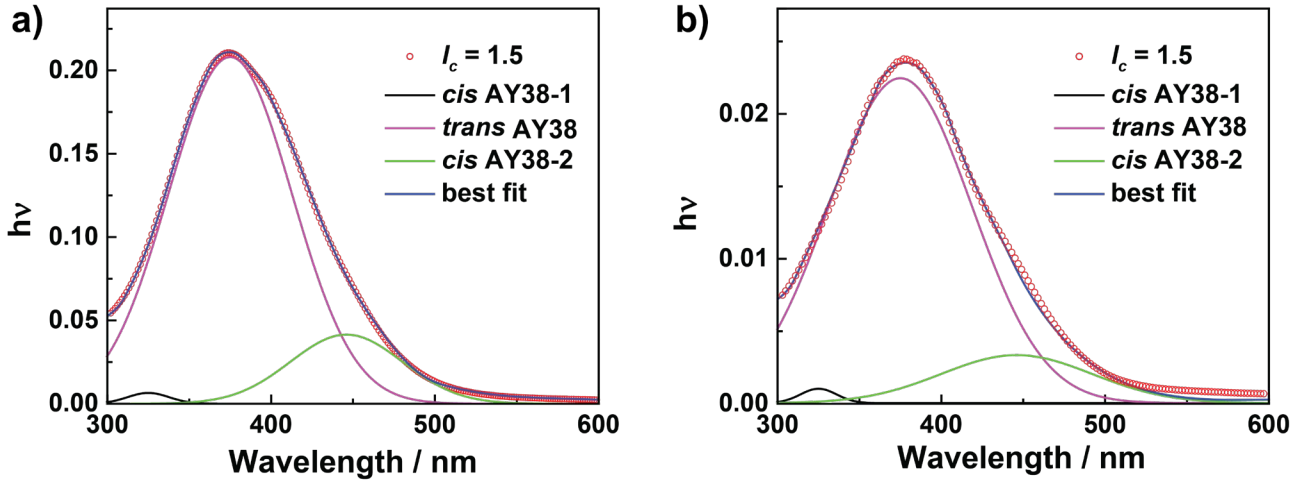


Figure S7 Analysis of UV-Vis spectra before irradiation for AY38/G5 at I_c = 1.5 for (d) before centrifugation and (e) supernatant after centrifugation. (Data is fitted using the Gauss model for multiple peaks from cis and trans-AY38. The centrifuge tube represents the irradiated sample after centrifugation.)

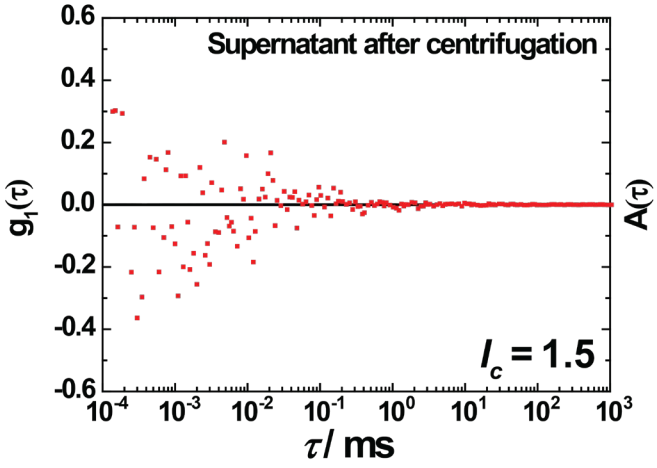


Figure S8 Electric field autocorrelation function $g_1(\tau)$ at a scattering angle of $\tau = 90°$ for the supernatant received after centrifugation of I_c = 1.5 prior to irradiation.

No particles were observed from the supernatant, as can be seen from the DLS result of AY38/G5 assemblies at I_c = 1.5 in Figure S8 after centrifuging the assemblies using the ultracentrifuge for 15 min at the speed of 10000 rpm.

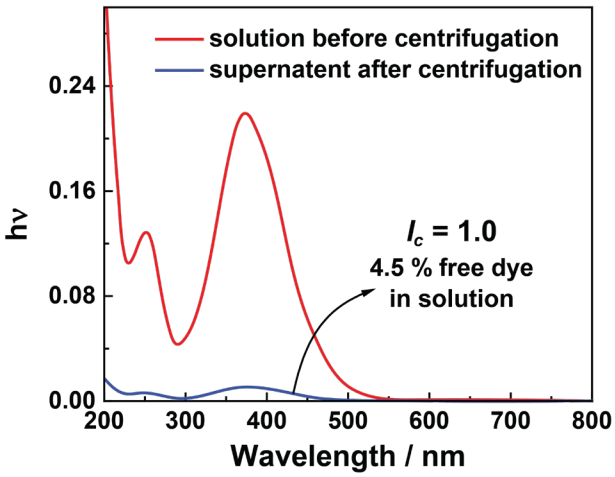


Figure S9 The effect of centrifugation on the absorbance of AY38/G5 at I_c = 1.0 is recorded by UV-Vis studies.

In the case of I_c = 1.0, approximately 4.5% of the free dye is available in the solution, which ultimately decreases the value of the original I_c from 1.0 to 0.95. Due to this, the assemblies are not entirely neutral at the balanced charge ratio and show positive charges in ζ-potential studies.

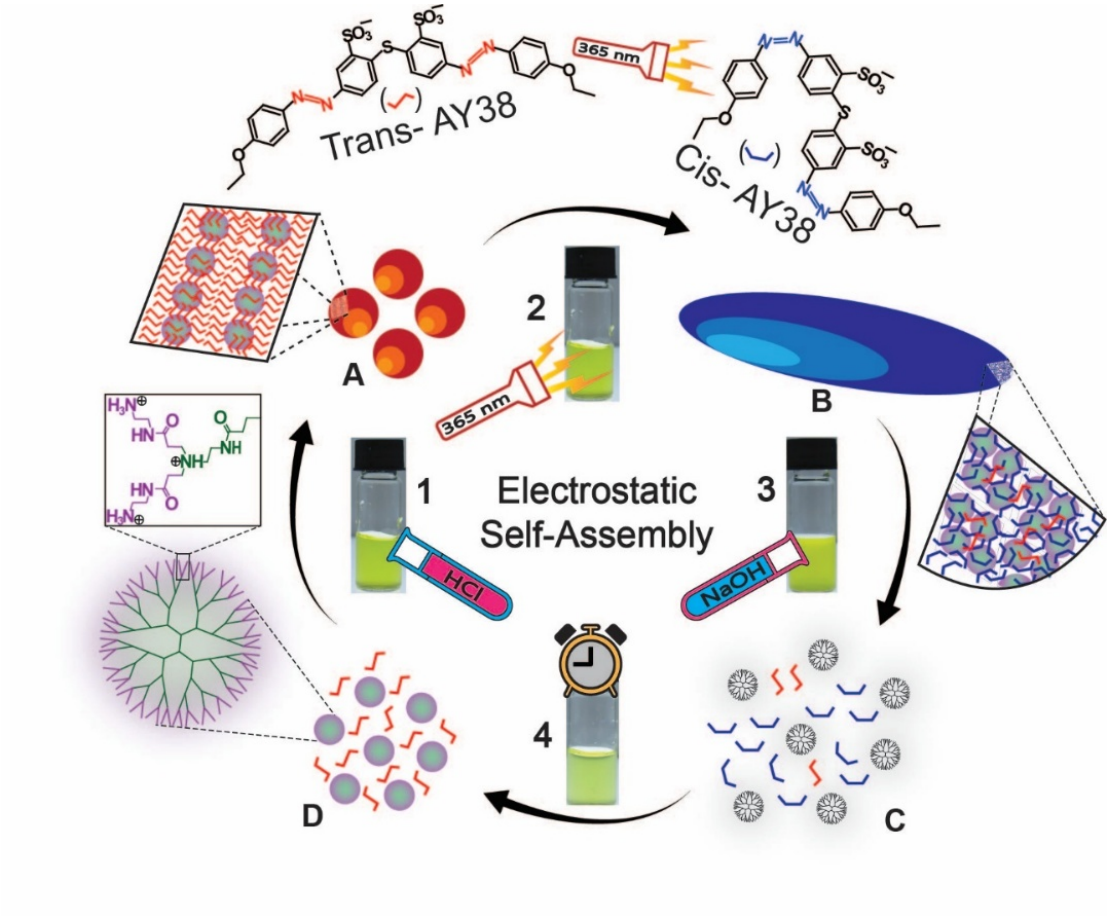
References:

1. Willerich, I.; Li, Y.; Gröhn, F. Influencing Particle Size and Stability of Ionic Dendrimer-Dye Assemblies. *J. Phys. Chem. B* **2010**, *114*, 15466–15476, doi:10.1021/jp107358q.

2. Willerich, I.; Gröhn, F. Thermodynamics of Photoresponsive Polyelectrolyte-Dye Assemblies with Irradiation Wavelength Triggered Particle Size. *Macromolecules* **2011**, *44*, 4452–4461, doi:10.1021/ma200538e.

7.2.2. The Role of Light Irradiation and Dendrimer Generation in Directing Electrostatic Self-Assembly

Mohit Agarwal, Alexander Zika, Müge Yücel, Joachim Kohlbrecher, Ralf Schweins, Franziska Gröhn; *Polymers, **2025**, 17(2), 170*



polymers

MDPI

Article

The Role of Light Irradiation and Dendrimer Generation in Directing Electrostatic Self-Assembly

Mohit Agarwal [1,2], Alexander Zika [1], Müge Yücel [1], Ralf Schweins [2], Joachim Kohlbrecher [3] and Franziska Gröhn [1,*]

[1] Department of Chemistry and Pharmacy, Interdisciplinary Center for Molecular Materials, Friedrich-Alexander Universität Erlangen-Nürnberg, Egerlandstr. 3, 91058 Erlangen, Germany
[2] Institut Laue-Langevin, Large Scale Structures Group, 71 Avenue des Martyrs, F-38000 Grenoble, France
[3] Paul Scherrer Institut PSI, Forschungsstrasse 111, 5232 Villigen, Switzerland
* Correspondence: franziska.groehn@fau.de; Tel.: +49-913-185-20731

Abstract: pH-responsive polyamidoamine (PAMAM) dendrimers are used as well-defined building blocks to design light-switchable nano-assemblies in solution. The complex interplay between the photoresponsive di-anionic azo dye Acid Yellow 38 (AY38) and the cationic PAMAM dendrimers of different generations is presented in this study. Electrostatic self-assembly involving secondary dipole–dipole interactions provides well-defined assemblies within a broad size range (10 nm–1 µm) with various shapes. The size and shape of these assemblies were determined using dynamic and static light scattering (DLS/SLS) and small-angle neutron scattering (SANS); ζ-potential measurements were performed to elucidate the charge characteristics, revealing the effective surface charge density of the nano-objects as an important parameter in the size and shape control. UV–vis spectroscopy and isothermal titration calorimetry (ITC) were employed to investigate the interaction on a molecular level and from a thermodynamic point of view. The results show that the amount of isomerized *cis* dye depends on the dendrimer generation because of a photoprotective effect through electrostatics for lower generations and through dipole–dipole interactions for higher generations; as the *cis* dye and *trans* dye bind with different strength, the amount of *cis* dye then again encodes the charge density and thereby the particle size and shape.

Keywords: azo dye; dendrimer; electrostatic self-assembly; light irradiation; photoresponsive; switchability

check for updates

Academic Editor: Felix H. Schacher

Received: 1 December 2024
Revised: 4 January 2025
Accepted: 7 January 2025
Published: 11 January 2025

Citation: Agarwal, M.; Zika, A.; Yücel, M.; Schweins, R.; Kohlbrecher, J.; Gröhn, F. The Role of Light Irradiation and Dendrimer Generation in Directing Electrostatic Self-Assembly. *Polymers* **2025**, *17*, 170. https://doi.org/10.3390/polym17020170

Copyright: © 2025 by the authors. Licensee MDPI, Basel, Switzerland. This article is an open access article distributed under the terms and conditions of the Creative Commons Attribution (CC BY) license (https://creativecommons.org/licenses/by/4.0/).

1. Introduction

Self-assembly, a feasible and effective process, offers a powerful tool to construct defined nanoparticles via various noncovalent interactions such as π-π stacking [1,2], amphiphilicity [3–5], H-bonding [6], and ionic interactions [7–10]. Electrostatic self-assembly refers to the self-assembly process driven by ionic interactions between components [11–16]. These interactions include Coulombic attraction (or repulsion) between charged species, often in conjunction with other non-covalent interactions such as π-π interactions, hydrogen bonding, or dipole–dipole interactions [17–19], referred to as secondary interactions as they only come into play when the building blocks approach each other due to their opposite charge. Electrostatic interactions are non-directional; therefore, secondary interactions often play a crucial role in producing desired structures [16]. This approach can be used to produce nano-objects of various shapes, such as spheres, cylinders, disks, and ellipsoids [16]. In particular, electrostatic self-assembly is a powerful technique that is capable of creating

nanostructures in aqueous solution that respond to various stimuli, e.g., changes in temperature, pH, concentration, light irradiation, or the presence of certain chemicals [12,19–22]. This responsiveness can be built into nano-assemblies by using components that respond to the desired stimuli [23–25]. Our group demonstrated the electrostatic self-assembly of macroions and stiff multivalent counterions, e.g., dendrimer-dye nano-objects in solution, showcasing how charge interactions govern size and shape [21,26,27].

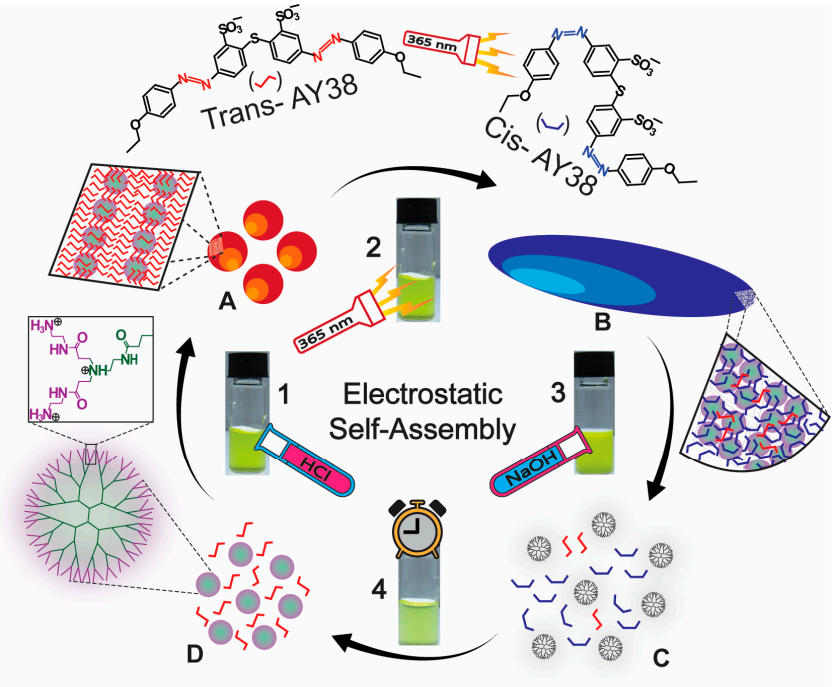
Photo-driven systems are especially very interesting for altering the nanostructure in aqueous solution [16,28,29]. Classical surfactants capable of UV-induced isomerization or dimerization can form light-responsive micelles [30]. Higashi et al. reported the first light-responsive electrostatically self-assembled nanostructures in 2007, where an anionic azobenzene derivative and a cationic β-sheet peptide formed nanofibers [31]. Upon UV irradiation, azobenzene isomerized to its *cis* state, causing the nanofibers to dissolve, while reassembly occurred in the *trans* state. In 2009, Ghoreishi et al. investigated the interactions between anionic azo dye and the cationic surfactant tetradecyltrimethylammonium bromide (TTAB) [32]. Despite advancements in light-triggered assembly and disassembly, controlling the nano-object size through photo-irradiation in solution had remained challenging, and this was first demonstrated by our group in 2010 using an aqueous system of azo-switchable anionic dyes combined with a cationic dendrimer macroion [12]. Up to then, *trans-cis* isomerization had led to triggerable oligomers or gel formation, but switching the particle size had not been achieved with any association interaction type [33,34]. Later, in 2016, Guo et al. fabricated supramolecular structures responsive to UV light, pH changes, and metal ions, highlighting the combination of azobenzene surfactants and Eu-POMs [35].

The first light-switchable particle shape change of an electrostatically self-assembled nano-object was described by us in 2018, where assemblies of a linear polyelectrolyte and an isomerizable azo dye changed from long fibers to more globular structures upon irradiation [22]. Furthermore, Xie et al. explored light-induced isomerization using azobenzene-functionalized peptides [36], demonstrating how light manipulation can dynamically alter supramolecular architectures by exploiting non-equilibrium conditions. More recently, Fathalla et al. used ionic self-assembly to develop pH-responsive porphyrin-silica nanoparticles [37]. The particles released encapsulated drugs in response to pH changes, leveraging the disruption of ionic interactions at acidic pH to achieve controlled release [15,38,39]. These systems underline the key role of macroions' behavior in stimuli-responsive materials. Electrostatic self-assembly provides a foundation for the structuring of nanomaterials, where stimuli like light and pH offer tunable mechanisms for dynamic responses. However, structure-directing principles, for the first time, were investigated in our recent study in this journal (based on the dependence on the loading ratio) [19] and in this manuscript (influence of the dendrimer generation).

The properties of such photoresponsive electrostatic self-assembly systems can be controlled by changing the intermolecular interactions between building blocks, leading to structural changes in the material. Willerich et al. previously developed a method where we were able to achieve photoswitchable assemblies with nearly monodisperse nanoparticles using an excess of azo dyes, in which the surplus dye molecules bound by secondary interactions electrostatically stabilized these assemblies through the excess of opposite charges [12]. Later, in a study by Mariani et al., we observed the effects of dendrimer generation on electrostatic assemblies with various (non-switchable) multivalent anionic dye molecules as connecting counterions, finding an increase in shape anisotropy when the dendrimer generations increased in the presence of excess dendrimer [21]. Yet, still missing so far is a study targeting the gain in the fundamental understanding of directing photoswitchable electrostatic self-assembly into nano-objects of various shapes and sizes.

The present study aims to gain further insight into structure-directing effects and photoresponsiveness by creating and investigating photoswitchable electrostatically self-assembled nano-objects in terms of their dependence on the dendrimer generation. As a model system, a divalent azo dye (AY38, Acid Yellow 38) and cationic polyamidoamine (PAMAM) dendrimers of generation 2 to 8 were employed as the building blocks. The photo-isomerization ability of AY38 and the pH responsiveness of the dendrimers make them suitable candidates for tuning the size and shape of the self-assembled particles by light irradiation and the degree of protonation. In an acidic medium (pH = 3.5), the PAMAM dendrimer contains a maximum number of cationic charges (e.g., 126 charges for the generation 4 dendrimer), where both sets of amino groups (primary end groups and tertiary branching groups) are charged ($–NH_3^+$, $–NR_2H^+$). Here, PAMAM dendrimers are of particular value as model polyelectrolytes, not only because they represent very-well-defined structures but also especially because of their structure change with the generation: early generations of dendrimers exhibit open, star-like morphologies with accessible surface functionalities, while later generations transition into more compact, spherical shapes—still highly swollen with water but with a higher density of organic material inside an overall spherical dendrimer molecule [40–43]. As the generation increases, the internal part of the dendrimer becomes more "filled", and the surface functionality becomes increasingly dense, with increased internal crowding and decreased flexibility as well as branching effects constraining diffusion rates or the growth of nanoparticles within the dendrimer [44–46]. Various special generation-dependent properties result from this [43]. Overall, with increasing the dendrimer generation, a transition from a typical low-molecular-mass molecule to a typical branched polymer "particle", or polyelectrolyte in this case, occurs. The AY38 azo dye molecule contains two anionic sulfonate groups ($–SO_3^-$). To build self-assembled nano-structures, the positive amino groups on the dendrimers at pH = 3.5 electrostatically interact with the AY38 dyes, which again are readily isomerized from the *trans* state into the *cis* state by illumination with λ = 365 nm. The half-life ($t_{1/2}$) of the *cis* state is about 12 h, which is a reasonable timespan to analyze the structural changes due to isomerization. Through the combination of light and pH sensitivity, the electrostatically self-assembled system can undergo recurring assembly (Scheme 1).

Due to the increasing number of branching units and terminal functional groups, higher-generation dendrimers offer more potential binding sites for dye molecules, which could lead to larger nanoparticles in solution. However, the dendrimers become more densely packed with branches, increasing the steric hindrance, making the dendrimer molecules less flexible with increasing the generation. Possibly, this steric hindrance may limit the accessibility of the dye to the internal amino groups, resulting in a lower loading capacity of the dye. In addition, a higher "stiffness" may improve the overall definition and stability of the self-assembled nanoparticles by reducing structural deformations. Lower-generation dendrimers tend to be more flexible and adopt a more extended conformation with a high degree of internal freedom. G0 PAMAM dendrimers, for example, represent "small molecules" and do not form stable assemblies [47]. In contrast, higher-generation dendrimers are less flexible and more constrained, resulting in a stiffer and more compact conformation. Thus, overall, a complex scenario results, guided by several interplaying effects that are yet to be understood.



Scheme 1. Simplified sketch of the recurring assembly formation at the nanoscale. The molecular structures of the dendrimers and AY38 are shown. A–D represent different nanoassembly structures. Red objects represent simplified *trans* dye molecules, and blue objects indicate *cis* dye molecules. The glass vials carry the same sample solution at different steps of the cycle. A UV lamp with a 365 nm wavelength is used in the experiment.

2. Materials and Methods

2.1. Chemicals

Polyamidoamine dendrimers with tertiary amino group branches and primary amino groups as surface end groups of generations 2, 3, 4, 5, 6, 7, and 8 were purchased from Aldrich (Darmstadt, Germany). DLS confirmed the radius and size distribution given by the manufacturer Dendritech (Midland, MI, USA), as shown in Figure S1 [48]. Acid Yellow 38 (AY38; >40% purity) was purchased from Merck (Darmstadt, Germany) and purified to >98% by multiple recrystallizations from water and ethanol [49]. D_2O, NaOD, and DCl were purchased from Merck, Darmstadt, Germany, and NaOD and DCl were used to adjust the pD of the solution.

2.2. Sample Preparation

AY38 and PAMAM dendrimer stock solutions were prepared using D_2O solvent at pD = 10.5 (pD = pH + 0.4) [50]. Both stock solutions were mixed at room temperature while stirring. An apposite amount of DCl was then added to the solution to reach a pH/pD of 3.5 to induce self-assembly. The concentration of AY38 dye was kept constant at $c = 1.0 \times 10^{-4}$ mol L^{-1} in the majority of the samples throughout the study with varied dendrimer concentrations. In one part of the results, the dendrimer concentrations were kept constant at $c = 1.0 \times 10^{-7}$ mol L^{-1} and the dye concentration was varied. The samples were prepared according to their charge ratio, l_c (a ratio of the number of anionic dye sulfonate groups to the number of cationic amine groups). A ratio below unity (<1.0) corresponds to an excess of positive dendrimer charges, and a ratio higher than unity (>1.0) corresponds to an excess of negatively charged AY38 molecules.

The sample vials were illuminated with a UV lamp (power = 230 Volts) at λ = 365 nm for 20 min while continuously stirring. The AY38 dye readily achieved its photostationary state (≈20 min). Measurements were performed immediately after irradiation.

2.3. Light Scattering

Static and dynamic light scattering are highly suitable techniques for characterizing polyelectrolytes in solution. Dynamic light scattering (DLS) probes the temporal fluctuations in the scattered intensity by using coherent laser light. Instead of the scattering angle θ, the scattering vector $\vec{q}$ (also known as momentum transfer) is used and is shown as follows [51]:

$$\vec{q} = \vec{k_s} - \vec{k_i} \quad (1)$$

where $\vec{k_i}$ and $\vec{k_s}$ are the propagation vectors of the incident and the scattered light. The magnitude of $\vec{q}$ is given by:

$$q = \left|\vec{q}\right| = \frac{4\pi n_D}{\lambda} sin\left(\frac{\theta}{2}\right) \quad (2)$$

with λ being the wavelength of incident light in the solution, and n_D is the refractive index of the solvent.

The intensity–time autocorrelation function, $g_2(q, \tau)$, is given by:

$$g_2(q,\tau) = \frac{\langle I(q,t)I(q,t+\tau)\rangle}{\langle I(q,t)\rangle^2} \quad (3)$$

The above function describes the correlation between the scattering intensity at time t with the one at time $t + \tau$, where τ is the shift in time. The intensity–time autocorrelation function can be converted into the electric field–time autocorrelation function $g_1(q, \tau)$ using the Siegert relation:

$$g_2(q,\tau) = 1 + [g_1(q,\tau)]^2 \quad (4)$$

The $g_1(\tau)$ function was further analyzed by a regularized inverse Laplace transformation using the CONTIN algorithm by S. Provencher to obtain the relaxation time distribution [52,53]. The mean relaxation times were then transferred into the apparent diffusion coefficient D_{app} using the relation:

$$D_{app} = q^{-2}\tau^{-1} \quad (5)$$

The measurements covered a broad range of q by measuring a scattering angle of $20^\circ \leq \theta \leq 150^\circ$ with 5-degree steps. In case of an angular dependence, D_{app} was extrapolated to $q = 0$ to yield D_0. In the absence of an angular dependence, the average value of D_{app} was taken as D_0. From the latter, the hydrodynamic radius (R_H) can be calculated using the Stokes–Einstein relationship:

$$R_H = \frac{kT}{6\pi\eta D_0} \quad (6)$$

where k is the Boltzmann constant, T is the absolute temperature in Kelvin, and η is the solvent viscosity.

Static light scattering (SLS) uses visible light as a characterization probe for particles in solution. In an SLS experiment, the macroscopic scattering cross-section $\frac{d\sum}{d\Omega}(q)$ is measured and is commonly denoted as the Rayleigh ratio, ΔR_θ:

$$\frac{d\sum}{d\Omega}(q) = R_\theta = KcM_wP(q) \quad (7)$$

where K is the optical constant, c is the mass concentration, M_w is the weight-averaged molecular weight, and $P(q)$ is the form factor. The Rayleigh ratio, ΔR_θ, is essentially a

measure of the intensity of light scattered by a sample relative to the intensity of the incident light, normalized by the volume of the scattering medium and the distance to the detector. It can be calculated using the formula below:

$$\Delta R_\theta = \frac{I_\theta r^2}{I_0 V} \tag{8}$$

where I_θ is the scattered intensity at an angle θ, with the incident light intensity I_0, V is the scattering volume, and r is the distance of the scattering volume to the detector.

The optical constant, K, in Equation (7) is given by:

$$K = \frac{4\pi^2}{\lambda_0^4 N_A}\left(n_{std}\frac{\mathrm{d}n}{\mathrm{d}c}\right)^2 \tag{9}$$

with λ_0 being the wavelength of the incoming light in a vacuum, N_A is the Avogadro constant, n_{std} is the refractive index of the standard (toluene) used for calibration of the absolute intensity, and $\mathrm{d}n/\mathrm{d}c$ is the refractive index increment (and also equivalent to the scattering length density $\Delta\rho$ used in SANS experiments). The scattering intensity at low q can be approximated by either the Guinier approximation for the form factor $P(q)$:

$$P(q) \approx \exp\left(\frac{-q^2 R_G^2}{3}\right) \tag{10}$$

or by the Zimm equation [54]:

$$\frac{Kc}{\Delta R_\theta} = \frac{1}{M_w}\left(1 + \frac{1}{3}q^2\langle R_G^2\rangle\right) + 2A_2 c \tag{11}$$

with R_G being the radius of gyration and A_2 being the second osmotic virial coefficient. The Zimm and Guinier equations are only valid for $q \times R_G \leq 1.2$ [55]. The ratio of R_G/R_H provides essential information on the particle topology.

Measurements were carried out using an ALV CGS3 goniometer with an ALV 5004 correlator (ALV, Langen, Germany) equipped with a HeNe laser with a wavelength of λ = 632.8 nm and a maximum output power of 23 mW.

2.4. Small-Angle Neutron Scattering

Polymers and polyelectrolytes are typically analyzed in solution and have a low contrast for electron microscopy and small-angle X-ray scattering (SAXS). Since the neutron scattering length b depends on the isotope and differs significantly for hydrogen and deuterium, it is advantageous to use deuterated compounds or solvents to achieve better contrast with neutrons. Here, SANS measurements were carried out using the D11 instrument (https://doi.ill.fr/10.5291/ILL-DATA.9-12-662, accessed on 30 November 2024) at the Institut Laue Langevin (ILL) in Grenoble, France, and using the SANS-I instrument (Proposal 20221454) in PSI, Villigen, Switzerland.

The SANS samples were prepared in D_2O with an AY38 concentration of c = 0.07 gL^{-1} and transferred into Hellma 404-QX quartz cells with a 2 mm path length.

At the ILL, the irradiated samples with different PAMAM generations (G2 to G8) were measured. For this, a particular setup was used, where the employed neutron beam had a diameter of 15 mm. A neutron wavelength λ = 6.0 Å (FWHM 9%) with three different sample–detector distances (1.4 m, 8 m, and 38 m) with collimation distances of 8 m, 8 m, and 40.5 m were used, respectively. In total, a scattering vector range of $0.016\ \mathrm{nm}^{-1} \leq q \leq 4.5\ \mathrm{nm}^{-1}$ was investigated.

Scattered neutrons were detected using a multitube ^{3}He gas detector consisting of three detector panels: a central one with 192 horizontally oriented tubes and a left- and right-side panel of 32 vertically oriented tubes. Each tube was 1 m long, with a pixel size of 4 mm along the tube, with the inner tube diameter being 8 mm. The detector was, therefore, composed of 256 × 256 pixels. Two-dimensional data were corrected for empty cell scattering, electronic background, detector uniformity via measuring 1 mm H_2O scattering, and transmissions using the Mantid 6.0 software package [56]. Data were put on an absolute scale via the attenuated direct beam intensity, measured per instrument configuration. Azimuthally averaged scattering curves were then used to subtract the solvent scattering and incoherent background.

The SANS q-range was extended in the low-q region by $0.0046\ \text{nm}^{-1} \leq q \leq 0.025\ \text{nm}^{-1}$ using SLS data. SLS data were merged with SANS data to extend the low-q range to obtain a more reliable insight into the shape and size of the nanoparticles. The extended low-q range allows for the coverage of the dimensions of larger aggregates. The exact same samples were measured with both techniques.

Parts of the samples were measured using the PSI SANS-I instrument with a different setup, where the experiments were carried out at 3 different sample-to-detector distances (1.6 m, 6 m, and 18 m) with collimation distances of 6 m, 6 m, and 18 m, respectively. A neutron wavelength of λ = 6 Å was used to cover a total q range of $0.03\ \text{nm}^{-1} \leq q \leq 4.0\ \text{nm}^{-1}$. The circular diameter of the employed neutron beam was 14 mm. The scattered neutrons were detected using a 2D MWPC CERCA ^{3}He detector with 128 × 128 elements of 7.5 × 7.5 mm^2. Similar to the experiments at the ILL, the detector images were corrected using a water sample, and the BerSANS (2002) software was used to correct transmissions and to azimuthally average the samples. All the measurements were performed at room temperature (25 °C). In the end, the solvent scattering and the incoherent background were subtracted from the samples' scattering curves.

The shapes and dimensions of the nanoparticles were determined by fitting the data with appropriate structural models using the SasView 4.2.2 software. The SasView 4.2.2 software fits the scattering data using various model form factors.

The solvent scattering length density was known and fixed while fitting. The reduced χ^2 values were used to determine the quality of the SANS data fit. All the fitted models were well fit, as observed by their χ^2 value ($\leq$3.0).

The SANS intensity after data correction is as follows [57]:

$$I(q) = \varnothing V_{NP} (\Delta\rho_{SLD})^2 P(q) S(q) \tag{12}$$

where $\varnothing$ is the volume fraction, V_{NP} is the particle volume, $\Delta\rho_{SLD}$ is the difference in scattering length densities between solute and the solvent, and $P(q)$ is the particle form factor corresponding to the particle shape. The structure factor $S(q)$ represents the interparticle correlations and was considered to be equal to 1, as the samples were diluted such that no interparticle interactions were present. The form factor is the square of the normalized total scattering amplitude $F(q)$.

For example, for a sphere with radius R, the scattering amplitude $F(q)$ is [55]:

$$F(q) = 3\frac{sinqR - qRcosqR}{(qR)^3} \tag{13}$$

For a cylinder with length L and radius R, $P(q)$ is [58,59]:

$$P(q,\alpha) = \frac{scale}{V} F^2(q,\alpha)\sin(\alpha) + background \tag{14}$$

where

$$F(q,\alpha) = 2(\Delta\rho)V\frac{sin\left(\frac{1}{2}qLcos\alpha\right)}{\frac{1}{2}qLcos\alpha}\frac{J_1(qRsin\alpha)}{qRsin\alpha} \quad (15)$$

where α is the angle between the cylinder's axis, $V = \pi R^2 L$ is the volume of the cylinder, $\Delta\rho$ (contrast) is the scattering length density difference between the scatterer and the solvent, and J_1 is the first-order Bessel function.

For an ellipsoid, the scattering amplitude $F(q)$ is [60]:

$$F(q,\alpha) = \Delta\rho V\frac{3(\sin qr - qr\ cos\ qr)}{(qr)^3} \quad (16)$$

where

$$r = \left[R_e^2 sin^2\alpha + R_p^2 cos\alpha\right]^{1/2} \quad (17)$$

where α is the angle between the axis of the ellipsoid, $V = (4/3)\pi R_p R_e^2$ is the volume of the ellipsoid, R_p is the polar radius along the rotational axis of the ellipsoid, and R_e is the equatorial radius perpendicular to the rotational axis of the ellipsoid.

2.5. ζ-Potential Measurements

The particles and their microenvironment determine the electrostatic properties of nanostructures in a solution. Such properties of nanostructures can be characterized by ζ-potential measurements. This technique measures the difference in the electrostatic potential between the medium and the fluid layer of the dispersed nanostructures. The ζ-potential was calculated from the electrophoretic mobility using the Helmholtz–Smoluchowski equation [61,62]:

$$\zeta = \frac{\mu_e \eta}{\varepsilon_{rs}\varepsilon_0} \quad (18)$$

where μ_e is the electrophoretic mobility, η is the dynamic viscosity of the liquid, ε_{rs} is the dielectric constant of the electrolyte solution, and ε_0 is the electric permittivity of the vacuum.

The ζ-potential measurements were conducted on a Zetasizer Nano ZS analyzer with an integrated 4 mW HeNe laser, with λ = 633 nm (Malvern Instruments Ltd., Malvern, UK).

2.6. UV–vis Spectroscopy

The absorption spectra were recorded with a JASCO V-630 spectrometer using quartz cuvettes with a 1 mm path length. Each measurement was performed at room temperature. UV–vis spectroscopy was used for determining the amount of dye in the solution and the dye involved in the nanoassemblies by combining it with centrifugation and calculating the dye concentration from the UV–vis spectra. In this method, centrifugation can remove all the aggregates (which will also remove all the bound dye) and only unbound dye molecules will remain in the solution.

2.7. Isothermal Titration Calorimetry (ITC)

This work used the platforms of the Grenoble Instruct-ERIC center (ISBG; UAR 3518 CNRS-CEA-UGA-EMBL) within the Grenoble Partnership for Structural Biology (PSB), supported by FRISBI (ANR-10-INBS-0005-02) and GRAL, financed within the University Grenoble Alpes graduate school (Ecoles Universitaires de Recherche) CBH-EUR-GS (ANR-17-EURE-0003). ITC experiments were performed at the VP-ITC microcalorimeter.

ITC is a technique that measures the heat changes (released or absorbed) when two solutions are mixed. Two identical reference and sample cells, with a volume of 1.442 mL, were enclosed in an adiabatic jacket. In this study, the reference cell was filled with the

solvent (D_2O), and the working cell contained the sample solution. A 288 µL volume of AY38 azo dye (titrant) from the syringe was injected stepwise into the sample cell containing the dendrimer solution under constant stirring. All measurements were carried out at 25 °C. Small aliquots of titrant (typically 2 µL) were injected in 50–60 steps to achieve a charge ratio range of $0.2 \leq I_c \leq 4.4$. The duration of each injection was 300 s, with a total measurement time of 4–4.5 h (including the equilibration time). Due to the absorption or release of heat, each injection produced a distinct peak. A separate measurement was performed with the titrant and the solvent for data subtraction. Data analysis and fitting were performed using the MicroCal Origin 7.0 software. The data were fitted using the two-site model. The Gibbs free energy (ΔG) is calculated using the following:

$$\Delta G = \Delta H - T\Delta S = -RTlnK \quad (19)$$

3. Results

This study focused on developing a system of self-assembled nanostructures with a light-tunable particle size and shape in a wide size range (10 nm–2 µm). The structural characterization was based on static and dynamic light scattering and small-angle neutron scattering analyses to investigate the size and shape of the nanoparticles. Systematic surface potential studies investigated the cause of the stability of the nanoparticles in an aqueous solution. UV-vis and ITC measurements were performed to analyze the interactions at a molecular level and from a thermodynamic perspective, respectively.

Scheme 1 represents the four assembly steps, where step 1 creates the nanoassemblies before irradiation in the acidic medium (pD = 3.5). Step 2 occurred after the irradiation. Step 3 and step 4 were carried out to bring the sample into its initial stage by adding NaOD (until pD = 11.5) and DCl (until pD = 3.5) sequentially. The cycle could be reproduced multiple times without any major influence on the assembly structures.

3.1. Structural Characterization

3.1.1. Light Scattering: Size Distributions Before and After Irradiation

Figure 1 illustrates the DLS electric field autocorrelation functions $g_1(\tau)$ for the assemblies of AY38 with four different dendrimer generations: G3, G4, G6, and G8 (all $c_{AY38} = 1 \times 10^{-4}$ mol L^{-1}) with their corresponding distribution of relaxation times $A(\tau)$ for a scattering angle of $\theta = 90°$. The DLS results of the other dendrimer generations (G2, G5, and G7) are shown in Figure S2. The hydrodynamic radius, R_H, was calculated by extrapolating the angular-dependent diffusion coefficient values to a zero-degree angle and using the Stokes–Einstein relationship (Equation (6)). The σ-value, the standard deviation, represents the polydispersity of the nanoparticles in the solution, which is the average polydispersity of all the scattering angles measured (20–150°). Before irradiation, the hydrodynamic radii of the different nanostructures were found to be in the range of 31 nm $\leq R_H \leq$ 42 nm with a low polydispersity of $0.05 \leq \sigma \leq 0.18$, where the aggregate size increased up to G6 (R_H = 42 nm) and decreased again in the higher-generation assemblies. Interestingly, the generation dependency was opposite to the outcome of the study of Mariani et al., where higher generations formed larger aggregates [21]. Such a stark difference was likely due to the nature of the dye–dendrimer and/or dye–dye interactions, as a different azo dye (AY38) was used in the present study, as will be further discussed below. Upon irradiation, the nanoparticles reassembled to form larger (up to 15-fold) and highly monodisperse ($0.06 \leq \sigma \leq 0.10$) assemblies. Overall, the light scattering results (before and after irradiation) were consistent with a previous proof-of-concept study, in which photoresponsive AY38/G4 assemblies with a similar size range were found [12].

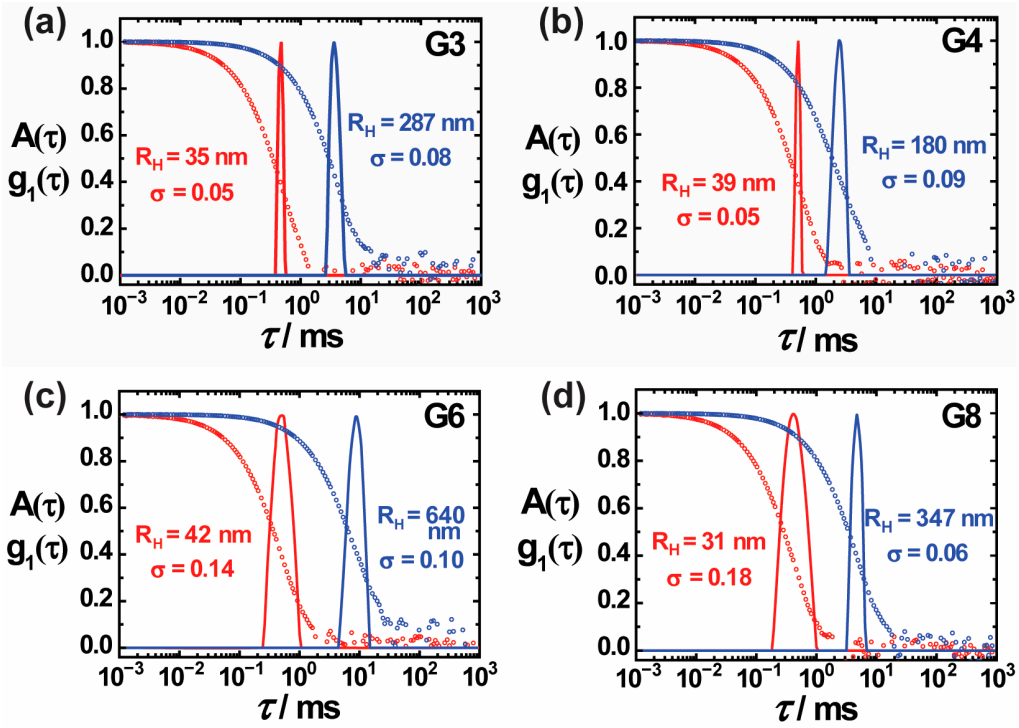


Figure 1. Multi-angle DLS at a charge ratio (dye charges/dendrimer charges) of l_c = 1.5 before (red) and after irradiation (blue): electric field autocorrelation $g_1(\tau)$ (open circular symbols) and distribution of relaxation times A(τ) (lines) at a scattering angle of $\theta = 90^\circ$ for different dendrimer generations: (**a**) G3, (**b**) G4, (**c**) G6, and (**d**) G8. (The R_H values were obtained by extrapolation to a 0° angle, and σ represents the particle size distribution at a 90° scattering angle, $c_{AY38} = 1 \times 10^{-4}$ mol L^{-1}.)

Dynamic light scattering (DLS) measurements at a scattering angle of $\theta = 90^\circ$ revealed monomodal assemblies, as shown in Figure 1. However, at lower angles ($\theta \leq 70^\circ$), a small intensity-weighted peak (<5%) corresponding to larger particles (≈1 μm) was observed for the high-generation dendrimers (≥G6), as shown in Figure S3. The effects of the multi-angle scattering are further illustrated in Figure S4, where bimodal particle size distributions were detected at small angles ($\theta < 90^\circ$), while only single particle size distributions were observed at larger angles ($\theta \geq 90^\circ$). The diffusion coefficient, D, is also shown as a function of the square of the scattering vector, q^2, for the monomodal (AY38-G3) assemblies in Figure S5 and the bimodal assemblies (AY38-G7) in Figure S6. These observations align with the principles of light scattering: the detection angle is inversely related to the particle size, meaning larger particles are more easily detected at smaller angles. Thus, it is plausible that "very large" aggregates are exclusively observed at smaller angles.

Evidently, the dendrimer generation plays a crucial role in the structure formation. These large aggregates were likely formed in the high-generation dendrimers due to their reduced flexibility and significant steric hindrance. This steric constraint may limit the extent of the interaction between the dye ions and the charged functional groups on the dendrimers, leaving a portion of dye ions binding via secondary dipole–dipole interactions to electrostatically bound dye ions. This interaction was proposed as the primary mechanism inducing bimodality in the electrostatic self-assemblies [19] and will be elucidated in the following sections using complementary analytical methods.

Figure 2 represents the overall structural change in the nano-assemblies found through multi-angle DLS at a charge ratio of l_c = 1.5. Previously, the PAMAM generation 2 dendrimer had not been able to form stable electrostatic assemblies, as it had only been explored in solutions with a dendrimer excess [47]. By extension, in the present study, G2 could form stable particles with an excess of AY38 azo dye, though with a large polydispersity

(see Figure S2). The surplus dye—bound through secondary dipole-dipole interactions to the electrostatically bound dye molecules (see below)—provides extra charges and, ultimately, extra electrostatic stability to the aggregates. Hence, stabilizing structures with G2 dendrimer might be possible here due to the nature of AY38 azo dye that yields additional stability due to two anionic groups and secondary interactions. However, the larger polydispersity and limited charge ratio range in which stable nano-assemblies can be built with the G2 dendrimer demonstrate that macromolecular—nano-scale—building blocks rather than small-molecular building blocks are required for a versatile and defined structure formation by this type of electrostatic self-assembly.

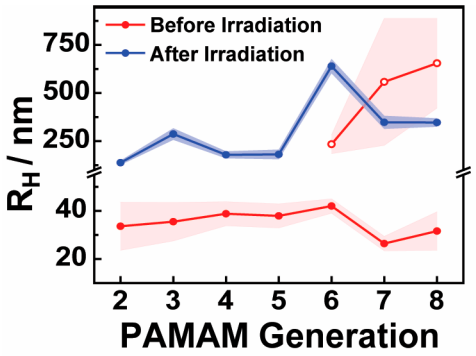


Figure 2. Effect of the irradiation on the hydrodynamic radius R_H for various dendrimer generations at a charge ratio of l_c = 1.5 and constant dendrimer mass concentration. Results are from multi-angle DLS. The shaded areas in blue and red color represent the polydispersity in particle size Three open-circle data points in red represent a second size species in particles for samples with high-generation dendrimers.

Furthermore, higher-generation dendrimers were explored, which exhibited highly stable assemblies in the solution with a low polydispersity. Before irradiation, the assemblies did not show any significant size change upon increasing the dendrimer generation ≤G6, but there was a slight decrease in size from G6 to G7 (which is opposite to what was observed by Mariani et al. [21]). The G8 dendrimer seems to form slightly larger nanoparticles than G7 but with a higher polydispersity, which, therefore, is not considered a significant change here. This remarkable dependence on the generation with a maximum and minimum size and generation 6 and 7, respectively, indicates a complex interplay of effects. Higher-generation dendrimers have a greater number of functional groups, i.e., they are densely populated with cationic amine charges. When these dendrimers interact with anionic AY38 azo dye molecules, the resulting dendrimer-dye complexes can exhibit enhanced electrostatic repulsion due to the high number of charged groups. According to previous studies by us, the assembly size (aggregation number) increases with decreasing the free enthalpy ΔG of the association, which would mean larger aggregates for more highly charged building blocks, i.e., for higher-generation dendrimers [47]. On the other hand, the observation for higher generations may be attributed to their denser structure and decreased flexibility causing the functional groups to be less accessible for the attachment of dye molecule stacks, yielding smaller particles with G7 and G8.

Upon light irradiation, the smaller assemblies, along with a fraction of the larger aggregates observed in the higher-generation dendrimers (as shown in Figure 2), for all dendrimer generations reorganized into larger monomodal assemblies, consistent with observations from previous studies [19]. The increased monodispersity is evident from the reduction in the shaded area of the blue data points following irradiation. This phenomenon arises from the photoisomerization of the azo dye to its *cis* state, which interacts differently with dendrimer molecules compared to the *trans* state due to its altered conformation. This

caused the system to reconfigure, forming larger aggregates, ultimately stabilizing the nanoparticles in the solution. Specifically, the *cis* molecule showed a lower dipole moment, resulting in less expressed secondary dipole–dipole interactions [12]. The connection of this molecular effect with the particle size will be discussed further below.

The low-generation dendrimers are small in size, highly flexible, and exhibit a small number of functional groups, resulting in only weakly sterically hindered structures; therefore (similar to before irradiation), the size of the assemblies within the early-generation dendrimers (≤G5) did not differ significantly in terms of the dependence on the generation after irradiation. However, with the G6 dendrimer upon irradiation, the azo dye formed the largest aggregates, which again decreased in size with the higher dendrimer generations. In the case of the G6 dendrimer, there must be a balance of flexibility and steric hindrance, leading to the most favorable conditions for extended particle aggregation. This will be further discussed in detail in conjunction with the UV–vis and ITC studies below.

For the results in Figures 1 and 2, the concentration of AY38 was kept constant at $c = 1.0 \times 10^{-4}$ mol L^{-1}. However, to further illustrate the role of the dendrimer generation in the size and shape control, in a further set of experiments, the molar dendrimer concentration was set to $c = 1.0 \times 10^{-7}$ mol L^{-1}, such that the number of dendrimer molecules was identical in the samples with different generations. A moderate excess of dye charges was again used. The results are shown in Figure 3. Figure 3a represents the size of the assemblies at $l_c = 1.5$, showing a similar trend in sizes to that noticed above in the case of constant dye concentrations. Bimodality was also detected for the higher dendrimer generations (≥G6). For a more detailed understanding, generation-dependent samples with $l_c = 2.0$ were also investigated (Figure S7a). In the case of $l_c = 2.0$, bimodality was encountered even earlier, that is, from generation G5 onwards, which was likely due to the higher excess of dye molecules at higher charge ratios, which increased the possibility of secondary dye–dye interactions. This again supports the direct involvement of dye-dye interactions in the control of the polydispersity of the nanoassemblies [19], which will be discussed further alongside the ζ-potential studies below.

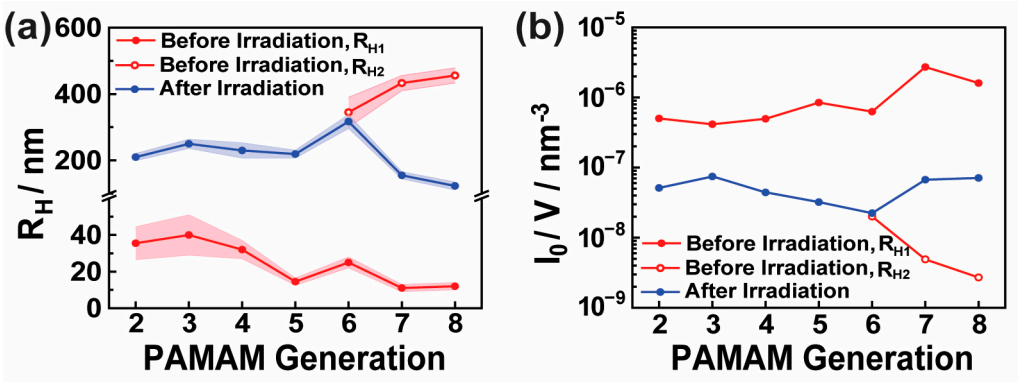


Figure 3. Generation dependence of the dendrimer-dye assemblies at a constant dendrimer number concentration ($c = 1.0 \times 10^{-7}$ mol L^{-1}) for a charge ratio $l_c = 1.5$ (**a**) Hydrodynamic radius R_H as a function of the dendrimer generation. The shaded areas in blue and red color represent the polydispersity of the particle size. (**b**) Number concentration of the assemblies (approximated using the ratio of the total scattering intensity and the volume ($4/3\ \pi\ R_H{}^3$) of the assemblies) as a function of the dendrimer generation. The open red symbols represent the second species of the bimodal distributions.

If all the dendrimer generations showed similar interactions within the assemblies (regardless of their size), the number of assemblies in the solution would not change, and the number of dendrimer molecules per aggregate would remain the same. Figure 3b depicts the relative number concentration of the assembled nanoparticles as a function

of the generation before and after irradiation. This was estimated by dividing the total scattering intensity (I_0) obtained from the extrapolation of the $1/\Delta R_\theta$ values to a 0° angle ($q = 0$) by the volume of the assemblies approximated as the volume of a sphere, $V = \frac{4}{3}\pi R_H^3$. It becomes evident that there is an influence of the dendrimer generation on the assembly number concentration, both before and after irradiation.

Before irradiation, a similar trend to when the dye concentration was kept constant in I_0/V was observed up to G6, yet increased relative assembly number concentrations were found for the G7 and G8 dendrimers. As a constant molar dendrimer concentration (c = 1.0 × 10^{-7} mol L^{-1}) was used throughout the samples with different generations, the same number of dendrimer molecules was present in the solution. As the size of the dendrimer increased with increasing the generation, there were fewer dendrimer molecules in the assembly with increasing the generation, as the assembly size was comparable (assuming a similar density). However, in the case of the G7 and G8 dendrimers, where the dendrimer sizes were the largest, smaller assemblies formed, as seen in the DLS studies (Figures 2 and 3a). This led to a higher number concentration of the assemblies for the higher dendrimer-generations. The value of I_0/V was the lowest in the samples with two distinct species before irradiation for two significant reasons. First, the low-intensity weighted peak observed for the large particles in the DLS measurements (Figure S3) belonged to the very low I_0 values. Second, the majority of the dendrimer molecules were consumed in the smaller assemblies before irradiation, leaving only a few polyelectrolytes to form the larger aggregates. Upon irradiation, the larger nanoassemblies involved a higher number of dendrimer molecules per particle, which decreased the overall number of particles in the solution. Therefore, the number concentration decreased significantly after irradiation. With the G6 dendrimer, the value observed for I_0/V was the lowest. This was because the largest assembly size formed with the G6 dendrimer. Again, a sharp increase in the number concentration was observed in the >G6 generations due to similar reasons as those mentioned above. Overall, interestingly, this consideration showed similar trends to the experiments with a constant mass concentration, which, in return, confirms that the dependencies observed for the experiments with a constant mass concentration were not just an effect of the different number concentration but indeed originated in the dendrimer structure.

3.1.2. LS-SANS: Assembly Shapes Before and After Irradiation

Small-angle neutron scattering was performed to gain insights into the effects of photoirradiation and the dendrimer generation on the shape and dimensions of the self-assembled nanoparticles in solution. The dependency of the size and shape of the assemblies with a constant dye concentration of 1 × 10^{-4} mol L^{-1}, i.e., a constant dendrimer mass concentration, on the dendrimer generation, G3 through G8, and photoirradiation is illustrated in Figure 4, and the data for G2 are shown in Figure S8.

Prior to irradiation, spherical particles were observed for the assemblies of all the dendrimer generations except G2. With increasing the generation from G3 to G6, the particle sizes were found to be within the range of 53–59 nm, and smaller assemblies were observed for G7 (39 nm) and G8 (38 nm), which was in accordance with the light scattering results. In some cases, a few data points in the low-q region (Figure 4d–f) were not included in the fitting. This observation was consistent with the bimodal particle size distribution of 40–60 nm and >500 nm found in the dynamic light scattering experiment, but the larger assemblies were in a very low quantity. The larger assemblies only started to significantly appear in the low-q range obtained from the SLS data. Due to insufficient data points, it was not possible to fit the larger assemblies. Since the scattering vector $\vec{q}$ is inversely proportional to the real space size of the particles (Equation (2)), the low q-range from the

SANS data did not show any hints of larger assemblies, and they only appeared in the SLS data at very low q ($q \leq 0.006$ nm^{-1}). In the case of the G2 dendrimer, small cylindrical nanoparticles were observed (Figure S8). This must be due to the small size of the G2 dendrimer molecules, which evidently affected the overall shape of the assemblies.

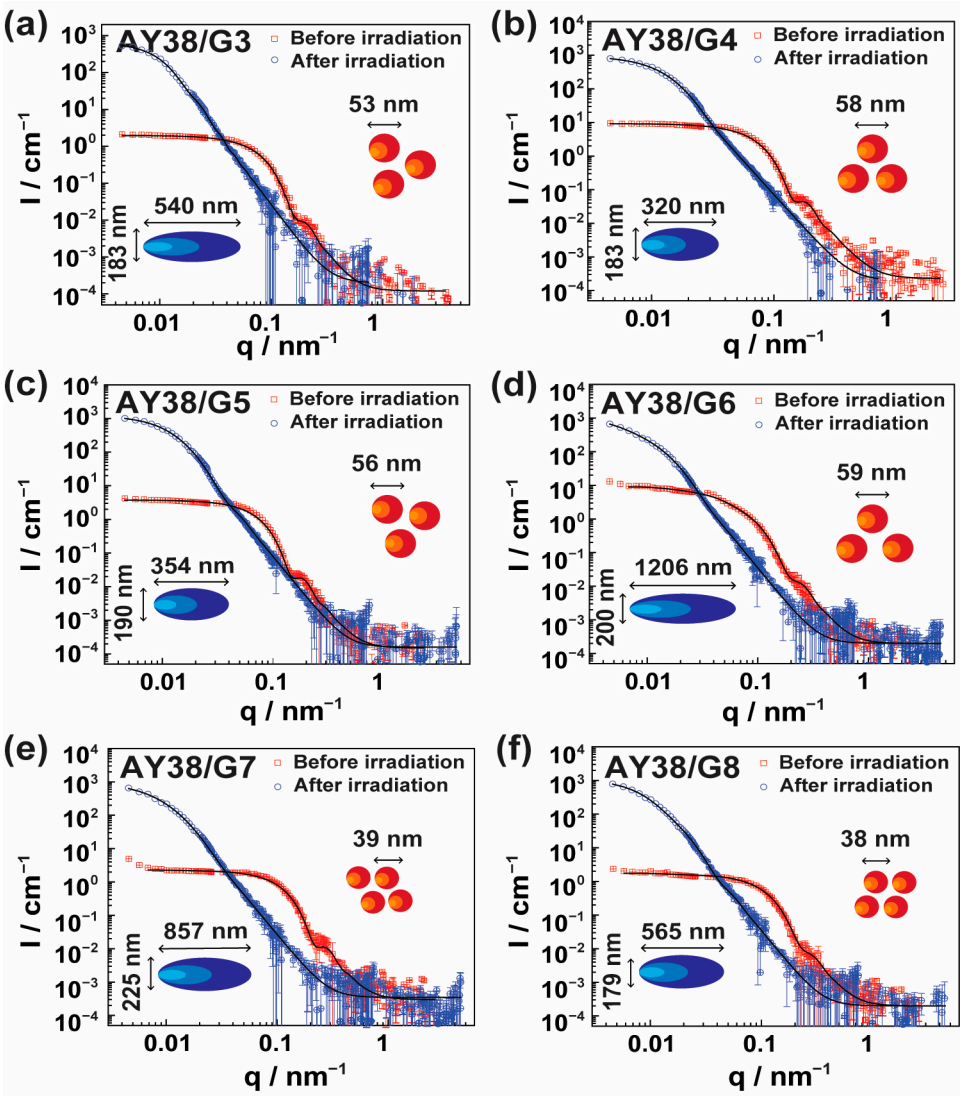


Figure 4. SLS-SANS particle shape analysis: (**a**) AY38-G3; (**b**) AY38-G4, (**c**) AY38-G5, (**d**) AY38-G6; (**e**) AY38-G7, and (**f**) AY38-G8, before (red) and after (blue) irradiation at l_c = 1.5, with data points (symbols) and structural fits (lines). The inserts indicate the particle structures resulting from the structural fitting. Detailed parameters are given in Table S2.

After irradiating the samples for 20 min, SANS measurements were carried out, showing that except for G2, all the dye-dendrimer aggregates rearranged into defined ellipsoidal structures. In the case of the G6 dendrimer, the dye-dendrimer interactions resulted in the largest ellipsoid upon irradiation, again in good agreement with the light scattering analysis. The shapes obtained from the SLS-SANS data are summarized in Figure 5.

By combining the information on the particle shape and size, the particle volume—and, consequently, the aggregation number of dendrimers per particle—could be determined from the SLS-SANS analysis more exactly than from the DLS analysis above. This was achieved by dividing the nanoparticle volume by the combined volume of a single dendrimer molecule plus a dye "shell", as illustrated in Figure S9. The aggregation number

decreased with increasing the dendrimer generation, confirming the relative approximation from the DLS analysis, again showing that the size of the dendrimer molecule directly influenced the aggregation number. For instance, the aggregation number (prior to irradiation) decreased from approximately 10^4 for the G2 dendrimer assemblies to about 10^1 for the G8 dendrimer assemblies (Figure S9a). However, as shown in Figure S1, the hydrodynamic radius of the G8 dendrimer (5.6 nm) was only 3–4 times larger than that of the G2 dendrimer (R_H = 1.6 nm). This result again suggests that beyond the dendrimer size, steric hindrance played a significant role in limiting the ability of additional dendrimer molecules to interact and form larger aggregates. Upon irradiation, the aggregation number increased, as discussed above.

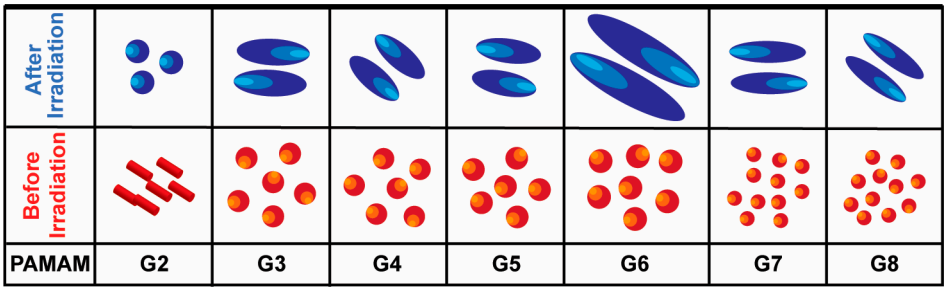


Figure 5. Nanoparticle shapes of dendrimer-dye assemblies with different dendrimer generations obtained from SLS-SANS experiments (the sizes shown in the figure are not scaled.).

3.2. Charge Characteristics Before and After Irradiation

To obtain a comprehensive understanding of the structure, ζ-potential analysis was conducted to evaluate the influence of the dendrimer generation on the charge status of the assemblies in solution. The results are given in Figure 6. The samples exhibited slightly negative ζ-potential values within the range from −17 to −25 mV, characteristic of well-stabilized assemblies [63]. For the samples with bimodal size distributions (observed prior to irradiation at dendrimer generations ≥G6), the ζ-potential values represented an average across the two particle populations. The ζ-potential contribution from these bimodal distributions is denoted by open red symbols in Figure 6a and should not be interpreted quantitatively.

Upon irradiation, the ζ-potential values increased, shifting closer to 0 mV, indicating a reduction in the electrostatic charge of the particles. It is likely that a decrease in the charge status caused by the molecular equilibria drove further aggregation into larger particles, leading to the formation of electrostatically better-stabilized assemblies because the total surface needing to be stabilized was decreased. The negative ζ-potential originates from the excess dye molecules bound to the dye-dendrimer electrostatic assemblies via dye.dye interactions. The weakening of the ζ-potential upon irradiation suggests that the over-stoichiometric dye ions were less strongly associated with the electrostatic dye-dendrimer complexes. The dye-dye interactions, particularly, were weakened upon irradiation, as the *cis* isomer bound less strongly than the *trans* isomer (see below). This disruption of secondary interactions reduced the surface charge density of the assemblies, making it insufficient to stabilize the numerous smaller particles. Consequently, the particles aggregated to form larger, more stable assemblies, which achieved sufficient stabilization through their remaining charge. Up to this point, the findings and conclusions are in agreement with our previous publications on this type of system [12,19].

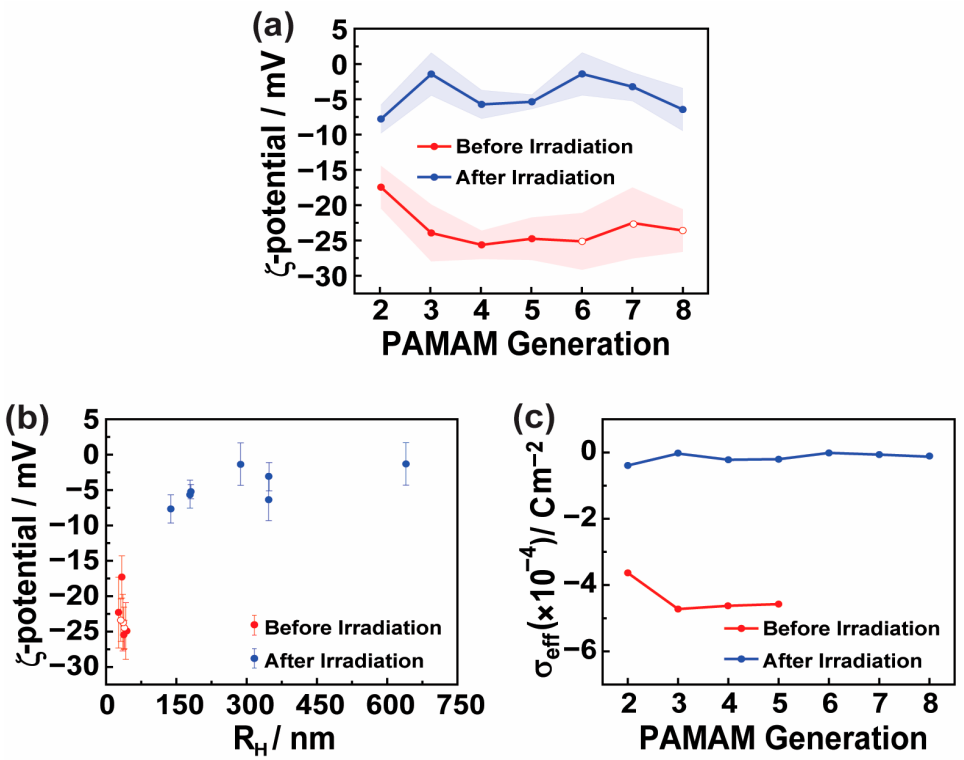


Figure 6. Charge characteristics of dendrimer–dye assemblies: ζ-potential as a function of the (**a**) dendrimer generation and (**b**) hydrodynamic radius, R_H, before and after irradiation. Open red circles represent the biomodal samples. (**c**) Effective surface charge density, σ_{eff}, of the monomodal assemblies as function of the dendrimer generation. The shaded area in blue and red color in (**a**) shows the error bar of the ζ-potential values.

The smaller assemblies generally exhibited stronger ζ-potential values, as illustrated in Figure 6b, providing insight into the relationship between the ζ-potential and particle size. Before irradiation, the assemblies were characterized by relatively small particle sizes (R_H < 50 nm), as determined by DLS and exibited strongly negative ζ-potential values. In contrast, the larger assemblies that formed post-irradiation displayed smaller ζ-potential values.

Following irradiation, the reduction in the ζ-potential allowed the particles to come into closer proximity, leading to the formation of larger assemblies. To further interpret these results, the effective charge density (σ_{eff}) was analyzed using Equation (S1), as shown in Figure 6c for the samples with monomodal size distributions.

Upon irradiation, a decrease in the charge density was observed, caused by the decrease in dye–dye interactions. This reduction was associated with the isomerization of the dye molecules to their *cis* form, which weakened the dipole–dipole interactions. Remarkably, the charge density was almost constant, with a characteristic value before and another one after the irradiation independent of the dendrimer generation. Thus, these experiments identified the charge density as a key parameter controlling the particle size. The molecular interactions determined a characteristic effective surface charge density, which, again, was realized by adopting a certain particle size and shape.

As a preferred effective surface charge density of the self-assembled nano-objects was evidently realized, both before and after irradiation (Figure 6b), rather than a specific ζ-potential or effective particle charge (Figures 6a and S12c,d), it can be concluded that an adjustment in the particle morphology is needed to realize this effective surface charge density. Given that on a molecular level, based on association equilibria (see below), a certain degree of dye binding, and thereby a charge excess, occurred, while at the same

time the building blocks occupied certain volumes, it is likely that certain effective charge density/volume scenarios can only be realized by non-spherical shapes. As visible in Figure S12b, the nano-object aspect ratio increases with its particle size, indicating the need of a surface area increase per particle. Further discussion will follow below.

3.3. Elucidating Interactions Before and After Irradiation by UV–vis Spectroscopy

In addition to the nano-structural (colloidal) characterization of the dye–dendrimer assemblies, molecular alterations arising from the dendrimer generation and photoisomerization were examined by UV–vis spectroscopy. As observed in the previous studies, the structural change was triggered by the *trans–cis* isomerization of the azo dye [12,20]. Before irradiation, the more stable *trans* isomer was in the majority (>90%), which was converted to the *cis* isomer at about 83% after 20 min of light irradiation with a λ = 365 nm UV lamp. In the dye–dendrimer assemblies, the spectral changes were analogous to the pure dye spectra before irradiation without any shifts, as shown in Figure 7.

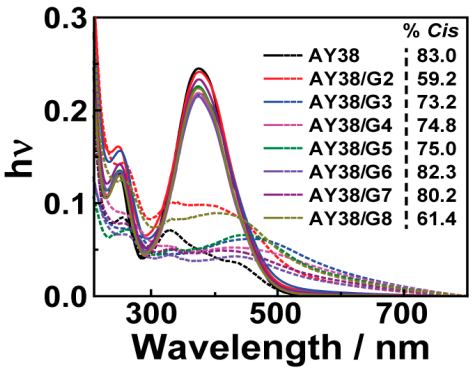


Figure 7. Effect of photoirradiation on dendrimer–dye assemblies at l_c = 1.5 as analyzed by UV-vis spectroscopy. Straight lines: data before irradiation; dashed lines: after irradiation. The percentage of *cis* dye is given in the legend. Each color represents a UV-Vis spectrum of a different dye-dendrimer sample with the dendtrimer generation given in the plot.

The stability of the over-stoichiometric samples, as well as the negative ζ-potential of the assemblies, showed the involvement of secondary interactions among the dye molecules. The UV-vis spectra of the AY38 dye-dendrimer assemblies did not exhibit significant changes compared to the free dye, indicating that these secondary interactions were not dominated by π-π bonding. Such bonding would typically produce noticeable effects on the absorbance spectra of azo dyes. Instead, the origin of these interactions appears to be dipole-dipole interactions [19]. The *trans* dye molecules possessed a substantially higher dipole moment (27.96 Debye) compared to their *cis* counterparts (12.96 Debye), which increased the propensity for dye–dye interactions among the *trans* dye molecules as well as the strength of their mutual interactions. These interactions enhanced the binding capabilities of the dye molecules within the electrostatic assemblies [64]. Dipole-dipole interactions were particularly pronounced in the higher-generation dendrimers ($\geq$G5), where the less flexible amino groups limited full dye-dendrimer binding, thereby promoting the formation of secondary dipole-dipole interactions.

The UV-vis and DLS measurements of the dye in water (without dendrimers) revealed no signs of aggregation [19]. This lack of aggregation highlights that the mutual dye–dye interactions only arose when the anionic dye solution was combined with the positively charged dendrimers. The electrostatic binding between the dye and dendrimers was more long-ranged and caused the "primary" aggregation. When associating, a dye preferably binds adjacently to another dye, undergoing both attractive dendrimer-dye ionic and "secondary" attractive dye-dye dipole-diploe interactions. These secondary

dipole-dipole interactions among the dye molecules subsequently drive the formation of larger aggregates.

The UV-vis spectroscopy enabled the quantification of the *trans* and *cis* dye species in the samples [19]. Upon irradiation, the percentage of *cis* isomers increased, with its extent varying across the different dendrimer generations. The G2 dye assemblies exhibit the lowest *cis* content (≈59%), which progressively increased through the G3, G4, and G5 dendrimer samples, reaching its peak with the G6 (≈82%) and G7 (≈80%) assemblies before decreasing again in the G8 assemblies. This behavior is likely due to photoprotective effects observed in both the low- and high-generation dendrimer samples, driven by the predominance of interactions that hindered the isomerization. In the low-generation dendrimers, the flexible dendrimer structures favored electrostatic interactions, and the dye molecules strongly bound electrostatically, which partially hindered the isomerization of the *trans* dye molecules into the *cis* form.

On the other hand, as discussed, the higher-generation dendrimers were characterized by less flexible, sterically hindered architectures, causing an association with expressed dye-dye interactions. The steric conditions limited the dye binding, such that the attachment of only one sulfonate group of AY38 to the protonated amino groups and surplus dye ions occurred via dipole–dipole interactions. This again limited the dye isomerization. Hence, the largest *cis* amount existed with the medium generations.

Figure 8 further considers the described scenario on a quantitative basis, displaying the dependence of the percentage of *cis* isomers present in the solution as function of the "dendrimer density". Here, the average density of the dendrimer molecules was approximated using their molar mass and the volume of a sphere with the dendrimer extension (using the dendrimer diameter given by the supplier, which is accordance with the R_H values determined by DLS (Figure S1, Table S1) and the radii of gyration from molecular dynamics simulations carried out by Maiti et al. [42]).

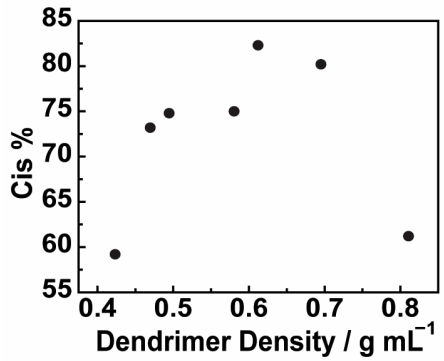


Figure 8. Relation between the percentage of *cis* isomers present in the dendrimer-dye samples after irradiation (*cis* %) and the average dendrimer density for the different dendrimer generations.

Interestingly, the total quantity of *cis* isomers in the solution (excluding G8) appeared to correlate directly with the change in the assembly size upon irradiation, as shown in Table 1. Similar to the highest *cis* percentage, the percentage change in size was also the largest in the G6 and G7 dendrimer assemblies. In a very different context, a comparable relationship between the size change and *cis* isomer content was previously reported by Willerich et al., who varied the *cis* amount in the solution by altering the irradiation wavelength [20]. In the G6 and G7 dendrimer assemblies, the dye molecules partially interacted with the tertiary amino group charges but also possibly predominantly bound to the primary amino groups (RNH_3^+) due to greater accessibility. The surplus dye ions engaged in secondary dipole–dipole interactions. This balance of interactions likely resulted in the dye ions binding to primary the amine charges of the G6 and G7 dendrimers via one sulfonate group (RSO_3^-),

while the second sulfonate group remained unbound in solution. This flexibility allowed the unbound dye molecules to isomerize more easily, explaining the higher isomerization percentages observed in these assemblies.

Table 1. Relationship between the percentage of cis dye in the sample (cis %) and the change in the aggregate size (R_H %) upon irradiation for dendrimer–dye assemblies with PAMAM dendrimers of different generations.

PAMAM Generation	*cis*%	R_H%
G2	59.2	411
G3	73.2	808
G4	74.8	461
G5	75.0	478
G6	82.3	1524
G7	80.2	1318
G8	61.2	1098

From a molecular perspective, *cis* isomers, as previously described, possess a lower dipole moment compared to their *trans* counterparts and are less effective at forming strong dipole-dipole interactions between dye molecules [19]. Consequently, as the proportion of *cis* isomers increased under light irradiation, the weakened secondary interactions led to their reorganization into larger, again stable electrostatic assemblies.

The G8 PAMAM dendrimers exhibit the highest density and lowest flexibility among the studied generations, which limited the dye molecules' ability to interact with the tertiary amine charges (R_3NH^+) electrostatically. Consequently, the dye molecules preferentially interact with the more accessible primary amino charges (RNH_3^+), leaving surplus dye ions available for secondary dye–dye interactions, limiting the isomerization of the dye molecules into the *cis* state in the G8 dendrimer assemblies but promoting their interconnection into larger assemblies.

3.4. Thermodynamic Analysis of the Assembly Formation

ITC was performed to develop a fundamental understanding of the molecular interactions and thermodynamic parameters involved in the assembly formation. Recent findings indicate that the *trans* isomers of the dye molecules bind better over-stoichiometrically to the G4 dendrimer as compared to the *cis* isomers due to their different geometric structures. The *cis* isomers show almost no dye-dye interactions resulting from the low dipole moment in the *cis* state [19,64]. Previous studies have examined titrating the dendrimer solution (only G4) into the dye solution, where we observed a single-step reaction corresponding to the combination of the *trans* dye–dendrimer electrostatic interactions and the secondary dye-dye interactions [12,20,27]. Herein, for the first time, we elucidate the above-described dependence on the generation, where the dye-dye interactions were found to affect the assembly structures, necessitating a quantitative assessment of their impact. Figure 9 shows the titration of the dye AY38 into the dendrimer solutions with dendrimer generations of G3, G6, and G8, and the thermodynamic parameters of all the other measured generations are listed in Table 2, all before irradiation. As these measurements were performed before irradiation, the ITC results investigated only the *trans* isomers in the solution. The ITC curves in Figure 8 indicate a two-step reaction; the first step was found to be endothermic, characterized by an enthalpy change $\Delta H \geq 6.7$ kJ mol^{-1}, which was accompanied by an increase in entropy ($\Delta S \geq 1.3$ kJ mol^{-1}). In this first step, the excess of protonated amino groups of the dendrimer molecules led to electrostatic interactions, mainly due to the exchange of chloride ions (from DCl) with sulfonate groups from the AY38 molecules. During this process, the dye ions initially broke down the hydration shell around the

dendrimer and counterion cloud, replacing the Cl^- ions with $-SO_3^-$ groups [65]. Therefore, this step resulted in a positive enthalpy change and entropy gain by the release of counterions, with an overall negative free energy change ($\Delta G \leq -0.2$ kJ mol^{-1}) [66,67]. Additionally, the binding stoichiometry of the first step of the reaction is represented by N_1, where N_1 contributes less than 25% of the total number of available dendrimer sites. This suggests that the doubly charged azo dye molecules were only electrostatically bound per dendrimer. In this entropically driven first step, a decrease in ΔG upon increasing the dendrimer generation further hinted at the increment in the steric hindrance that primarily affected the electrostatic dye–dendrimer interactions, and this will be discussed in the following discussion section.

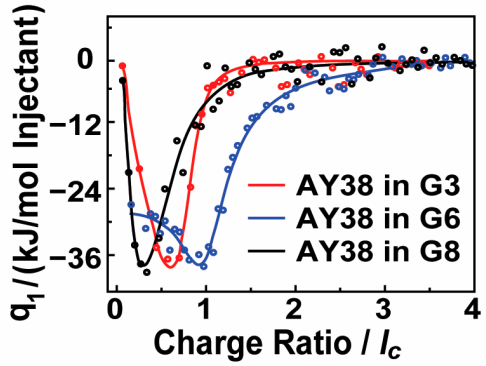


Figure 9. Isothermal titration calorimetry (ITC) to study the thermodynamics of the electrostatic dye–dendrimer assembly formation for varying dendrimer generations: AY38-G3, AY38-G6, and AY38-G8 (where the AY38 dye solution was titrated into the dendrimer solution). Here, q_1 represents the energy produced by the system upon titrating per mole of azo dye into the solution and is plotted against the system's charge ratios. Circles represent data, which were fitted by MicroCal Origin 7.0 software as shown by lines in the respective color.

Table 2. ITC results of dye-dendrimer systems. AY38 was titrated into the dendrimer solution. Data are described with a two-site model (error bars ΔH: 3–5%, ΔG: 10–20%, N: 5–10%).

PAMAM Generation	G3	G5	G6	G7	G8
N_1/sites	15	51	68	186	256
ΔH_1 per site/kJ mol^{-1}	89.2	6.7	30.3	58.9	28.4
ΔS_1/kJ mol^{-1}	4.4	1.3	69,036	367.7	24.5
ΔG_1 per site/ kJ mol^{-1}	−2.3	−1.1	−0.8	−0.3	−0.2
N_2/sites	47	217	239	442	599
ΔH_2 per site/kJ mol^{-1}	−11.3	−34.6	−79.3	−43.1	−32.4
ΔS_2/kJ mol^{-1}	−1.6	−24.8	−63.2	−63.6	−64.8
ΔG_2 per site/kJ mol^{-1}	−1.1	−0.3	−0.2	−0.1	−0.1

The second step was exothermic and enthalpically driven, with a binding enthalpy of $\Delta H \leq -11.3$ kJ mol^{-1} and a free energy change of $\Delta G \leq -0.1$ kJ mol^{-1}. The second step corresponds to the combination of electrostatic and secondary dipole-dipole interactions [19]. The initial stage of the second step changed with the different dendrimer generations, but the step corresponded to a similar phenomenon for all generations. The binding sites of the divalent azo dye molecules per dendrimer increased as compared to the first step, where only electrostatic interactions were involved. In the second step, the charge capacity of the dendrimer was surpassed by an excess dye amount ($I_c > 1.0$), leading to the above-mentioned stabilization of the negatively charged assemblies.

In the second step, the unique properties of the high-generation dendrimers became evident. The G6 dendrimer showed the most negative value of ΔH (compared to the

other generations), showing that the assembly process was the most exothermic in the AY38/G6 system. This was due to the more significant number of terminal groups in the high-generation dendrimers available for binding with the dye molecules, which led to a more substantial number of favorable interactions, resulting in a decrease in free energy. However, the dye ions could only partially bind (one of the two binding sites) to the high-generation dendrimer molecules due to their strong steric hindrance, as mentioned above.

4. Discussion

In examining the generation dependence of dendrimer-dye assemblies prior to irradiation, up to the G6 dendrimer, no significant variation in the assembly size was observed with increasing the dendrimer generation. A decrease in size was noted with further increasing the dendrimer generation. Evidently, the structural changes in the conformation of the dendrimer molecules with increasing the dendrimer generation could significantly influence the characteristics of the dye-dendrimer assemblies. The lower-generation dendrimers (<G4) exhibited star-like, open molecular structures, while the medium-generation dendrimers (G4 and G5) resembled small, cross-linked polymer spheres. At higher generations (G6, G7, and G8), the dendrimers adopted nearly spherical shapes, with increasingly crowded internal structures (higher average density) and reduced molecular flexibility.

The percentage of dendrimer binding sites occupied by dye sulfonate groups per dendrimer molecule was quantitatively determined. It was calculated using the ratio of the total number of occupied sites (step 1 + step 2) determined via ITC to the theoretical number of available sites for each dendrimer generation. The results, presented in Figure 10, show that the lower-generation dendrimers (≤G5) exhibited near-complete site occupancy. This can be attributed to their high flexibility and thereby facile access of the dendrimer ionic groups for electrostatic interactions with the oppositely charged dye molecules.

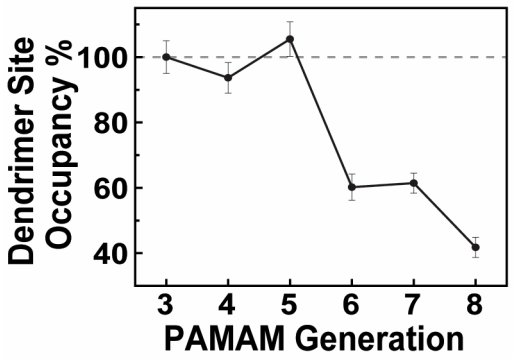


Figure 10. Dendrimer site occupancy of (primary + tertiary) dendrimer amino groups with Acid Yellow 38 dye sulfonate groups as a function of the dendrimer generation. (The value for the G4 PAMAM dendrimer was obtained from Willerich et al. [20].)

For the G6 and G7 dendrimers, the site occupancy decreased to approximately 60%, and for the G8 dendrimers, it dropped further to around 40%. This finding can be attributed to the exponential increase in the number of amino groups with increasing the dendrimer generation. The AY38 molecules could not easily penetrate the increasingly crowded interior to a large extend, and dye stacks could not easily be formed in the inside of the higher-generation dendrimers; i.e., from the point of view of electrostatic interactions, a portion of the dye molecules was left free in the solution, which could then bind by dipole-dipole interactions to other (electrostatically bound) dye molecules. It is likely that most of the primary amines (which constitute 50% of the total amine charges) and only a limited number of the tertiary amines participated in interactions with the dye ions, as suggested by the UV–vis studies. The *cis* isomer percentage was also the highest for these

mid-generation dendrimers, indicating that the bound dye ions remained readily accessible for isomerization. This suggests that the majority of the dye ions were attached to the outer branches of the dendrimers, and the dye–dye interactions did not dominate either, which minimized the photoprotective effect in these mid-generation dendrimers.

In the case of the G8 dendrimers, only about 40% of the sites were occupied by dye molecules, with additional dye molecules bound via dye.dye dipole interactions. These interactions again limited the isomerization process. Further, Figure S10 displays the dependency of the occupied dendrimer sites by dye sulfonate groups as a function of the average dendrimer density, confirming the above.

Thus, while increasing the dendrimer generation led to a rise in the number of amine groups and a potential for more electrostatic interactions with the dye molecules, the reduced flexibility of the higher-generation dendrimers restricted the dye-dendrimer interactions, promoting dye-dye interactions. This counterplay between an increased amine group availability and reduced structural flexibility is the origin of the observed generation-dependent site occupancy.

The change in the percentage of the hydrodynamic radius upon irradiation (R_H %) from the light scattering results is plotted as a function of the dendrimer site occupancy in Figure S11a. Interestingly, the change upon irradiation was highest when a smaller number of dendrimer sites were occupied, which was also linked directly with the high *cis* %. This confirms that the dye molecules bound with the dendrimer ions via a single site and/or the dye molecules involved in only dipole-dipole interactions were the major contributors to the size change upon irradiation.

As the SANS data revealed, the assembly shape also varied with the dendrimer generation and changed with photoirradiation. Upon irradiation, all the samples (except the G2 dendrimer) transitioned from spherical to ellipsoidal structures with different aspect ratios. Figure S11b represents the aspect ratio as a function of dendrimer site occupancy. Here, it is evident that the dendrimer molecules that interacted with a lower number of dye molecules formed more anisotropic structures, and the dendrimers with a high site occupancy formed less elongated ellipsoidal assemblies. It is likely that the structures with less occupied binding sites exhibited more remaining flexibility to adopt different particle shapes beyond globular structures. To understand why the elongated structures formed, it is interesting to consider the relationship between the particle shape and particle size. Remarkably, as Figure S12a,b shows, the aspect ratio of the ellipsoidal particles exhibited a direct relationship with the size of the assemblies rather than with the dendrimer generation. When the assembly size increased, the assemblies grew more anisotropically. It is likely that this was due to the charge stabilization and importance of the effective surface charge density, possibly in conjunction with other structural and density features. Certain effective surface charge densities per particle volume can rather be realized by anisotropic shapes. A direct connection between the surface charge density and the aspect ratio was observed, as shown in Figure 11. The aspect ratio increased when the effective charge density diminished (the negative value increased), i.e., the charge density was not only related to the particle size but also the particle shape. It is probable that an anisotropic shape on the nanoscale was adopted to avoid an energetically unfavorable charge-crowding (high surface charge density), as would occur for spherical particles. It is possible that the charge distribution played an additional role here. On a molecular level, this may also have been due to the anisotropy introduced through the dye dipole stacks within the structure, in addition to the above-mentioned nanoscale consideration.

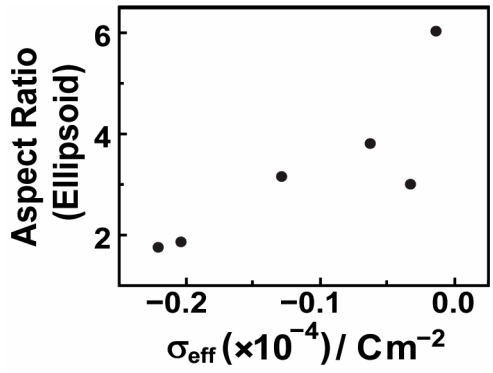


Figure 11. Nano-assembly aspect ratio obtained from SANS as function of the effective surface charge density.

5. Conclusions

In summary, we demonstrated an approach to control the size and shape of well-defined electrostatically self-assembled nanoparticles in an aqueous solution using different dendrimer generations and the dye AY38, as well as using UV light irradiation as a trigger to change the assembly structures. A complex scenario was found, where smaller assemblies were observed for small and large dendrimer generations and larger assemblies were observed for medium generations. On a molecular level, it was observed that the amount of *cis* dye depended on the dendrimer generation. We established a direct relationship between the amount of *cis* dye and the change in the size of the nanoparticles upon irradiation and elucidated the key role of the effective charge density in the size and shape control. In particular, the dendrimer generation encoded the number of dye molecules that interacted electrostatically, where electrostatics was more dominant at low generations, while secondary dipole–dipole interactions dominated at higher dendrimer generations, which is again what determines the degree of the photoprotective effect and thereby the amount of *cis* dye. This relationship may be used to predict the size increase by calculating the amount of *trans–cis* isomers in the solution based on UV-vis measurements only. Despite variations in the thermodynamic parameters (H, S, G, and K) with changing the dendrimer generation, the overall thermodynamics of these assemblies remained consistent, highlighting the robustness of the self-assembly process.

While dendrimers of different generations represent ideal model systems in this regard, the important role of molecular flexibility and charged group availability for association can be expected to be transferable to other linear and cross-linked polymer structures. As we have demonstrated a general association concept based on charges rather than specifically designed (and synthesized) binding motifs, the fundamental results will be usable in a broad field. Hence, these results are expected to be widely transferable within the versatile field of electrostatic self-assembly, combining ionic and secondary (here, dipole–dipole) interactions. Therefore, it is a potentially powerful and versatile method for producing desired assemblies with switchable sizes and shapes that could be used in various future applications.

Supplementary Materials: The following supporting information can be downloaded at: https://www.mdpi.com/article/10.3390/polym17020170/s1, Figure S1: Multiangle DLS for the dendrimers of different dendrimer generations in D_2O solution: electric field autocorrelation $g_1(\tau)$ (open circular symbols), and distribution of relaxation times $A(\tau)$ (lines) at a scattering angle of $\theta = 90°$: (**a**) G2, (**b**) G3, (**c**) G4, (**d**) G5, (**e**) G6, (**f**) G7, and (**g**) G8 (The R_H values are obtained by extrapolation to a 0° angle); Figure S2: Multiangle DLS at a charge ratio (dye charges/dendrimer charges) of $l_c = 1.5$ before (red) and after irradiation (blue): electric field autocorrelation $g_1(\tau)$ (open circular symbols), and distribution of relaxation times $A(\tau)$ (lines) at a scattering angle of $\theta = 90°$ for different dendrimer

generations: (**a**) G2, (**b**) G5, and (**c**) G7. (The R_H values are obtained by extrapolation to a 0°angle and σ represents the particle size distribution at a 90° scattering angle, $c_{AY38} = 1 \times 10^{-4}$ mol L^{-1}); Figure S3: Multiangle DLS of dendrimer-AY38 assemblies with high generation dendrimers (G6, G7, and G8) at l_c = 1.5, before irradiation: electric field autocorrelation $g_1(\tau)$ (open circular symbols), and distribution of relaxation times $A(\tau)$ (lines) at a scattering angle of $\theta = 70°$ (The R_H values are obtained by extrapolation to a 0°angle and σ represents the particle size distribution at a 90° scattering angle, $c_{AY38} = 1 \times 10^{-4}$ mol L^{-1}); Figure S4: Multiangle DLS of dendrimer-AY38 assemblies with G8 dendrimer at l_c = 1.5, before irradiation: electric field autocorrelation $g_1(\tau)$ (open circular symbols), and distribution of relaxation times $A(\tau)$ (lines) at multiple scattering angles of θ: (**a**) 40°, (**b**) 70°, (**b**) 120°, and (**b**) 150°; Figure S5: Diffusion coefficient, D as a function of the square of the scattering vector (q^2) for monomodal assemblies in AY38/G3 system before irradiation, where D is extrapolated to $q^2 = 0$ (= 0° scattering angle) to calculate the precise hydrodynamic radius of the nanoassemblies using Stokes-Einstein equation; Figure S6: Diffusion coefficient, D as a function of the square of the scattering vector (q^2) for bimodal assemblies in AY38/G7 system before irradiation: (**a**) small assemblies (observed at all the scattering angles from $\theta = 30°$ to 150° with high-intensity peak size), (**b**) large aggregates (observed only at smaller scattering angles of $\theta < 90°$, with low-intensity peak sizes), where D is extrapolated to $q^2 = 0$ (= 0° scattering angle) to calculate the precise hydrodynamic radius of the nanoassemblies using Stokes-Einstein equation; Figure S7: Generation dependence of dendrimer-dye assemblies at a constant dendrimer number concentration. (1.0×10^{-7} mol L^{-1}), for charge ratio l_c = 2.0 (**a**) R_H measured using multiangle DLS. The shaded area represents the polydispersity of the particle size. (**b**) Number concentration of the assemblies (approximated using the ratio of total scattering intensity and the volume ($4/3\ \pi\ {R_H}^3$) of the assemblies) as a function of dendrimer generation. The open red symbols represent the second species of bimodal distributions; Figure S8: SLS-SANS of AY38/G2 system at l_c = 1.5 before (red) and after irradiation (blue). The black lines represent the structural fits, corresponding to the particle shapes indicated in the plot; Figure S9: The effect of irradiation on aggregation number (the number of dendrimer units present in a particle) is calculated for dye-dendrimer assemblies at l_c = 1.5 by varying dendrimer generations using (**a**) DLS and (**b**) SANS; Figure S10: Relation between the experimental site occupancy (of Acid Yellow 38 dye sulfonate groups with primary and tertiary amines in different PAMAM generations) with the respective dendrimer molecular density. (The site occupancy for G4 PAMAM dendrimer is obtained from Willerich et al. [20]). (The dendrimer density is calculated by dividing the molar mass of the dendrimer molecules by their molecular volume [43]; Figure S11: (**a**) Percentage difference in R_H change upon irradiation and (**b**) Aspect ratio of the nano-assemblies after irradiation from SANS as function of dendrimer site occupancy; Figure S12: Further investigation of the structural control of the dendrimer-dye assemblies: (**a**) Aspect ratio of the nano-assemblies (from SANS) as function of dendrimer generation; (**b**) aspect ratio of the nano-assemblies (from SANS) as function of the hydrodynamic radius; (**c**) effective assembly charge (from the ζ-potential) as function of dendrimer generation; (**d**) effective assembly charge (from the ζ-potential) as function of the hydrodynamic radius.; Table S1: Comparison of theoretical (as given by supplier), experimental (as obtained from DLS), and R_G values (observed by Maiti et al. [43] of dendrimer radius from different PAMAM generations.; Table S2: Structural parameters obtained from SANS for dendrimer-AY38 assemblies with and PAMAM dendrimers of different generations at l_c = 1.5. All shapes were fitted using SasView 4.2.2 software with a high-quality fit ($\chi^2 \leq 3.0$).

Author Contributions: Conceptualization, R.S. and F.G.; methodology, M.A., A.Z., M.Y. and R.S.; validation, R.S. and F.G.; formal analysis, M.A.; investigation, M.A. and J.K.; resources, R.S., F.G. and J.K.; writing—original draft, M.A. and A.Z.; writing—review and editing, A.Z., M.Y., R.S., J.K. and F.G.; visualization, M.A.; supervision, R.S. and F.G.; funding acquisition, R.S. and F.G. All authors have read and agreed to the published version of the manuscript.

Funding: Funding of the Institut Laue Langevin (ILL), Grenoble, France (ILL PhD student program) and the Interdisciplinary Center for Molecular Materials (ICMM, Friedrich-Alexander-Universität Erlangen-Nürnberg) is gratefully acknowledged.

Institutional Review Board Statement: Not applicable.

Data Availability Statement: The data presented are included in this study. SANS data will be available at https://doi.ill.fr/10.5291/ILL-DATA.9-12-662, accessed on 30 November 2024.

Acknowledgments: Support by Institut Laue-Langevin (ILL) Grenoble, France, the German Science Foundation (DFG), and the interdisciplinary Center for Molecular Materials (ICMM, Universität Erlangen-Nürnberg) is gratefully acknowledged. The partnership for Soft Condensed Matter (PSCM) is thankfully acknowledged. This work benefited from the SasView 4.2.2 application, initially developed by the DANSE project under NSF award DMR-0520547.

Conflicts of Interest: The authors declare no conflicts of interest.

References

1. Rehm, T.; Schmuck, C. How to Achieve Self-Assembly in Polar Solvents Based on Specific Interactions? Some General Guidelines. *Chem. Commun.* **2008**, 801–813. [CrossRef] [PubMed]
2. Luong, D.X.; Bets, K.V.; Algozeeb, W.A.; Stanford, M.G.; Kittrell, C.; Chen, W.; Salvatierra, R.V.; Ren, M.; McHugh, E.A.; Advincula, P.A.; et al. Gram-Scale Bottom-up Flash Graphene Synthesis. *Nature* **2020**, *577*, 647–651. [CrossRef]
3. Discher, D.E.; Eisenberg, A. Polymer Vesicles. *Science* **2002**, *297*, 967–973. [CrossRef] [PubMed]
4. Liu, X.; Zhou, J.; Yu, T.; Chen, C.; Cheng, Q.; Sengupta, K.; Huang, Y.; Li, H.; Liu, C.; Wang, Y.; et al. Adaptive Amphiphilic Dendrimer-Based Nanoassemblies as Robust and Versatile SiRNA Delivery Systems. *Angew. Chem. Int. Ed.* **2014**, *53*, 11822–11827. [CrossRef] [PubMed]
5. Honnigfort, C.; Campbell, R.A.; Droste, J.; Gutfreund, P.; Hansen, M.R.; Ravoo, B.J.; Braunschweig, B. Unexpected Monolayer-to-Bilayer Transition of Arylazopyrazole Surfactants Facilitates Superior Photo-Control of Fluid Interfaces and Colloids. *Chem. Sci.* **2020**, *11*, 2085–2092. [CrossRef] [PubMed]
6. Tazawa, T.; Yagai, S.; Kikkawa, Y.; Karatsu, T.; Kitamura, A.; Ajayaghosh, A. A Complementary Guest Induced Morphology Transition in a Two-Component Multiple H-Bonding Self-Assembly. *Chem. Commun.* **2010**, *46*, 1076–1078. [CrossRef]
7. Faul, C.F.J.; Antonietti, M. Facile Synthesis of Optically Functional, Highly Organized Nanostructures: Dye-Surfactant Complexes. *Chem.–A Eur. J.* **2002**, *8*, 2764–2768. [CrossRef]
8. Grzelczak, M.; Vermant, J.; Furst, E.M.; Liz-marza, L.M. Directed Self-Assembly of Nanoparticles. *ACS Nano* **2010**, *4*, 3591–3605. [CrossRef]
9. Willerich, I.; Li, Y.; Gröhn, F. Influencing Particle Size and Stability of Ionic Dendrimer-Dye Assemblies. *J. Phys. Chem. B* **2010**, *114*, 15466–15476. [CrossRef]
10. Faul, C.F.J. Ionic Self-Assembly for Functional Hierarchical Nanostructured Materials. *Acc. Chem. Res.* **2014**, *47*, 3428–3438. [CrossRef]
11. Grzybowski, B.A.; Winkleman, A.; Wiles, J.A.; Brumer, Y.; Whitesides, G.M. Electrostatic Self-Assembly of Macroscopic Crystals Using Contact Electrification. *Nat. Mater.* **2003**, *2*, 241–245. [CrossRef]
12. Willerich, I.; Gröhn, F. Photoswitchable Nanoassemblies by Electrostatic Self-Assembly. *Angew. Chem. Int. Ed.* **2010**, *49*, 8104–8108. [CrossRef] [PubMed]
13. Kostiainen, M.A.; Hiekkataipale, P.; Laiho, A.; Lemieux, V.; Seitsonen, J.; Ruokolainen, J.; Ceci, P. Electrostatic Assembly of Binary Nanoparticle Superlattices Using Protein Cages. *Nat. Nanotechnol.* **2013**, *8*, 52–56. [CrossRef]
14. Liljeström, V.; Mikkilä, J.; Kostiainen, M.A. Self-Assembly and Modular Functionalization of Three-Dimensional Crystals from Oppositely Charged Proteins. *Nat. Commun.* **2014**, *5*, 4445. [CrossRef] [PubMed]
15. Li, S.; Moosa, B.A.; Croissant, J.G.; Khashab, N.M. Electrostatic Assembly/Disassembly of Nanoscaled Colloidosomes for Light-Triggered Cargo Release. *Angew. Chem. Int. Ed.* **2015**, *54*, 6804–6808. [CrossRef]
16. Krieger, A.; Zika, A.; Gröhn, F. Functional Nano-Objects by Electrostatic Self-Assembly: Structure, Switching, and Photocatalysis. *Front. Chem.* **2022**, *9*, 779360. [CrossRef]
17. Li, L.; Wu, R.; Guang, S.; Su, X.; Xu, H. The Investigation of the Hydrogen Bond Saturation Effect during the Dipole-Dipole Induced Azobenzene Supramolecular Self-Assembly. *Phys. Chem. Chem. Phys.* **2013**, *15*, 20753–20763. [CrossRef]
18. Sun, P.; Li, L.; Guang, S.; Xu, H. The Investigation of the Dipole-Dipole Action Direction and Molecular Space Configuration Effect during the Dipole–Dipole Induced Azobenzene Supramolecular Self-Assembly. *Colloids Surf. A Physicochem. Eng. Asp.* **2019**, *580*, 123742. [CrossRef]
19. Agarwal, M.; Zika, A.; Schweins, R.; Gröhn, F. Controlling the Morphology in Electrostatic Self-Assembly via Light. *Polymers* **2023**, *16*, 50. [CrossRef] [PubMed]
20. Willerich, I.; Gröhn, F. Thermodynamics of Photoresponsive Polyelectrolyte-Dye Assemblies with Irradiation Wavelength Triggered Particle Size. *Macromolecules* **2011**, *44*, 4452–4461. [CrossRef]

21. Mariani, G.; Moldenhauer, D.; Schweins, R.; Gröhn, F. Elucidating Electrostatic Self-Assembly: Molecular Parameters as Key to Thermodynamics and Nanoparticle Shape. *J. Am. Chem. Soc.* **2016**, *138*, 1280–1293. [CrossRef] [PubMed]
22. Mariani, G.; Krieger, A.; Moldenhauer, D.; Schweins, R.; Gröhn, F. Light-Responsive Shape: From Micrometer-Long Nanocylinders to Compact Particles in Electrostatic Self-Assembly. *Macromol. Rapid Commun.* **2018**, *39*, 1700860. [CrossRef]
23. Park, J.; Sun, L.B.; Chen, Y.P.; Perry, Z.; Zhou, H.C. Azobenzene-Functionalized Metal-Organic Polyhedra for the Optically Responsive Capture and Release of Guest Molecules. *Angew. Chem. Int. Ed.* **2014**, *53*, 5842–5846. [CrossRef] [PubMed]
24. Qi, Z.; Schalley, C.A. Exploring Macrocycles in Functional Supramolecular Gels: From Stimuli Responsiveness to Systems Chemistry. *Acc. Chem. Res.* **2014**, *47*, 2222–2233. [CrossRef]
25. Engel, S.; Möller, N.; Stricker, L.; Peterlechner, M.; Ravoo, B.J. A Modular System for the Design of Stimuli-Responsive Multifunctional Nanoparticle Aggregates by Use of Host–Guest Chemistry. *Small* **2018**, *14*, 1704287. [CrossRef] [PubMed]
26. Willerich, I.; Gröhn, F. Switchable Nanoassemblies from Macroions and Multivalent Dye Counterions. *Chem.–A Eur. J.* **2008**, *14*, 9112–9116. [CrossRef] [PubMed]
27. Willerich, I.; Gröhn, F. Molecular Structure Encodes Nanoscale Assemblies: Understanding Driving Forces in Electrostatic Self-Assembly. *J. Am. Chem. Soc.* **2011**, *133*, 20341–20356. [CrossRef] [PubMed]
28. Kundu, P.K.; Samanta, D.; Leizrowice, R.; Margulis, B.; Zhao, H.; Börner, M.; Udayabhaskararao, T.; Manna, D.; Klajn, R. Light-Controlled Self-Assembly of Non-Photoresponsive Nanoparticles. *Nat. Chem.* **2015**, *7*, 646–652. [CrossRef]
29. Wang, L.; Li, Q. Photochromism into Nanosystems: Towards Lighting up the Future Nanoworld. *Chem. Soc. Rev.* **2018**, *47*, 1044–1097. [CrossRef]
30. Ikeda, T.; Mamiya, J.I.; Yu, Y. Photomechanics of Liquid-Crystalline Elastomers and Other Polymers. *Angew. Chem. Int. Ed.* **2007**, *46*, 506–528. [CrossRef]
31. Koga, T.; Ushirogochi, M.; Higashi, N. Regulation of Self-Assembling Process of a Cationic β-Sheet Peptide by Photoisomerization of an Anionic Azobenzene Derivative. *Polym. J.* **2007**, *39*, 16–17. [CrossRef]
32. Ghoreishi, S.M.; Behpour, M.; Shabani-Nooshabadi, M. Interaction of Anionic Azo Dye and TTAB—Cationic Surfactant. *J. Braz. Chem. Soc.* **2009**, *20*, 460–465. [CrossRef]
33. Percec, V.; Rudick, J.G.; Peterca, M.; Wagner, M.; Obata, M.; Mitchell, C.M.; Cho, W.D.; Balagurusamy, V.S.K.; Heiney, P.A. Thermoreversible Cis-Cisoidal to Cis-Transoidal Isomerization of Helical Dendronized Polyphenylacetylenes. *J. Am. Chem. Soc.* **2005**, *127*, 15257–15264. [CrossRef] [PubMed]
34. Grzybowski, B.A.; Wilmer, C.E.; Kim, J.; Browne, K.P.; Bishop, K.J.M. Self-Assembly: From Crystals to Cells. *Soft Matter* **2009**, *5*, 1110–1128. [CrossRef]
35. Guo, Y.; Gong, Y.; Gao, Y.; Xiao, J.; Wang, T.; Yu, L. Multi-Stimuli Responsive Supramolecular Structures Based on Azobenzene Surfactant-Encapsulated Polyoxometalate. *Langmuir* **2016**, *32*, 9293–9300. [CrossRef] [PubMed]
36. Xie, X.; Wang, L.; Liu, X.; Du, Z.; Li, Y.; Li, B.; Wu, L.; Li, W. Light-Powered and Transient Peptide Two-Dimensional Assembly Driven by: Trans -to- Cis Isomerization of Azobenzene Side Chains. *Chem. Commun.* **2020**, *56*, 1867–1870. [CrossRef]
37. Fathalla, M.; Sinatra, L. PH-Responsive Porphyrin-Silica Nanoparticles Conjugate via Ionic Self-Assembly. *J. Porous Mater.* **2021**, *28*, 183–189. [CrossRef]
38. Fischer, W.; Quadir, M.A.; Barnard, A.; Smith, D.K.; Haag, R. Controlled Release of DNA from Photoresponsive Hyperbranched Polyglycerols with Oligoamine Shells. *Macromol. Biosci.* **2011**, *11*, 1736–1746. [CrossRef] [PubMed]
39. Markiewicz, G.; Pakulski, D.; Galanti, A.; Patroniak, V.; Ciesielski, A.; Stefankiewicz, A.R.; Samorì, P. Photoisomerisation and Light-Induced Morphological Switching of a Polyoxometalate-Azobenzene Hybrid. *Chem. Commun.* **2017**, *53*, 7278–7281. [CrossRef] [PubMed]
40. Tomalia, D.A.; Naylor, A.M.; Goddard, W.A. Starburst Dendrimers: Molecular-Level Control of Size, Shape, Surface Chemistry, Topology, and Flexibility from Atoms to Macroscopic Matter. *Angew. Chem. Int. Ed. Engl.* **1990**, *29*, 138–175. [CrossRef]
41. Prosa, T.J.; Bauer, B.J.; Amis, E.J.; Tomalia, D.A.; Scherrenberg, R. A SAXS Study of the Internal Structure of Dendritic Polymer Systems. *J. Polym. Sci. Part B Polym. Phys.* **1997**, *35*, 2913–2924. [CrossRef]
42. Maiti, P.K.; Çağin, T.; Wang, G.; Goddard, W.A. Structure of PAMAM Dendrimers: Generations 1 through 11. *Macromolecules* **2004**, *37*, 6236–6254. [CrossRef]
43. Tomalia, D.A. Dendritic Effects: Dependency of Dendritic Nano-Periodic Property Patterns on Critical Nanoscale Design Parameters (CNDPs). *New J. Chem.* **2012**, *36*, 264–281. [CrossRef]
44. Gröhn, F.; Bauer, B.J.; Akpalu, Y.A.; Jackson, C.L.; Amis, E.J. Dendrimer Templates for the Formation of Gold Nanoclusters. *Macromolecules* **2000**, *33*, 6042–6050. [CrossRef]
45. Katsoulis, D.; Argyrakis, P.; Pimenov, A.; Vitukhnovsky, A. Diffusion and Trapping in Dendrimer Structures. *Chem. Phys.* **2002**, *275*, 261–269. [CrossRef]
46. Lorén, N.; Shtykova, L.; Kidman, S.; Jarvoll, P.; Nyden, M.; Hermansson, A.M. Dendrimer Diffusion in κ-Carrageenan Gel Structures. *Biomacromolecules* **2009**, *10*, 275–284. [CrossRef]

47. Willerich, I.; Schindler, T.; Gröhn, F. Effect of Polyelectrolyte Architecture and Size on Macroion-Dye Assemblies. *J. Phys. Chem. B* **2011**, *115*, 9710–9719. [CrossRef]
48. Tomalia, D.A.; Baker, H.; Hall, M.; Kallos, G.; Martin, S.; Ryder, J.; Smith, P. Dendritic Macromolecules:1 Synthesis of Starburst Dendrimers. *Macromolecules* **1986**, *19*, 2466–2468. [CrossRef]
49. Robinson, C.; Mills, H.A.T. The Colloid Chemistry of Dyes: The Aqueous Solutions of Benzopurpurine 4B and Its Isomer Prepared from m-Tolidine. Part I. *Proc. R. Soc. London. Ser. A* **1931**, *131*, 576–595.
50. Krężel, A.; Bal, W. A Formula for Correlating PKa Values Determined in D_2O and H_2O. *J. Inorg. Biochem.* **2004**, *98*, 161–166. [CrossRef] [PubMed]
51. Schärtl, W. *Light Scattering from Polymer Solutions and Nanoparticle Dispersions*; Springer: Berlin/Heidelberg, Germany, 2007; pp. 1–24, ISBN 9783540719519.
52. Provencher, S.W. A Constrained Regularization Method for Inverting Data Represented by Linear Algebraic or Integral Equations. *Comput. Phys. Commun.* **1982**, *27*, 213–227. [CrossRef]
53. Provencher, S.W. Contin: A General Purpose Constrained Regularization Program for Inverting Noisy Linear Algebraic and Integral Equations. *Comput. Phys. Commun.* **1982**, *27*, 229–242. [CrossRef]
54. Zimm, B.H. The Scattering of Light and the Radial Distribution Function of High Polymer Solutions. *J. Chem. Phys.* **1948**, *16*, 1093–1099. [CrossRef]
55. Guinier, A.; Fournet, G.; Walker, C.B.; Yudowitch, K.L. *Small Angle Scattering of X-Rays*; Wiley: New York, NY, USA, 1955; Volume 594.
56. Arnold, O.; Bilheux, J.C.; Borreguero, J.M.; Buts, A.; Campbell, S.I.; Chapon, L.; Doucet, M.; Draper, N.; Ferraz Leal, R.; Gigg, M.A.; et al. Mantid—Data Analysis and Visualization Package for Neutron Scattering and μ SR Experiments. *Nucl. Instrum. Methods Phys. Res. Sect. A Accel. Spectrometers Detect. Assoc. Equip.* **2014**, *764*, 156–166. [CrossRef]
57. Feigin, L.A.; Svergun, D.I. *Structure Analysis by Small-Angle X-Ray and Neutron Scattering*; Plenum Press: New York, NY, USA, 1987.
58. Onsager, L. The Effects of Shape on the Interaction of Colloidal Particles. *Ann. N. Y. Acad. Sci.* **1949**, *51*, 627–659. [CrossRef]
59. Pedersen, J.S. Analysis of Small-Angle Scattering Data from Colloids and Polymer Solutions: Modeling and Least-Squares Fitting. *Adv. Colloid Interface Sci.* **1997**, *70*, 171–210. [CrossRef]
60. Isihara, A. Determination of Molecular Shape by Osmotic Measurement. *J. Chem. Phys.* **1950**, *18*, 1446–1449. [CrossRef]
61. Smoluchowski, M.V. Molekular-Kinetische Theorie Der Opaleszenz von Gasen Im Kritischen Zustande, Sowie Einiger Verwandter Erscheinungen. *Ann. Phys.* **1908**, *330*, 205–226. [CrossRef]
62. Polaczyk, A.L.; Amburgey, J.E.; Alansari, A.; Poler, J.C.; Propato, M.; Hill, V.R. Calculation and Uncertainty of Zeta Potentials of Microorganisms in a 1:1 Electrolyte with a Conductivity Similar to Surface Water. *Colloids Surf. A Physicochem. Eng. Asp.* **2020**, *586*, 124097. [CrossRef]
63. Kadu, P.J.; Kushare, S.S.; Thacker, D.D.; Gattani, S.G. Enhancement of Oral Bioavailability of Atorvastatin Calcium by Self-Emulsifying Drug Delivery Systems (SEDDS). *Pharm. Dev. Technol.* **2011**, *16*, 65–74. [CrossRef] [PubMed]
64. Zika, A.; Agarwal, M.; Schweins, R.; Gröhn, F. Joining Two Switches in One Nano-object: Photoacidity and Photoisomerization in Electrostatic Self-assembly. *Chem.–A Eur. J.* **2022**, *29*, e202203373. [CrossRef] [PubMed]
65. Sinn, C.G.; Dimova, R.; Antonietti, M. Isothermal Titration Calorimetry of the Polyelectrolyte/Water Interaction and Binding of Ca^{2+}: Effects Determining the Quality of Polymeric Scale Inhibitors. *Macromolecules* **2004**, *37*, 3444–3450. [CrossRef]
66. Gummel, J.; Cousin, F.; Boué, F. Counterions Release from Electrostatic Complexes of Polyelectrolytes and Proteins of Opposite Charge: A Direct Measurement. *J. Am. Chem. Soc.* **2007**, *129*, 5806–5807. [CrossRef] [PubMed]
67. Fu, J.; Schlenoff, J.B. Driving Forces for Oppositely Charged Polyion Association in Aqueous Solutions: Enthalpic, Entropic, but Not Electrostatic. *J. Am. Chem. Soc.* **2016**, *138*, 980–990. [CrossRef]

Disclaimer/Publisher's Note: The statements, opinions and data contained in all publications are solely those of the individual author(s) and contributor(s) and not of MDPI and/or the editor(s). MDPI and/or the editor(s) disclaim responsibility for any injury to people or property resulting from any ideas, methods, instructions or products referred to in the content.

Supporting Information

The Role of Light-Irradiation and Dendrimer Generation in Directing Electrostatic Self-Assembly

Mohit Agarwal [1,2], Alexander Zika [1], Müge Yücel [1], Ralf Schweins [2], Joachim Kohlbrecher [3], and Franziska Gröhn[1,*]

Additional Results:

Figure S1 shows the sizes of the PAMAM dendrimers of different generations measured in D_2O as solvent. Multiangle DLS is used to determine the dendrimer size in solution. The concentration of the dendrimer solution was 1.0×10^{-6} mol L^{-1} for all samples. All dendrimer generations yield monomodal distributions. The resulting sizes are in agreement with the simulated values as given in Table S1.

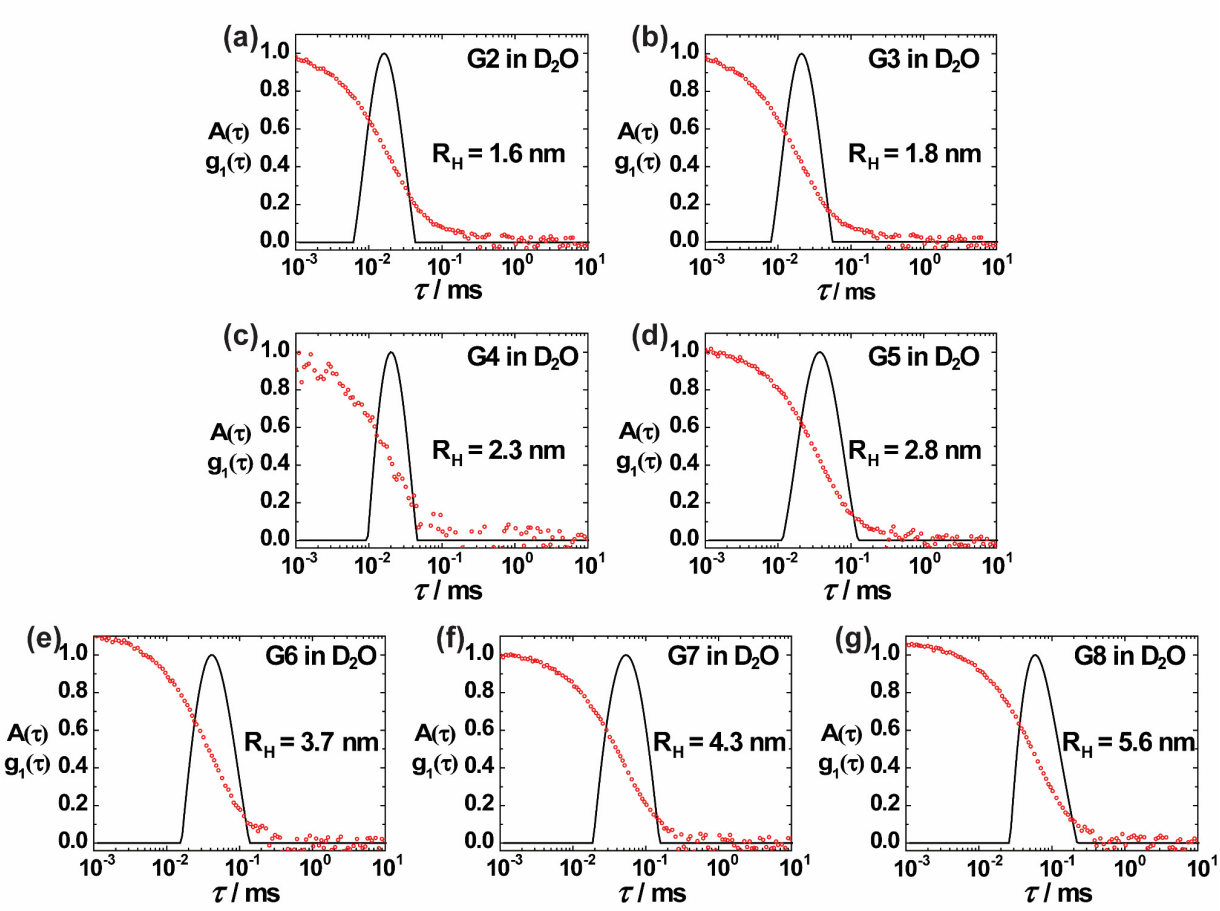


Figure S1 Multi-angle DLS for the dendrimers of different dendrimer generations in D_2O solution: electric field autocorrelation $g_1(\tau)$ (open circular symbols), and distribution of relaxation times $A(\tau)$ (lines) at a scattering angle of $\theta = 90°$: **(a)** G2, **(b)** G3, **(c)** G4, **(d)** G5, **(e)** G6, **(f)** G7, and **(g)** G8 (The R_H values are obtained by extrapolation to a 0° angle).

Table S1 Comparison of theoretical (as given by supplier), experimental (as obtained from DLS), and R_G values (observed by *Maiti et al*. [43] of dendrimer radius from different PAMAM generations.

Dendrimer Generation	**G2**	**G3**	**G4**	**G5**	**G6**	**G7**	**G8**

Theoretical radius/nm	1.5	1.8	2.3	2.7	3.4	4.1	4.9
Experimental Size(R_H)/nm	1.6	1.8	2.3	2.8	3.7	4.3	5.6
R_G/nm	0.9	1.1	1.5	1.8	2.2	2.9	3.6

In Figure S2, electric field autocorrelation functions $g_1(\tau)$ are plotted with their corresponding relaxation of distribution times $A(\tau)$ at a 90° angle obtained from the dynamic light scattering instrument for dye-dendrimer assemblies at I_c = 1.5. Different generations of PAMAM dendrimers (G2, G5, and G7) were used.

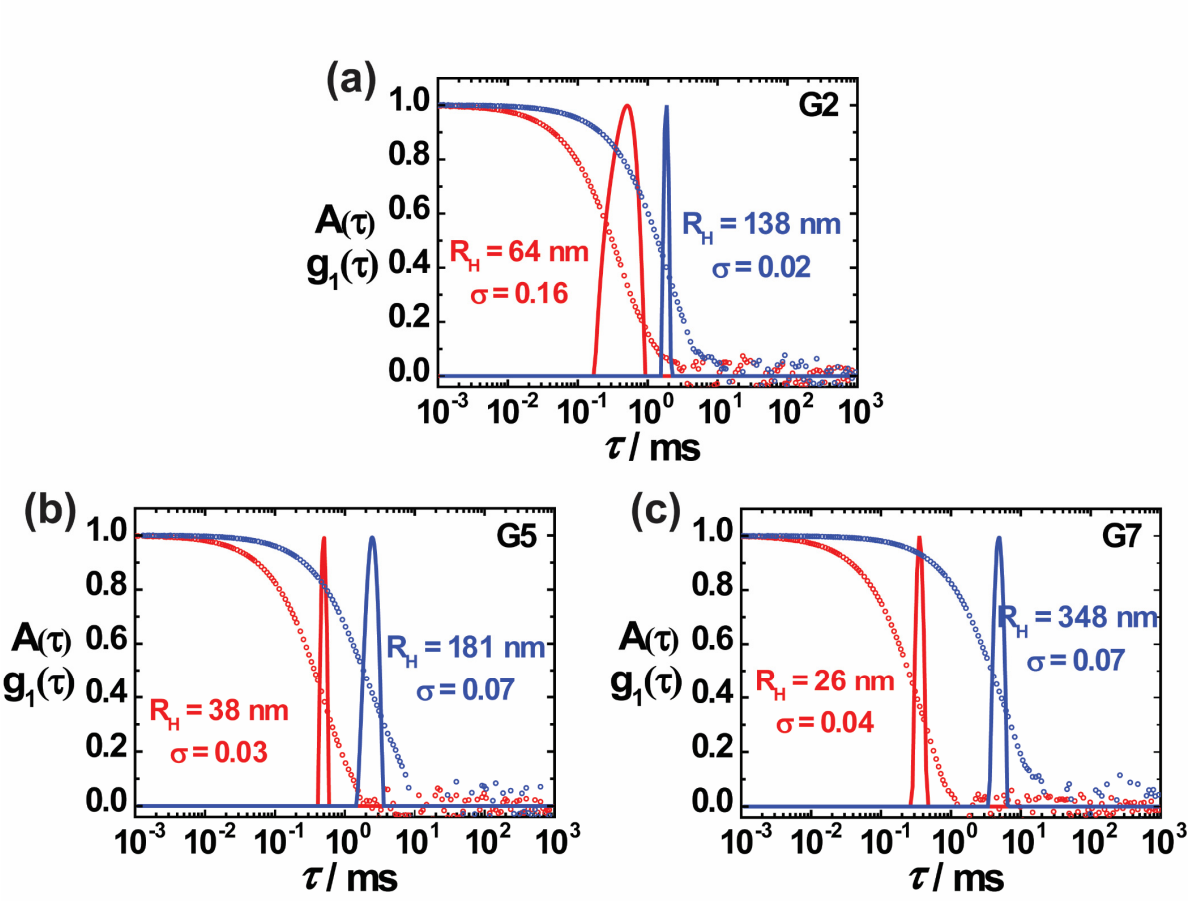


Figure S2 Multi-angle DLS at a charge ratio (dye charges/dendrimer charges) of I_c = 1.5 before (red) and after irradiation (blue): electric field autocorrelation $g_1(\tau)$ (open circular symbols), and

distribution of relaxation times $A(\tau)$ (lines) at a scattering angle of $\theta = 90°$ for different dendrimer generations: **(a)** G2, **(b)** G5, and **(c)** G7. (The R_H values are obtained by extrapolation to a 0°angle and σ represents the particle size distribution at a 90° scattering angle, $c_{AY38} = 1 \times 10^{-4}$ mol L^{-1}).

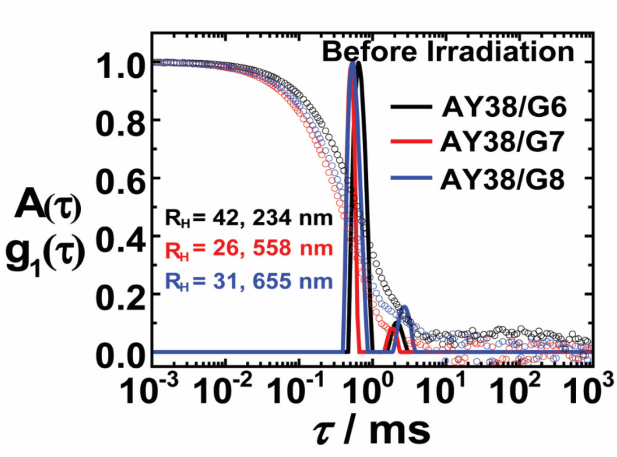


Figure S3 Multi-angle DLS of dendrimer-AY38 assemblies with high generation dendrimers (G6, G7, and G8) at I_c = 1.5, before irradiation: electric field autocorrelation $g_1(\tau)$ (open circular symbols), and distribution of relaxation times $A(\tau)$ (lines) at a scattering angle of $\theta = 70°$ (The R_H values are obtained by extrapolation to a 0°angle and σ represents the particle size distribution at a 90° scattering angle, $c_{AY38} = 1 \times 10^{-4}$ mol L^{-1}).

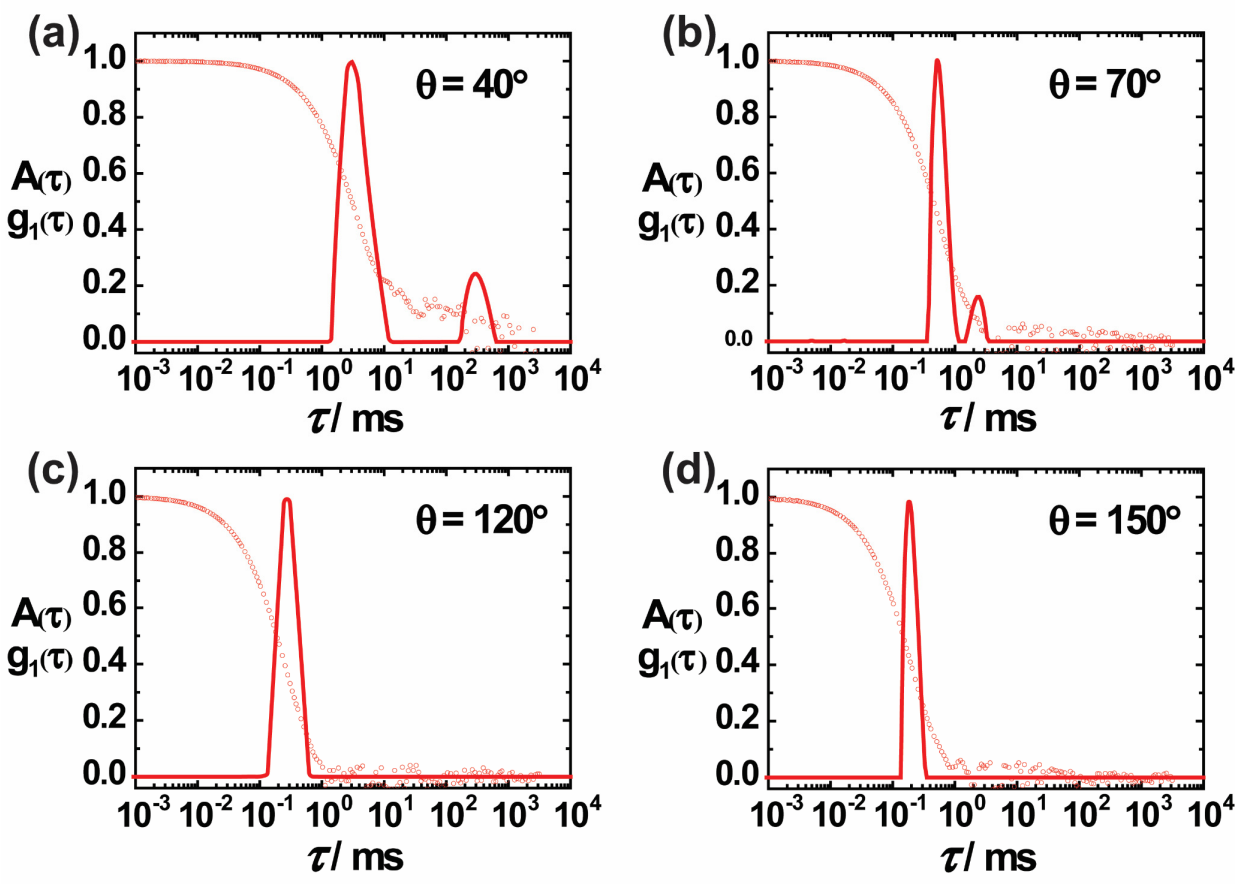


Figure S4 Multiangle DLS of dendrimer-AY38 assemblies with G8 dendrimer at I_c = 1.5, before irradiation: electric field autocorrelation $g_1(\tau)$ (open circular symbols), and distribution of relaxation times $A(\tau)$ (lines) at multiple scattering angles of θ: **(a)** 40°, **(b)** 70°, **(b)** 120°, and **(b)** 150°.

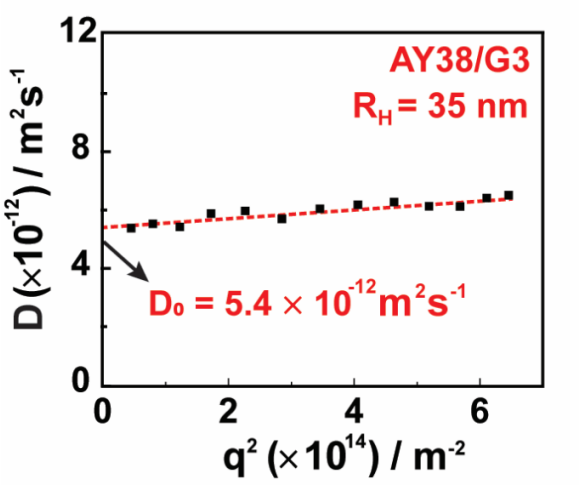


Figure S5 Diffusion coefficient, *D* as a function of the square of the scattering vector (q^2) for monomodal assemblies in AY38/G3 system before irradiation, where *D* is extrapolated to $q^2 = 0$ (= 0° scattering angle) to calculate the precise hydrodynamic radius of the nanoassemblies using Stokes-Einstein equation.

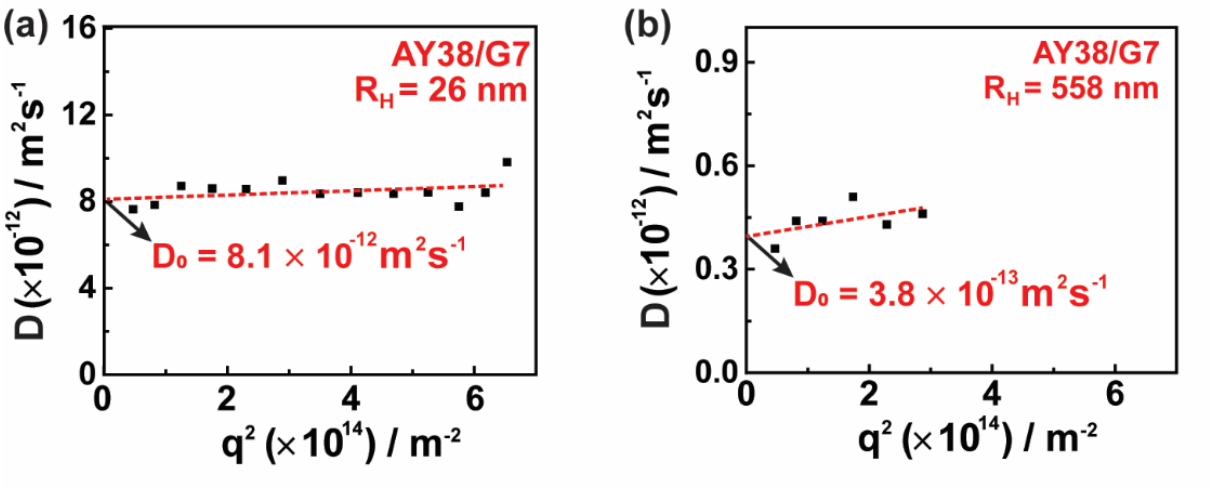


Figure S6 Diffusion coefficient, D as a function of the square of the scattering vector (q^2) for bimodal assemblies in AY38/G7 system before irradiation: **(a)** small assemblies (observed at all the scattering angles from θ = 30° to 150° with high-intensity peak size), **(b)** large aggregates (observed only at smaller scattering angles of θ < 90°, with low-intensity peak sizes), where D is extrapolated to $q^2 = 0$ (= 0° scattering angle) to calculate the precise hydrodynamic radius of the nanoassemblies using Stokes-Einstein equation.

A different study is conducted at I_c = 2.0, where the molar dendrimer concentration is kept constant at 1.0×10^{-7} mol L^{-1}. Different dendrimer generations and light irradiation show similar patterns as for the experiments with constant ass concentration (Figure S7). There is a difference in aggregate size (± 10 - 20%) observed in this case; still, the pattern remains identical, and the G6 dendrimer shows the most prominent size change upon irradiation. No significant size change occurs due to irradiation in the case of dendrimer excess, as reported in the literature [12].

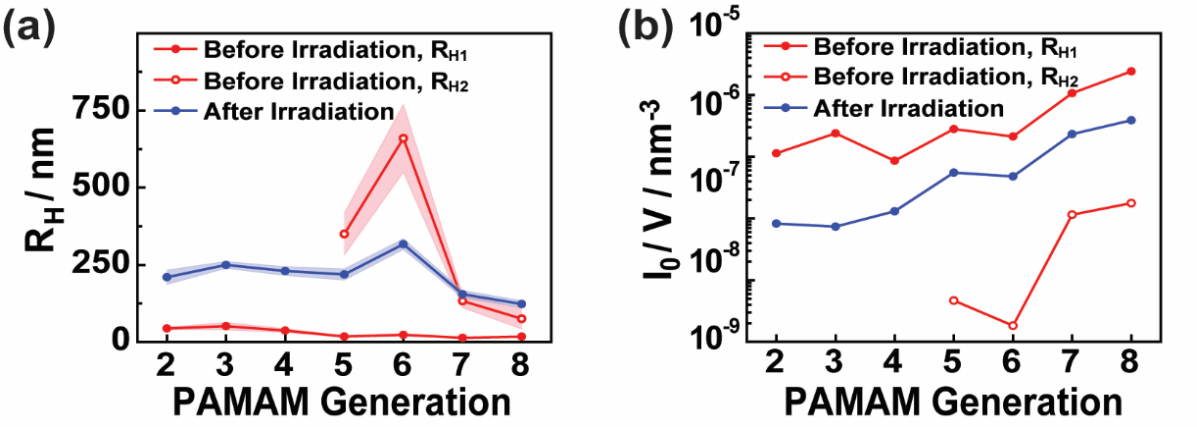


Figure S7 Generation dependence of dendrimer-dye assemblies at a constant dendrimer number concentration. (1.0×10^{-7} mol L^{-1}), for charge ratio I_c = 2.0 **(a)** R_H measured using multiangle DLS. The shaded area represents the polydispersity of the particle size. **(b)** Number concentration of the assemblies (approximated using the ratio of total scattering intensity and the volume ($4/3\ \pi\ R_H^3$) of the assemblies) as a function of dendrimer generation. The open red symbols represent the second species of bimodal distributions.

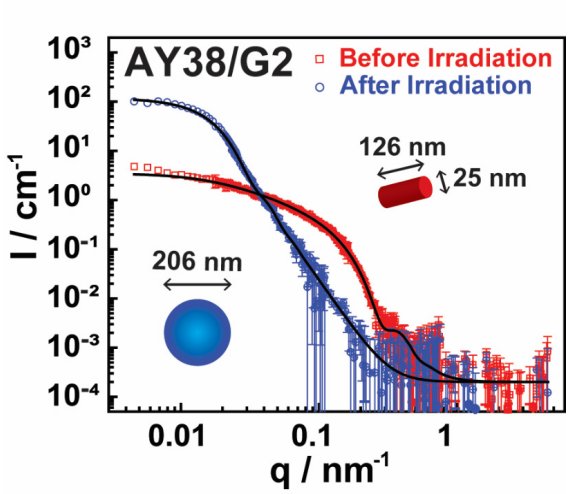


Figure S8 SLS-SANS of AY38/G2 system at I_c = 1.5 before (red) and after irradiation (blue). The black lines represent the structural fits, corresponding to the particle shapes indicated in the plot.

Table S2 Structural parameters obtained from SANS for dendrimer- AY38 assemblies with and PAMAM dendrimers of different generations at I_c = 1.5. All shapes were fitted using SasView 4.2.2 software with a high-quality fit ($\chi^2 \leq 3.0$).

System	Irradiation Condition	Shape	Cross section		Length /nm	Aspect Ratio
			R_{min} / nm	R_{maj} / nm		
AY38 + G2	Before	Cylinder	13 ± 2		126 ± 11	4.8
	After	Sphere	103 ± 6			1.0
AY38 + G3	Before	Sphere	26 ± 3			1.0
	After	Ellipsoid	91 ± 12	270 ± 22		2.9
AY38 + G4	Before	Sphere	29 ± 1			1.0
	After	Ellipsoid	92 ± 8	160 ± 14		1.7
AY38 + G5	Before	Sphere	283 ± 3			1.0
	After	Ellipsoid	95 ± 7	177 ± 15		1.8
AY38 + G6	Before	Sphere	30 ± 2			1.0
	After	Ellipsoid	100 ± 6	603 ± 48		6.0
AY38 + G7	Before	Sphere	20 ± 2			1.0
	After	Ellipsoid	113 ± 11	427 ± 34		3.8
AY38 + G8	Before	Sphere	19 ± 1			1.0
	After	Ellipsoid	90 ± 5	283 ± 24		3.1

The size of the assemblies varies depending on the dendrimer generations. Therefore, it is crucial to calculate the aggregation number of dendrimers within a single nanoparticle. From the results of light scattering, all the particles are assumed to be spherical, and the volume of the particles was calculated using the volume of a sphere. The aggregation number was calculated using the volume of the assembled particle divided by a sphere volume with a diameter of a single dendrimer molecule plus the extension of a bound dye molecule (Figure S9a). Further, the particle volumes were calculated from the SANS structural fit results; i.e. considering the particle shapes (Figure S9b) Both measurements

show the decay in aggregation number while increasing the charge ratio, which differs after irradiation.

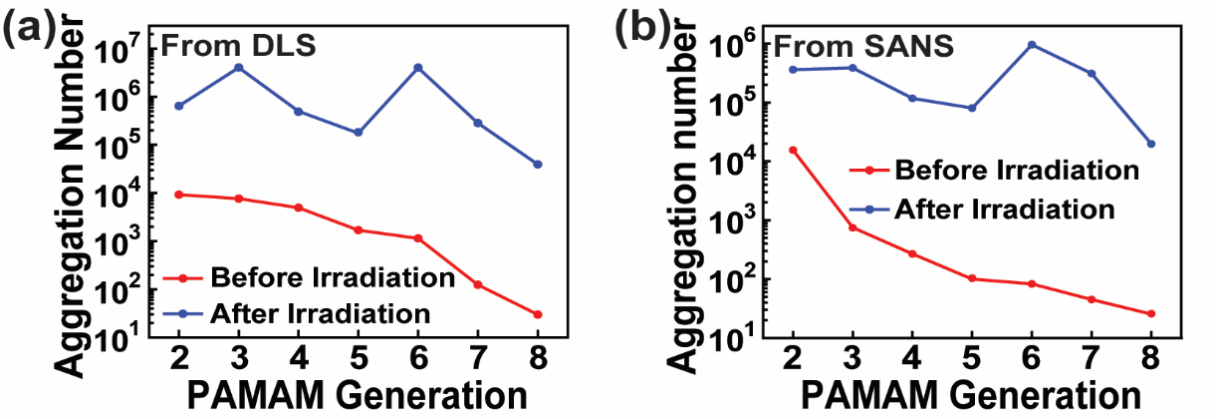


Figure S9 The effect of irradiation on aggregation number (the number of dendrimer units present in a particle) is calculated for dye-dendrimer assemblies at I_c = 1.5 by varying dendrimer generations using **(a)** DLS and **(b)** SANS.

To understand the electrostatic properties further, the effective surface charge density σ_{eff} and effective charge Q_{eff} are of interest in addition to the measured ζ-potential itself. To receive the σ_{eff}, the following equation is used:

$$\sigma_{eff} = \frac{Q_{eff}}{S_{assembly}} = \frac{4\pi\varepsilon\zeta R_{eff}}{4\pi R_{eff}^2} = \frac{\varepsilon\zeta}{R_{eff}} \approx \frac{\varepsilon\zeta}{R_H} \qquad \textbf{(S1)}$$

Where Q_{eff} is the effective surface charge, $S_{assembly}$ is the assembly surface, ε is the permittivity constant, and R_{eff} is the effective radius, approximated as the hydrodynamic radius, R_H. High σ_{eff} values refer to densely charged particles.

Further, the dendrimer site occupancy can be determines. The number of occupied binding sites, i.e. the sum of the two binding site numbers two-site model in ITC, is divided

by the total number of dendrimer binding sites theoretically available for dye interactions, i.e. the number of dendrimer amine groups.

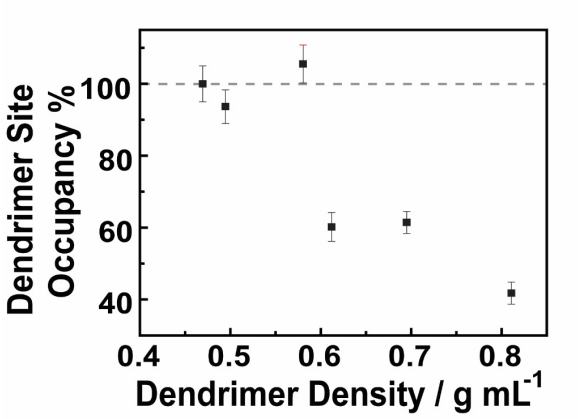


Figure S10 Relation between the experimental site occupancy (of Acid Yellow 38 dye sulfonate groups with primary and tertiary amines in different PAMAM generations) with the respective dendrimer molecular density. (The site occupancy for G4 PAMAM dendrimer is obtained from *Willerich et al.* [20]). (The dendrimer density is calculated by dividing the molar mass of the dendrimer molecules by their molecular volume [43]

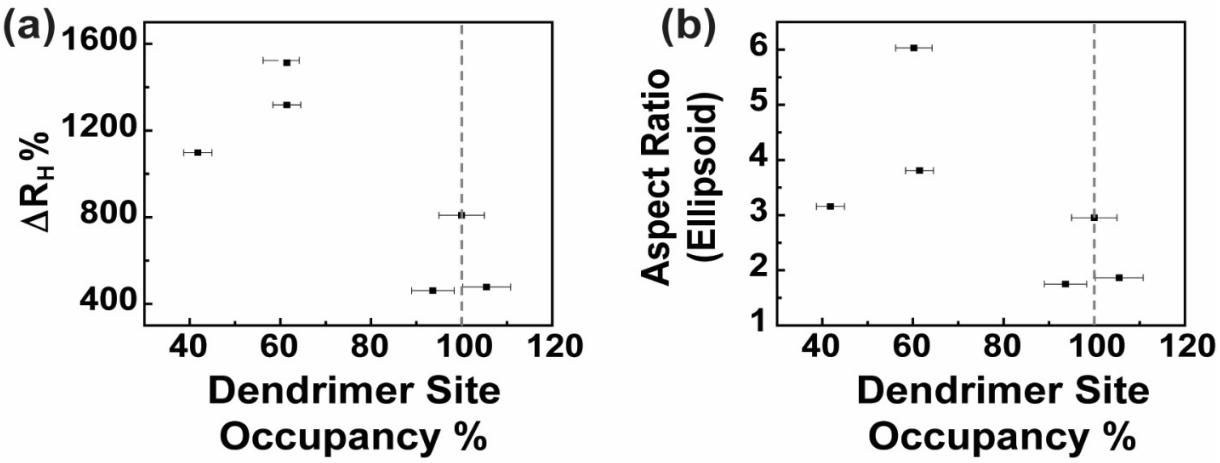


Figure S11 (a) Percentage difference in R_H change upon irradiation and **(b)** Aspect ratio of the nano-assemblies after irradiation from SANS as function of dendrimer site occupancy

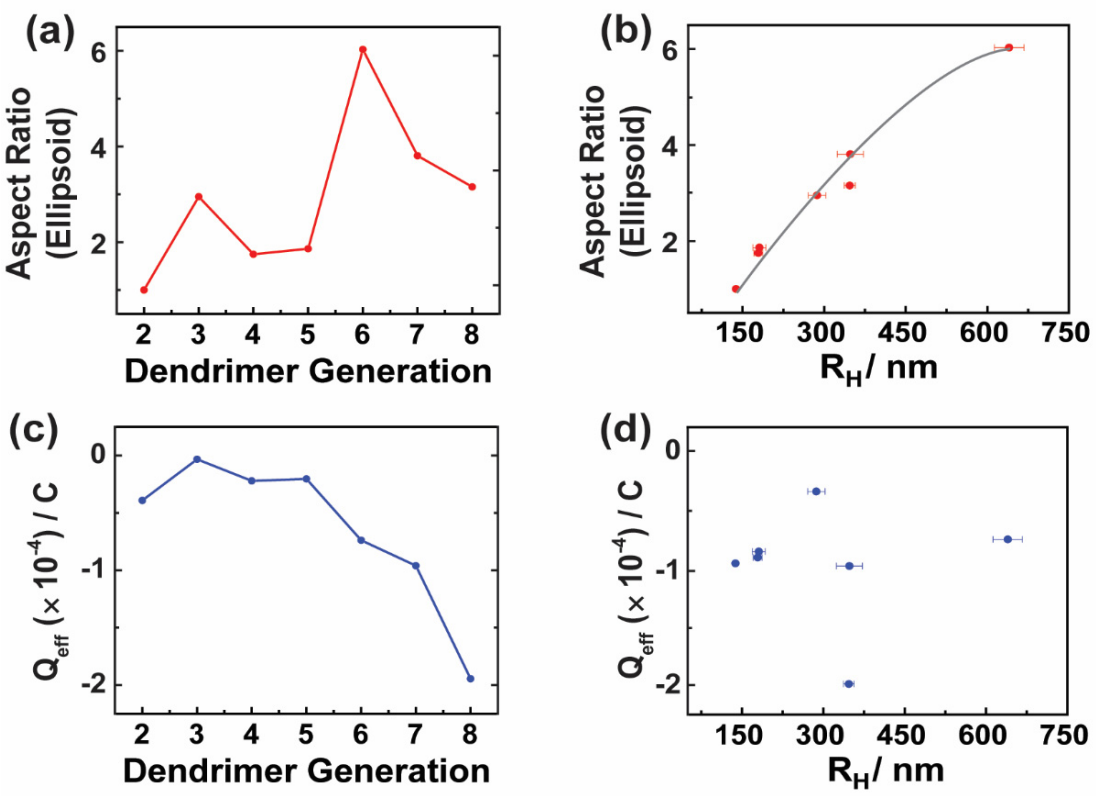


Figure S12 Further investigation of the structural control of the dendrimer-dye assemblies: **(a)** Aspect ratio of the nano-assemblies (from SANS) as function of dendrimer generation; **(b)** aspect ratio of the nano-assemblies (from SANS) as function of the hydrodynamic radius; **(c)** effective assembly charge (from the ζ-potential) as function of dendrimer generation; **(d)** effective assembly charge (from the ζ-potential) as function of the hydrodynamic radius.

References:

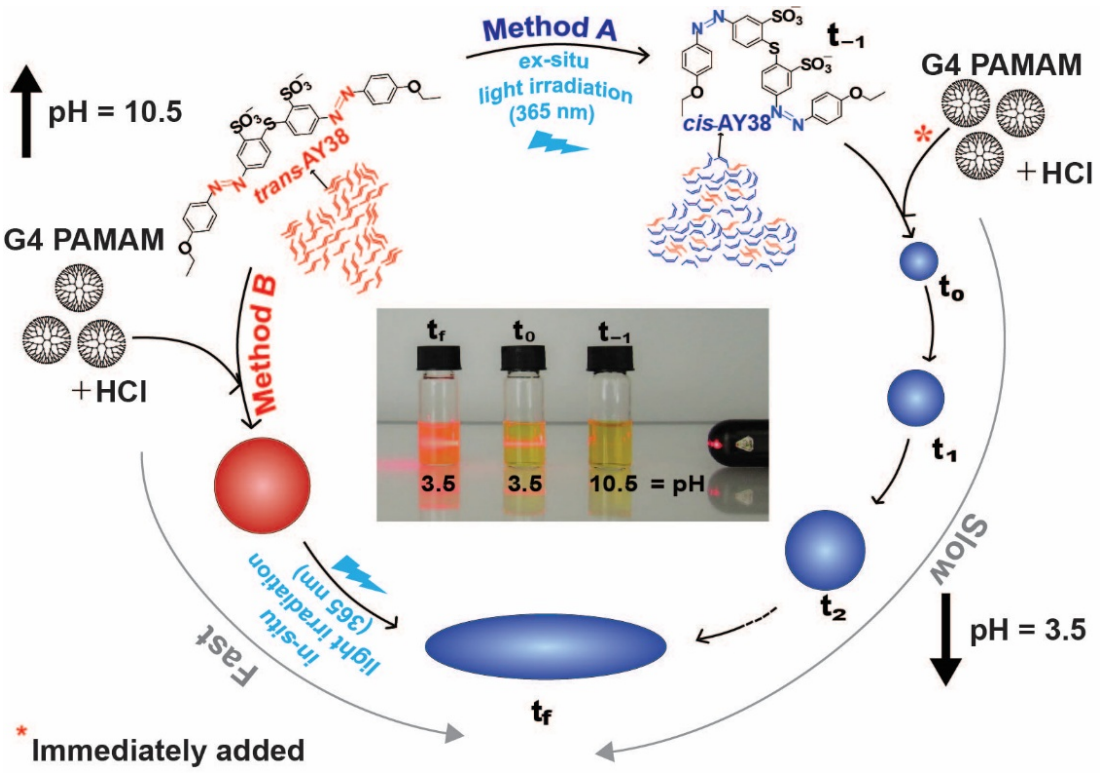
12. Willerich, I.; Gröhn, F. Photoswitchable Nanoassemblies by Electrostatic Self-Assembly. *Angew. Chemie - Int. Ed.* **2010**, *49*, 8104–8108, doi:10.1002/anie.201003271.

20. Willerich, I.; Gröhn, F. Thermodynamics of Photoresponsive Polyelectrolyte-Dye Assemblies with Irradiation Wavelength Triggered Particle Size. *Macromolecules* **2011**, *44*, 4452–4461, doi:10.1021/ma200538e.

43. Maiti, P.K.; Çağin, T.; Wang, G.; Goddard, W.A. Structure of PAMAM Dendrimers: Generations 1 through 11. *Macromolecules* **2004**, *37*, 6236–6254, doi:10.1021/ma035629b.

7.2.3. Light-Induced Structural Evolutions in Electrostatic Nanoassemblies

Mohit Agarwal, Ralf Schweins, Franziska Gröhn, Polymers, **2026**, 18(2), 190.



polymers

MDPI

Article

Light-Induced Structural Evolutions in Electrostatic Nanoassemblies

Mohit Agarwal [1,2], Ralf Schweins [2] and Franziska Gröhn [1,*]

[1] Department of Chemistry and Pharmacy, Interdisciplinary Center for Molecular Materials, Friedrich-Alexander Universität Erlangen-Nürnberg, Egerlandstr. 3, D-91058 Erlangen, Germany; mohit.agarwal@fau.de

[2] Institut Laue-Langevin, DS/LSS, 71 Avenue des Martyrs, F-38000 Grenoble, France; schweins@ill.eu

* Correspondence: franziska.groehn@fau.de; Tel.: +49-913-185-20731

Abstract

Studying nanoscale self-assembly in real time using external stimuli unlocks new opportunities for dynamic and adaptive materials. While electrostatic self-assembly is well-established, real-time monitoring of its structural evolution under light irradiation remains largely unexploited. In this study, we employ light-responsive azobenzene dyes (Acid Yellow 38, AY38) and pH-sensitive polyamidoamine (PAMAM) dendrimers to investigate the kinetics of electrostatic self-assembly under UV irradiation. Using a custom in situ small-angle neutron scattering (SANS) setup, we track the real-time morphological transformations of self-assembled structures with sub-minute resolution. We introduce two distinct pathways: method A (pre-irradiated *cis*-AY38 for controlled, slow kinetics) and method B (direct UV-induced self-assembly, fast kinetics). The results reveal that *trans-cis* isomerization kinetics dictate the rate of self-assembly, influencing aggregate stability, ζ-potential evolution, and final morphology. Structural analysis using dynamic and static light scattering (DLS and SLS) and SANS elucidates a transition from spherical to ellipsoidal morphologies governed by electrostatic and dipole-dipole interactions. These findings establish photoisomerization-driven self-assembly as a robust mechanism for tunable nanoscale architectures, paving the way for adaptive photonic materials, targeted drug delivery, and reconfigurable nanostructures.

Keywords: electrostatic self-assembly; in situ SANS; kinetics; nanoparticle morphology evolution; spherical-to-ellipsoidal transition

Academic Editor: Ian Wyman

Received: 10 December 2025
Revised: 31 December 2025
Accepted: 2 January 2026
Published: 9 January 2026

Copyright: © 2026 by the authors. Licensee MDPI, Basel, Switzerland. This article is an open access article distributed under the terms and conditions of the Creative Commons Attribution (CC BY) license.

1. Introduction

Achieving precise control over nanoscale self-assembly is crucial for designing responsive materials with applications in drug delivery, nanophotonics, and soft robotics. Electrostatic self-assembly, which relies on non-covalent interactions between charged building blocks, offers a promising route to such materials [1–6]. Conventional methods, such as *pH* changes [7–10], ionic strength variations [11,12], or temperature shifts [13,14], enable control over self-assembly. However, these methods require chemical modifications, external additives, or often disadvantageous temperature increases, making them less practical for real-time, reversible applications [15–18]. Light-responsive self-assembly provides a non-invasive, reversible, and highly tunable alternative to traditional methods [18–23]. Among light-responsive molecules, azobenzene dyes are

particularly promising because light switches their molecular geometry and polarity, enabling time-programmable self-assembly [24–27]. In 2010, we (Gröhn et al.) demonstrated for the first time a light-switchable particle size in nanoscale objects [4], in that case formed by electrostatic self-assembly.

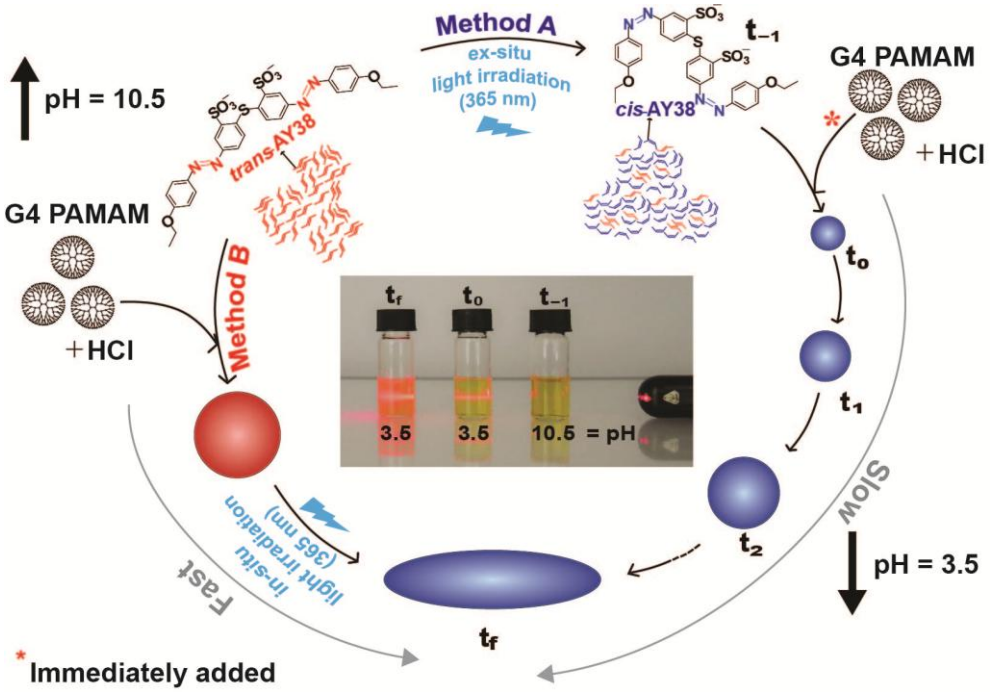
Despite extensive studies on equilibrium structures on azobenzene-based assemblies, time-resolved investigations of light-induced self-assembly are extremely rare—and, to our knowledge, absent for electrostatically driven systems. Existing work primarily examines endpoint morphologies rather than real-time dynamics [18,28,29]. Understanding these temporal processes is essential for creating truly adaptive nanomaterials.

To address this gap, in this study we investigate the assembly of Acid Yellow 38 (AY38), a di-anionic sulfonate-functionalized azobenzene dye, and polyamidoamine (PAMAM) dendrimers, a class of pH-responsive cationic macromolecules, to elucidate the mechanism of light-controlled electrostatic self-assembly. AY38 azo dye offers a *cis*-enriched photostationary state upon irradiation and slow thermal back-isomerization, enabling time-resolved tracking of protocol-dependent restructuring [30,31].

Unlike previous investigations that demonstrated the size and morphology changes upon UV irradiation in azobenzene-based assemblies, with notable studies focusing on equilibrium states and endpoint measurements [6], we herein systematically track structural changes in real-time, providing quantitative insight into the role of charge ratio, dendrimer generation, and isomerization kinetics in controlling self-assembly dynamics. This study addresses this critical gap by developing a dedicated in situ small-angle neutron scattering (SANS) setup to capture the kinetics of electrostatic self-assembly under UV irradiation.

Recent studies have explored real-time in situ dynamic self-assembly using advanced spectroscopic and scattering techniques. Huang et al. used fluorescence spectrometry to monitor kinetically controlled self-assembly via optical transitions [32], while Jensen et al. utilized synchrotron SAXS to capture the entire micelle formation process [33–35]. Kelly et al. were among the first to integrate in situ UV-Vis and SANS to reveal reversible micellar transformations from wormlike micelles to fractal-like aggregates in response to photoisomerization [36]. Building on these insights into light-responsive micellar transformations, i.e., a light response based on the classical concept of micelle formation, our study expands this concept to electrostatic macroion-dye assemblies, elucidating how photoisomerization determines real-time morphological evolutions, captured here for the first time via in situ UV irradiation using SANS.

To investigate the mechanism of electrostatic self-assembly between a di-anionic AY38 and cationic PAMAM dendrimer macroions, this study leverages the azo dye's photo switchability and the dendrimer's *pH* responsiveness. Two distinct self-assembly pathways were designed to explore these dynamics, as shown in Scheme 1: method A (slow kinetics, ≈3 h) and method B (fast kinetics, <20 min). Method A slows restructuring to resolve intermediates, whereas method B captures fast endpoint evolution under in situ SANS measurements. The prolonged half-life of *cis*-AY38 (≈12 h) enables a detailed structural characterization using SANS, dynamic light scattering (DLS), static light scattering (SLS), and ζ-potential measurements. Due to its fast kinetics, an in situ approach was necessary to capture the transient structural states. This was achieved using a dedicated in situ setup integrated with the D11 instrument, as detailed in the experimental section.



Scheme 1. Representation of the two different pathways to prepare electrostatic assemblies of anionic azo dye molecules and cationic dendrimer macroions (Acid Yellow 38 and G4 PAMAM dendrimer). Method A (pre-irradiation) slows down the formation of assemblies by a factor of 10 compared to method B (post-irradiation). The light irradiation occurs at λ = 365 nm for 20 min in both methods. The picture in the middle represents the scattering of samples in method A at different times (t_{-1} = before the addition of acid, t_0 = immediately after mixing the acid, t_f = after 3 h).

To investigate the real-time morphological evolution of photoresponsive assemblies, we focused primarily on method A, which exploits the prolonged lifetime of the *cis* isomer to slow down assembly kinetics. This allows for a detailed characterization of intermediate structures and a clearer understanding of the underlying (re)structuring pathway. In contrast, method B assists in elucidating the relationship between photoisomerization rates and nanoscale organization. By addressing key gaps in the understanding of photoresponsive electrostatic self-assembly, we investigate how the isomeric states of the azobenzene dye influence the structure and dynamics of the resulting assemblies. Through this dual-method approach of method A (slow kinetics) and method B (fast kinetics), we establish a direct correlation between photoisomerization rates and nanoscale organization, offering a new paradigm for light-controlled nanostructure fabrication. These findings advance the understanding of photoisomerization-driven self-assembly and establish a framework for designing photoresponsive materials with applications in adaptive nanomaterials, optoelectronic devices, and targeted drug delivery systems.

2. Materials and Methods

2.1. Chemicals

Polyamidoamine dendrimers of generations 4 (10 wt. % in methanol) and 5 (5 wt. % in methanol) were purchased from Aldrich (Darmstadt, Germany). DLS confirmed the radius and size distribution given by the manufacturer, Dendritech (Midland, MI, USA). Acid Yellow 38 with >40% purity was purchased from Merck (Darmstadt, Germany) and purified to >98% by multiple recrystallizations using water and ethanol, as described previously [37,38]. D_2O, NaOD, and DCl were purchased from Merck, Darmstadt, Germany, and NaOD and DCl were used to adjust the *pD* of the solution.

2.2. Sample Preparation

D_2O was used as a solvent to prepare all samples, and all the reagents used throughout the study, except for the assembly components, were deuterated. The stock solutions of azo dye (1.4×10^{-3} mol L^{-1}) and PAMAM dendrimers (4.0×10^{-5} mol L^{-1}) were prepared with D_2O solvent in basic medium ($pD = 10.5$). The samples were prepared based on their charge ratio, l_c, which represents the ratio of anionic dye sulfonate groups to cationic amine groups. The standard solutions of NaOD and DCl were prepared at 1.0×10^{-1} mol L^{-1} concentration. The pH measurements were performed with a Mettler Toledo pH meter. The pH values were converted into pD values using the formula given [39–42]:

$$pD = pH + 0.41 \quad (1)$$

In method A, the dye was pre-irradiated out of the neutron beam for 20 min at λ = 365 nm. An appropriate amount of dendrimer solution and 0.1 M DCl was mixed immediately to induce the assembly formation. The slow evolution of assemblies is monitored using various techniques, including dynamic and static light scattering, UV-Vis spectroscopy, ζ-potential, and small-angle neutron scattering.

In method B, an appropriate amount of azo dye stock solution was diluted with D_2O, followed by mixing with the dendrimer solution under continuous stirring. Later, the appropriate amount of 0.1 M DCl is added to induce the assembly formation process. The sample was then irradiated using a novel, custom-built, state-of-the-art in situ setup built at the D11 beamline. The setup consists of a UV lamp emitting 365 nm light, which is focused on the sample cuvette using a convex lens. The UV lamp can be controlled via a long cable from outside the interlocked SANS sample area. In situ UV light illumination of the samples, while being exposed to the neutron beam, takes place for 20 min.

2.3. Light Scattering

Dynamic and static light scattering (DLS and SLS) measurements were carried out on an ALV CGS3 (ALV, Langen, Germany) instrument with an ALV 5004 correlator using a HeNe laser with a wavelength of λ = 632.8 nm and 23 mW output power. The DLS and SLS experiments were performed simultaneously within the angular range of $20° \leq \theta \leq 150°$ with 5°-degree steps at room temperature (25 °C).

The Brownian motion of the assemblies in the solution was detected by the fluctuations in the scattered intensity at a given scattering angle as a function of time. The intensity-time autocorrelation function $g_2(q, \tau)$ is converted into the electric field-time correlation function, $g_1(q, \tau)$, using the Siegert relation [43]:

$$g_2(q,\tau) = 1 + [g_1(q,\tau)]^2 \quad (2)$$

where $\vec{q}$ is the scattering vector (momentum transfer), and τ is the shift in time. $g_2(q, \tau)$ is:

$$g_2(q,\tau) = \frac{\langle I(q,t)I(q,t+\tau)\rangle}{\langle I(q,t)\rangle^2} \quad (3)$$

which describes the correlation of the intensity at time t = 0 and $t + \tau$, and $I(q, t)$ is the scattered intensity at time t. The scattering vector $\vec{q}$, is related to the scattering angle θ as:

$$q = |\vec{q}| = \frac{4\pi n_D}{\lambda} sin\left(\frac{\theta}{2}\right) \quad (4)$$

where n_D is the refractive index of the solvent.

The electric field-time autocorrelation function, $g_1(q, \tau)$, was further analyzed by a regularized Laplace transformation using the CONTIN algorithm provided by S. Provencher to obtain the distribution of relaxation times [44,45]. The apparent diffusion coefficient, D_{app}, is calculated as given below:

$$D_{app} = q^{-2}\tau^{-1} \quad (5)$$

Measurements covered a broad range of q by measuring a scattering angle of $20° \leq \theta \leq 150°$ with 5-degree steps. In the case of an angular dependence, D_{app} was extrapolated to $q = 0$ to yield D_0. In the absence of an angular dependence, the average value of D_{app} is taken as D_0. From the latter, the hydrodynamic radius (R_H) can be calculated using the Stokes-Einstein relationship:

$$R_H = \frac{kT}{6\pi\eta D_0} \quad (6)$$

where k is the Boltzmann constant, T is the absolute temperature in Kelvin, and η is the solvent viscosity.

Static light scattering was employed to determine the structural characteristics of the assemblies. By measuring the angular dependence of scattered light intensity, key parameters such as the radius of gyration, R_G were extracted, providing insights into particle size, shape (using the ratio of R_G and R_H), and overall topology in solution. The Rayleigh ratio, ΔR_θ is required to calculate the R_G value. The ΔR_θ is given using the formula:

$$\Delta R_\theta = KcM_wP(q) \quad (7)$$

where c is the mass concentration, M_w is the weight-averaged molecular weight, $P(q)$ is the form factor, and K is the optical constant. K is given by:

$$K = \frac{4\pi^2}{\lambda_0^4 N_A}\left(n_{std}\frac{dn}{dc}\right)^2 \quad (8)$$

where n_{std} is the refractive index of the standard (toluene) and dn/dc the refractive index increment. The form factor $P(q)$ can be described by the Guinier approximation:

$$P(q) \approx exp\left(\frac{-q^2R_G^2}{3}\right) \quad (9)$$

or the Zimm equation [46]:

$$\frac{Kc}{\Delta R_\theta} = \frac{1}{M_w}\left(1 + \frac{1}{3}q^2\langle R_G^2\rangle\right) + 2A_2c \quad (10)$$

A_2 is the second osmotic virial coefficient, which determines the solvent-solute interactions. In the case of ideal solutions, A_2 is zero when polymer-polymer and polymer-solvent interactions are equal, and the polymer shows an ideal chain behavior. The Zimm and Guinier equations are only valid for $q \times R_G \leq 1.2$ [47]. The ratio of R_G/R_H provides essential information on particle topology. While the hydrodynamic radius, R_H, is the radius of a friction-equivalent sphere in a fluid, R_G is the root-mean-square distance of a molecule's mass points from its center of mass, which can be further interpreted using the value of the R_G/R_H ratio as the shape information of nanoparticles in the solution.

For further analysis, SLS and small-angle neutron scattering (SANS) data have been merged, providing an extended q-range for examining nanoparticles at a wide scale.

2.4. ζ-Potential Measurements

ζ-potential measurements were performed on a Zetasizer Nano ZS analyzer equipped with a 4mW HeNe laser, λ = 633 nm (Malvern Instruments Ltd., Malvern, UK). All the measurements were performed with 1 mL of sample volume in disposable folded capillary cells (DTS 1070) at room temperature with five replicated measurements.

This technique measures the electrophoretic mobility μ_e of the dispersed particles, including a fluid layer in the surrounding medium. Using the Helmholtz-Smoluchowski equation, the value of ζ-potential is calculated as [48,49]:

$$\zeta = (\mu_e * \eta)/\varepsilon_{rs}\varepsilon_0 \quad (11)$$

with μ_e the electrophoretic mobility of charged particles, η the viscosity of the solution, ε_{rs} the dielectric constant of the electrolyte solution, and ε_0 the electric permittivity of vacuum.

2.5. UV-Vis Spectroscopy

The absorbance spectra were recorded with a JASCO V-630 spectrometer (JASCO Corporation, Tokyo, Japan) using a 200 µL sample volume in 1 mm path length quartz cuvettes to quantify the amount of dye isomers and measure the dye concentration. Measurements were performed at room temperature (25 °C). The *cis*-to-*trans* isomerization rate constant of AY38 azo dye is determined using kinetic measurements with 5 min time slices over a total measurement time of 5 h. The rate constant is calculated assuming a first-order reaction as given:

$$ln[A] = -Kt + \ln[A]_0 \quad (12)$$

Here, A_0 is the initial concentration of *cis*-moiety, A is the concentration of *cis* isomer at a given time t, and K is the rate constant of the reaction.

2.6. Small-Angle Neutron Scattering

SANS is a non-destructive technique that utilizes the unique properties of neutrons to analyze the size, shape, and spatial arrangements of nanoscale assemblies in solution formed, for example, by polyelectrolytes and organic counterions. SANS measurements were performed at the D11 beamline (doi:10.5291/ILL-DATA.9-11-2079, doi:10.5291/ILL-DATA.9-12-662) at the Institut Laue-Langevin, Grenoble, France.

The SANS technique is based on the determination of intensity I of the scattered neutrons as a function of the scattering angle (can also be converted into scattering vector q using Equation (4)). The scattered intensity I, is given as [50]:

$$I(q) = \emptyset V_{NP}(\Delta\rho_{SLD})^2 P(q) S(q) \quad (13)$$

where $\emptyset$ is the volume fraction, V_{NP} is the particle volume, $\Delta\rho_{SLD}$ is the difference in scattering length densities between the solute and the solvent, and $P(q)$, the particle form factor, corresponds to the particle shape. The structure factor $S(q)$ represents the interparticle correlations, considered equal to 1 in our case, as the samples have been diluted such that no interparticle interactions are present. The form factor is the square of the normalized total scattering amplitude $F(q)$.

For example, for a sphere with a radius R, the form factor amplitude $F(q)$ is [47].

$$F(q) = 3\frac{sinqR - qRcosqR}{(qR)^3} \quad (14)$$

While for an ellipsoid, the amplitude $F(q)$ is [51]:

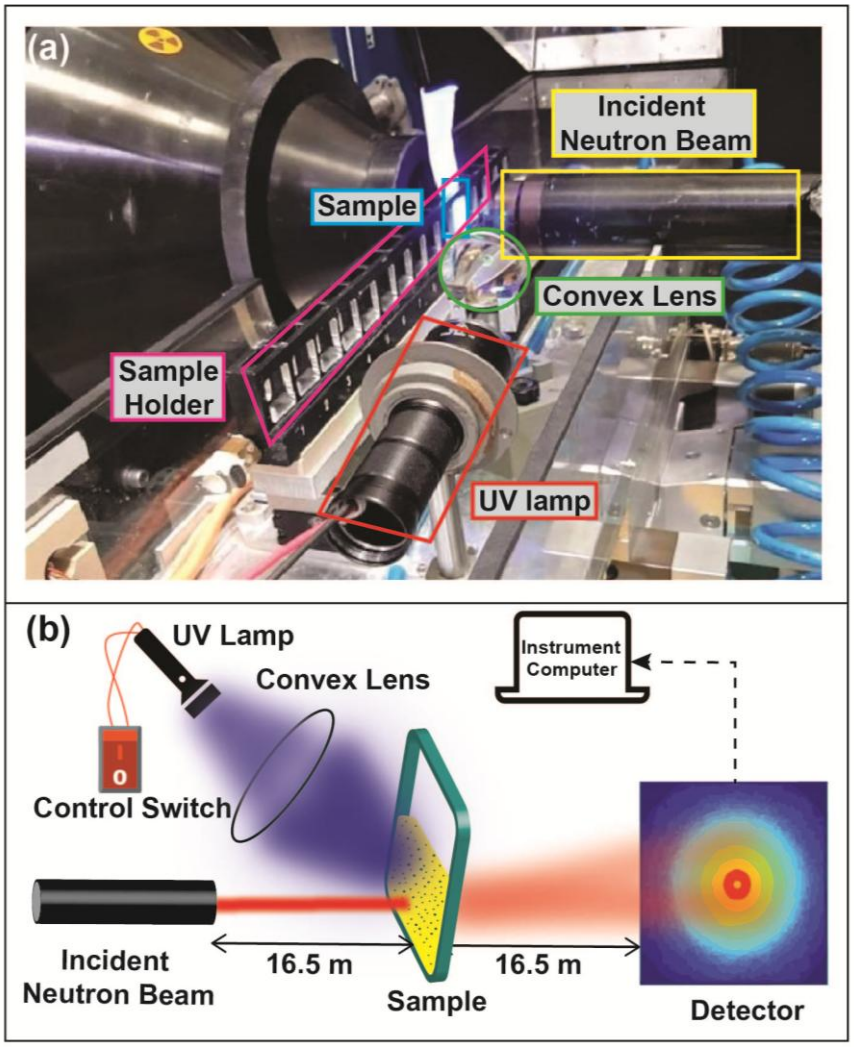
$$F(q) = \Delta\rho V \frac{3(\sin qr - qr\ cosqr)}{(qr)^3} \quad (15)$$

where

$$r = [R_e^2 sin^2\alpha + R_p^2 cos\alpha]^{\frac{1}{2}} \quad (16)$$

where α is the angle between the ellipsoidal axes and $V = (4/3)\pi R_p R_e^2$ is the volume of the ellipsoid, R_p is the polar radius along the rotational axis, and R_e is the equatorial radius perpendicular to the rotational axis of the ellipsoid.

To investigate the effects of UV irradiation on the sample at a wavelength of λ = 365 nm, a custom in situ setup was designed, as illustrated in Scheme 2. The upper section of the figure shows a photo of the complete experimental setup. In contrast, the lower section provides a simplified schematic of the small-angle neutron scattering (SANS) apparatus under in situ UV irradiation. To replicate results obtained from static measurements, samples were exposed to UV light for a duration of 20 min, and SANS data were recorded simultaneously in the first 3 min with the scans of 10 s each and the next 17 min of 60-s time slices. Upon reaching the end of the irradiation, the scattering data did not vary much, and more than one short measurement could be added to make a single scattering curve. The sample environment was fully enclosed within a light-proof black cover during the SANS experiment to prevent unintended light exposure.



Scheme 2. (**a**) Photograph and (**b**) schematic of the in situ UV irradiation setup used during SANS measurements. The UV lamp is positioned to ensure full illumination of the cuvette region intersected by the neutron beam (the irradiation geometry was kept fixed for all in situ experiments and thus does not substantially influence the outcome, as maximum irradiation is assured).

This in situ setup operates as an independent system controlled manually via a switch outside the sample chamber. A convex lens positioned between the UV lamp and the sample cuvette concentrates the UV light onto the sample, ensuring uniform illumination. During irradiation, the sample-to-detector and sample-to-collimation distances are fixed at 16.5 m to maintain consistent measurement conditions. This setup facilitates precise monitoring of structural changes induced by UV light in real time.

The UV lamp was positioned at an angle relative to the neutron beam to ensure that the sample volume probed by SANS is fully illuminated. (The angle was therefore chosen for geometrical/space constraints and was kept fixed for all in situ measurements towards the sample cuvette. The angle of these with the sample cuvette is approximately 30°. Under these conditions, the assembly behavior is governed by the UV irradiation and by maintaining consistent irradiation conditions across measurements.)

For experiments targeting slow kinetics, a sample-to-detector and collimation distance of 28 m was used in beamtime 9-12-662, while a configuration of 38 m with a collimation distance of 40.5 m was employed during beamtime 9-11-2079. These extended distances enabled the resolution of structural changes in assemblies over longer timescales (a total time of 3–4 h). In experiments with a 28 m sample-to-detector distance, 30 min time slices were taken, whereas in a 38 m distance, 1 min time slices were measured for the entire measurement duration. In contrast, a shorter sample-to-detector distance of 16.5 m with an equivalent collimation length was used for fast kinetic experiments, maximizing neutron flux to capture rapid structural transitions. The measured scattering vector ranges (q) measured were $0.018\ nm^{-1} \leq q \leq 0.22\ nm^{-1}$ for slow kinetics and $0.038\ nm^{-1} \leq q \leq 0.58\ nm^{-1}$ for fast kinetics. The scattering vector q is inversely related to the real-space length scale (d) by $d = 2\pi/q$.

The 28 m configuration was selected for slow kinetics experiments to access lower q values (larger real-space length scales), which is essential to resolve the growth and restructuring of larger aggregates during the multi-hour evolution. Because the kinetics are slow, we could afford longer acquisition times (e.g., minute-to-30 min slicing depending on configuration), so the reduced flux associated with longer distances does not limit temporal resolution.

Samples for SANS were prepared in D_2O to minimize incoherent background scattering from hydrogen. Measurements were conducted in Hellma 404-QX quartz cells (2 mm path length), with all samples containing AY38 dye at a concentration of $c_{AY38} = 1 \times 10^{-4}$ mol L^{-1}. The experiments utilized a 15 mm diameter neutron beam with a wavelength $\lambda = 6.0$ Å (FWHM = 10%). A multi-tube ^3He gas detector, consisting of a central panel with 192 horizontal tubes and two side panels with 32 vertical tubes each, provided a detection area of 256 × 256 pixels (tube length: 1 m with a diameter of 8 mm; pixel size: 4 × 8 mm^2). Two-dimensional scattering data were corrected for empty cell scattering, electronic background, and detector non-uniformity using measurements of a 1 mm H_2O standard. Transmission corrections were performed using Mantid 6.0 [52], and the data were normalized to absolute intensity using attenuated direct beam measurements specific to each instrument setup. Solvent and incoherent background scattering were subtracted from the azimuthally averaged scattering curves.

To extend the low q range for larger assemblies observed in slow kinetics, the SANS data were merged with static light scattering (SLS) data, yielding a combined q range of $0.0068\ nm^{-1} \leq q \leq 0.22\ nm^{-1}$. The scattering data were analyzed and modeled using the SasView 4.2.2 software, applying various form factors. The quality of the fit was evaluated using the reduced χ^2 values (SasView 4.2.2: https://www.sasview.org/ (last accessed 16 September 2025)).

3. Results

To understand the dynamics of light-induced structural changes in self-assembly, we employed two distinct experimental pathways, each offering complementary insights into the role of azobenzene photoisomerization in driving nanoscale structural evolution. Method A utilizes pre-irradiated dye solutions to facilitate high-resolution, time-resolved structural characterization over extended timescales using SANS, dynamic light scattering (DLS), and ζ-potential measurements. In contrast, method B involves real-time UV

irradiation of dye-dendrimer mixtures, enabling sub-minute resolution of the self-assembly process via an in situ UV-SANS setup.

3.1. Slow Kinetics (Method A)

3.1.1. Light Scattering Measurements

To enable time-resolved structural analysis, we developed a modified sample preparation strategy referred to as method A that decelerates the assembly kinetics through pre-irradiation of the AY38 dye. UV irradiation converts ≈80% of the dye to its *cis* form, which, due to its sterically hindered geometry and lower dipole moment, binds less effectively to PAMAM dendrimers than the *trans* isomer [23]. As the dye gradually returns to the thermodynamically stable *trans* state (*cis* isomer half-life ≈ 12 h), the increasing population of *trans* isomers with higher dipole-dipole interaction strength and favorable binding geometry progressively drives aggregate formation [18,23]. This controlled, slow evolution enables detailed monitoring of assembly dynamics using SLS-SANS, DLS, and ζ-potential measurements.

These properties of AY38 are used in method A to slow down the growth of the aggregates. The dye was pre-irradiated, leading to a maximum *cis* dye amount, followed by the swift addition of dendrimer solution and acid. This leaves ≈ 20% of *trans*- and ≈ 80% of *cis* dye molecules to interact electrostatically with the dendrimer molecules and by dipole-dipole interactions with other dye molecules. Since *trans* isomers have a more suitable geometry and dipole moment, *trans*-molecules preferably bind with both dendrimers and other dye ions, while *cis* isomers primarily interact via electrostatic interactions with dendrimer molecules only [18,23]. Over time, the *cis* isomers gradually convert back to their *trans* state, thereby increasing the driving forces for assembly, such that the nanoassemblies grow.

To gain deeper insight into the factors governing the self-assembly process, it is important to explore how the charge ratio of l_c and dendrimer generation influences the kinetics and final morphology of the resulting aggregates. Figure 1 presents the results of angular-dependent dynamic light scattering in terms of the change in the R_H values during the *cis*-to-*trans* (back) isomerization for assemblies formed with AY38 azo dye and two different generations of PAMAM dendrimers, generations 4 and 5 (G4 and G5), prepared using method A at a charge ratio of $l_c = 2.0$. The experiment reveals three critical stages of the self-assembly process. Initially, at $t_0 \approx 5$ min, small particles with hydrodynamic radii $R_H < 100$ nm are observed. As the system evolves, a gradual increase in size is recorded, reaching $R_H = 402$ nm for AY38/G4 and $R_H = 456$ nm for AY38/G5 at $t_f \approx 180$ min. This progression indicates a slow but continuous growth of the assemblies as *cis*-AY38 isomers convert to their more interacting *trans* state.

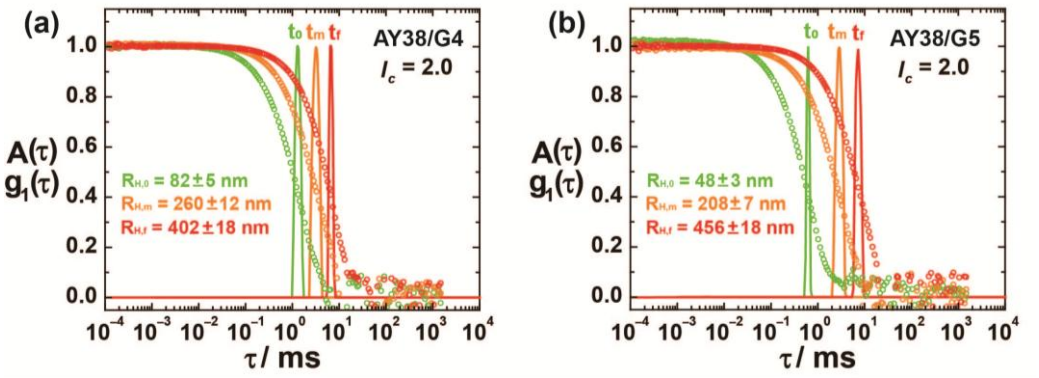


Figure 1. DLS data at a charge ratio (dye charges/dendrimer charges) of $l_c = 2.0$ recorded at three key stages of the kinetics process: $t_0 \approx 5$ min (start, $R_{H,0}$), $t_m \approx 60$ min (midpoint, $R_{H,m}$), and $t_f \approx 180$

min (end $R_{H,f}$). The plots display electric field autocorrelation $g_1(\tau)$ (open circles) and the corresponding relaxation times distributions $A(\tau)$ (solid lines) at a scattering angle of $\theta = 90°$ for two dendrimer generations: (**a**) G4 and (**b**) G5. (The R_H values are obtained by extrapolation to a 0° angle, and σ represents the particle size distribution at a 90° scattering angle, $c_{AY38} = 1 \times 10^{-4}$ mol L^{-1}).

Figure 2 illustrates the kinetics profiles, where DLS measurements were recorded every 8–10 min. Higher charge ratios ($l_c \geq 3.0$) lead to smaller assemblies, while lower charge ratios ($l_c = 2.0$) yield larger aggregates. This trend aligns with the prior observations in polyelectrolyte-dye systems, where the excess of dye charges enhances intermolecular attraction, leading to denser packing, even though those studies employed different preparation methods [4,18,23]. Similar charge-ratio-dependent behavior has been observed in cationic-anionic block copolymer assemblies, indicating that this principle may extend beyond azo-dye systems [9].

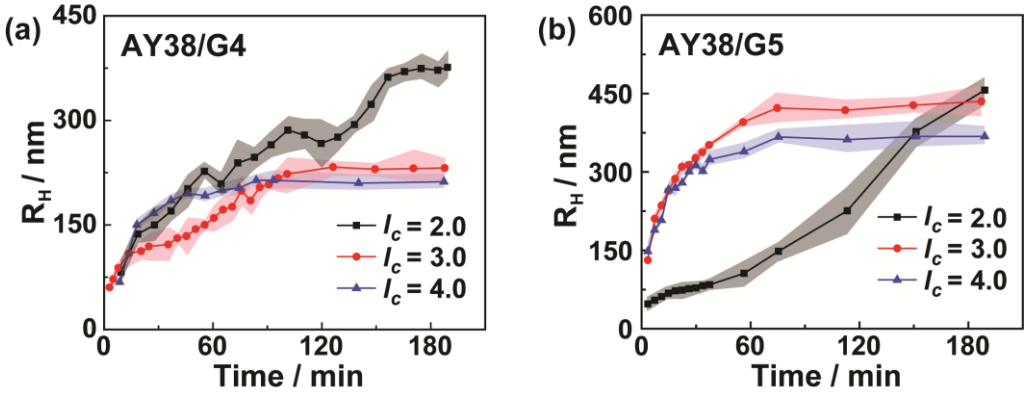


Figure 2. R_H obtained from multi-angle DLS on prolonged kinetics of multiple charge ratios (l_c = 2.0, 3.0, and 4.0) using AY38 dye with (**a**) G4 and (**b**) G5 PAMAM dendrimers. The total duration for the kinetics was fixed at 3 h for all measurements. The different colored shaded areas represent the error bars obtained from several repeat measurements.

As Figure 2a displays, AY38/G4 assemblies at $l_c = 2.0$ form aggregates with a stable size after 2.5 h. In contrast, at $l_c = 3.0$, the aggregates stabilized in less than two hours, and at $l_c = 4.0$, it took even less time (≈1.25 h) to form assemblies with a time-independent size. In contrast, with the G5 dendrimer, at $l_c = 2.0$, aggregates with a stable size do not form within 3 h, but for $l_c = 3.0$ and 4.0, stabilized aggregates build in 1–1.25 h. Thus, the G4 and G5 dendrimers exhibit a slow growth of the assemblies in the case of $l_c = 2.0$, whereas the rate of aggregate size evolution increases with increasing l_c. The assemblies stabilize quickly for higher charge ratios and do not aggregate further. Additionally, the assemblies grow the largest at $l_c = 2.0$ as compared to the higher charge ratios where the stabilizing time was smaller.

3.1.2. UV-Vis Spectroscopy

The different growth rates of assemblies at multiple charge ratios and with different PAMAM generations can be further understood in more detail by mapping the rate of back isomerization (i.e., rate constant, k/s^{-1}) of the *cis* to *trans* state. The UV-Vis absorption was measured in 10 min intervals for a total duration of 10 h. The amounts of *cis* and *trans* isomers of the azo dye present in the sample solution were calculated [23]. The back isomerization process of AY38 azo dye is a first-order reaction. Using the amount of *cis* isomer and the first-order kinetics, the rate constant is calculated according to Equation (12).

In Figure 3, the UV-Vis absorbance spectrum shows an immediate change upon mixing the pre-irradiated AY38 dye with the dendrimer and acid, indicating the beginning of *cis*-to-*trans* isomerization. Initially, approximately 80% of the dye is in the *cis*

state, which gradually converts to the more thermodynamically stable *trans* isomer over several hours. To analyze the isomerization kinetics, absorbance measurements were recorded at regular 10 min intervals, and the decay of the c*is* isomer peak was tracked over time. The kinetic profile fits well to a first-order reaction model, which assumes that the rate of isomerization depends linearly on the concentration of the *cis* isomer. The rate constant k was determined to be 3.5×10^{-6} s^{-1} in the presence of dendrimer, significantly lower than the value observed for pure dye in solution (1.6×10^{-5} s^{-1}). This reduced rate may arise from a photoprotective effect, wherein *cis*-AY38 bound to dendrimer molecules experiences restricted mobility and/or shielding, thereby slowing its relaxation to the *trans* state. Moreover, under excess dye conditions ($l_c \geq 1.5$), a surplus of unbound *cis* dye remains in solution, gradually isomerizing back to the *trans* state over time. The resulting increase in *trans* isomer concentration promotes secondary dipole–dipole interactions, which further drive the growth of electrostatic aggregates into larger nanostructures.

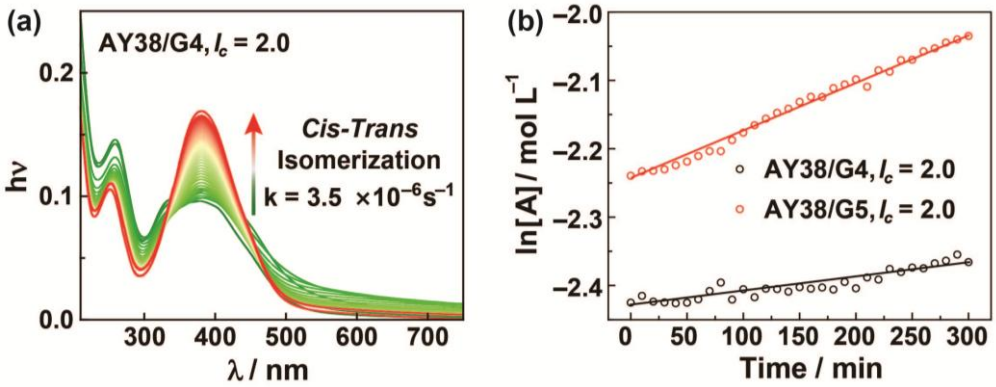


Figure 3. Slow kinetics of dye-dendrimer self-assembly characterized by UV-Vis absorption spectroscopy. (**a**) UV-Vis absorption spectra of AY38/G4 assemblies at $l_c = 2.0$, recorded every 10 min over a 10 h period. The initial spectrum (dark green) corresponds to the pre-irradiated *cis*-AY38 dye. Upon mixing with dendrimer and acid, the dye gradually isomerizes back to the *trans* form. The isomerization rate constant (k) reflects the conversion kinetics. (**b**) First-order kinetic fits of *trans* isomer formation for AY38/G4 and AY38/G5 assemblies at $l_c = 2.0$, based on Equation (12). On the y-axis, [A] represents the concentration of *trans* isomer in solution.

Regardless of the charge ratio and dendrimer generation, all systems in the present study exhibit approximately 80% of the dye in the *cis* state, which gradually undergoes back-isomerization to form *trans* dye molecules. This behavior contrasts with earlier studies, where variations in charge ratio and dendrimer generation significantly influenced dye-dendrimer interactions, which were discussed in the context of a different proportion of *cis* isomers in the solution [18,23,30]. The key difference lies in approach: in earlier studies dye-dendrimer aggregate formation occurred prior to irradiation under acidic conditions, and the change of the nano-object upon irradiation was observed. These preformed complexes limited photoisomerization efficiency due to constrained dye mobility. In contrast, the current approach maintains the dendrimers in an uncharged state, preventing aggregation while allowing unhindered isomerization dynamics of the dye upon irradiation. Only after irradiation is the acid added so that the pre-irradiated dye and the dendrimer form assemblies.

The results, summarized in Table 1, reveal a direct relationship between the rate constant of the back-isomerization and the growth rate of the assemblies. Stabilizing the assemblies correlates with the increasing formation of *trans* isomers in the solution. Due to a lower dipole-dipole moment, *cis* dye molecules exhibit minimal dye-dye interactions compared to their *trans* counterparts [23,31]. With their linear and extended structure,

trans dye molecules offer a larger surface area for interaction with dendrimer molecules, maximizing electrostatic binding. This spatial configuration allows *trans* isomers to align more closely and orderly along the dendrimer surface, reducing steric hindrance and enabling dense packing. Furthermore, the higher dipole moment of *trans* dye molecules (27.96 Debye) compared to *cis* isomers (12.96 Debye) increases the likelihood of dye-dye interactions, enhancing their binding ability in electrostatic self-assemblies. The influence of dendrimer generation is also evident: assemblies formed with G4 dendrimers stabilize more slowly than those with G5, particularly at lower charge ratios. This difference likely stems from the increased number of terminal amine groups and higher surface charge density of G5 dendrimers, which provide more binding sites and stronger electrostatic attraction for the dye molecules. As a result, G5 dendrimers facilitate faster assembly formation compared to G4 dendrimers. This comparison highlights how dendrimer architecture and generation modulate the kinetics and final morphology of electrostatic self-assemblies.

Table 1. Rate constant, k (s^{-1}), as calculated from UV-Vis spectroscopy for prolonged kinetics at different charge ratios (l_c = 2.0, 3.0, and 4.0) for G4 and G5 PAMAM dendrimer—AY38 dye assemblies. The back isomerization process (*cis* to *trans* state) is considered a first-order reaction to calculate k. The overall uncertainty in calculating k is within 10%.

l_c	Rate Constant, k/s^{-1}	
	AY38/G4	AY38/G5
2.0	3.5×10^{-6}	2.0×10^{-6}
3.0	9.7×10^{-6}	1.2×10^{-5}
4.0	1.0×10^{-5}	1.3×10^{-5}

3.1.3. Small-Angle Neutron Scattering

Small-angle neutron scattering (SANS) provides detailed structural insights into the slow kinetics of dye-dendrimer electrostatic assemblies. Figure 4a illustrates the evolution in the AY38/G4 system at l_c = 2.0. The measurements were conducted over 4 h using the D11 instrument at a sample-detector distance of 28 m, with data collected in eight 30 min segments. The progression of the kinetics is represented by the color gradient from dark green to dark red. While the self-assembly process continues until stabilization, 30 min time slices were chosen due to the low sample count rate at the extended detector distance. After applying background corrections, the data were analyzed using various structural models (SasView 4.2.2 application), with all calculated parameters detailed in Table 2.

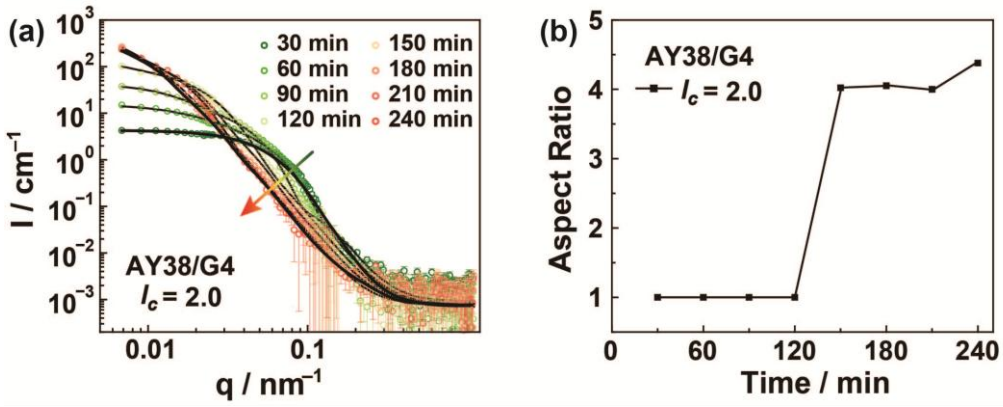


Figure 4. SANS on the long kinetics of the AY38/G4 system at l_c = 2.0 (**a**) SLS-SANS data where both SLS and SANS measurements were performed separately on the same system with the same time intervals. The total duration of the experiment with both instruments was 4 h. In SANS, each measurement was performed at a 28 m sample-detector distance for 30 min. The color change from

dark green to dark red represents the course of the kinetics. (**b**) The change in the aspect ratio (length/width) of the nano-objects resulting from structural model fitting as a function of time.

The scattering curves of the AY38/G4 system display distinct temporal evolution over 150 min, characterized by an increasing slope in the low q region, indicative of progressive particle growth. This observation aligns with the results from complementary light-scattering measurements, confirming a gradual increase in aggregate dimensions during the self-assembly process. The SANS data were best described by a spherical form factor during the first 120 min, corresponding to the initial growth phase where small, nearly isotropic particles (R ≈ 25 nm) gradually expanded to R ≈ 60 nm. Beyond this period, the scattering profile could no longer be satisfactorily fit with a spherical model, and an elongated ellipsoidal model provided a significantly improved fit (a comparison of spherical and ellipsoidal fits is shown with their residuals in Figure S1 and fitting details in Table S1 to confirm the fit quality of the measurement at 150 min). The transition occurred between 120 and 150 min, at which point the assemblies evolved into stable ellipsoidal structures with a semi-minor axis (R_{ax}) of ≈ 35 nm and a semi-major axis (R_{eq}) of ≈ 139 nm. The reduced χ^2 values for all fits remained below 3.0, demonstrating excellent agreement between the experimental data and the applied models.

Table 2. SANS results: structural model fit parameters of AY38/G4 prolonged kinetics at l_c = 2.0 (as shown in Figure 4a), obtained in SasView 4.2.2 using a polydisperse sphere model (30–120 min) and a polydisperse prolate ellipsoid model (150–240 min). The radius of the spherical particles is given as R_{min}; in the case of ellipsoidal particles, R_{min} shows two axial radii, and R_{maj} shows the equatorial radius. Polydispersity in size is given as PDI. The reduced χ^2 shows the quality of the fit.

Time/min	Shape	R_{min}/nm	PDI (R_{min})	R_{maj}/nm	PDI (R_{maj})	χ^2
30		25	0.25			2.9
60		34	0.20			2.4
90		43	0.23			2.6
120		60	0.29			2.8
150		35	0.30	139	0.02	2.0
180		33	0.40	132	0.07	1.7
210		33	0.40	132	0.10	2.2
240		30	0.40	136	0.03	1.9

The corresponding aspect ratios (length/width) corresponding to the structural model fit results are illustrated in Figure 4b. A value of unity represents spherical geometry, whereas larger values indicate anisotropy. Remarkably, the aspect ratio increases sharply from ≈ 1 to ≈ 4 between 120 and 150 min, consistent with the morphological transformation from spherical to elongated ellipsoidal assemblies. This shape evolution reflects a reorganization process driven by the increasing population of *trans*-AY38 isomers over time. Possibly, as the more linear *trans* dye molecules gradually replace the bent *cis* isomers, the local packing within the dye-dendrimer complexes may become increasingly directional and could promote anisotropic association along one preferred axis, leading to elongation rather than isotropic growth. This anisotropic association favors elongation, while the electrostatic confinement by the dendrimer

framework prevents unrestricted one-dimensional growth, yielding ellipsoids as the most energetically favorable intermediate morphology.

In previous studies employing method B, our group established the influence of charge ratio and dendrimer generations on the size and shape of electrostatic assemblies. [4,23] In the present work, we extend this investigation using method A to address the missing details in prior research, focusing on elucidating the evolution mechanism and the role of *cis*- and *trans* dye molecules in forming these assemblies. To explore the influence of charge ratio and dendrimer generations on the light response of electrostatic assembly using method A, the AY38/G5 system was used with l_c = 2.0 and 3.0.

Figure 5 displays the SANS measurements of AY38 dye with generation 5 PAMAM dendrimer under slow kinetics conditions. During the early stages of self-assembly, both charge ratios (l_c = 2.0 and 3.0) exhibit a steady increase in the size of spherical structures (Tables 3 and 4). For l_c = 2.0, the radius of the particles reaches R = 87 nm within 4 min and increases to R = 105 nm over the following 4 min. The spherical morphology is maintained throughout the growth phase, with the radius gradually expanding to R = 176 nm by the 100 min mark, after which no further significant growth is observed. Although measurements continued for three hours, the assemblies remained stable in size beyond this point.

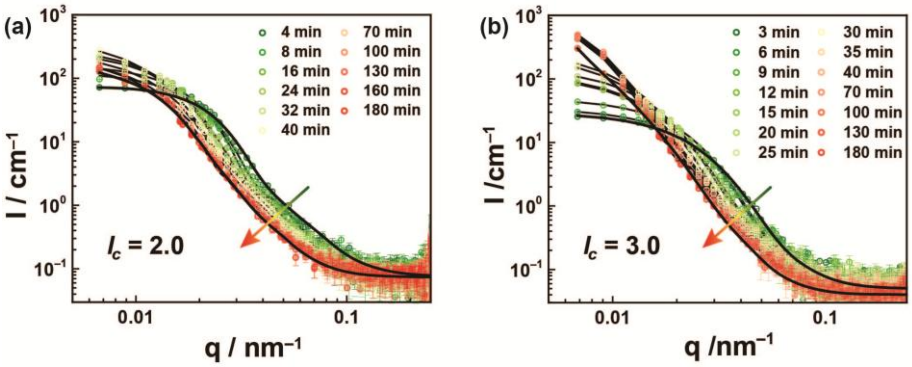


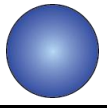
Figure 5. SLS-SANS on AY38/G5 long kinetics system at l_c: (**a**) 2.0 and (**b**) 3.0. Both (SLS and SANS) measurements were performed separately on the same system at the same time intervals. The total duration of the experiment with both instruments was 3 h. SANS measurements were performed at a 38 m sample-detector distance. The color change from dark green to dark red represents the course of the kinetics.

Table 3. SANS results: structural model fit parameters of AY38/G5 prolonged kinetics at l_c = 2.0 (as shown in Figure 5a). The polydispersity of the spherical particles in size is given as PDI. The reduced χ^2 shows the quality of the fit.

Time/min	Shape	Radius/nm	PDI	χ^2
4		87	0.24	1.5
8		105	0.23	1.2
16		118	0.24	1.0
24		134	0.24	1.0
32		145	0.26	1.2
40		152	0.27	1.1

70		171	0.33	0.8
100		176	0.36	0.7
130		179	0.39	0.8
160		178	0.43	0.9
180		180	0.40	0.8

Table 4. SANS results: structural model fit parameters of AY38/G5 prolonged kinetics at l_c = 3.0 (as shown in Figure 5b). The polydispersity of the spherical particles in size is given as PDI. The reduced χ^2 shows the quality of the fit.

Time/min	Shape	Radius/nm	PDI	χ^2
3		59	0.30	1.3
6		76	0.20	1.4
9		84	0.23	1.3
12		92	0.22	0.9
15		100	0.22	0.9
20		106	0.26	0.9
25		121	0.22	1.1
30		123	0.30	0.8
35		126	0.34	0.9
40		132	0.25	1.0
70		181	0.30	0.9
100		206	0.36	0.7
130		189	0.40	0.8
180		202	0.38	0.9

At l_c = 3.0, smaller spherical particles were observed compared to those at l_c = 2.0. This trend aligns with observations from post dye irradiation, where systems with higher charge ratios (l_c > 1.0) form smaller assemblies than those with lower charge ratios [23]. The underlying mechanism in both the methods involves an excess of azo dye molecules, which contribute additional free sulfonate groups and thus increase the overall charge density of the system. Each *cis* dye molecule retains two negatively charged sulfonate groups, similar to its *trans* counterpart, but exhibits a lower dipole moment, which significantly reduces its propensity for dipole-dipole interactions. As a result, the *cis* isomers remain primarily engaged in electrostatic interactions with the positively charged PAMAM dendrimers, rather than aggregating among themselves. The presence of these surplus *cis* dye ions plays a crucial stabilizing role: they provide an abundance of accessible sulfonate charges, effectively saturating the available dendrimer binding sites and leading to the formation of compact, monodisperse assemblies.

To compare growth across conditions when particle shapes evolve, we followed the single-particle geometric volume $V(t)$ extracted from the SANS structural model fits (Figure 6). Volumes were computed using $V_{Sphere} = \frac{4}{3}\pi R^3$ during the spherical stage and $V_{Ellipsoid} = \frac{4}{3}\pi abc$ (axes a, b, and c from the ellipsoidal stage with rotational symmetry) after the sphere → ellipsoid transition. For G4 at l_c = 2.0, $V(t)$ increases monotonically and plateaus at around 150 min, coincident with the spherical → ellipsoidal morphology change and the aspect-ratio jump reported above in Figure 4b. In contrast, AY38/G5 reaches a volume plateau earlier, at l_c = 2.0 and 3.0, with stabilization occurring at around 100 min, reflecting accelerated growth and earlier stabilization at higher generations. This generation-dependent kinetic acceleration is consistent with the higher valency of G5 (more charged amine groups) and more efficient charge compensation, which increases the capture rate of *trans*-AY38 and shortens the time required to reach electrostatic neutrality and structural stabilization. After the plateau has been reached, no further change in volume is observed within experimental uncertainty, indicating that an aggregation number increase via coalescence or continued unimer uptake may be negligible. Furthermore, from the SLS-SANS data, the forward-scattering intensity extrapolated to $q \rightarrow 0$ (I_0) can serve as an approximation for a relative aggregation number. It was determined and plotted versus time and versus SLS-SANS-derived particle volume in Figures S2 and S3. I_0 versus time tracks the volume growth one-to-one and plateaus at the same time, confirming that the intensity-based aggregation metric is consistent with the particle volume (Figure S2). In contrast, however, towards the end of the kinetic I_0 plateaus whereas volume keeps increasing as shown in Figure S3. As I_0 approximately represents the aggregation number, it suggests that the particles do not grow in terms of aggregation number anymore but the particle volume increases; i.e., particles rearrange into a looser structure.

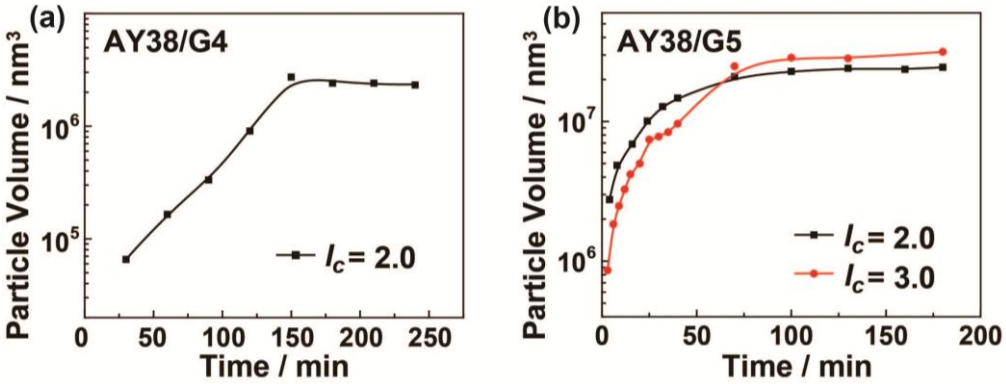


Figure 6. Time evolution of single-particle volume V(t) from SLS-SANS structural model fits for AY38/PAMAM assemblies (**a**) G4 at l_c = 2.0 and (**b**) G5 at l_c = 2.0 and 3.0. Volumes were calculated

from the fitted dimensions using $V_{sphere} = \frac{4}{3}\pi R^3$ and $V_{ellipsoid} = \frac{4}{3}\pi abc$ (ellipsoid with rotational symmetry). G4 at $l_c = 2.0$ shows a monotonic increase and plateau at ~150 min; G5 stabilizes earlier (≈100 min) at l_c = 2.0 and 3.0, consistent with higher dendrimer valency and faster charge-compensation–driven growth. Lines are guides to the eye.

Although the SANS data were initially collected at 1 min intervals with 38 m sample-to-detector distance experiments, the smallest time segment presented in Figure 5 is 3 min. This adjustment was necessary due to two limiting factors: a low signal-to-noise (S/N) ratio and minimal discernible changes in scattering profiles at shorter intervals. To address these issues, data were consolidated into 3 min segments to improve S/N and ensure meaningful kinetic trends could be observed between consecutive measurements.

Another notable difference is the size distribution of assemblies. In previous studies, high charge ratio samples ($l_c \geq 2.0$) often exhibit bimodal distributions, possibly due to the predominance of *trans* dye molecules, which promote dipole-dipole interactions [23]. In contrast, the slow kinetics method starts with irradiated azo dye solutions dominated by *cis* isomers. The limited dye-dye interactions in this case result in the formation of only monomodal assemblies, eliminating any bimodal distribution characteristic.

3.1.4. Charge Characteristics

Figure 7 presents the temporal evolution of the ζ-potential for assemblies formed via method A for AY38/G4 at $l_c = 2.0$ and AY38/G5 at $l_c = 2.0$ and $l_c = 3.0$. Since the self-assembly is electrostatically driven, the ζ-potential provides a complementary readout of the assembly charge development helping to understand the particle size control. For AY38/G4 at l_c = 2.0, ζ shifts from near-neutral values (≈0 mV) to strongly negative (≈–40 mV) over about 150 min, coinciding with the sphere → ellipsoid transition and the volume plateau (cf. Figure 6a). For AY38/G5 at $l_c = 2.0$, ζ is also near neutral initially but reaches a stable negative value at around 100 min; at $l_c = 3.0$, ζ is negative from the outset, reflecting excess anionic dye and stabilizes most rapidly. This behavior contrasts with post dye irradiation systems, where small, freshly formed aggregates exhibit strongly negative ζ and relax toward ≈ 0 mV as larger clusters form [4,18,23].

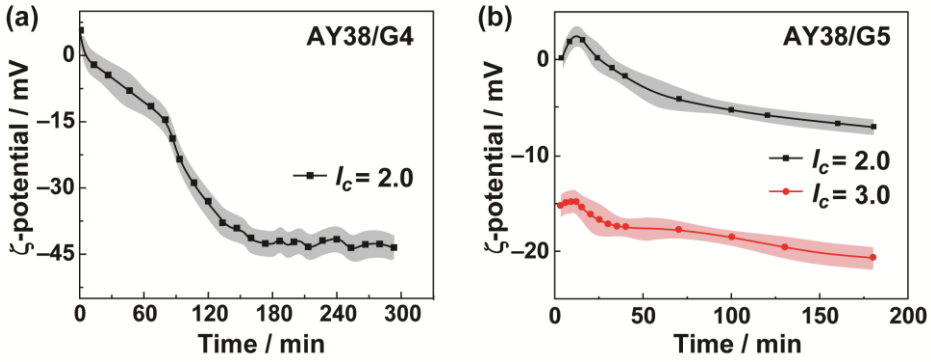


Figure 7. Time evolution of ζ-potential for AY38/PAMAM assemblies (**a**) G4 at $l_c = 2.0$ and (**b**) G5 at l_c = 2.0 and 3.0. The different colored shaded areas represent the error bars obtained from several repeated measurements.

Under method A, pre-irradiation enriches *cis*-AY38, yielding weak initial binding; as *cis* → *trans* proceeds, the more linear, highly ordered *trans* isomers pack densely on the dendrimer, increasing the density of sulfonate groups on the dendrimer-dye assembly and driving ζ to more negative values. The earlier plateau for G5 and/or higher l_c arises from higher dendrimer charges (more amine groups) and more efficient charge

compensation, which accelerates dye uptake and halts further growth once electrostatic neutrality is approached.

The corresponding time of the ζ potential reaching a plateau as seen in Figure 7 with the volume plateau observed in Figure 6 demonstrates (which is clearly expressed for G4 but also indicated for G5) that charge accumulation and morphological changes occur and stop simultaneously. From this correlation, we infer that once electrostatic neutrality is approached, further aggregation ceases, defining the charge saturation threshold for structural stabilization. The inverse relationship between size (or particle volume/surface area) and ζ-potential underscores the interplay between size growth and charge stabilization (Figure S4). The steady decrease in ζ-potential likely reduces electrostatic repulsion between partially formed aggregates, enabling further association and enlargement. After approximately 3 h, both parameters, ζ-potential and particle volume, plateau, indicating that the system has reached an equilibrium state where isomerization-driven assembly is complete and no further structural reorganization occurs.

To understand the interplay of the particle charge characteristics with growth across changing morphologies, we track the effective (electrokinetic) charge ζR as a function of time as shown in Figure 8. Here, R is the particle size taken from the SANS fits, $R = R_{sphere}$ during the spherical stage, and the equivalent-sphere radius $R_{eq} = (abc)^{1/3}$ from the ellipsoidal volume thereafter to enable shape-independent comparison. For AY38/G4 at l_c = 2.0, the charge increases from near zero to a stable negative plateau over about 150 min, coincident with the sphere → ellipsoid transition (Figure 4b) and the volume plateau (Figure 6a). AY38/G5 reaches a negative charge plateau earlier (≈120 min) at l_c = 2.0 and earliest (≈100 min) at l_c = 3.0, reflecting charge as a determining factor for assembly formation. The stronger (more negative) charge plateau at l_c = 3.0, despite smaller final sizes, indicates denser anionic charge per particle, consistent with excess dye charges at higher charge ratios. Interpreted within standard electrokinetic models at fixed ionic strength, ζ reflects the electrostatic potential at the particle's shear plane; multiplying by a characteristic length R provides a qualitative, effective charge indicator per particle. The temporal co-location of the charge plateau with the stabilization of volume and aspect ratio shows that morphological stabilization occurs once interfacial charge saturation is reached, even though *cis* → *trans* isomerization continues on longer timescales (cf. Figure 3).

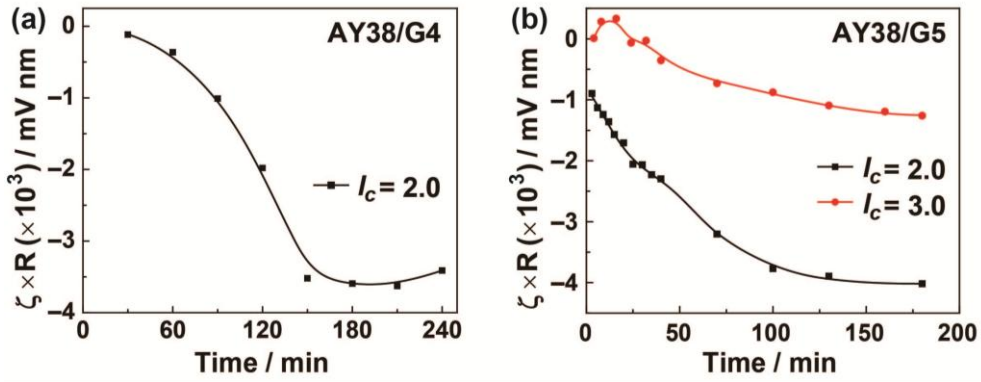


Figure 8. Time evolution of the effective (electrokinetic) particle charge ζR for AY38/PAMAM assemblies: (**a**) G4, l_c = 2.0; (**b**) G5, l_c = 2.0 and l_c =3.0. The size (R) of the particles is taken from SANS fits: $R = R_{sphere}$ for spherical particles and $R = (abc)^{1/3}$ from the fitted ellipsoidal axes for anisotropic particles (shape equivalence by volume).

Figure 9 shows the coordinated evolution of aspect ratio, single-particle volume, and effective charge (ζR) for AY38/G4 at l_c = 2.0. All three quantities change synchronously between 120 and 150 min: the aspect ratio jumps from 1 to ≈ 4, the volume plateaus, and

ζR reaches its inflection. This concurrence identifies the moment at which charge saturation halts further mass growth and initiates the sphere → ellipsoid transition. To visualize the coupling between morphology and interfacial charging, Figure 9 overlays three order parameters for AY38/G4 at l_c = 2.0: the aspect ratio (length/width) from SANS fits, the single-particle geometric volume $V(t)$, and the charge ζR. All traces change coordinately within the (120–150) min window: the aspect ratio jumps from 1 to ≥ 4, (t) approaches a plateau indicating that net mass uptake slows before shape fully arrests, and the charge reaches its plateau nearly concurrently. Together with Figures 6–8, this establishes the kinetic sequence: (i) dye uptake and surface charge buildup suppress further growth (volume plateau), (ii) once a charge saturation threshold is crossed (ζR plateau), (iii) anisotropic packing of *trans*-AY38 drives the sphere → ellipsoid reorganization to completion, after which both aspect ratio and electrokinetic signal remain stable.

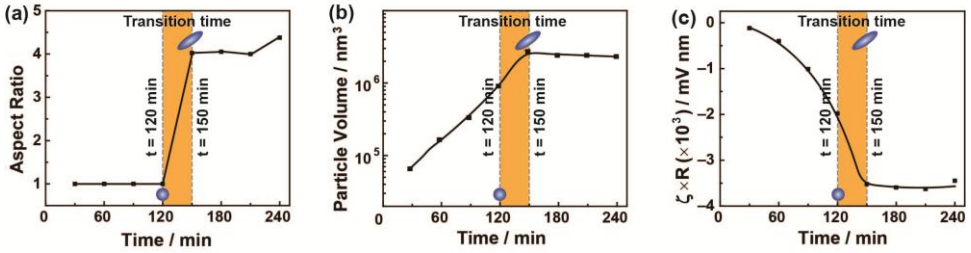


Figure 9. Coordinated transitions during the sphere → ellipsoid transformation for AY38/G4 at l_c = 2.0. (**a**) Aspect ratio (length/width) from SANS fits (unity for spheres; > 1 for ellipsoids). (**b**) Single-particle volume, computed from best-fit SANS data. (**c**) Charge (ζR), tracking effective charge. The shaded band denotes the 120–150 min transition window.

Having identified the time and charge thresholds for the sphere → ellipsoid transformation, we further examine how particle volume (mass) and the particle surface co-evolve with particle charge and with aspect ratio as shown in Figure 10. The Figure 10a relates the single-particle volume V to both the surface area S and the charge (ζR) for AY38/G4 at l_c = 2.0. Two regimes emerge. (i) Growth: volume and surface area increase together while charge becomes progressively more negative (stronger), reflecting dye uptake and interfacial charging. (ii) Reorganization: after the charge threshold is reached, the volume is essentially constant while the surface area continues to rise as assemblies convert from spheres to ellipsoids, consistent with the fact that spheres minimize surface area at a fixed volume. In Figure 10b, the co-location of the volume plateau with the ζR inflection and the rapid increase in aspect ratio indicates charge saturation-driven morphological arrest. Here, mass addition slows first, and then anisotropic packing of *trans*-AY38 increases interfacial area at near-constant volume until the ellipsoidal morphology stabilizes. Figure S5 shows the relation between charge and volume for AY38/G5 at l_c = 2.0 and 3.0, where charge decreases similarity to the AY38/G4 system with an increase in the particle volume.

Hence, UV-Vis spectroscopy and ζ-potential measurements were used to monitor dye isomerization and the evolution of surface charge during assembly formation. Once ionic saturation is reached, excess dye molecules promote further aggregation through dipole–dipole interactions until the system reaches equilibrium. As demonstrated by light and neutron scattering data presented above, the assemblies typically cease growing in size and shape after 1 to 3 h, depending on the charge ratio and dendrimer generation. Notably, UV-Vis absorption measurements (Figure 3a) continued to show ongoing *cis*-to-*trans* isomerization over a 10 h period. This indicates that, despite continued isomerization, the assemblies reach a structurally stable equilibrium and no longer

undergo further morphological changes. Importantly, the kinetics of assembly growth can be tuned by varying the charge ratio: lower charge ratios result in slower assembly growth, whereas higher charge ratios accelerate the process due to a greater availability of *trans* dye ions, which facilitates more efficient and stable binding with the dendrimer molecules.

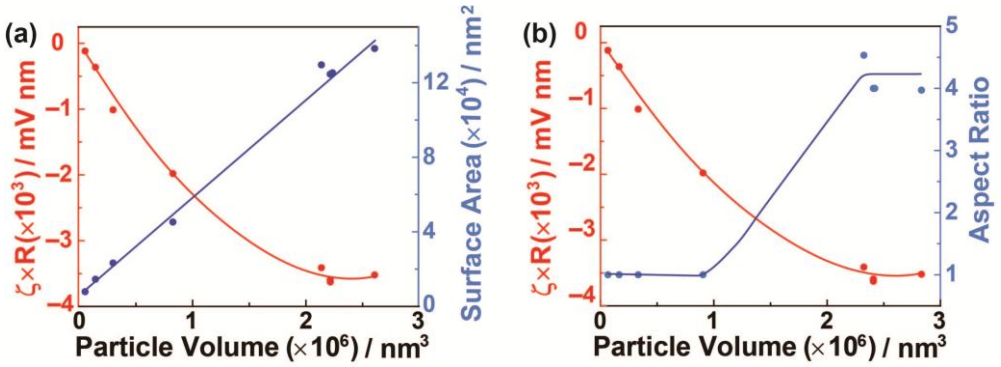


Figure 10. Coupling of particle volume V and particle surface area A with (**a**) particle charge ζR and (**b**) aspect ratio for AY38/G4 at l_c = 2.0. The particle volume, surface area, and the R (in $\zeta \times R$) are taken from the SANS results.

3.2. Fast Kinetics (Method B)

While method A enables a detailed, time-resolved view of the restructuring process, real-world applications often demand faster responsiveness. To this end, we employed method B, a rapid in situ irradiation strategy (Scheme 2) that induces self-assembly within minutes. Although the fast kinetics make it challenging to resolve intermediate states, method B validates the endpoint structures and supports the mechanism inferred from method A. Comparing both approaches provides a holistic understanding of the system's tunability, from slow, stepwise restructuring to rapid, responsive switching.

3.2.1. Light Scattering

Figure 11 illustrates the change in size distribution upon irradiation in the AY38/G4 system at l_c = 2.0 (preparation method B). The results are obtained using angular-dependent DLS, and the R_H values are calculated using Equation (6). Before irradiation, the nanoassemblies were R_H = (32 ± 4) nm in size, increasing to more than 10-fold, R_H = (396 ± 13) nm upon irradiation. Willerich et al. observed a similar trend but a lower size evolution (≈5-fold) under slightly different conditions [4].

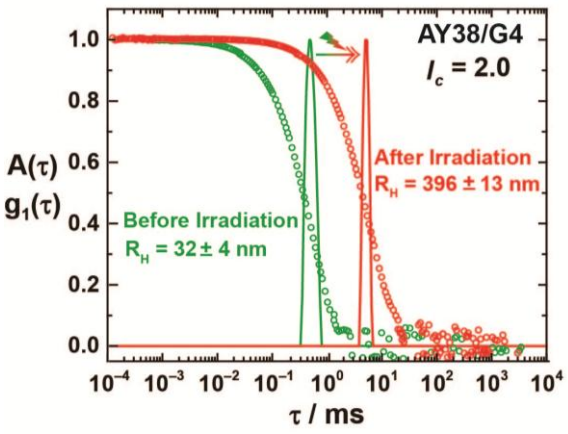


Figure 11. DLS of AY38/G4 system at l_c = 2.0 before (green) and after irradiation (red): electric field autocorrelation $g_1(\tau)$ (open circular symbols) and distribution of relaxation times $A(\tau)$ (lines) at a

scattering angle of $\theta = 90°$. (The R_H values are obtained by extrapolation to a 0° angle, $c_{AY38} = 1 \times 10^{-4}$ mol L^{-1}).

Using method B, the change caused by irradiation could be determined. However, the interest of the current study is to understand how the structures evolve and form while irradiating the sample and how the change in the degree of isomerization affects the structure. To the best of our knowledge, no prior work has systematically captured the formation dynamics of electrostatic assemblies under continuous UV irradiation. In situ monitoring using conventional techniques such as DLS, UV-Vis spectroscopy, or ζ-potential measurements poses significant technical challenges due to limitations in optical access and time resolution.

3.2.2. Small-Angle Neutron Scattering

As discussed, SANS under in situ UV irradiation was developed at the D11 beamline (Scheme 2a). Additionally, before and after 20 min of irradiation (when the particles are in a stable state), an extended SANS and SLS scan (0.0046 $nm^{-1} \leq q \leq 0.58$ nm^{-1}) has been performed to explore the whole structure of the nanoassemblies. The scan can take up to ≈ 1.5 to 2 h for the entire q-range. Whereas, to track the structural changes during irradiation, live SANS scans of 10 s each have been performed for the first 3 min and 60-s time slices for the next 17 min within a limited selected q-range (0.038 $nm^{-1} \leq q \leq 0.58$ nm^{-1}) at a 16.5 m sample-detector distance.

Results for the AY38/G5 system at l_c = 1.5 and 2.0 are shown in Figure 12. A quick evolution in the structure has been detected for up to 180 s, which then slows down later. This initial phase is likely driven by the fast *trans*-to-*cis* isomerization of AY38 under UV irradiation, which induces immediate changes in electrostatic interactions and triggers aggregation. As the irradiation continues, the system approaches a *cis*-enriched photostationary state, where the availability of *trans* dye molecules for further isomerization becomes limited, and the system begins to stabilize. Consequently, the rate of structural evolution slows down, transitioning into a more gradual reorganization process as the system asymptotically approaches a new equilibrium morphology. This biphasic behavior—initial rapid restructuring followed by a slower relaxation phase—is characteristic of many photoresponsive self-assembly systems and reflects the kinetic limitations imposed by the isomerization dynamics [35,36]. A transition from small aggregates to larger assemblies is indicated by the quickly declining plateau at the mid-q slope (0.038 $nm^{-1} \leq q \leq 0.060$ nm^{-1}), which increases from q^0 to q^4 over time. Although the full structure cannot be predicted with this limited q-range (0.038 $nm^{-1} \leq q \leq 0.58$ nm^{-1}), the particles certainly grow over time, as also confirmed by the end product in DLS studies.

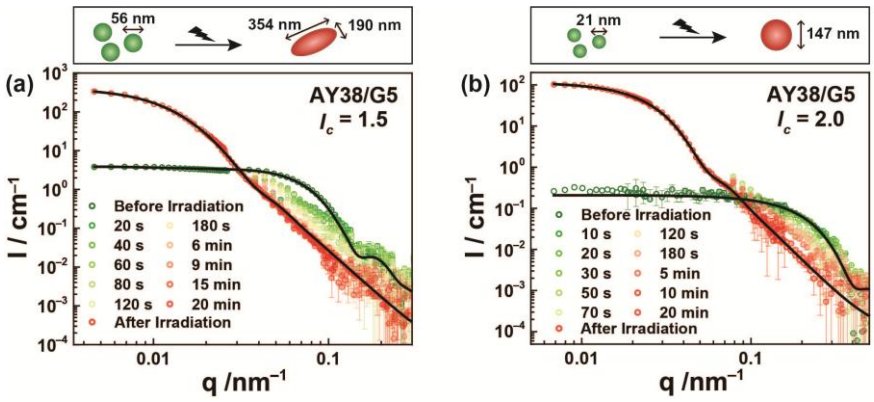


Figure 12. SANS of the AY38/G5 system at l_c = (**a**) 1.5, and (**b**) 2.0 before, during, and after UV irradiation at λ = 365 nm using method B. Irradiation was applied for 20 min. The illustrations at the

top of panels (**a**,**b**) represent the size and shape of the nanoassemblies before and after irradiation and correspond to the respective SANS data shown below. Each time-resolved SANS measurement was performed over 10-s intervals at a 16.5 m sample-to-detector distance and later summed when no further changes were observed across consecutive scans. To capture the complete structural profile, additional SANS and static light scattering (SLS) measurements were conducted separately on the same system before and after irradiation, once the assemblies had stabilized. These datasets were merged to extend the accessible q-range to 0.0046 $nm^{-1} \leq q \leq 4.9$ nm^{-1}. SANS measurements were performed at sample-detector distances of 1.4 and 16.5 m.

SANS helps in understanding the growth mechanism of the electrostatic assemblies. In Figure 12a,b, a substantial difference in size and shape can be observed, caused by irradiation. At $l_c = 1.5$, small spherically shaped nanoparticles of diameter 56 nm convert to ellipsoidal assemblies with an axial length of 190 nm and an equatorial length of 395 nm with a low polydispersity ($\sigma \leq 0.10$) due to irradiation. At $l_c = 2.0$, nanoparticle spheres of 21 nm convert into more than seven times larger spherical particles of 147 nm size. However, prior to irradiation, a few data points (obtained from SLS measurements) at low q do not fall within the range of a quality fit, which indicates traces of large aggregates coexisting with the small spherical particles.

Figure 13 presents the short-timescale SANS data for the AY38/G5 system at $l_c = 0.5$, 1.5, 2.0, and 3.0, along with their corresponding fits (particle volume is plotted as a function of time for the AY38/G5 system at $l_c = 0.5$, 1.5, 2.0, and 3.0 in Figure S6, and the detailed parameter information is provided in Tables S2–S5). As noted in our previous studies, an excess of positive charges from the dendrimers stabilizes the dye-dendrimer assemblies at $l_c = 0.5$. Consequently, no structural changes are observed upon irradiation in Figure 13a [4,23]. In contrast, for $l_c \geq 1.5$, significant changes in the scattering profiles are evident. These changes result from the excess dye ions that engage in dipole–dipole interactions. Upon UV irradiation, loosely bound dye ions partially dissociate from the assemblies. This weakens the electrostatic stabilization and leads to reduced particle stability. As a result, larger aggregates begin to form progressively over the course of the kinetics experiment.

The in situ SANS measurements under UV irradiation provide valuable insights into particle growth by self-assembly. The initial rapid increase in scattering intensity and the plateau behavior suggest a rapid assembly growth. The minimal changes in the scattering data observed beyond 180 s indicate a subsequent slower growth stage, revealing a two-step assembly process characterized by rapid initial aggregation followed by gradual structural evolution. However, the limited neutron flux on SANS instruments and large particle size (≈300–400 nm) do not allow for measuring the extended low q-range in a time-resolved manner as would be needed to identify the full assembly structures. Consequently, a full structural characterization using SANS is limited to the beginning and end of the irradiation period, where the sample remains stable and the full q-range can be effectively measured. In principle, this limitation could be mitigated by either increasing the concentration of the building blocks, thereby enhancing the scattering signal, or by slowing down the assembly process to allow adequate data collection within the accessible q-range. However, raising the concentration is not a viable option here, as it would introduce unwanted concentration-dependent effects on the self-assembly pathway [23].

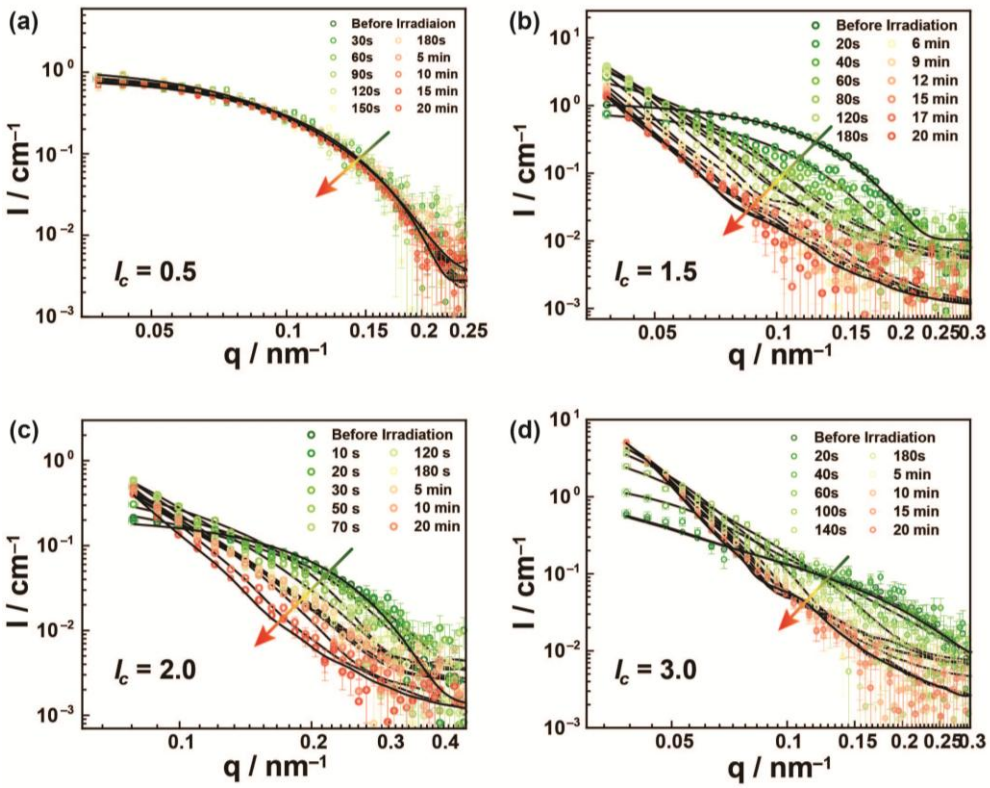


Figure 13. Short kinetics SANS results with their fitted data of the AY38/G5 system at l_c = (**a**) 0.5, (**b**) 1.5, (**c**) 2.0, and (**d**) 3.0. The colored arrows in the SANS plots represent the course of the dynamics.

4. Discussion

By integrating in situ SANS, multi-angle DLS and SLS, UV-Vis spectroscopy, and ζ-potential measurements, this study provides a mechanistic understanding of the dynamic (re)structuring process in photoresponsive dye-dendrimer assemblies in real time. The results demonstrate that photoisomerization kinetics directly dictate self-assembly dynamics. Across conditions, the kinetics follow a two-regime sequence: (i) a growth regime, in which particle volume $V(t)$ increases monotonically with nearly monodisperse size distributions (DLS $\sigma \leq 10\%$) and ζ becomes progressively more negative, and (ii) a reorganization regime, in which $V(t)$ has essentially plateaued while shape evolves from spheres to ellipsoids and charge ζR reaches an inflection/plateau (Figures 4–8).

The juxtaposition in Figure 9 shows a threshold behavior: the sphere → ellipsoid transition initiates once the charge trace crosses its inflection point, after which the aspect ratio rises sharply while the volume remains nearly constant. At the molecular level, this sequence reflects the increasing *cis* → *trans* isomerization (or slow thermal back-isomerization in method A). *Cis*-rich states exhibit weaker, less ordered binding and low initial surface coverage. As *trans*-AY38 accumulates, the more linear, highly ordered isomers promote denser, directional packing on the dendrimer, increasing the surface density of sulfonate groups and driving ζ to more negative values. Once a charge saturation threshold is reached (Figure 9), further mass uptake is suppressed (volume plateau), and anisotropic packing of *trans*-AY38 completes the sphere → ellipsoid reorganization.

The dendrimer generation and charge ratio l_c tune both the timescale and the endpoint of this pathway. G5 (higher valency) reaches electrokinetic plateaus and structural arrest earlier than G4, and higher l_c accelerates stabilization further (Figures 6–8). Mechanistically, a larger number of amine groups and/or greater dye excess enhance charge compensation and capture rates, allowing the system to attain the charge threshold

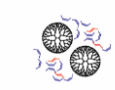
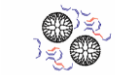
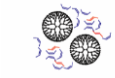
sooner and to stabilize at smaller final sizes. Conversely, lower l_c delays charge saturation and favors larger, more extended assemblies. Importantly, the kinetic protocol matters: under slow kinetics (method A) conditions, ζ evolves from near-neutral to strongly negative as *trans* content builds; in contrast, fast kinetics (method B) yields the opposite ζ trend at early times, underscoring that pathway dependence arises from how isomerization, adsorption, and growth are temporally coupled.

Together, these results move beyond endpoint characterization to deliver a predictive, process-aware framework: by jointly monitoring $V(t)$, aspect ratio, and charge ζR, one can identify (i) a diffusion-controlled uptake regime, (ii) a charge saturation threshold that precipitates morphological change, and (iii) a shape-locking regime governed by a balance between electrostatic repulsion and dipole–dipole attraction. Tables 5 and 6 summarize method sensitivities and the morphology map versus generation and l_c. This framework enables temporal programming of structure tuning, not only of the final morphology but also of when and how it is reached via light-controlled modulation of isomer populations and interfacial charge. While full reversibility and deliberate capture of intermediate states remain challenges, the demonstrated control over the restructuring pathway itself opens avenues for time-encoded delivery platforms, reconfigurable soft materials, and other stimuli-responsive nanotechnologies.

Table 5. Comparison between method A and method B.

Key Features	Pre-Irradiation (Method A)	Post-Irradiation (Method B)
Kinetics	Slow kinetics, ≈3 h	Fast kinetics, <20 min
Irradiation	Pre-irradiated AY38 (*cis* state) before assembly	UV irradiation during self-assembly
Properties	Allows controlled, stepwise formation, ideal for detailed analysis	Captures immediate, rapid transformations

Table 6. Summary of the shapes observed, calculated from SLS-SANS data prior to or after the irradiation using pre- and post-irradiation methods for AY38 assemblies with different dendrimer generations at multiple charge ratios. Method A represents multiple steps of the assembly growth until the system stabilizes (t_0 = 0–30 min, t_m = 30–150 min, and t_f = > 150 min), whereas method B only shows the start and the end product.

Pre-Irradiation (Method A)					
System ID	l_c	**After Irradiation (t_{-1})**	**t_0**	**t_m**	**t_f**
AY38/G4	2.0				
AY38/G5	2.0				
	3.0				
Post-Irradiation (Method B)					
System ID	l_c	**Before Irradiation**		**After Irradiation**	
AY38/G4	1.5				

AY38/G5	1.5		
	2.0		

5. Conclusions

This work establishes a direct, time-resolved link between photoisomerization kinetics and self-assembly dynamics in AY38/PAMAM systems. By combining in situ SANS with multi-angle DLS and SLS, UV-Vis, and ζ-potential measurements, it shows that light-controlled *cis* → *trans* conversion governs both when and how structure forms: particle volume grows first, an electrokinetic charge threshold is reached, and only then does a sphere → ellipsoid reorganization complete. The result is a mechanistic picture in which the interplay of photoisomerization and electrostatic interactions determines the resulting morphology.

Two kinetic pathways underscore the role of the protocol employed. Method A (slow kinetics; pre-irradiated *cis*, then assembly) spreads growth and restructuring over hours, enabling detailed mapping of thresholds and transitions, while Method B (fast kinetics; in situ irradiation) yields rapid aggregation and switching (≈20 min). System parameters tune both rate and endpoint: higher charge ratio ($l_c \geq 3.0$) and higher dendrimer generation accelerate charge compensation, advance the onset of shape change, and stabilize smaller aggregates; a lower l_c prolongs growth and favors larger, more extended assemblies. Across conditions, the observed sphere → ellipsoid transition confirms that electrostatics coupled with dipole–dipole interactions, regulates morphology.

Together, these findings move beyond endpoint characterization to provide a process-aware design framework for adaptive nanomaterials: morphology and timescale of response can be programmed by modulating isomer populations and interfacial charge in real time. The approach is broadly transferable, and future work can extend it to alternative photochromes, ionic strengths, and solvent environments to refine control over light-mediated self-assembly and to realize temporally encoded functions in delivery, reconfigurable soft matter, and other stimuli-responsive technologies.

Supplementary Materials: The following supporting information can be downloaded at: https://www.mdpi.com/article/10.3390/polym18020189/s1, Figure S1: Comparison of spherical and ellipsoidal model fits to the long-kinetics SANS data of AY38/G4 at $l_c = 2.0$ for the 30 min acquisition spanning 120–150 min. (**a**) Best fits of the spherical and ellipsoidal form-factor models to the scattering data. (**b**) Corresponding fit residuals; Figure S2: Time evolution of the forward-scattering intensity extrapolated to $q \to 0$ (I_0) from SANS, used here as a proxy for aggregate mass. The data is shown for AY38/G4 assemblies at $l_c = 2.0$ and AY38/G5 assemblies at $l_c = 2.0$ and $l_c = 3.0$; Figure S3: Direct relation between I_0 and the particle volume V calculated using SANS data for AY38/PAMAM dendrimer assemblies of (**a**) G4, $l_c = 2.0$, and (**b**) G5, $l_c = 2.0$ and $l_c = 3.0$. The dotted lines are to guide the eyes to follow the particle volume increase with I_0; Figure S4: For the AY38/PAMAM dendrimer assemblies, ζ-potential values are plotted as a function of particle volume for (a) G4, at $l_c = 2.0$, (b) G5 at $l_c = 2.0$, $l_c = 3.0$ and as a function of particle surface area for (c) G4, at $l_c = 2.0$, and (d) G5 at $l_c = 2.0$, $l_c = 3.0$. The dotted lines are used to guide the eyes to follow the change in ζ-potential values when the particle volume and the surface area change. Volumes and areas are computed from SANS best-fit dimensions; Figure S5: Time evolution of the charge (ζR) for AY38/G5 assemblies at G5, $l_c = 2.0$ and $l_c = 3.0$. Size R is taken from SANS fits. The dotted lines are used to guide the eyes to follow the change in charge values when the particle volume changes; Figure S6: Particle volume calculated

using fast kinetics SANS results with their fitted data of the AY38/G5 system at l_c = 0.5, 1.5, 2.0, and 3.0; Table S1: SANS Results: Comparison of ellipsoidal and spherical model fit parameters of AY38/G4 long kinetics at l_c = 2.0. The radius of the spherical particles is given as R_{min}; in the case of ellipsoidal particles, R_{min} shows two axial radii, and R_{maj} shows the equatorial radius. Polydispersity in size is given as PDI. The reduced χ^2 shows the quality of the fit; Table S2: SANS Results: Structural model fit parameters of AY38/G5 short kinetics at l_c = 3.0. The radius of the cylindrical particles is given as R and the length as L. The polydispersity of the particles is given as PDI. The reduced χ^2 shows the quality of the fit; Table S3: SANS Results: Structural model fit parameters of AY38/G5 short kinetics at l_c = 1.5. The radius of the spherical particles is given as R_{min}; in the case of ellipsoidal particles, R_{min} shows two axial radii, and R_{maj} shows the equatorial radius. Polydispersity in size is given as PDI. The reduced χ^2 shows the quality of the fit; Table S4: SANS Results: Structural model fit parameters of AY38/G5 short kinetics at l_c = 2.0. The polydispersity of the spherical particles in size is given as PDI. The reduced χ^2 shows the quality of the fit; Table S5: SANS Results: Structural model fit parameters of AY38/G5 short kinetics at l_c = 3.0. The polydispersity of the spherical particles in size is given as PDI. The reduced χ^2 shows the quality of the fit.

Author Contributions: Conceptualization, R.S. and F.G.; Methodology, M.A. and R.S.; Software, M.A.; Validation, R.S. and F.G.; Formal analysis, M.A.; Investigation, M.A.; Resources, R.S. and F.G.; Writing—original draft, M.A.; Writing—review and editing, R.S. and F.G.; Visualization, M.A.; Supervision, R.S. and F.G.; Funding acquisition, R.S. and F.G. All authors have read and agreed to the published version of the manuscript.

Funding: Funding of the Institute Laue Langevin (ILL), Grenoble, France (ILL PhD student program), and of the German Science Foundation (DFG, GR 2701/3-2) and the Interdisciplinary Center for Molecular Materials (ICMM, Friedrich-Alexander-Universität Erlangen-Nürnberg) is gratefully acknowledged.

Data Availability Statement: The data presented are included in this study. SANS data will be available at https://doi.ill.fr/10.5291/ILL-DATA.9-12-662 (accessed on 30 August 2021), and https://doi.ill.fr/10.5291/ILL-DATA.9-11-2079 (accessed on 28 September 2021).

Acknowledgments: Support by Institut Laue-Langevin (ILL) Grenoble, France, the German Science Foundation (DFG), and the interdisciplinary Center for Molecular Materials (ICMM, Universität Erlangen-Nürnberg) is gratefully acknowledged. The Partnership for Soft Condensed Matter (PSCM) is thankfully acknowledged. This work benefited from the SasView 4.2.2 application, initially developed by the DANSE project under NSF award DMR-0520547.

Conflicts of Interest: The authors declare no conflicts of interest.

References

1. Guan, Y.; Antonietti, M.; Faul, C.F.J. Ionic Self-Assembly of Dye-Surfactant Complexes: Influence of Tail Lengths and Dye Architecture on the Phase Morphology. *Langmuir* **2002**, *18*, 5939–5945. https://doi.org/10.1021/la0257182.
2. Faul, C.F.J.; Antonietti, M. Ionic Self-Assembly: Facile Synthesis of Supramolecular Materials. *Adv. Mater.* **2003**, *15*, 673–683. https://doi.org/10.1002/adma.200300379.
3. Rehm, T.; Schmuck, C. How to Achieve Self-Assembly in Polar Solvents Based on Specific Interactions? Some General Guidelines. *Chem. Commun.* **2008**, 801–813. https://doi.org/10.1039/b710951m.
4. Willerich, I.; Gröhn, F. Photoswitchable Nanoassemblies by Electrostatic Self-Assembly. *Angew. Chemie-Int. Ed.* **2010**, *49*, 8104–8108. https://doi.org/10.1002/anie.201003271.
5. Ghosh, A.; Haverick, M.; Stump, K.; Yang, X.; Tweedle, M.F.; Goldberger, J.E. Fine-Tuning the PH Trigger of Self-Assembly. *J. Am. Chem. Soc.* **2012**, *134*, 3647–3650. https://doi.org/10.1021/ja211113n.
6. Krieger, A.; Zika, A.; Gröhn, F. Functional Nano-Objects by Electrostatic Self-Assembly: Structure, Switching, and Photocatalysis. *Front. Chem.* **2022**, *9*, 1–46. https://doi.org/10.3389/fchem.2021.779360.
7. Dai, S.; Ravi, P.; Tam, K.C. PH-Responsive Polymers: Synthesis, Properties and Applications. *Soft Matter* **2008**, *4*, 435–449. https://doi.org/10.1039/b714741d.

8. Dai, S.; Ravi, P.; Tam, K.C. Thermo- and Photo-Responsive Polymeric Systems. *Soft Matter* **2009**, *5*, 2513–2533. https://doi.org/10.1039/b820044k.
9. Reinhold, F.; Kolb, U.; Lieberwirth, I.; Gröhn, F. Assemblies of Double Hydrophilic Block Copolymers and Oppositely Charged Dendrimers. *Langmuir* **2009**, *25*, 1345–1351. https://doi.org/10.1021/la8027594.
10. Ruthard, C.; Schmidt, M.; Gröhn, F. Porphyrin-Polymer Networks, Worms, and Nanorods: PH-Triggerable Hierarchical Self-Assembly. *Macromol. Rapid Commun.* **2011**, *32*, 706–711. https://doi.org/10.1002/marc.201100097.
11. Mariani, G.; Schweins, R.; Gröhn, F. Electrostatic Self-Assembly of Dendrimer Macroions and Multivalent Dye Counterions: The Role of Solution Ionic Strength. *Macromolecules* **2016**, *49*, 8661–8671. https://doi.org/10.1021/acs.macromol.6b00565.
12. Fuentes, E.; Gerth, M.; Berrocal, J.A.; Matera, C.; Gorostiza, P.; Voets, I.K.; Pujals, S.; Albertazzi, L. An Azobenzene-Based Single-Component Supramolecular Polymer Responsive to Multiple Stimuli in Water. *J. Am. Chem. Soc.* **2020**, *142*, 10069–10078. https://doi.org/10.1021/jacs.0c02067.
13. Faul, C.F.J. Ionic Self-Assembly for Functional Hierarchical Nanostructured Materials. *Acc. Chem. Res.* **2014**, *47*, 3428–3438. https://doi.org/10.1021/ar500162a.
14. Grzybowski, B.A.; Fitzner, K.; Paczesny, J.; Granick, S. From Dynamic Self-Assembly to Networked Chemical Systems. *Chem. Soc. Rev.* **2017**, *46*, 5647–5678. https://doi.org/10.1039/c7cs00089h.
15. Klajn, R. Spiropyran-Based Dynamic Materials. *Chem. Soc. Rev.* **2014**, *43*, 148–184. https://doi.org/10.1039/c3cs60181a.
16. Bian, T.; Chu, Z.; Klajn, R. The Many Ways to Assemble Nanoparticles Using Light. *Adv. Mater.* **2019**, *32*, 1905866. https://doi.org/10.1002/adma.201905866.
17. Blayo, C.; Kelly, E.A.; Houston, J.E.; Khunti, N.; Cowieson, N.P.; Evans, R.C. Light-Responsive Self-Assembly of a Cationic Azobenzene Surfactant at High Concentration. *Soft Matter* **2020**, *16*, 9183–9187. https://doi.org/10.1039/d0sm01512a.
18. Agarwal, M.; Zika, A.; Yücel, M.; Schweins, R.; Kohlbrecher, J.; Gröhn, F. The Role of Light Irradiation and Dendrimer Generation in Directing Electrostatic Self-Assembly. *Polymers* **2025**, *17*, 170. https://doi.org/10.3390/polym17020170.
19. Klajn, R.; Bishop, K.J.M.; Grzybowski, B.A. Light-Controlled Self-Assembly of Reversible and Irreversible Nanoparticle Suprastructures. *Proc. Natl. Acad. Sci. USA* **2007**, *104*, 10305–10309. https://doi.org/10.1073/pnas.0611371104.
20. Nalluri, S.K.M.; Ravoo, B.J. Light-Responsive Molecular Recognition and Adhesion of Vesicles. *Angew. Chemie-Int. Ed.* **2010**, *49*, 5371–5374. https://doi.org/10.1002/anie.201001442.
21. Fischer, W.; Quadir, M.A.; Barnard, A.; Smith, D.K.; Haag, R. Controlled Release of DNA from Photoresponsive Hyperbranched Polyglycerols with Oligoamine Shells. *Macromol. Biosci.* **2011**, *11*, 1736–1746. https://doi.org/10.1002/mabi.201100248.
22. Kundu, P.K.; Samanta, D.; Leizrowice, R.; Margulis, B.; Zhao, H.; Börner, M.; Udayabhaskararao, T.; Manna, D.; Klajn, R. Light-Controlled Self-Assembly of Non-Photoresponsive Nanoparticles. *Nat. Chem.* **2015**, *7*, 646–652. https://doi.org/10.1038/nchem.2303.
23. Agarwal, M.; Zika, A.; Schweins, R.; Gröhn, F. Controlling the Morphology in Electrostatic Self-Assembly via Light. *Polymers* **2023**, *16*, 50. https://doi.org/10.3390/polym16010050.
24. Xu, J.F.; Chen, Y.Z.; Wu, D.; Wu, L.Z.; Tung, C.H.; Yang, Q.Z. Photoresponsive Hydrogen-Bonded Supramolecular Polymers Based on a Stiff Stilbene Unit. *Angew. Chemie-Int. Ed.* **2013**, *52*, 9738–9742. https://doi.org/10.1002/anie.201303496.
25. Stricker, L.; Fritz, E.C.; Peterlechner, M.; Doltsinis, N.L.; Ravoo, B.J. Arylazopyrazoles as Light-Responsive Molecular Switches in Cyclodextrin-Based Supramolecular Systems. *J. Am. Chem. Soc.* **2016**, *138*, 4547–4554. https://doi.org/10.1021/jacs.6b00484.
26. Crespi, S.; Simeth, N.A.; König, B. Heteroaryl Azo Dyes as Molecular Photoswitches. *Nat. Rev. Chem.* **2019**, *3*, 133–146. https://doi.org/10.1038/s41570-019-0074-6.
27. Carl, N.; Müller, W.; Schweins, R.; Huber, K. Controlling Self-Assembly with Light and Temperature. *Langmuir* **2020**, *36*, 223–231. https://doi.org/10.1021/acs.langmuir.9b03040.
28. Gröhn, F. Soft Matter Nanoparticles with Various Shapes and Functionalities Can Form through Electrostatic Self-Assembly. *Soft Matter* **2010**, *6*, 4296–4302. https://doi.org/10.1039/c0sm00411a.
29. Aida, T.; Meijer, E.W.; Stupp, S.I. Functional Supramolecular Polymers. *Science* **2012**, *335*, 813–817. https://doi.org/10.1126/science.1205962.
30. Willerich, I.; Gröhn, F. Thermodynamics of Photoresponsive Polyelectrolyte-Dye Assemblies with Irradiation Wavelength Triggered Particle Size. *Macromolecules* **2011**, *44*, 4452–4461. https://doi.org/10.1021/ma200538e.
31. Zika, A.; Agarwal, M.; Schweins, R.; Gröhn, F. Joining Two Switches in One Nano-object: Photoacidity and Photoisomerization in Electrostatic Self-assembly. *Chem.–A Eur. J.* **2022**, *29*, 1–7. https://doi.org/10.1002/chem.202203373.
32. Huang, Z.; Jiang, T.; Wang, J.; Ma, X.; Tian, H. Real-Time Visual Monitoring of Kinetically Controlled Self-Assembly. *Angew. Chemie* **2021**, *133*, 2891–2896. https://doi.org/10.1002/ange.202011740.

33. Jensen, G.V.; Lund, R.; Gummel, J.; Monkenbusch, M.; Narayanan, T.; Pedersen, J.S. Direct Observation of the Formation of Surfactant Micelles under Nonisothermal Conditions by Synchrotron SAXS. *J. Am. Chem. Soc.* **2013**, *135*, 7214–7222. https://doi.org/10.1021/ja312469n.
34. Jensen, G.V.; Lund, R.; Gummel, J.; Narayanan, T.; Pedersen, J.S. Monitoring the Transition from Spherical to Polymer-like Surfactant Micelles Using Small-Angle X-Ray Scattering. *Angew. Chemie-Int. Ed.* **2014**, *53*, 11524–11528. https://doi.org/10.1002/anie.201406489.
35. Lund, R.; Brun, G.; Chevallier, E.; Narayanan, T.; Tribet, C. Kinetics of Photocontrollable Micelles: Light-Induced Self-Assembly and Disassembly of Azobenzene-Based Surfactants Revealed by TR-SAXS. *Langmuir* **2016**, *32*, 2539–2548. https://doi.org/10.1021/acs.langmuir.5b04711.
36. Kelly, E.A.; Houston, J.E.; Evans, R.C. Probing the Dynamic Self-Assembly Behaviour of Photoswitchable Wormlike Micelles in Real-Time. *Soft Matter* **2019**, *15*, 1253–1259. https://doi.org/10.1039/c8sm01948g.
37. Robinson, C.; Mills, H.A.T. The Colloid Chemistry of Dyes: The Aqueous Solutions of Benzopurpurine 4B and Its Isomer Prepared from m-Tolidine. *Part I. Proc. R. Soc. London Ser. A* **1931**, *131*, 576–595.
38. Moldenhauer, D.; Gröhn, F. Nanoassemblies with Light-Responsive Size and Density from Linear Flexible Polyelectrolytes. *J. Polym. Sci. Part B Polym. Phys.* **2013**, *51*, 802–816. https://doi.org/10.1002/polb.23276.
39. Glasoe, P.K.; Long, F.A. Use of Glass Electrodes to Measure Acidities in Deuterium Oxide. *J. Phys. Chem.* **1960**, *64*, 188–190. https://doi.org/10.1021/j100830a521.
40. Covington, A.K.; Paabo, M.; Robinson, R.A.; Bates, R.G. Use of the Glass Electrode in Deuterium Oxide and the Relation between the Standardized PD (PaD) Scale and the Operational PH in Heavy Water. *Anal. Chem.* **1968**, *40*, 700–706. https://doi.org/10.1021/ac60260a013.
41. Krężel, A.; Bal, W. A Formula for Correlating PKa Values Determined in D 2O and H2O. *J. Inorg. Biochem.* **2004**, *98*, 161–166. https://doi.org/10.1016/j.jinorgbio.2003.10.001.
42. Rubinson, K.A. Practical Corrections for p(H,D) Measurements in Mixed H2O/D2O Biological Buffers. *Anal. Methods* **2017**, *9*, 2744–2750. https://doi.org/10.1039/c7ay00669a.
43. Schärtl, W. *Light Scattering from Polymer Solutions and Nanoparticle Dispersions*; Springer: Berlin/Heidelberg, Germany, 2007; pp. 1–24, ISBN 9783540719519.
44. Provencher, S.W. Contin: A General Purpose Constrained Regularization Program for Inverting Noisy Linear Algebraic and Integral Equations. *Comput. Phys. Commun.* **1982**, *27*, 229–242.
45. Provencher, S.W. Inverse Problems in Polymer Characterization: Direct Analysis of Polydispersity with Photon Correlation Spectroscopy. *Die Makromol. Chemie* **1979**, *180*, 201–209.
46. Zimm, B.H. The Scattering of Light and the Radial Distribution Function of High Polymer Solutions. *J. Chem. Phys.* **1948**, *16*, 1093–1099. https://doi.org/10.1063/1.1746738.
47. Guinier, A.; Fouret, G. *Small-Angle Scattering of X-Rays*; John Wiley Sons, Inc.: New York, NY, USA, 1955; Volume 18, pp. 5–78. https://doi.org/10.1016/0146-3535(89)90023-3.
48. Smoluchowski., M.v. Molekular-Kinetische Theorie Der Opaleszenz von Gasen Im Kritischen Zustande, Sowie Einiger Verwandter Erscheinungen. *Ann. Phys.* **1908**, *330*, 205–226. https://doi.org/10.1002/andp.19083300203.
49. Polaczyk, A.L.; Amburgey, J.E.; Alansari, A.; Poler, J.C.; Propato, M.; Hill, V.R. Calculation and Uncertainty of Zeta Potentials of Microorganisms in a 1:1 Electrolyte with a Conductivity Similar to Surface Water. *Colloids Surf. A Physicochem. Eng. Asp.* **2020**, *586*, 124097. https://doi.org/10.1016/j.colsurfa.2019.124097.
50. Feigin, L.A.; Svergun, D.I. *Structure Analysis by Small-Angle X-Ray and Neutron Scattering*; Plenum Press: New York, NY, USA;, 1987.
51. Isihara, A. Determination of Molecular Shape by Osmotic Measurement. *J. Chem. Phys.* **1950**, *18*, 1446–1449. https://doi.org/10.1063/1.1747510.
52. Arnold, O.; Bilheux, J.C.; Borreguero, J.M.; Buts, A.; Campbell, S.I.; Chapon, L.; Doucet, M.; Draper, N.; Ferraz Leal, R.; Gigg, M.A.; et al. Mantid—Data Analysis and Visualization Package for Neutron Scattering and μ SR Experiments. *Nucl. Instrum. Methods Phys. Res. Sect. A Accel. Spectrometers Detect. Assoc. Equip.* **2014**, *764*, 156–166. https://doi.org/10.1016/j.nima.2014.07.029.

Disclaimer/Publisher's Note: The statements, opinions and data contained in all publications are solely those of the individual author(s) and contributor(s) and not of MDPI and/or the editor(s). MDPI and/or the editor(s) disclaim responsibility for any injury to people or property resulting from any ideas, methods, instructions or products referred to in the content.

Supporting Information

Light-Induced Structural Evolutions in Electrostatic Nanoassemblies

Mohit Agarwal [1,2], Ralf Schweins [2] and Franziska Gröhn [1,*]

[1] Department of Chemistry and Pharmacy, Interdisciplinary Center for Molecular Materials, Friedrich-Alexander Universität Erlangen-Nürnberg, Egerlandstr. 3, D-91058 Erlangen, Germany; mohit.agarwal@fau.de
[2] Institut Laue-Langevin, DS/LSS, 71 Avenue des Martyrs, F-38000 Grenoble, France; schweins@ill.eu
* Correspondence: franziska.groehn@fau.de; Tel.: +49-913-185-20731

Additional Results:

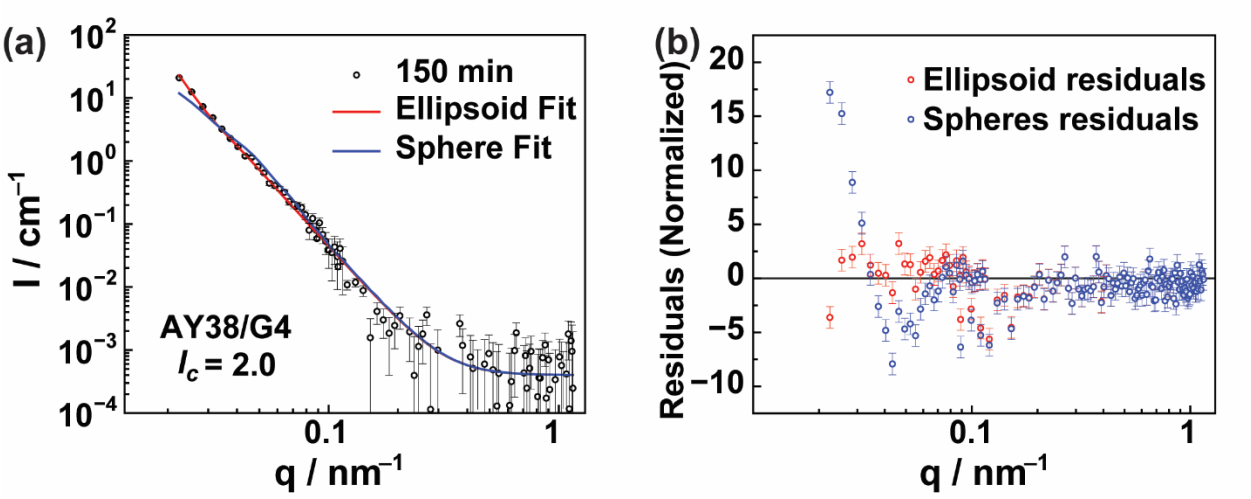


Figure S1. Comparison of spherical and ellipsoidal model fits to the long-kinetics SANS data of AY38/G4 at l_c = 2.0 for the 30 min acquisition spanning 120–150 min. **(a)** Best fits of the spherical and ellipsoidal form-factor models to the scattering data. **(b)** Corresponding fit residuals.

Table S1. SANS Results: Comparison of Ellipsoidal and spherical model fit parameters of AY38/G4 long kinetics at l_c = 2.0. The radius of the spherical particles is given as Rmin; in the case of ellipsoidal particles, Rmin shows two axial radii, and Rmaj shows the equatorial radius. Polydispersity in size is given as PDI. The reduced χ^2 shows the quality of the fit.

Time/min	Shape	R_{min} /nm	PDI (R_{min})	R_{maj} /nm	PDI (R_{maj})	χ^2
150		35	0.30	139	0.02	2.0
150		130	0.30			8.2

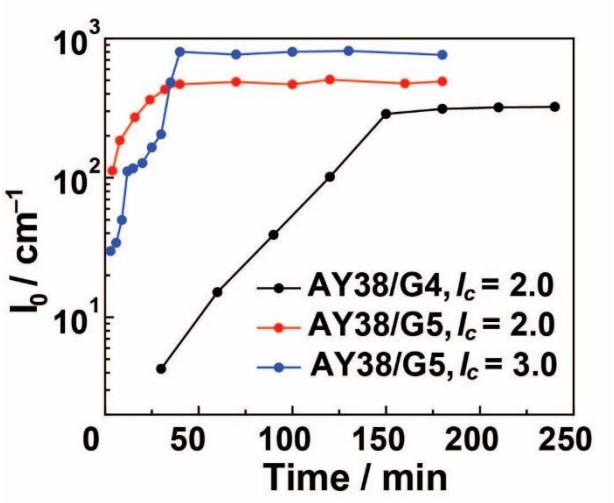


Figure S2. Time evolution of the forward-scattering intensity extrapolated to q→0 (I_0) from SANS, used here as a proxy for aggregate mass. The data is shown for AY38/G4 assemblies at l_c = 2.0, and AY38/G5 assemblies at l_c = 2.0 and l_c = 3.0.

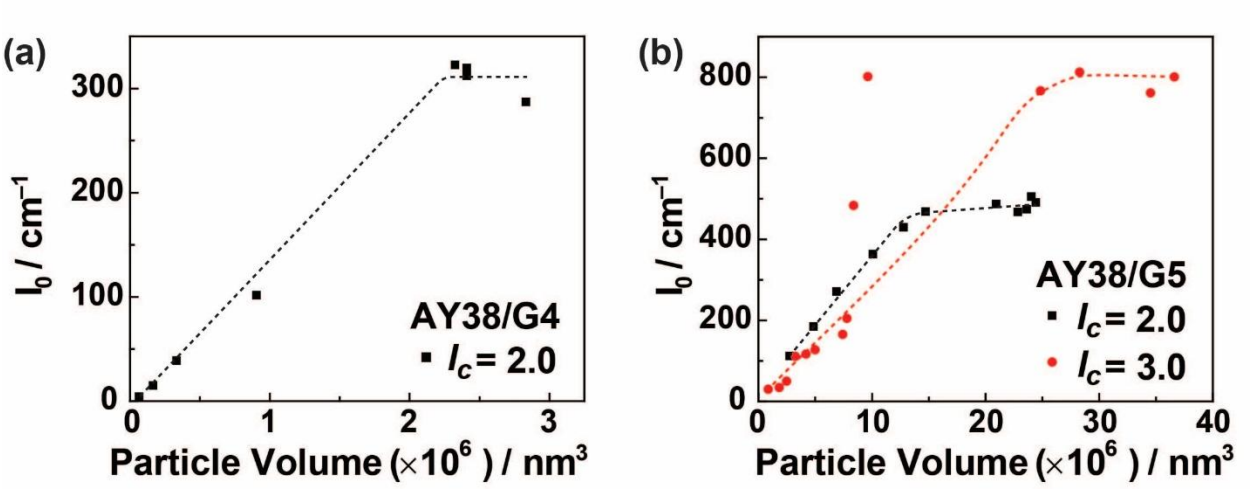


Figure S3. Direct relation between I_0 and the particle volume V calculated using SANS data for AY38/PAMAM dendrimer assemblies of **(a)** G4, l_c = 2.0, and **(b)** G5, l_c = 2.0 and l_c = 3.0. The dotted lines are guide to the eyes to follow the particle volume increase with I_0.

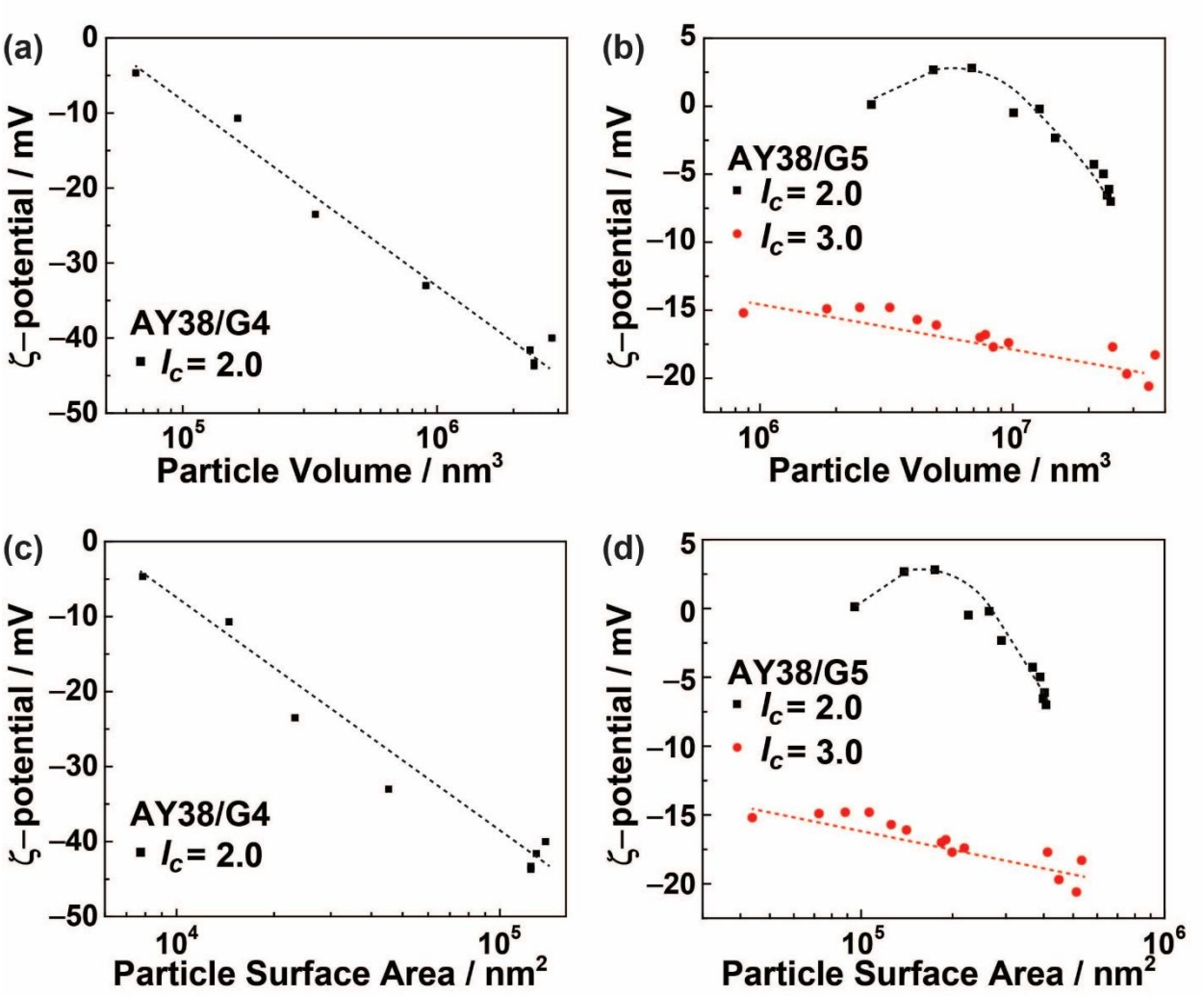


Figure S4. For the AY38/PAMAM dendrimer assemblies, ζ-potential values are plotted as a function of particle volume for (a) G4, at l_c = 2.0, (b) G5 at l_c = 2.0, l_c = 3.0 and as a function of particle surface area for (c) G4, at l_c = 2.0, (d) G5 at l_c = 2.0, l_c = 3.0. The dotted lines are used to guide the eyes to follow the change in ζ-potential values when the particle volume and the surface area change. Volumes and areas are computed from SANS best-fit dimensions.

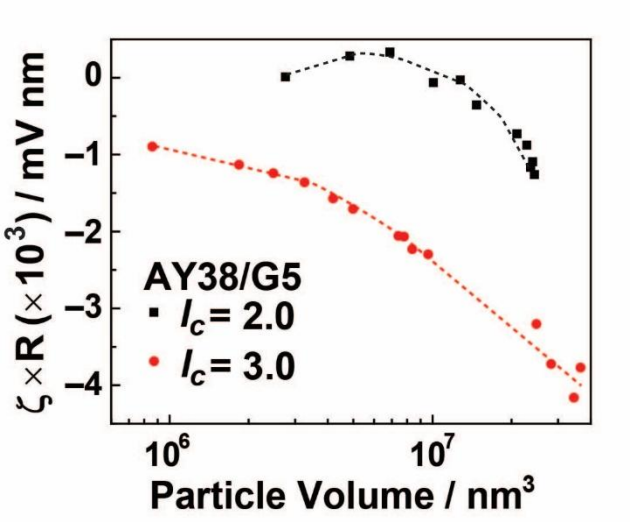


Figure S5. Time evolution of the charge (ζR) for AY38/G5 assemblies at G5, l_c = 2.0 and l_c =3.0. Size R is taken from SANS fits. The dotted lines are used to guide the eyes to follow the change in charge values when the particle volume changes.

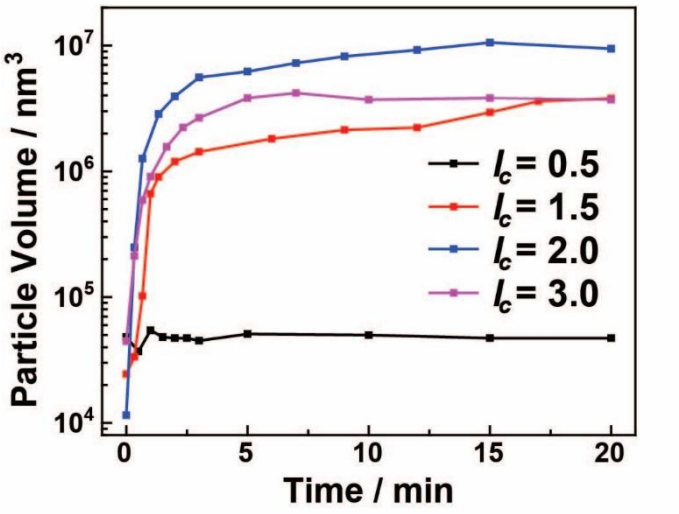


Figure S6. Particle volume calculated using fast kinetics SANS results with their fitted data of AY38/G5 system at l_c = 0.5, 1.5, 2.0, and 3.0.

Table S2. SANS Results: Structural model fit parameters of AY38/G5 short kinetics at l_c = 3.0. The radius of the cylindrical particles is given as R and the length as L. The Polydispersity of the particles is given as PDI. The reduced χ^2 shows the quality of the fit.

Time	Shape	R/nm	PDI (R)	L /nm	PDI (L)	χ^2
Before Irradiation		17	0.03	53	0.05	1.6
30 s		16	0.05	46	0.01	0.9
60 s		17	0.01	60	0.10	1.3
90 s		17	0.04	53	0.02	1.1
120 s		17	0.03	52	0.04	1.1
150 s		17	0.05	52	0.10	1.3
180 s		16	0.03	56	0.03	0.9
5 min		17	0.04	56	0.05	1.5
10 min		17	0.01	55	0.04	1.6
15 min		17	0.04	52	0.02	1.9
20 min		17	0.05	52	0.10	1.9

Table S3. SANS Results: Structural model fit parameters of AY38/G5 short kinetics at l_c = 1.5. The radius of the spherical particles is given as R_{min}; in the case of ellipsoidal particles, R_{min} shows two axial radii, and R_{maj} shows the equatorial radius. Polydispersity in size is given as PDI. The reduced χ^2 shows the quality of the fit.

Time	Shape	R_{min}/nm	PDI (R_{min})	R_{maj}/nm	PDI (R_{maj})	χ^2
Before Irradiation		18	0.14			1.5
20 s		20	0.20			1.3
40 s		29	0.30			1.3
60 s		20	0.40	89	0.10	1.2
80 s		32	0.20	82	0.11	1.2
120 s		36	0.30	89	0.10	1.4
180 s		44	0.20	88	0.11	1.9
6 min		50	0.20	93	0.02	1.6
9 min		47	0.11	104	0.01	1.1
12 min		51	0.20	102	0.02	0.8
15 min		54	0.33	114	0.10	0.9
17 min		55	0.30	125	0.10	1.3
20 min		57	0.20	126	0.02	1.0

Table S4. SANS Results: Structural model fit parameters of AY38/G5 short kinetics at l_c = 2.0. The polydispersity of the spherical particles in size is given as PDI. The reduced χ^2 shows the quality of the fit.

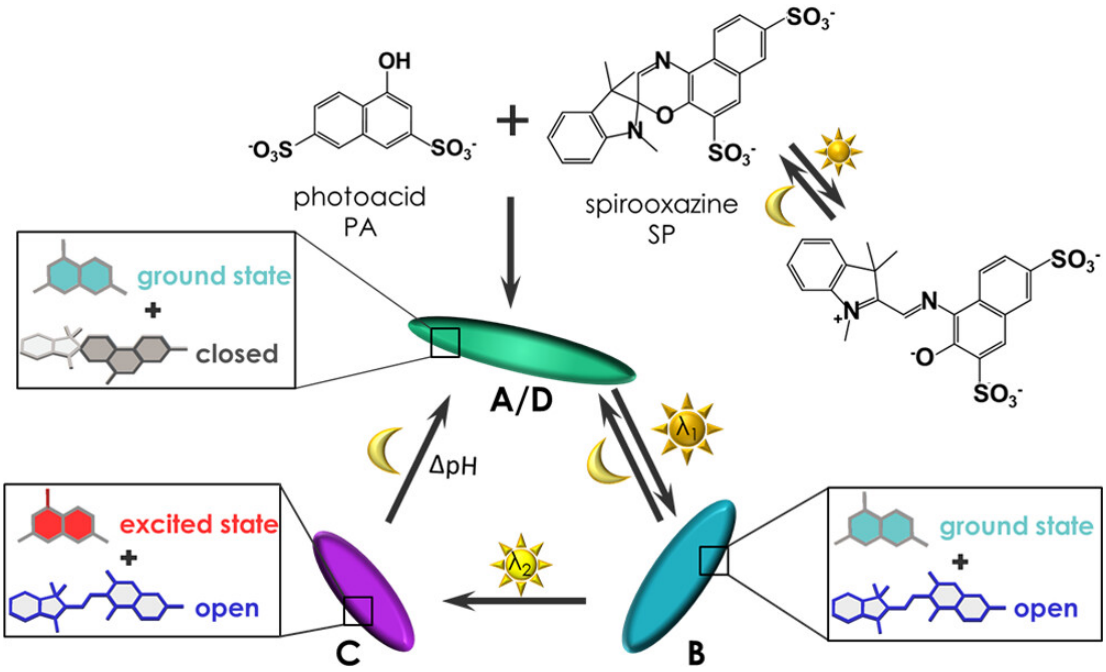
Time	Shape	Radius/nm	PDI	χ^2
Before Irradiation		14	0.23	1.9
20 s		39	0.03	1.3
40 s		67	0.05	1.6
80 s		88	0.20	1.6
120 s		98	0.20	1.5
180 s		110	0.11	1.6
5 min		114	0.22	2.1
7 min		120	0.18	2.2
9 min		125	0.20	2.3
12 min		130	0.03	2.5
15 min		136	0.04	1.7
20 min		131	0.06	1.8

Table S5. SANS Results: Structural model fit parameters of AY38/G5 short kinetics at l_c = 3.0. The polydispersity of the spherical particles in size is given as PDI. The reduced χ^2 shows the quality of the fit.

Time	Shape	Radius/nm	PDI	χ^2
Before Irradiation		22	0.03	0.9
20 s		37	0.03	1.3
40 s		52	0.05	1.3
60 s		60	0.10	1.2
100 s		72	0.28	1.6
140 s		81	0.20	1.1
180 s		86	0.22	2.1
5 min		97	0.20	1.0
7 min		100	0.11	1.0
10 min		96	0.26	0.9
15 min		97	0.16	1.5
20 min		96	0.21	0.9

7.2.4. Double-Wavelength-Switchable Molecular Self-Assembly of a Photoacid and Spirooxazine in an Aqueous Solution

Alexander Zika, **Mohit Agarwal**, Ralf Schweins, Franziska Gröhn; *J. Phys. Chem. Lett.*, **2023**, *14*, 9563-9568.



THE JOURNAL OF PHYSICAL CHEMISTRY LETTERS
A JOURNAL OF THE AMERICAN CHEMICAL SOCIETY

pubs.acs.org/JPCL

Letter

Double-Wavelength-Switchable Molecular Self-Assembly of a Photoacid and Spirooxazine in an Aqueous Solution

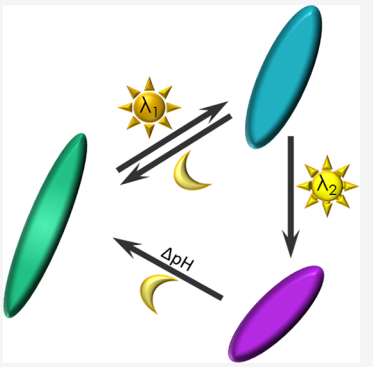
Alexander Zika, Mohit Agarwal, Ralf Schweins, and Franziska Gröhn*

Cite This: *J. Phys. Chem. Lett.* 2023, 14, 9563−9568

Read Online

ACCESS | Metrics & More | Article Recommendations | Supporting Information

ABSTRACT: Quadruple-switchable nanoscale assemblies are built by combining two types of water-soluble molecular photoswitches through dipole−dipole interaction. Uniting the wavelength-specific proton dissociation of a photoacid and ring-opening of an anionic spirooxazine results in an assembly that can be addressed by irradiation with two different wavelengths: pH and darkness.



Downloaded via FRIEDRICH-ALEXANDER-UNIV on January 11, 2026 at 22:28:07 (UTC).
See https://pubs.acs.org/sharingguidelines for options on how to legitimately share published articles.

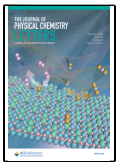
Self-assembled nano-objects bear potential in drug development,[1−3] catalysis,[4−6] and solar energy conversion.[7] Next to established amphiphilicity-based approaches, supramolecular structures can be based on $\pi-\pi$ interactions,[8,9] hydrogen bonding,[10,11] and electrostatic self-assembly.[12−14] Recently, dipole−dipole interactions have been combined with other noncovalent forces such as $\pi-\pi$ stacking or hydrogen bonding to form well-defined structures such as helices.[15−17] The design of nanoassemblies, which can change their properties induced by external triggers, bears particular significance. Nanoassemblies that are capable of altering their structure through temperature[18,19] or pH[20−23] are well-known, especially for amphiphilic systems.[24−27] Light as a noninvasive readily available trigger is especially valuable.[28−39] Switching via isomerization and dimerization has been well established.[40−43] Nanoassemblies with light-switchable size and shape were formed by electrostatic self-assembly through interplaying ionic and $\pi-\pi$ interactions, involving *cis*−*trans* isomerization, spiro-compound ring-opening, or—more recently—photoacids.[35,44−47] On the other hand, based on dipole−dipole interactions, only light-triggered particle aggregation has been reported.[48,49]

Regarding more complex addressable structures, the supramolecular combination of more than one photoswitch in one molecular assembly would be especially desirable, but it continues to pose a challenge. Meanwhile, several multi-switchable supramolecular systems exist,[10,11] and recently, gold particles functionalized with two azo compounds,[12] and a solid polymer-quantum dot material have been reported,[13] but to our knowledge, no scholarly attention has been paid to a nanoscale assembly that can alternatively respond to two specific wavelengths in an aqueous solution. In certain cases, the light was used to switch one molecule forth and back,[50,51] but the assembly of two types of light-triggerable units for orthogonal switching in aqueous solution is yet to be exploited.

Herein, we demonstrate the combination of two types of photoswitchable molecular building blocks into a multi-switchable molecular nanoassembly that is quadruple-triggerable by irradiation with two wavelengths, pH, and darkness (darkness corresponds here to the thermal back-isomerization at room temperature and might thus also be seen as a "temperature" being the trigger). As shown in Scheme 1, it comprises a photoresponsive dianionic spiro compound (SP) and a photo- and pH-responsive dianionic photoacid (PA) associating via dipole−dipole interaction in aqueous solution. Upon excitation, photoacids undergo a proton dissociation and change from a dianion to a trianion, whereas the spiro-compound conformation changes from a closed to open state upon irradiation with a second wavelength.

To elucidate the interaction of the two molecule types, UV−vis spectroscopy is performed for a molar concentration ratio l_m = 0.5, where $l_m = c(\mathrm{SP})/c(\mathrm{PA})$. In the spectrum of the irradiated (λ = 366 nm) open spirooxazine−photoacid assembly (Figure 1a), the peak positions are slightly shifted, both for the spiro ($\Delta\lambda$ = 4 nm) and for the photoacid ($\Delta\lambda$ = 9

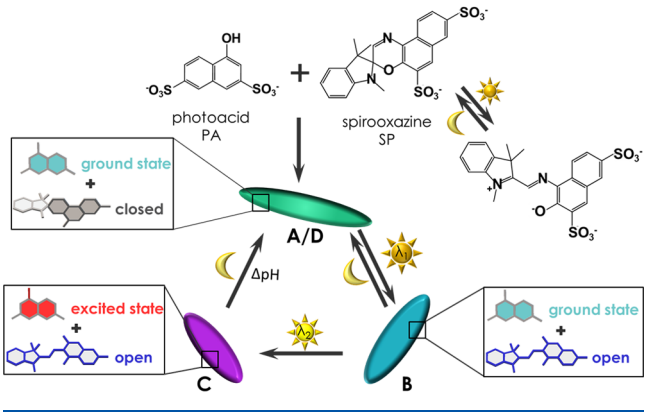
Received: August 27, 2023
Accepted: October 6, 2023
Published: October 20, 2023



ACS Publications

© 2023 American Chemical Society

Scheme 1. Nano-assemblies from a Spirooxazine and Photoacid



nm), while the nanoparticle scattering also causes the intensity to vary.

To interpret these changes, concentration dependent measurements of the SP solutions (without PA) were carried out (Figure 1b). For the nonirradiated species, no changes can be observed at higher concentrations, although DLS detects aggregates. The nonlinear increase in intensity can be attributed to the scattering contribution of these assemblies at lower wavelengths. As no changes in UV−vis are visible, $\pi-\pi$ interactions can be excluded. Due to the high dipole moment of SP of μ= 26.5 D (Figure 2), the association into nanoscale assemblies can be attributed to dipole−dipole interaction. [Dipole−dipole interactions do not always show a shift in UV−vis spectroscopy, as has been reported for other systems.[49]] For the SP-PA assemblies, this confirms that the photoacid associates with the spiro stacks, in contrast to the photoacid alone, which does not form aggregates. Given that other interaction types can be excluded, it can be surmised that these heterointeractions also occur via dipole−dipole interaction (photoacid dipole moment $\mu_{PA,nonirradiated}$ = 2.5 D, $\mu_{PA,irradiated}$ = 8.2 D), possibly supported by induced $\pi-\pi$ interaction occurring when molecules approach through the dipole−dipole interaction, which, however, if present, is so weak that no shift in the UV−vis spectra becomes evident. [Cationic-π interaction can be excluded as a solution of the photoacid alone does not show any association.] Further, as urea is known to break hydrogen bonds, we mixed it with the assemblies since two photoacid molecules could possibly connect via a hydrogen bond between the − OH groups. As the assembly size did not vary, the presence of hydrogen bonds could be excluded (Figure S5). Thus, we consider a mixed molecular dipole−dipole bound stack with additional $\pi-\pi$ interaction after irradiation.

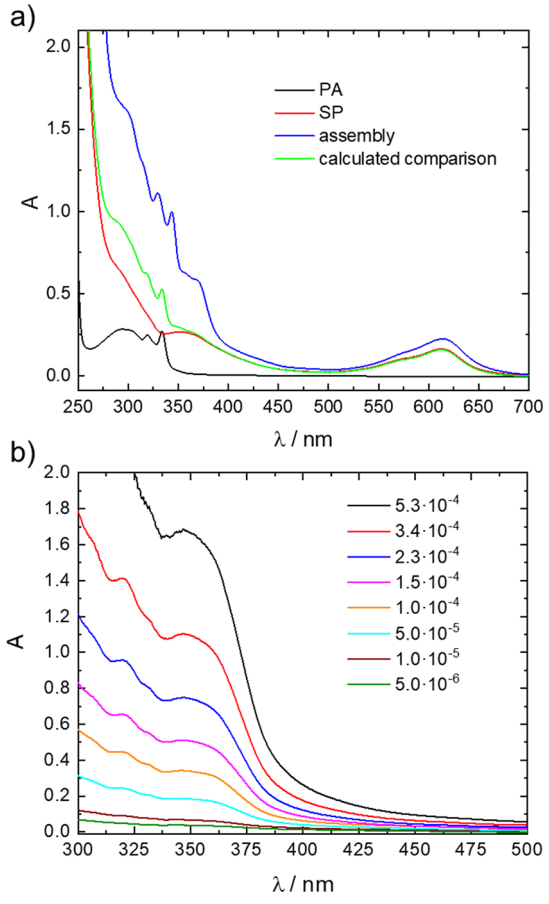


Figure 1. UV−vis spectroscopy of (a) the building block solutions (black, PA; red, irradiated SP), the irradiated nanoassemblies at l_m = 0.5 (blue) with c(SP) = 1 × 10^{-4} mol/L, and the calculated sum spectrum (green), representing the addition of the two building block spectra (black plus red curve). (b) SP solutions with SP in its closed state prior to irradiation at different concentrations with no shift.

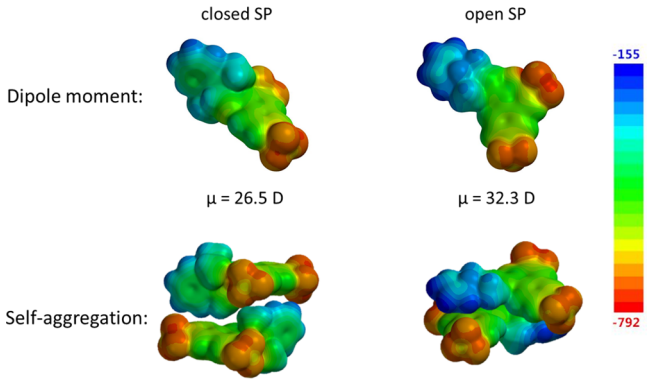


Figure 2. Electrostatic potential at the molecular surface for the closed (left) and open (right) SP and their self-aggregation.

Light scattering helps investigate the association on a nanoscale. Figure 3a illustrates the dynamic light scattering (DLS) results for molar concentration ratios of building blocks l_m before irradiation. It shows nanoassemblies with hydrodynamic radii R_H = 178 nm (l_m = 0.5) and R_H = 201 nm (l_m = 4.0) with narrow size distributions (σ = 0.11 and σ = 0.12). As mentioned above, they spontaneously form when mixing the building block solutions due to the dipole−dipole interaction and possibly some $\pi-\pi$ stacking contribution. DLS reveals a clear dependence of the assembly size (R_H) on the molar concentration ratio (Figure 3b). In the case of a spiro compound excess (l_m > 1), the size increases, indicating that the spirooxazine causes a more expressed particle growth. Even though two kinds of building blocks are used here, the process of self-assembly may be described by the isodesmic model (1D self-assembly model). While R_H is determined by particle diffusion, the radius of gyration R_G is mass-weighted. The combination of both radii indicates the particle shape.[52,53] R_G/R_H decreases with increasing molar ratio, indicating that the

https://doi.org/10.1021/acs.jpclett.3c02392
J. Phys. Chem. Lett. 2023, 14, 9563−9568

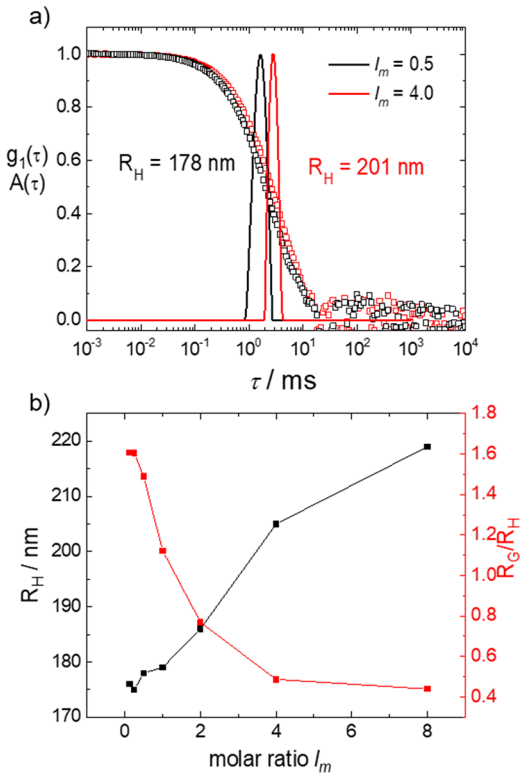


Figure 3. DLS of PA-SP assemblies with c(SP) = 1×10^{-4} mol/L: (a) Electric field autocorrelation function $g_1(\tau)$ and distributions of relaxation times $A(\tau)$ for two molar ratios l_m before irradiation. (b) Hydrodynamic radius R_H and the shape sensitive R_G/R_H as a function of molar ratio.

assemblies are more compact when fewer photoacid molecules are present.[54]

The multiswitchability was investigated directly in solution for nanoassemblies with l_m = 0.5 by DLS, as at this ratio an excess of photoacid molecules is present and thus guarantees that the PA molecules are incorporated in the assemblies. In the first step, switching of the spiro compound to the open state by irradiation at λ = 366 nm leads to a decline in size from R_H = 179 nm to R_H = 141 nm. The subsequent excitation of the photoacid with λ = 302 nm results in even smaller assemblies with R_H = 98 nm. Here, the decline in size following the first irradiation may be attributed to an interplay of effects: In the ground state the photoacid is undissociated (pK_a = 8.6), while photoexcitation leads to a pK_a decrease and dissociation of the hydroxyl group (pK_a^* = − 2.6).[55] Due to the formation of more charges, electrostatic repulsion may lead to some disassembly and thus a decrease in size. At the same time, the increased dipole−dipole interaction together with the set-in of the $\pi-\pi$ interaction plays a role, leading to a less anisotropic structure (as evident from a change in R_G/R_H and small-angle neutron scattering, SANS, see below). As the second irradiation with λ = 302 nm does not influence the spiro compound (Figure S3a), the following behavior can be understood as follows: the second irradiation causes a charge increase in the photoacid, enhancing the electrostatic repulsion of the molecular building blocks, which then leads to a smaller aggregation number and assembly size.

In addition, due to the dissociation of the photoacid, this irradiation results in a pH change from pH = 7.0 to pH = 5.8. Due to the electrostatic interaction with the SP the photoacid remains unprotonated even when the irradiation stops. Thus, to switch the assemblies back to the beginning, the pH is changed back to 7.0 so that the photoacid becomes protonated again. With time, the spiro compound also switches back to the closed state, that is, the starting point. This cycle can be repeated up to at least five times (Figure 4a). It is also possible to just switch the spiro component back and forth (red pathway in Figure 5a).

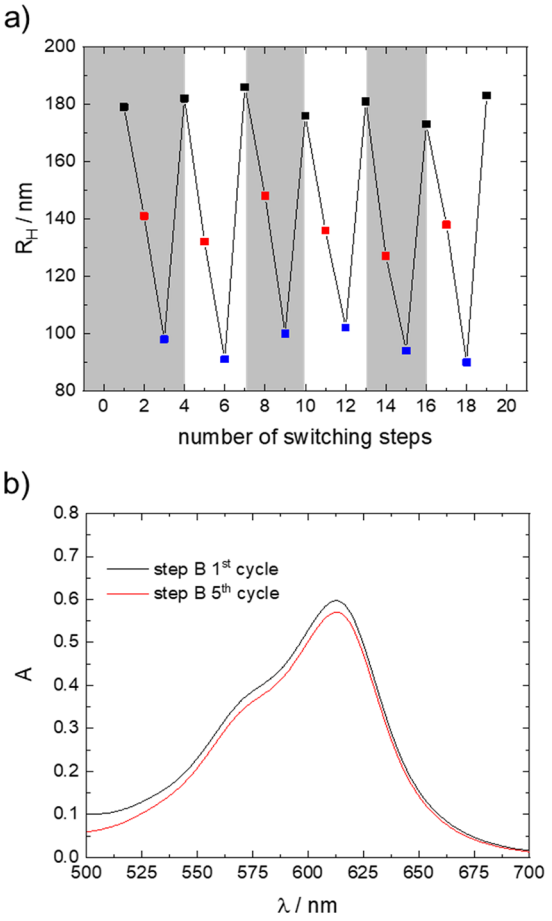


Figure 4. (a) Multiple switching cycles: DLS results of the various cycles. Black squares: step A/D. Red squares: step B. Blue squares: step C. At least 5 cycles are possible with repeatable changes in the size of the assemblies. (b) UV-vis spectroscopy of the 1st and 5th cycles to assess the stability of the assemblies.

In-situ small-angle neutron scattering (in situ SANS) under irradiation was performed on beamline D11 at the Institut Laue-Langevin (ILL), Grenoble, France, to reveal the particle shapes in the solution. The combined SLS-SANS curves were fitted with different structural models to determine the shapes and dimensions of the assemblies. The overall shape of the particles is a prolate ellipsoid with R_{maj} = 171 nm and R_{min} = 12 nm (Figure 5c). Upon irradiation, the ellipsoidal structure type remains unchanged, but the size of the nanostructures is influenced by the ellipsoid aspect ratio changing from 14 to 10 (Figure 5b, Table S1), in agreement with the R_G/R_H from SLS/DLS.

To investigate the difference in the interactions of the open and closed state spiro molecules with the photoacid, the isothermal titration calorimetry (ITC) of the mixed system and of diluting SP was performed (Figure S7, Table 1). The

https://doi.org/10.1021/acs.jpclett.3c02392
J. Phys. Chem. Lett. 2023, 14, 9563−9568

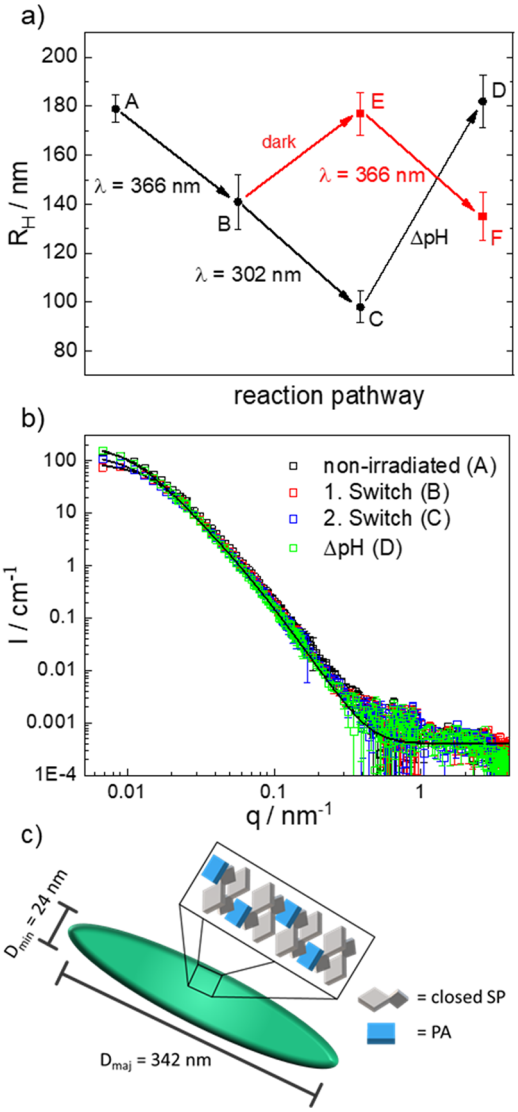


Figure 5. (a) DLS: R_H depending on the different switching steps for l_m = 0.5 (c(SP) = 1 × 10^{-4} mol/L). The error bars are from the measurement of the same reaction pathway multiple times. (b) SLS-SANS scattering (symbols) and fits (solid lines) for the different steps. (c) Scheme of the structure at l_m = 0.5.

Table 1. ITC Results after Fitting the Data with a One-Site Binding Model[a]

	SP into water	Closed SP in PA	Open SP in PA
N		1.7 ± 0.01	2.0 ± 0.02
ΔH (kJ mol^{-1})	−2.0 ± 0.12	−5.9 ± 0.53	−13.6 ± 0.55
ΔS (J mol^{-1} K^{-1})	12.4 ± 0.37	18.8 ± 1.8	2.7 ± 0.23
K (M^{-1})	9.9 ± 0.8	103 ± 6	331 ± 12
ΔG (kJ mol^{-1})	−5.7	−11.5	−14.4

[a]N: binding stoichiometry (SP/PA), ΔH: enthalpy change, ΔS: entropy change, K: association equilibrium constant, ΔG: Gibbs free energy change (error of ΔH 5−9%, of ΔS 3−10%).

titration of SP into deionized water represents the dissociation of the spiro compound assemblies present at higher concentrations. The dissociation constant K_{diss} = 0.101 M lower than one, corresponding to an association constant of K = 9.9 M^{-1} shows that the equilibrium is on the side of the aggregates, congruent with DLS and UV−vis. Accordingly, the (reverse) spiro-homoassociation is exothermic with a binding enthalpy of ΔH = −2.0 kJ/mol and entropically favored with ΔS = 13.2 J/(mol/K), which can be ascribed to a dipole−dipole interaction with an entropic gain due to released water molecules or possible salt ions or both

Upon titration of the spiro compound into the photoacid solution, the ITC raw data can be fitted with a one-site binding model, considering the equilibrium given in equation I

$$n\mathrm{SP} + \mathrm{PA} \rightleftharpoons (\mathrm{SP})_n\mathrm{PA} \quad \text{(I)}$$

It becomes evident that the association of these two molecules is energetically and entropically driven with a binding enthalpy of ΔH = −5.9 kJ/mol and an entropy of ΔS = 18.5 J/(mol/K) per spiro molecule. The binding stoichiometry of N = 1.7 corresponds to the binding of about two spiro molecules per one photoacid molecule. Valuable insights are yielded by comparing the data of the nonirradiated (closed) spiro form and the irradiated (open) one: For the open form, the association is also both enthalpically and entropically favored, but compared to the closed state, it is much more enthalpically driven (ΔH = −13.6 kJ/mol). This is attributable to the strong electrostatic interaction of the positive charge in the open state and the negative charge of the photoacid while the dipole moment is also higher at the same time (Figure 2). Comparing the binding equilibrium constants, the overall binding affinity in the irradiated case is three times higher, which also corresponds to the stronger interaction and higher dipole moment of the open-state spiro molecule. The aggregates' binding stoichiometry before and after irradiation is about the same as that with N = 2. Given that the photoacid itself does not aggregate, i.e., that photoacid−photoacid dipole−dipole interaction is not sufficient to cause association under the current conditions, aggregates must consist of stacks of singular photoacids incorporated in self-stacking spiro molecules, which again for 2:1 stoichiometry means a sequence of spiro dimers alternating with photoacid molecules, as indicated in the zoom in Figure 4c.

In conclusion, this study has shown that assemblies of the two light triggerable molecules, the spirooxazine SP and the photoacid PA, form through the dipole−dipole interaction combined with the thereby induced π−π interactions and can respond to light irradiations of two wavelengths, pH changes, and temperature (darkness). Assemblies with an elliptical shape consisting of photoacid-spiro dipole stacks in form of ..−SP−SP−PA−SP−SP−PA−SP−SP−.. result. The growth in diameter likely originates from the dipole−dipole interaction between the sulfonate groups and the aromatic ring of different SP molecules. The photoresponsive size is caused by the change in dipole−dipole and π−π interaction strength caused by changes in charge status and dipole moment, where a stronger interaction results in the formation of smaller, more compact aggregates. Here, the photoresponsiveness alters the strength of the interaction by changing the molecular structure. By combining light and pH responsiveness, the supramolecular system can undergo a complete reversible cycle of switches between different particle sizes. To our knowledge, this is the first time that light-switchable molecular assemblies based on dipole−dipole or π−π interaction in aqueous solution have been presented and that a double-switch assembly in an aqueous solution has been presented at all. Furthermore, in contrast to other studies, the size change of the nano-objects is not accompanied by a full dissolution of the assemblies. The type of the interactions and principle of the assembly remains

https://doi.org/10.1021/acs.jpclett.3c02392
J. Phys. Chem. Lett. 2023, 14, 9563−9568

after irradiation such that nano-objects of the same type and in the same size range still exist, but with altered dimensions. This new type of molecular nanoscale assembly with light-and pH-addressable size may pave the way for novel sensors, actuators, or molecular machines.

■ ASSOCIATED CONTENT

Supporting Information

The Supporting Information is available free of charge at https://pubs.acs.org/doi/10.1021/acs.jpclett.3c02392.

Experimental section and SANS setup (Figure S1), SANS data (Table S1), characterization of the spiro compound (Figures S2 and S3), concentration dependency of the assemblies (Figure S4), characterization of the interaction between the building blocks (Figure S4), urea experiment (Figure S5), multiple switching cycles (Figure S6), and ITC measurement (Figure S7) (PDF)

■ AUTHOR INFORMATION

Corresponding Author

Franziska Gröhn − *Department of Chemistry and Pharmacy & Interdisciplinary Center for Molecular Materials, Bavarian Polymer Institute, Friedrich-Alexander-Universität Erlangen-Nürnberg, D-91058 Erlangen, Germany;* orcid.org/0000-0003-1016-2583; Email: Franziska.groehn@fau.de

Authors

Alexander Zika − *Department of Chemistry and Pharmacy & Interdisciplinary Center for Molecular Materials, Bavarian Polymer Institute, Friedrich-Alexander-Universität Erlangen-Nürnberg, D-91058 Erlangen, Germany*

Mohit Agarwal − *Department of Chemistry and Pharmacy & Interdisciplinary Center for Molecular Materials, Bavarian Polymer Institute, Friedrich-Alexander-Universität Erlangen-Nürnberg, D-91058 Erlangen, Germany; DS/LSS Institut Laue-Langevin, 38042 Grenoble CEDEX 9, France*

Ralf Schweins − *DS/LSS Institut Laue-Langevin, 38042 Grenoble CEDEX 9, France;* orcid.org/0000-0001-8078-2089

Complete contact information is available at: https://pubs.acs.org/10.1021/acs.jpclett.3c02392

Notes

The authors declare no competing financial interest.

■ ACKNOWLEDGMENTS

We gratefully acknowledge the funding from the German Science Foundation (DFG, Grant GR 2701/3-2), the Institut Laue-Langevin (ILL) for beamtime, and the Partnership for Soft Condensed Matter (PSCM) for light-scattering instrument support. This work was also supported by the Interdisciplinary Center for Molecular Materials, Friedrich-Alexander-Universität Erlangen-Nürnberg. This work benefited from the SasView application (www.sasview.org), originally developed under NSF (DMR-0520547). DOI for the D11/ILL-beamtime: 10.5291/ILL-DATA.9-11-2077.

■ REFERENCES

(1) Liu, K.; Xing, R.; Zou, Q.; Ma, G.; Möhwald, H.; Yan, X. Simple Peptide-Tuned Self-Assembly of Photosensitizers towards Anticancer Photodynamic Therapy. *Angew. Chem., Int. Ed.* **2016**, *55* (9), 3036−3039.

(2) Yang, L.; Sun, H.; Liu, Y.; Hou, W.; Yang, Y.; Cai, R.; Cui, C.; Zhang, P.; Pan, X.; Li, Y.; Li, L.; Sumerlin, P. S.; Tan, W. Self-Assembled Aptamer-Grafted Hyperbranched Polymer Nanocarrier for Targeted and Photoresponsive Drug Delivery. *Angew. Chem., Int. Ed.* **2018**, *130* (52), 17294−17298.

(3) Zhang, W. J.; Hong, C. Y.; Pan, C. Y. Polymerization-Induced Self-Assembly of Functionalized Block Copolymer Nanoparticles and Their Application in Drug Delivery. *Macromol. Rapid Commun.* **2019**, *40*, No. 1800279.

(4) Hunt, S. T.; Milina, M.; Alba-Rubio, A. C.; Hendon, C. H.; Dumesic, Y. A.; Román-Leshkov, Y. Self-Assembly of Noble Metal Monolayers on Transition Metal Carbide Nanoparticle Catalysts. *Science* **2016**, *352* (6288), 974−978.

(5) Zhao, Z.; Fu, J.; Dhakal, S.; Johnson-Buck, A.; Liu, M.; Zhang, T.; Woodbury, N. W.; Liu, Y.; Walter, N. G.; Yan, X. Nanocaged Enzymes with Enhanced Catalytic Activity and Increased Stability Against Protease Digestion. *Nat. Commun.* **2016**, *7*, 10619.

(6) Eisenreich, F.; Meijer, E. W.; Palmans, A. R. A. Amphiphilic Polymeric Nanoparticles for Photoredox Catalysis in Water. *Chem. Eur. J.* **2020**, *26*, 10355−10361.

(7) Hendsbee, A. D.; Sun, J. P.; Law, W. K.; Yan, H.; Hill, I. G.; Spasyuk, D. M.; Welch, G. C. Synthesis, Self-Assembly, and Solar Cell Performance of N-Annulated Perylene Diimide Non-Fullerene Acceptors. *Chem. Mater.* **2016**, *28* (19), 7098−7109.

(8) Hirschberg, J. H. K. K.; Brunsveld, L.; Ramzi, A.; Vekemans, J. A. J. M.; Sijbesma, R. P.; Meijer, E. W. Helical Self-Assembled Polymers from Cooperative Stacking of Hydrogen-Bonded Pairs. *Nature* **2000**, *407*, 167−170.

(9) Schenning, A. P. H. J.; Meijer, E. W. Supramolecular Electronics; Nanowires from Self-Assembled π-Conjugated Systems. *Chem. Commun.* **2005**, 3245−3258.

(10) Azuma, W.; Terashima, T.; Sawamoto, M. Precision Synthesis of Imine-Functionalized Reversible Microgel Star Polymers via Dynamic Covalent Cross-Linking of Hydrogen-Bonding Block Copolymer Micelles. *Macromolecules* **2017**, *50* (2), 587−596.

(11) Krieg, E.; Bastings, M. M. C.; Besenius, P.; Rybtchinski, B. Supramolecular Polymers in Aqueous Media. *Chem. Rev.* **2016**, *116*, 2414−2477.

(12) Willerich, I.; Gröhn, F. Molecular Structure Encodes Nanoscale Assemblies: Understanding Driving Forces in Electrostatic Self-Assembly. *J. Am. Chem. Soc.* **2011**, *133* (50), 20341−20356.

(13) Willerich, I.; Gröhn, F. Switchable Nanoassemblies from Macroions and Multivalent Dye Counterions. *Chem. Eur. J.* **2008**, *14* (30), 9112−9116.

(14) Frühbeißer, S.; Gröhn, F. Porphyrin−Polyelectrolyte Nanoassemblies: The Role of Charge and Building Block Architecture in Self-Assembly. *Macromol. Chem. Phys.* **2017**, *218* (17), No. 1600526.

(15) Würthner, F. Dipole−Dipole Interaction Driven Self-Assembly of Merocyanine Dyes: From Dimers to Nanoscale Objects and Supramolecular Materials. *Acc. Chem. Res.* **2016**, *49*, 868−876.

(16) Kulkarni, C.; Bejagam, K. K.; Senanayak, S. P.; Narayan, K. S.; Balasubramanian, S.; George, S. J. Dipole-Moment-Driven Cooperative Supramolecular Polymerization. *J. Am. Chem. Soc.* **2015**, *137*, 3924−3932.

(17) Berrocal, J. A.; Mabesoone, M. F. J.; García Iglesias, M. G.; Huizinga, A.; Meijer, E. W.; Palmans, A. R. A. Selenoamides Modulate Dipole−Dipole Interactions in Hydrogen Bonded Supramolecular Polymers of 1,3,5-Substituted Benzenes. *Chem. Commun.* **2019**, *55*, 14906−14909.

(18) Qiao, S.; Wang, H. Temperature-Responsive Polymers: Synthesis, Properties, and Biomedical Applications. *Nano Research* **2018**, *11*, 5400−5423.

(19) Dreher, M. W.; Simnick, A. J.; Fischer, K.; Smith, R. J.; Patel, A.; Schmidt, M.; Chilkoti, A. Temperature Triggered Self-Assembly of Polypeptides into Multivalent Spherical Micelles. *J. Am. Chem. Soc.* **2008**, *130* (2), 687−694.

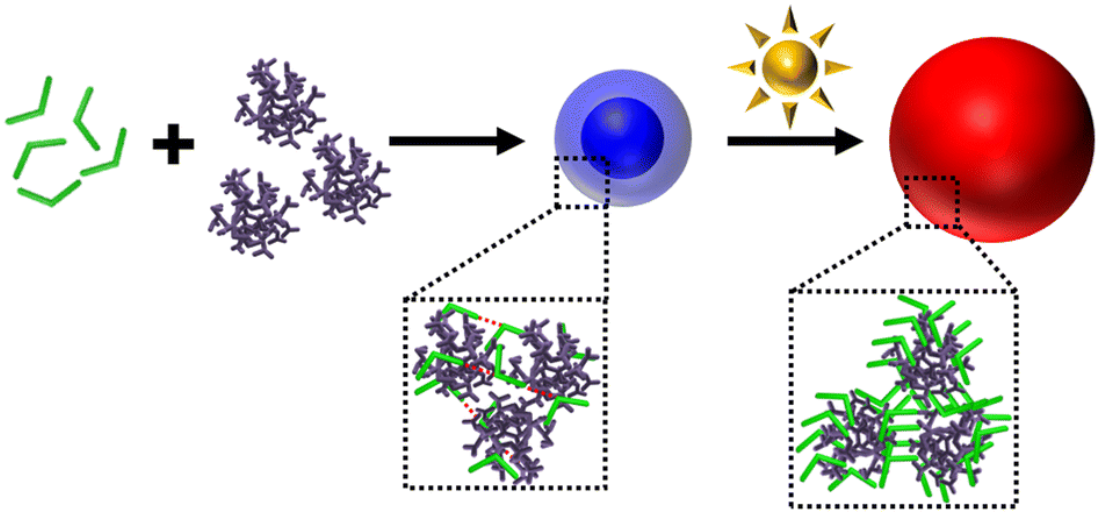
(20) Canning, S. L.; Neal, T. J.; Armes, S. P. pH-Responsive Schizophrenic Diblock Copolymers Prepared by Polymerization-Induced Self-Assembly. *Macromolecules* **2017**, *50* (16), 6108−6116.

(21) Duan, Q.; Cao, Y.; Li, Y.; Hu, X.; Xiao, T.; Lin, C.; Pan, Y.; Wang, L. pH-Responsive Supramolecular Vesicles Based on Water-Soluble Pillar(6)arene and Ferrocene Derivative for Drug Delivery. *J. Am. Chem. Soc.* **2013**, *135* (28), 10542−10549.
(22) Ling, D.; Park, W.; Park, S. J.; Lu, Y.; Kim, K. S.; Hackett, M. J.; Kim, B. H.; Yim, H.; Jeon, Y. S.; Na, K.; Hyeon, T. Multifunctional Tumor pH-Sensitive Self-Assembled Nanoparticles for Bimodal Imaging and Treatment of Resistant Heterogeneous Tumors. *J. Am. Chem. Soc.* **2014**, *136* (15), 5647−5655.
(23) Annegarn, M.; Dirksen, M.; Hellweg, T. Importance of pH in Synthesis of pH-Responsive Cationic Nano- and Microgels. *Polymers* **2021**, *13* (5), 827.
(24) Yang, X.; Wang, Z.; Sun, J. Morphological Transitions of Photoresponsive Vesicles from Amphiphilic Polypeptoid Copolymers for Controlled Release. *Polymers* **2020**, *12* (4), 798.
(25) Catti, L.; Kishida, N.; Kai, T.; Akita, M.; Yoshizawa, Y. Synthetic Control Over Orientational Degeneracy of Spacer Cations Enhances Solar Cell Efficiency in Two-Dimensional Perovskites. *Nat. Commun.* **2019**, *10*, 1948.
(26) Fuentes, E.; Gerth, M.; Berrocal, J. A.; Matera, C.; Gorostiza, P.; Voets, I. K.; Pujals, S.; Albertazzi, L. An Azobenzene-Based Single-Component Supramolecular Polymer Responsive to Multiple Stimuli in Water. *J. Am. Chem. Soc.* **2020**, *142* (22), 10069−10078.
(27) Xu, F.; Pfeifer, L.; Stuart, M. C. A.; Leung, F. K. C.; Feringa, B. L. Multi-Modal Control Over the Assembly of a Molecular Motor Bola-Amphiphile in Water. *Chem. Commun.* **2020**, *56*, 7451−7454.
(28) Yan, T.; Li, F.; Qi, S.; Tian, J.; Tian, R.; Hou, J.; Luo, Q.; Dong, Z.; Xu, J.; Liu, J. Light-Responsive Vesicles for Enantioselective Release of Chiral Drugs Prepared From a Supra-Amphiphilic M-Helix. *Chem. Commun.* **2020**, *56*, 149−152.
(29) Xia, C. X.; Wang, N.; Sun, P. P.; Tang, S. X.; Xu, X. D.; Tan, Y. B.; Xin, X. Self-Assembly of an Alkynylpyrene Derivative for Multi-Responsive Fluorescence Behavior and Photoswitching Performance. *Soft Matter* **2020**, *16*, 7390−7399.
(30) Lee, J.; Lee, W.; Kim, D.; Kim, M.; Kim, J. Independent Multi-states of Photo-Responsive Polymer/Quantum Dot Nanocomposite Induced via Different Wavelengths of Light. *Sci. Rep.* **2019**, *9*, 1.
(31) Moldenhauer, D.; Fuenzalida Werner, J. P.; Strassert, C. A.; Gröhn, F. Light-Responsive Size of Self-Assembled Spiropyran-Lysozyme Nanoparticles with Enzymatic Function. *Biomacromolecules* **2019**, *20* (2), 979−991.
(32) Grzelczak, M.; Liz-Marzan, L. M.; Klajn, R. Stimuli-Responsive Self-Assembly of Nanoparticles. *Chem. Soc. Rev.* **2019**, *48*, 1342−1361.
(33) Mariani, G.; Krieger, A.; Moldenhauer, D.; Schweins, R.; Gröhn, F. Light-Responsive Shape: From Micrometer-Long Nanocylinders to Compact Particles in Electrostatic Self-Assembly. *Macromol. Rapid Commun.* **2018**, *39*, No. 1700860.
(34) Wang, Y.; Deng, Y.; Luo, H.; Zhu, A.; Ke, H.; Yang, H.; Chen, H. Light-Responsive Nanoparticles for Highly Efficient Cytoplasmic Delivery of Anticancer Agents. *ACS Nano* **2017**, *11* (12), 12134−12144.
(35) Zhao, D.; van Leeuwen, T.; Cheng, J.; Feringa, B. L. Dynamic Control of Chirality and Self-Assembly of Double-Stranded Helicates With Light. *Nat. Chem.* **2017**, *9*, 250−256.
(36) Zhang, D.; Lu, X.; Li, Y.; Wang, G.; Chen, Y.; Jiang, J. Dual Stimuli-Responsive Wormlike Micelles Based on Cationic Azobenzene Surfactant and Sodium Azophenol. *Colloids Surf. A: Physicochem. Eng. Asp.* **2018**, *543*, 155−162.
(37) Manna, D.; Udayabhaskararao, T.; Zhao, H.; Klajn, R. Orthogonal Light-Induced Self-Assembly of Nanoparticles using Differently Substituted Azobenzenes. *Angew. Chem., Int. Ed.* **2015**, *54*, 12394−12397.
(38) Zhuang, J.; Gordon, M. R.; Ventura, J.; Li, L.; Thayumanavan, S. Multi-Stimuli Responsive Macromolecules and Their Assemblies. *Chem. Soc. Rev.* **2013**, *42*, 7421−7435.
(39) Willerich, I.; Gröhn, F. Photoswitchable Nanoassemblies by Electrostatic Self-Assembly. *Angew. Chem., Int. Ed.* **2010**, *49*, 8104−8108.
(40) Mariani, G.; Moldenhauer, D.; Schweins, R.; Gröhn, F. Elucidating Electrostatic Self-Assembly: Molecular Parameters as Key to Thermodynamics and Nanoparticle Shape. *J. Am. Chem. Soc.* **2016**, *138*, 1280−1293.
(41) Mariani, G.; Kutz, A.; Di, Z.; Schweins, R.; Gröhn, F. Inducing Hetero-aggregation of Different Azo Dyes through Electrostatic Self-Assembly. *Chem. Eur. J.* **2017**, *23*, 6249−6254.
(42) Mariani, G.; Schweins, R.; Gröhn, F. Structure Tuning of Electrostatically Self-Assembled Nanoparticles through pH: The Role of Charge Ratio. *Macromol. Chem. Phys.* **2017**, *218*, No. 1700191.
(43) Horowitz, R. V.; Janowitz, L. A.; Modic, A. L.; Heiney, P. A.; Collings, P. J. Aggregation Behavior and Chromonic Liquid Crystal Properties of an Anionic Monoazo Dye. *Phys. Rev. E* **2005**, *72*, No. 041710.
(44) Moldenhauer, D.; Gröhn, F. Water-Soluble Spiropyrans with Inverse Photochromism and Their Photoresponsive Electrostatic Self-Assembly. *Chem. Eur. J.* **2017**, *23* (16), 3966−3978.
(45) Zika, A.; Bernhardt, S.; Gröhn, F. Photoresponsive Photoacid-Macroion Nano-Assemblies. *Polymers* **2020**, *12* (8), 1746.
(46) Zika, A.; Gröhn, F. Multiswitchable Photoacid−Hydroxyflavylium−Polyelectrolyte Nano-Assemblies. *Beilstein J. Org. Chem.* **2021**, *17*, 166−185.
(47) Wagner, M.; Krieger, A.; Minameyer, M.; Hämisch, B.; Huber, K.; Drewello, T.; Gröhn, F. Multiresponsive Polymer Nanoparticles Based on Disulfide Bonds. *Macromolecules* **2021**, *54* (6), 2899−2911.
(48) Zhao, H.; Sen, S.; Udayabhaskararao, T.; Sawczyk, M.; Kučanda, K.; Manna, D.; Kundu, P. K.; Lee, J. W.; Král, P.; Klajn, R. Reversible Trapping and Reaction Acceleration Within Dynamically Self-Assembling Nanoflasks. *Nat. Nanotechnol.* **2016**, *11*, 82−88.
(49) Yang, Y.; Yue, L.; Li, H.; Maher, E.; Li, Y.; Wang, Y.; Wu, L.; Yam, V. W. W. Photo-Responsive Self-Assembly of an Azobenzene-Ended Surfactant-Encapsulated Polyoxometalate Complex for Modulating Catalytic Reactions. *Small* **2012**, *8* (20), 3105−3110.
(50) Lendlein, A.; Jiang, H.; Jünger, O.; Langer, R. Light-Induced Shape-Memory Polymers. *Nature* **2005**, *434*, 879−882.
(51) Chen, Q.; Yang, Q.; Gao, P.; Chi, B.; Nie, J.; He, A. Photopolymerization of Coumarin-Containing Reversible Photoresponsive Materials Based on Wavelength Selectivity. *Ind. Eng. Chem. Res.* **2019**, *58* (8), 2970−2975.
(52) Xie, D.; Xu, K.; Bai, R.; Zhang, G. Structural Evolution of Mixed Micelles Due to Interchain Complexation and Segregation Investigated by Laser Light Scattering. *J. Phys. Chem. B* **2007**, *111*, 778−781.
(53) Bantle, S.; Schmidt, M.; Burchard, W. Simultaneous Static and Dynamic Light Scattering. *Macromolecules* **1982**, *15*, 1604−1609.
(54) Schärtl, W. *Light Scattering from Polymer Solutions and Nanoparticle Dispersions*; Springer-Verlag, Berlin and Heidelberg, Germany, 2007.
(55) Prémont-Schwarz, M.; Barak, T.; Pines, D.; Nibbering, E. T. J.; Pines, E. Ultrafast Excited-State Proton-Transfer Reaction of 1-Naphthol-3,6-Disulfonate and Several 5-Substituted 1-Naphthol Derivatives. *J. Phys. Chem. B* **2013**, *117* (16), 4594−4603.

https://doi.org/10.1021/acs.jpclett.3c02392
J. Phys. Chem. Lett. 2023, 14, 9563−9568

7.2.5. Photoacid-Macroion Assemblies: How Photo-Excitation Switches the Size of Nano-Objects

Alexander Zika, **Mohit Agarwal**, Wiebke Zika, Dirk Guldi, Ralf Schweins, Franziska Gröhn; *Nanoscale,* **2024,** *16*, 923-940.



Nanoscale

PAPER

View Article Online
View Journal | View Issue

Published on 13 December 2023. Downloaded by Universitat Erlangen Nurnberg on 1/11/2026 10:32:27 PM.

Check for updates

Cite this: *Nanoscale*, 2024, **16**, 923

Photoacid-macroion assemblies: how photo-excitation switches the size of nano-objects†

Alexander Zika,[a] Mohit Agarwal,[a,b] Wiebke Zika,[c] Dirk M. Guldi,[c] Ralf Schweins[b] and Franziska Gröhn *[a]

Electrostatic self-assembly of photoacids with oppositely charged macroions yields supramolecular nano-objects in aqueous solutions, whose size is controlled through light irradiation. Nano-assemblies are formed due to electrostatic attractions and mutual hydrogen bonding of the photoacids. Irradiation with UV light leads to the deprotonation of the photoacid and, consequently, a change in particle size. Overall, the hydrodynamic radii of the well-defined photoacid-macroion nano-objects lie between 130 and 370 nm. For a set of photoacids, we determine the acidity constants in the ground and excited state, discuss the sizes of photoacid-macroion nano-objects (by dynamic and static light scattering), their composition and the particle shapes (by small-angle neutron scattering), and relate their charge characteristics to size, structure and shape. We investigate the association thermodynamics and relate nanoscale structures to thermodynamics and, in turn, thermodynamics to molecular features, particularly the ionization energy of the photoacid hydroxyl group proton. Structure-directing effects completely differ from those for previously investigated systems, with hydrogen bonding and entropic effects playing a major role herein. This combined approach allows developing a comprehensive understanding of assembly formation and photo-response, anchored in molecular parameters (pK_a, ionization energy, substituent group location), charge characteristics, and the association enthalpy and entropy. This fundamental understanding again paves the way for tailoring application solutions with novel photoresponsive materials.

Received 11th September 2023,
Accepted 11th December 2023

DOI: 10.1039/d3nr04570f

rsc.li/nanoscale

1. Introduction

Functional supramolecular nanostructures are eliciting increasing importance owing to the wide range of possible applications such as, for example, carrier systems,[1–4] optoelectronics,[5–9] or sensors.[10–13] Electrostatic self-assembly is an approach recently established for the formation of supramolecular nano-objects in solution.[14–21] It allows for the formation of well-defined supramolecular particles in the range of several to a few hundred nanometers.[14–21] The driving force is electrostatic interactions between the charged organic dyes as counterions and the oppositely charged macroions. Equally important are structural features of the stiff organic or inorganic counterions and induced mutual secondary interactions, such as π–π interactions in-between the counterions.[17,18,22,23] Considering the large variety of sizes and shapes, thermodynamic investigations were performed to better understand the size and shape control during the assembly process.[16,24] For a model system of cationic dendrimer macroions and multivalent anionic dyes as counterions, we have demonstrated that the free energy of the assembly formation ΔG encodes the aggregation number and, thus, the assembly size.[24] Comparing a library of ionic dyes as interconnecting counterions revealed that a free energy gain of $\Delta G \leq -32$ kJ mol^{-1} per associating dye molecule is necessary to interconnect dendrimers and dyes into larger assemblies. Moreover, ΔG can be quantitatively described as the sum of the electrostatic dendrimer–dye interaction and the mutual dye–dye interaction. In addition, the entropy-to-enthalpy ratio was shown to control the shape of the assemblies, which will also play an important role in our study. With increasing enthalpy change the entropy change increased and at an entropy exchange $T\Delta S = -10$ kJ mol^{-1}, a threshold for the shape change from isotropic to also well defined anisotropic elongated nano-objects was observed, even though the all nano-assemblies were governed by π–π interactions.[16] Furthermore, the relation between molecular parameters and the association thermodynamics was taken into consider-

[a]*Department of Chemistry and Pharmacy & Interdisciplinary Center for Molecular Materials, and Bavarian Polymer Institute Friedrich-Alexander Universität Erlangen-Nürnberg, Egerlandstr. 3, D-91058 Erlangen, Germany.*
E-mail: franziska.gröhn@fau.de
[b]*DS LSS Institut Laue – Langevin, 71 Avenue des Martyrs, CS 20 156, 38042 Grenoble CEDEX 9, France*
[c]*Department of Chemistry and Pharmacy, Friedrich-Alexander Universität Erlangen-Nürnberg, Egerlandstr. 3, D-91058 Erlangen, Germany*

† Electronic supplementary information (ESI) available. See DOI: https://doi.org/10.1039/d3nr04570f

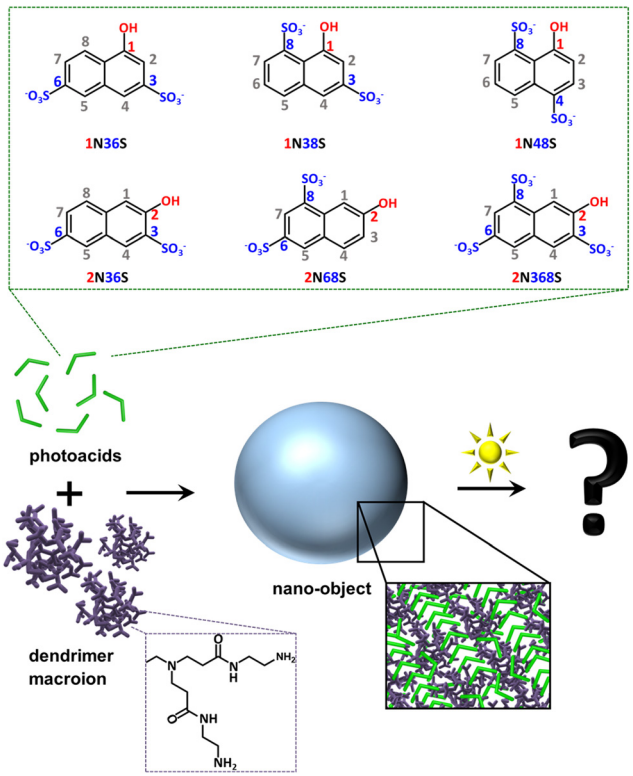
Published on 13 December 2023. Downloaded by Universitat Erlangen Nurnberg on 1/11/2026 10:32:27 PM.

ation:[16] In particular, it was the polar surface area (PSA) of the dye molecules, which quantified the substituent effect in the dye–dye interactions and thereby the free energy change upon association. Finally, a master-plot of the nanoscale aspect ratio in dependence on PSA was found. Hence, the association thermodynamics represents the crucial key to connecting nanoscale properties with molecular features.[16] Thus, an understanding of the underlying thermodynamics is crucial for exploiting the real potential that lies in the principle of electrostatic self-assembly, and can be expected to represent a major key to the understanding also of other systems, such as the one investigated herein.

Next to the versatility of electrostatic self-assembly, the possibility to trigger supramolecular structural properties is another great advantage. This becomes feasible when the nanostructures are formed by non-covalent interactions including π–π stacking,[25–29] hydrogen bonds,[30–34] and ionic interactions.[22,35,36] External triggers such as temperature,[37–40] light,[41–43] pH,[44–48] and electrochemistry[49–52] assist in addressing the size, shape, and properties of the nanostructures. Especially, light represents a non-invasive trigger. Typical motifs for light-switchability are *cis–trans* isomerization[14,53–55,56] and ring opening and closure.[42,57,58]

It is highly desirable to explore novel approaches for photoresponsive nano-assemblies. In recent years, we have used a photoacid to initiate assembly formation and very recently to direct self-assembled nano-objects in solutions.[59–61] Photoacids exhibit a higher degree of deprotonation in the excited state, which, in turn, leads to a higher anionic charge. This opens new avenues and perspectives for light-triggerable responsive materials, which so far – except for the first proofs of concepts mentioned – have largely remained unexplored for nano-assemblies. In a proof of concept, we investigated electrostatically self-assembled nanoparticles comprising an anionic photoacid and a cationic polyamidoamine dendrimer.[60] In that study, the photoacids 1-naphthol-3,6-disulfonate (1N36S), 1-naphthol-3,8-disulfonate (1N38S), and 2-naphthol-3,6-disulfonate (2N36S) as depicted in Scheme 1, were used. Upon exposure to UV light, electrostatically self-assembled nanoparticles consisting of cationic dendrimers and an excess of anionic photoacids changed their size, for example from R_H = 89 nm up to R_H = 252 nm.[60] In that study, the differences between the photoacids again seemed attributable to the PSA, which we revisit herein, showing that PSA, in contrast, is not the decisive factor. Crucial questions regarding the thermodynamics and structure have remained unanswered in that more phenomenological report. Therefore, to exploit the unique properties of photoacid assemblies in targeted applications, a comprehensive understanding of nano-assembly formation still is highly required.

The endeavor herein is to advance the comprehension in the emerging field of photoswitchable nano-objects, paving the way for tailored applications of photoresponsive materials. Specifically, we evaluate the driving forces to further understand the self-assembly and photo-excitation response of photoacid-macroion assemblies. For this purpose, we focused



Scheme 1 Schematic overview of the building blocks and assembly formation: anionic photoacids, 1-naphthol-3,6-disulfonate (1N36S), 1-naphthol-3,8-disulfonate (1N38S), 1-naphthol-4,8-disulfonate (1N48S), 2-naphthol-3,6-disulfonate (2N36S), 2-naphthol-6,8-disulfonate (2N68S) or 2-naphthol-3,6,8-trisulfonate (2N368S) associate with cationic dendrimer macroions to form nano-objects in aqueous solutions, which can respond to light-irradiation.

on a larger set of photoacids, additionally to the above-mentioned ones, including 1-naphthol-4,8-disulfonate (1N48S), 2-naphthol-6,8-disulfonate (2N68S) and 2-naphthol-3,6,8-trisulfonate (2N368S), with varying photoacidity as given in Table 1 (determination see ESI, Fig. S1 and Table S1†), as well as the influence of the charge ratio on the assembly formation and light responsiveness. In particular, the current study aims at understanding nanoscale particle properties and responses based on molecular structures, interaction forces, and equilibrium association thermodynamics. This should allow for establishing this novel approach to light-trigger size- and structure-controllable nanoparticle formation in aqueous solutions. The assembly formation and components used are schematically shown in Scheme 1.

Table 1 Strength of the different photoacids before irradiation (pK_a) and while irradiation (pK_a^*) determined as part of this study (from Förster cycle and direct measurements, see photoacid characterization in ESI†)

	1N36S	1N38S	1N48S	2N36S	2N68S	2N368S
pK_a	8.6	8.78	8.74	8.99	8.94	8.89
pK_a^*	−2.26	−0.64	−0.54	0.43	0.21	−0.7

This journal is © The Royal Society of Chemistry 2024

Published on 13 December 2023. Downloaded by Universitat Erlangen Nurnberg on 1/11/2026 10:32:27 PM.

2. Results and discussion

A. Sizes of photoacid-macroion nano-objects before and after photo-irradiation

Supramolecular assemblies were formed at pH = 7.0, where both the polycation and the hydroxyl group of the photoacids are protonated. Thus, the photoacid is dianionic, while the dendrimer has 64 positive charges due to the protonation of the primary amines. As previous studies have shown that the charge ratio is decisive for the nano-objects, we defined the initial charge ratio l as[24,62]

$$l = \frac{z^{-}(\text{sulfonate}) \times c(\text{photoacid})}{z^{+}(\text{amine}) \times c(\text{dendrimer})} \quad (1)$$

Light scattering assists in clarifying in how far the increased photoacidity influences the growth of the nanoparticles upon irradiation. As can be seen in dynamic light scattering (DLS) in Fig. 1a (and Fig. S2†), the autocorrelation function of the sample with 2N68S at l = 1 shows a well-defined and monodisperse size of the photoacid-dendrimer nano-objects before irradiation. After irradiation, the size of the nano-objects increases from a hydrodynamic radius R_H = 152 (distribution width σ = 0.09) to R_H = 255 nm (σ = 0.11).

Hydrodynamic radii depend on the photoacid and the charge ratio as given in Fig. 1b and c, ranging from R_H = 85 nm to R_H = 350 nm. All these assemblies represent equilibrium structures as was shown by the independence on preparation procedure (Fig. S3†). In this size characterization, disturbing inter nano-object interactions, polyelectrolyte effects and collective diffusion are avoided through the screening by added salt (see Experimental part in the ESI†), and no expressed concentration dependence has been observed (Fig. S4†).

Overall, assemblies with the 1-OH isomers (1N36S, 1N38S, and 1N48S) are considerably smaller before irradiation than the ones with 2-OH isomers (2N36S, 2N68S, and 2N368S), suggesting that the positioning of the hydroxide group not only influences the strength of the photoacidity, but also the assembly size on the nanoscale. Moreover, an altered behavior is evident concerning the charge ratio dependency. As the charge ratio increases, assemblies comprising the 1-OH isomers initially exhibit an increase in size followed by a decrease, whereas assemblies containing the 2-OH isomers exclusively experience a size reduction. This implies that the 2-OH isomers are initially more stabilized, leading to a consistent decrease in size, whereas the 1-OH isomers only demonstrate a size reduction in the presence of an excess of anionic charges. This observation implies that the positioning of the hydroxide group likely exerts an influence on photoacid-photoacid interactions, elucidating the charge ratio dependence. This will be discussed in chapter F in more detail. In the case of the 1-OH isomers, photoacids 1N38S and 1N48S exhibit larger assemblies at an excess of positive charges. In comparison, the assemblies with 1N36S are half in size, which demonstrates that the position of the sulfonate group also influences the size of the assembly. The 2-OH isomers exhibit the same behavior with only a small size decrease with increasing the charge ratio, although the position of the sulfonate group again influences the size of the nano-assemblies.

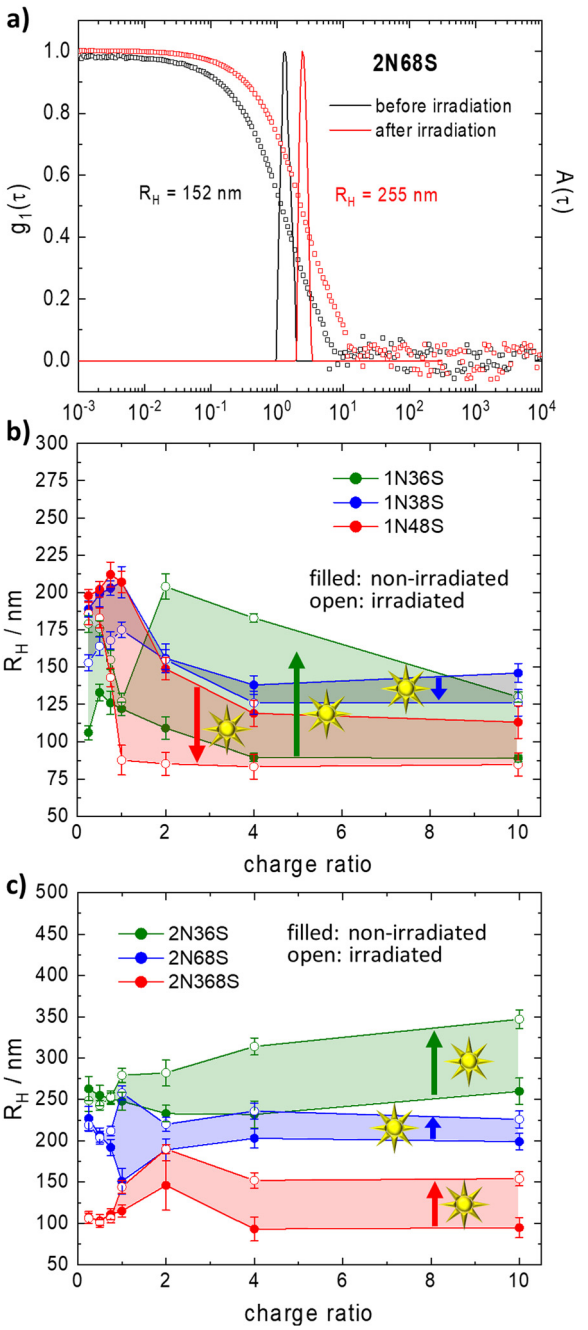


Fig. 1 Particle size analysis by DLS of photoacid-macroion nano-objects before and after photo-irradiation: (a) electric field autocorrelation function $g_1(\tau)$ and distribution of relaxation times $A(\tau)$ at a scattering angle of θ = 90° for assemblies with 2N68S at l = 1.0, and corresponding hydrodynamic radii R_H resulting from the angular dependent DLS extrapolated to zero scattering angle; (b) hydrodynamic radii R_H of the photoacid-macroion nano-objects determined by for 1-OH isomers (1N36S, 1N38S and 1N48S) and (c) 2-OH isomers (2N36S, 2N68S and 2N368S) as function of charge ratio (all: c(photoacid) = 1 × 10^{-4} mol l^{-1}).

Published on 13 December 2023. Downloaded by Universitat Erlangen Nurnberg on 1/11/2026 10:32:27 PM.

After photo-irradiating the 2-OH photoacids at an irradiation wavelength λ = 302 nm, the size of the assemblies increases for each photoacid (*e.g.* 2N36S from R_H = 253 nm to R_H = 349 nm). This is particularly pronounced for charge ratios $l \geq 1.0$. In contrast, the 1-OH photoacids behave differently after photo-irradiation. Assemblies made out of 1N38S or 1N48S and the macroions decrease in size rather than increase (*e.g.* 1N38S from R_H = 148 nm to R_H = 125 nm). One plausible explanation is the second sulfonate group, which is directly positioned next to a hydroxide group. Due to the close approximation of the functional groups, the electrostatic repulsions upon photo-irradiation bears a decrease in the size of the assemblies as a consequence. In the case of the remaining photoacids, the higher anionic charge results in stronger electrostatic interactions, consequently yielding greater interconnection and an enlargement in size. Similar to what transpired before photo-irradiation, after photo-irradiation the assemblies with 1N36S behave completely differently in comparison to those of 1N38S and 1N48S. They become larger because the sulfonate groups are now much further away from the hydroxyl group. Following photo-irradiation, the size of these assemblies doubles due to the more highly charged photoacid – *vide infra*. Overall, both the strength of the photoacid (Table S1†) and the positioning of the functional groups are determining factors.

Next to their hydrodynamic sizes, it is of interest to consider the number concentration of the nano-objects in solution. For this purpose, we regarded the scattering intensity in dependence on the charge ratio for the different photoacid assemblies (Fig. S7†). Taking the assembly sizes into consideration, we approximate the scattering intensity of one particle as proportional to its aggregation number and, thus, to its volume, which yields a relative particle number concentration – Fig. 2. Of course, this represents only a rough estimate, as particle shapes and densities may vary, but it allows for a general insight. Before irradiation, the particle number densities increases with increasing charge ratio, as more photoacids interact with the dendrimer macroion. Notably, the photoacids 1N38S and 1N48S manifest the lowest particle number density, primarily attributable to the close proximity of the sulfonate group and the OH-group. This spatial arrangement impedes the formation of photoacid–photoacid interaction and, consequently, interconnection. In contrast, the highest number density is observed for 2N368S, a difference that can be rationalized by the higher number of anionic charges. Given the electrostatic foundation of the self-assembly process, it is reasonable that the valency largely influences the number of particles. In general, aside from the assemblies involving 1N48S and 1N38S, the greatest quantity of nano-assemblies is present in the photoacids with the smallest nano-assemblies. After photo-irradiation, a drastic increase in the scattering intensity is discernable for most photoacids. The increase is not solely attributed to the size increase since the ratio $I_0/I_{rel,\ one\ particle} = I_0/R_H^3$ also increases; for 1N36S it goes from 1.16×10^{16} to 1.76×10^{17}. In other words, a higher number of particles per volume, that is a higher number concentration of photoacid-macroion nano-objects, is formed through photo-irradiation. At the same time the difference between 2N368S and the other photoacid decreases, which is due to the strength of the photoacids.

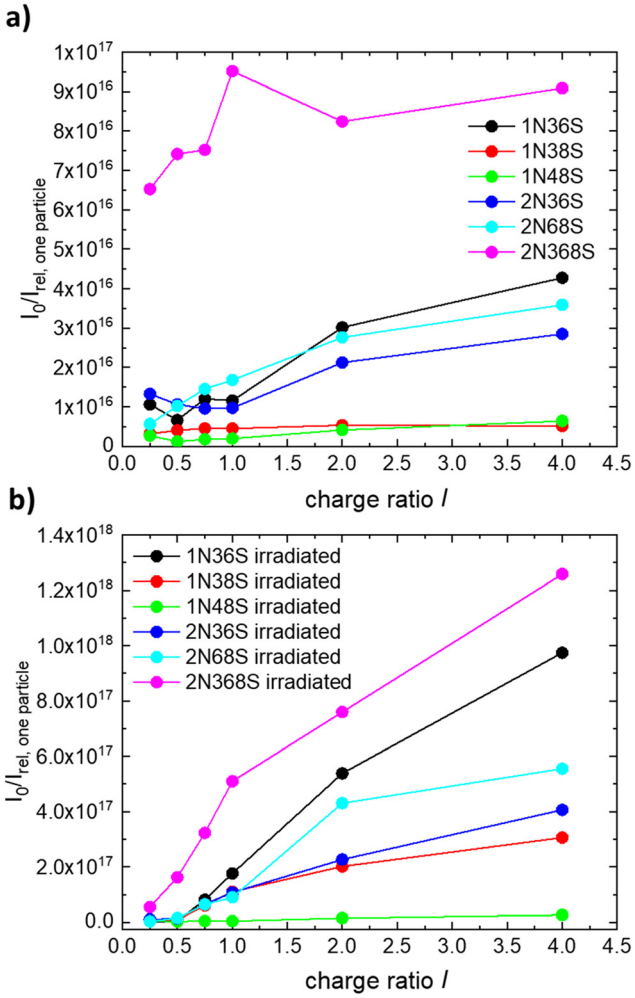


Fig. 2 Relative number concentration of photoacid-macroion nano-objects approximated from light scattering intensity analysis $I_0/I_{rel.\ one\ particle}$ as a function of the charge ratio (a) before and (b) after irradiation.

B. Nano-object composition: constituent ratio and hydrogen bonds

To elucidate the particle composition, we performed centrifugation and dialysis experiments (Fig. S8†) and determined the charge ratio of the assemblies itself $l_{assemblies}$.

With an assembly charge ratio below 1, the positive dendrimer charges significantly dominate. At an excess of photoacids, an assembly charge ratio $l_{assemblies}$ = 0.85 is observed independently of the amount of photoacid. Notably, a positive ζ-potential demonstrates that not every photoacid interacts with the dendrimer, even at an excess of the dendrimer. This indicates that the interactions of the photoacids with the dendrimer are weak without photo-irradiation, which can be attributed to their weak mutual secondary interaction, as will

 This journal is © The Royal Society of Chemistry 2024

Published on 13 December 2023. Downloaded by Universitat Erlangen Nurnberg on 1/11/2026 10:32:27 PM.

be discussed in more detail in chapter E. Photo-irradiation drastically changes the scenario. While nearly all photoacids are bound at an excess of cationic charges, free photoacids are observed at an excess of anionic charges. Here, the composition of the assemblies is strongly driven by the molecular structure of the photoacid. Photoacids carrying functional sulfonate groups not in close proximity (1N36S and 2N68S) exhibit the largest $l_{assemblies}$ in the order of $l_{assemblies} = 3$. Here, 1.5 photoacid molecules interact with one amine group of the dendrimer. In any other case, $l_{assemblies}$ is considerably lower, but still larger than 1.0. Thus, the relative position of the functional sulfonate groups determines the interactions and a close proximity between them strongly limits any electrostatic interaction with the dendrimer.

Experiments results indicate that one reason for the pivotal role of structure and the position of the functional sulfonate groups in the size of the nano-objects is a secondary non-covalent interaction in-between photoacid molecules. To address the question what kind of interactions are present between the photoacids, we measured O–H and SO_3-related IR signatures (Fig. 3a). ν(O–H)s are typically found at >3500 cm^{-1}, while the in-plane bending vibrations δ(O–H) occur between 1330 and 1430 cm^{-1}. The sulfonate groups form a strong band at ν(S=O) = 1345 cm^{-1}. Such a downward shift is typically due to hydrogen bonds, proving the existence of inter-photoacid hydrogen bonds as indicated in Fig. 3b. This presence of hydrogen bonds also allows to understand the reduction in size of nano-assemblies containing 1N38S and 1N48S. Following irradiation and subsequent deprotonation of the photoacid, these hydrogen bonds cease to exist. In the specific instances of 1N38S and 1N48S, the proximity of the sulfonate group to the newly formed $-O^-$ group results in both, the absence of further interconnection and mutual repulsion, thereby causing the reduction in size. In this context it should also be noted that the dendrimers are fully hydrophilic molecules and no influence of any hydrophobic effect is to be expected or has been observed.[63,64]

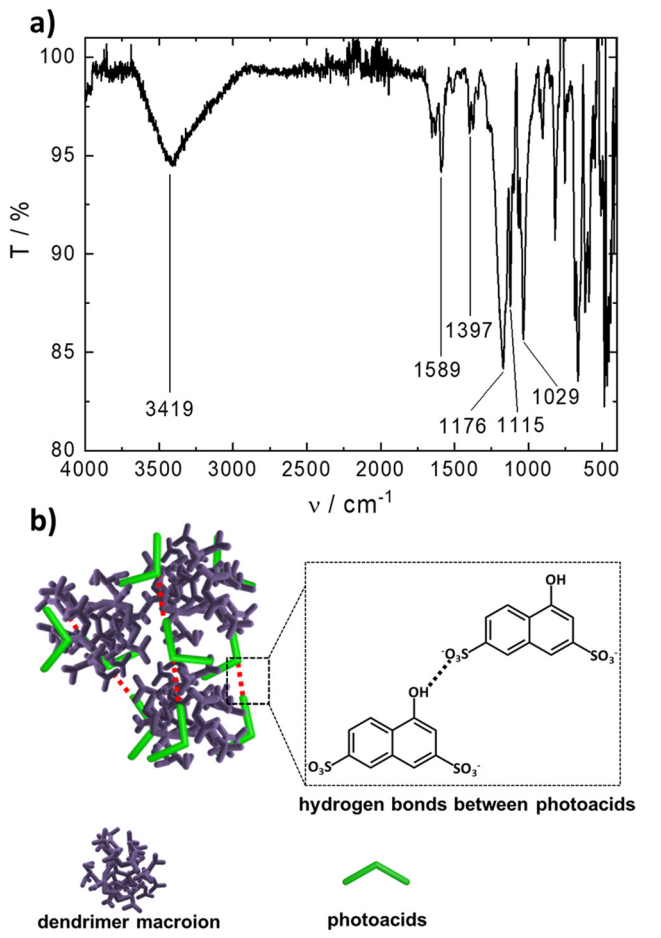


Fig. 3 Analysis of secondary interaction of photoacid-dendrimer assemblies before irradiation: (a) IR-spectroscopy of 1N36S; (b) scheme of the photoacid-photoacid hydrogen bonds in the nano-objects.

C. The structure of photoacid-macroion nano-objects

Static light scattering (SLS) and small angle neutron scattering (SANS) were performed to elucidate the particle shapes and internal structures. Fig. 4a and b display the structure-sensitive ratio of the radius of gyration to the hydrodynamic radius R_G/R_H as a function of the charge ratio before and after photo-irradiation (for R_G determination see Fig. S9†).

Before photo-irradiation the R_G/R_H for the nano-objects with the 1-OH isomers decreases until $l = 1.0$ from where it increases to a nearly constant value. In detail, with 1N38S and 1N48S, nano-objects show an overall R_G/R_H increase, while 1N36S shows a decrease with charge ratio. In the case of the 2-OH isomers, the R_G/R_H is almost independent of the charge ratio for 2N36S and 2N68S. For 2N368S, a behavior similar to that of the 1-OH isomers evolves. When photo-irradiated, for 2N36S and 2N68S, R_G/R_H is subject to only insignificant changes; 2N368S in contrast, follows the trends seen for the 1-OH isomers before and after irradiation.

Interestingly, all data fall onto one master curve for R_G/R_H as a function of R_H (Fig. 4c), regardless of photo-irradiation or not, except for 2N368S. As the radius increases, the R_G/R_H decreases to 0.5. These small values are known for microgel particles and polyelectrolyte complexes where the interior core is denser than the outer part of the nano-object.[65–67] The origin of this masterplot behavior based on molecular interactions will be discussed below – *vide infra*.

To further elucidate how photo-irradiation affects the structure, we performed SANS for two exemplary photoacids, 1N36S and 2N36S, at $l = 2.0$ (Fig. 5).

Before any photo-irradiation, the low intensity prompts only a small amount of assemblies. The data were fit with different structural models. The chosen fits exhibit small errors χ^2 (Table S2,† which is not the case for other models tested), and the R_G of the model is in agreement with a model-free R_G from a Zimm plot. In the case of 1N36S, before irradiation, the resulting structure is a core–shell sphere with a denser interior and looser outer shell with a total radius R_{tot} = (90 ± 19) nm and a shell thickness of R_{shell} = (44 ± 25) nm. In the high q region, additional smaller spherical particles with R

Published on 13 December 2023. Downloaded by Universitat Erlangen Nurnberg on 1/11/2026 10:32:27 PM.

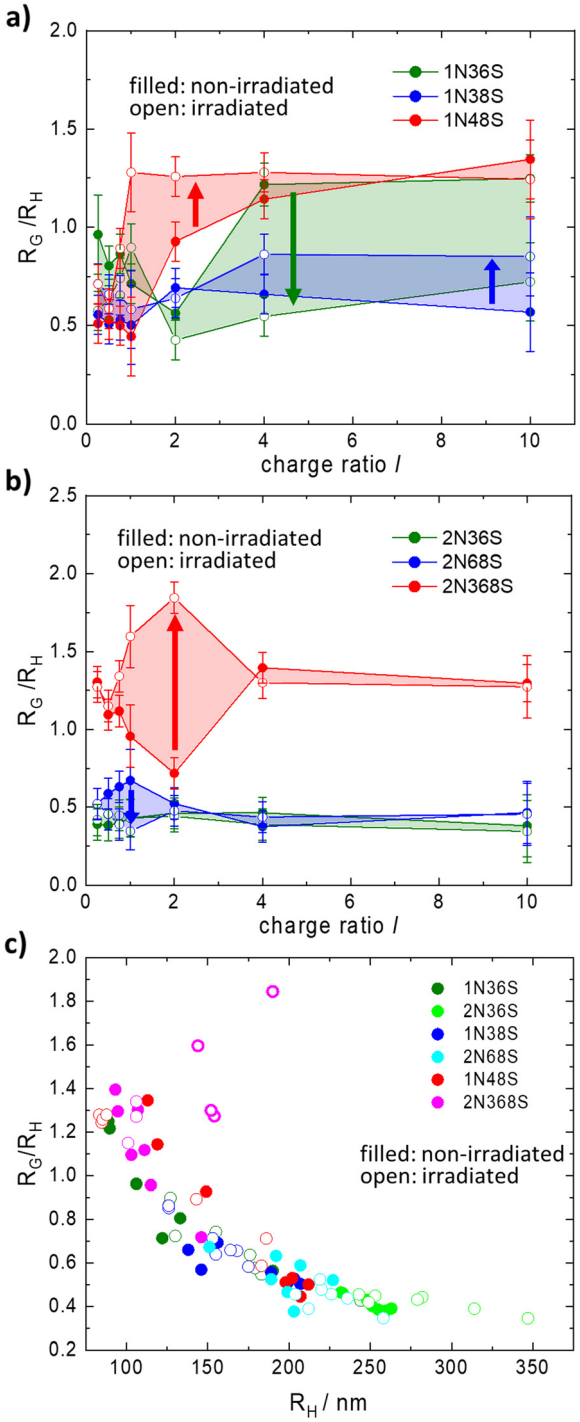


Fig. 4 Shape sensitive R_G/R_H of the nano-objects (from SLS/DLS) as a function of the charge ratio before and after irradiation for (a) the 1-OH isomers and (b) the 2-OH isomers; (c) R_G/R_H as a function of R_H (open symbols with thick edge: 2N368S).

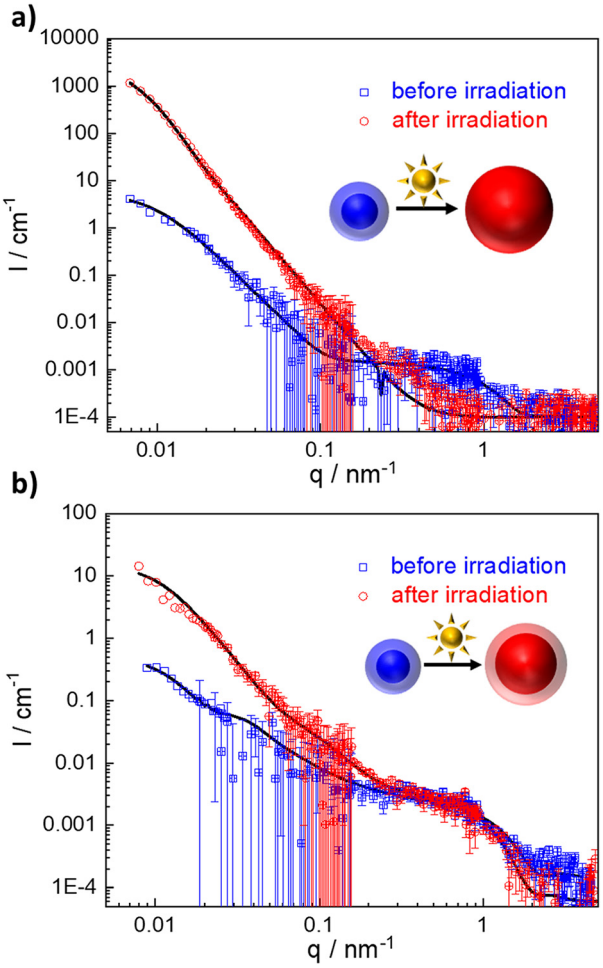


Fig. 5 Small-angle neutron and static light scattering of the nano-objects with l = 2.0: (a) 1N36S-macroion assemblies (R_G/R_H = 0.41 to R_G/R_H = 0.73) and (b) 2N36S-macroion assemblies (R_G/R_H = 0.46 to R_G/R_H = 0.44), each before and after irradiation in D_2O with the same concentration as in H_2O. Solid lines represent the model fit to the experimental data.

= 2 nm are seen, corresponding to the size of a G4-dendrimer. With 2N36S, it is R_{tot} = (98 ± 0.2) nm and R_{shell} = (2.0 ± 0.2) nm, again with some G4-dendrimer with R = 2 nm. Photo-irradiation causes an intensity increase. Like DLS and SLS, SANS also reveals that more particles are formed. The structure of the 1N36S nano-objects changes from a core–shell sphere to a homogeneous sphere with a radius of R = (180 ± 1) nm. In the case of 2N36S, the structure after irradiation is a core–shell sphere with R = (127 ± 24) nm and a thickness of R_{shell} = (15 ± 2) nm. For 2N36S, some free G4-dendrimers coexist, which are possibly loaded but not interconnected. Overall, the findings from SANS are also congruent with the SLS, where the larger assemblies show the smaller R_G/R_H.

Atomic force microscopy was then used to further elucidate the structure of the nano-assemblies, revealing a core–shell structure for 1N36S and 2N36S before irradiation (Fig. 6 and Fig. S10, S11†). After irradiation, the nano-assemblies with 1N36S also undergo a structural change to a homogenous sphere, in accordance with the scattering analysis. A more precise statistical analysis (Fig. S10 and S11†) revealed uniform and well-defined nano-assemblies both prior to and following irradiation. To gain more information on the internal structure, the volume shrinking upon drying was quantified by

This journal is © The Royal Society of Chemistry 2024

Published on 13 December 2023. Downloaded by Universitat Erlangen Nurnberg on 1/11/2026 10:32:27 PM.

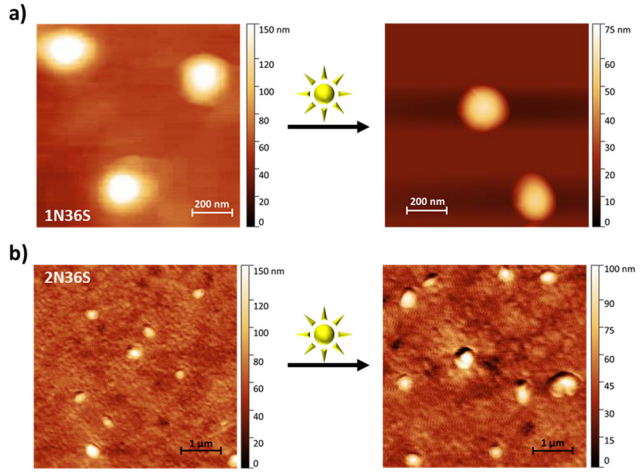


Fig. 6 AFM images of the photoacid-dendrimer assemblies with (a) 1N36S (core shell to sphere) and (b) 2N36S (core–shell to core–shell) before and after irradiation.

comparing AFM and DLS. Table S3† lists the volume ratio v_{AFM}/v_{DLS}, which decreases upon irradiation for all assemblies, *i.e.* the overall density of the nano-assemblies in solution becomes smaller upon irradiation, even though the structure changes from a core–shell to a homogeneous sphere.

D. Charge characteristics of photoacid-macroion nano-objects

To gain more information regarding the size control before and after photo-irradiation, we measured the ζ-potential for the nano-objects with the different photoacids, as illustrated in Fig. 7a and Fig. S12.† Interestingly, all of them have positive ζ-potentials before irradiation even at an excess of anionic photoacid charges in the solution. 2N368S is the only exception with a ζ-potential that is slightly negative. These findings are consistent with the results from the dialysis experiments, where it became evident that the photoacids do not associate to a large extent with the dendrimer macroions before photo-irradiation.

After photo-irradiation, the ζ-potential decreases significantly, especially at $l > 1.0$. Now, interactions between the building blocks increase in line with what is seen from light

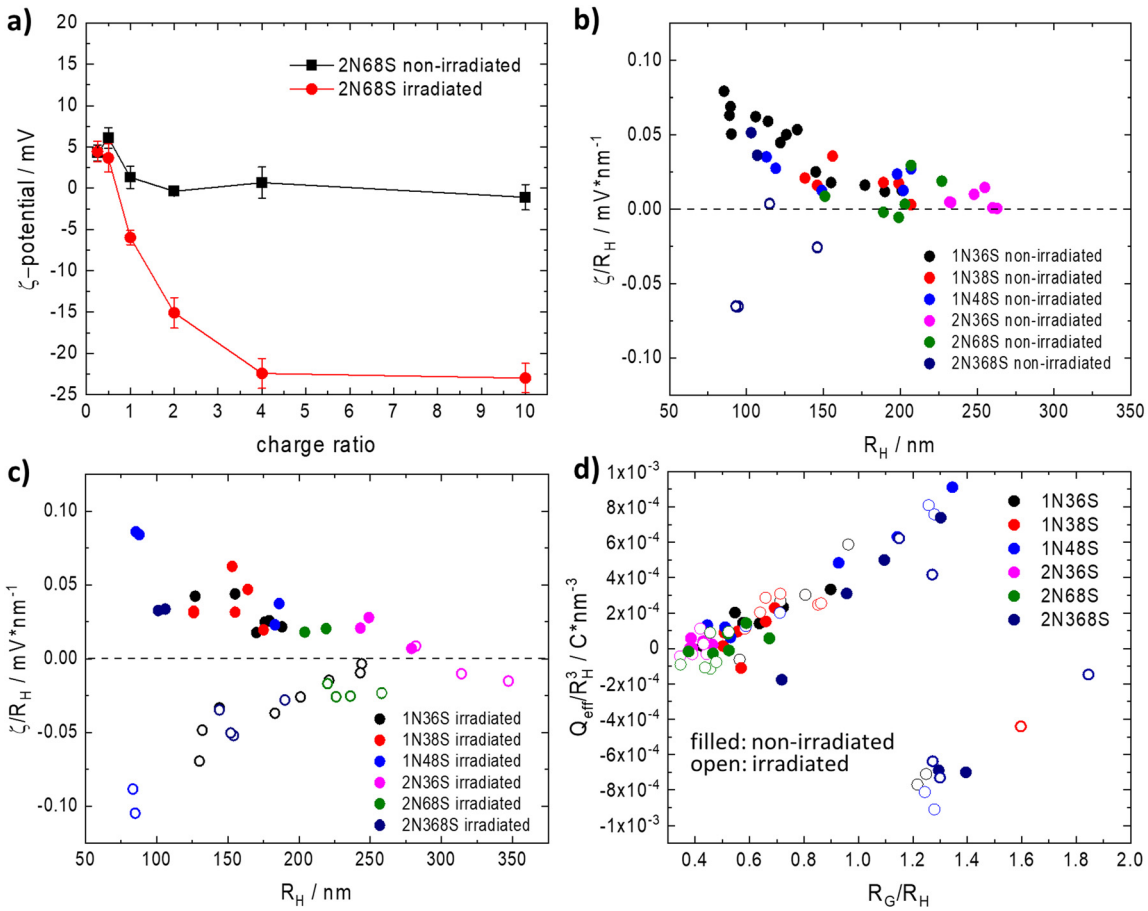


Fig. 7 ζ-potential analysis of macroion-photoacid nano-objects: (a) ζ-potential analysis of nano-objects with 2N68S and 2N368S as a function of the charge ratio *l*; (b) and (c) effective surface charge density ζ/R_H of photoacid-macroion nano-objects for the different photoacids as function of R_H: (b) before irradiation (open symbols correspond to assemblies with 2N368S, which do not follow the curve); (c) after irradiation (open symbols indicate charge ratios $l > 1.0$); (d) effective volume charge density Q_{eff}/R_H^3 in dependence on R_G/R_H before (filled) and after (open) photo-irradiation (open symbols indicate 2N368S, which does not follow the master dependency).

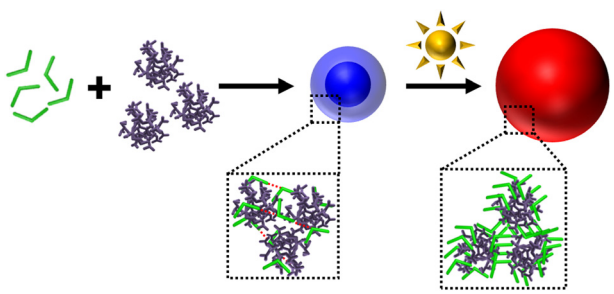
Published on 13 December 2023. Downloaded by Universitat Erlangen Nurnberg on 1/11/2026 10:32:27 PM.

scattering. At a cation excess, only small ζ-potential changes occur. Once again, the photoacids 1N36S and 2N68S represent the extreme cases with the most negative ζ-potential. From a molecular point of view, after photo-irradiation and proton dissociation from the hydroxyl group, the negatively charged oxide can interact much better in the case of the photoacid for which the sulfonate group is not in close proximity. This facilitates interactions with the polyelectrolyte and, thus, more negative charges are integrated in the assembly.

Previously we demonstrated with AY38, that the effective surface charge density (charge density at the shear plane) as a function of the hydrodynamic radius provides an adequate understanding of changes in size.[21,23,53,61] Fig. 7b and c illustrates the effective surface charge density approximated by ζ/R_H *versus* the hydrodynamic radius for each photoacid before and after photo-irradiation. In both cases, lower surface charge densities lead to larger assemblies. Each value is positive before photo-irradiation except for the trivalent 2N368S. After photo-irradiation, the surface charge density becomes smaller overall but still shows the same trend as before irradiation. Hence, the charge does play a key role in stabilizing the assemblies. Stabilizing finite-size aggregates may be seen in analogy to an electrostatic stabilization of hydrophobic colloids in aqueous solutions, despite the hydrophilic and water-swollen nature of the assemblies here.

Further, Fig. 7d documents that the absolute value of the volume charge density increases with increasing R_G/R_H. This indicates core–shell gel-like and more globular particles with low effective charge density and more anisotropic structures (R_G/R_H > 1.3) with higher charge density. Considering the master curve in Fig. 4c, small charge densities also relate to larger (more globular) assemblies. At this point, based on these results, likely, any association of the photoacids with the dendrimer macroion is weak before irradiation (to be quantified in paragraph E). Only a small surface area is stabilized. Consequently, the assemblies grow and at the same time, become more globular to be stabilized with a minimized surface area. In other words, the nano-assemblies are stabilized by the surplus charges at a specific stoichiometry within the nanoscale size range while also conforming to the larger surface area of the nanoscale particles.

Scheme 2 depicts the inner structure of the nano-objects and the different behavior of the photoacid molecules in regard to the interaction with the dendrimer macroion before and after irradiation. The origin of the behavior will be discussed in the following sections.



Scheme 2 Scheme of photoacid-macroion nano-objects and their internal structure before and after irradiation. Before irradiation, free photoacid molecules are also present, but all photoacid molecules are bound in the assembly after irradiation.

E. Thermodynamic analysis: association mechanism and interaction forces

To understand the binding mechanism from a thermodynamic standpoint, we measured the isothermal titration calorimetry (ITC) for the dendrimer macroion – divalent photoacid systems before photo-irradiation. The raw data in Fig. S13† and results in Table 2 reveal that the different photoacids qualitatively behave similarly. The titration curve contains direct information on the enthalpy and the equilibrium constant(s). Indirectly, information on the free energy change ΔG and the entropy change ΔS results. We employed a general model, which can be applied to any scenario with more than one ligand. It considers the interaction at multiple identical or non-identical binding sites (see Experimental section). Each photoacid first has an endothermic and, thus, entropically driven binding step (*e.g.* 1N36S: ΔH_1 = 98 kJ mol^{-1}; ΔS_1 = 0.4 kJ mol^{-1} K^{-1}; $K_1 = 2.8 \times 10^5$ mol^{-1}), followed by an exothermic association (*e.g.* 1N36S: ΔH_2 = −152 kJ mol^{-1}; ΔS_2 = −0.45 kJ mol^{-1} K^{-1}; $K_2 = 1.5 \times 10^5$ mol^{-1}) and then again an endothermic and entropically driven binding step (*e.g.* 1N36S: ΔH_3 = 45 kJ mol^{-1}; ΔS_3 = 0.16 kJ mol^{-1} K^{-1}; $K_3 = 3.0 \times 10^5$ mol^{-1}). To gain understanding of the different binding steps we performed different ITC reference measurements.

To further elucidate the first endothermic binding, we titrated the polyelectrolyte into a naphthol derivate with only one sulfonate group (1N6S) in an additional comparison

Table 2 Thermodynamic analysis of the photoacid-dye association by ITC for the divalent photoacids (overall, the error of ΔH is 4–10% and of ΔS 5–11%. Full results and errors can be found in Table S4†)

	1N38S	1N48S	1N36S	2N36S	2N68S
ΔH_1/(kJ mol^{-1})	86.3	86.9	98.9	88.9	80.2
ΔS_1/(kJ mol^{-1} K^{-1})	0.36	0.36	0.40	0.36	0.34
ΔH_2/(kJ mol^{-1})	−144.1	−143.7	−152.5	−150.0	−139.9
ΔS_2/(kJ mol^{-1} K^{-1})	−0.42	−0.41	−0.45	−0.43	−0.40
ΔH_{bind}/(kJ mol^{-1})	−57.8	−56.8	−53.6	−61.1	−59.7
ΔS_{bind}/(kJ mol^{-1} K^{-1})	−0.055	−0.052	−0.051	−0.071	−0.069
ΔG_{bind}/(kJ mol^{-1})	−41.6	−41.7	−38.6	−40.3	−39.4

This journal is © The Royal Society of Chemistry 2024

Published on 13 December 2023. Downloaded by Universitat Erlangen Nurnberg on 1/11/2026 10:32:27 PM.

experiment: two binding steps occur revealing a first exothermic binding step ($\Delta H_{1N6S,1}$ = −51 kJ mol^{-1}; $\Delta S_{1N6S,1}$ = −0.18 kJ mol^{-1} K^{-1}; $K_{1N6S,1}$ = 3.2 × 10^4 mol^{-1}) followed by an endothermic one ($\Delta H_{1N6S,2}$ = 125 kJ mol^{-1}; $\Delta S_{1N6S,2}$ = 0.42 kJ mol^{-1} K^{-1}; $K_{1N6S,2}$ = 7.8 × 10^5 mol^{-1}). Relative to 1N36S, the first endothermic binding step is missing. The only difference between the two systems is the presence of the second sulfonate group in 1N36S. Thus, the first step of the photoacid-dendrimer-assembly formation corresponds to the release of counterions of the sulfonate groups, which is known to be highly entropically driven.[68,69]

This necessitated another ITC reference measurement. The dendrimer was titrated into an aqueous solution of propane disulfonate, where no secondary dye–dye interactions occur. At pH 7.0, a first endothermic binding step ($\Delta H_{propane,1}$ = 107 kJ mol^{-1}; $\Delta S_{propane,1}$ = 0.4 kJ mol^{-1} K^{-1}; $K_{propane,1}$ = 2.3 × 10^5 mol^{-1}) was found (Fig. S14†). Compared to the photoacids, the strength of the endothermic binding and the gain in entropy is similar. This confirms the conclusions of the release of salt ions and water from the hydration shell as the first binding step in both systems. It is also valuable to compare the current results with electrostatic self-assembly involving simple dyes with two sulfonate groups at an aromatic backbone rather than photoacids, as investigated previously.[24] In stark contrast to the photoacids displaying endothermic and entropically driven interactions, those dyes exhibited strong exothermic interactions due to the overlap of electrostatic and dye–dye attractions.[16,24,55,70] Further, those dye binding isotherms could be fitted with one binding step, while the photoacids show three binding steps.

In the following, we revisited Acid Red (AR26)-dendrimer association under the experimental conditions as used for the photoacids herein, in order to understand this difference. We noted a complex binding process with three binding sites in contrast to one binding site reported previously (Fig. S14a†).[67] This difference can be attributed to the larger range of molar ratios, which we herein investigated. Nevertheless, this fails to explain the differences seen between the azo dye and the photoacid regarding the different binding behavior, despite their molecular resemblance. The difference between the photoacid and the azo dye is seen in the secondary interactions and the different pHs. Photoacids are prone to hydrogen bonding, while the dyes showed mutual π–π interactions next to dye-macroion interactions. Photoacids clearly do not interact strongly with each other. As such, an exothermic binding was found in the case of the AR26-dendrimer system. Despite similar electrostatic effects as with the photoacids, interactions are not entropically driven. This further underscores the importance of secondary dye–dye interactions.

Further, the second binding step is the only exothermic one of the interaction of the photoacid with the dendrimer. Here, induced by the increasing concentration of the dendrimer the exothermic intermolecular interaction of photoacid and dendrimer occurs.

Finally, the origin of the last endothermic step of the ITC measurements of the photoacid – dendrimer system is to be elucidated (1N36S: ΔH_3 = 45 kJ mol^{-1}; ΔS_3 = 0.16 kJ mol^{-1} K^{-1}; K_3 = 3.0 × 10^5 mol^{-1}). For this purpose, we repeated the measurements but titrated the photoacid into the dendrimer. In that case, we observed an initial endothermic binding step ($\Delta H_{reverse,1}$ = 78 kJ mol^{-1}; $\Delta S_{reverse,1}$ = 0.23 kJ mol^{-1} K^{-1}; $K_{reverse,1}$ = 3.8 × 10^5 mol^{-1}), followed by a subsequent exothermic one ($\Delta H_{reverse,2}$ = −140 kJ mol^{-1}; $\Delta S_{reverse,2}$ = −0.41 kJ mol^{-1} K^{-1}; $K_{reverse,2}$ = 2.2 × 10^5 mol^{-1}). Implicit is that this procedure lacks the last endothermic step. This indicates that the last endothermic step corresponds to the high concentration of the dendrimer leading to inter-dendrimer repulsion. This is accompanied by a decrease in the size of the assemblies confirmed by DLS. The finding matches previous results, where the addition of an excess of dendrimer disrupted the assemblies.[71]

F. Relating thermodynamics with the nanoscale structure

It is now particularly interesting to determine how the thermodynamic parameters relate to the structure of the nano-assemblies. Fig. 8a considers the hydrodynamic radii of the different photoacid-macroion assemblies as a function of the binding enthalpy. Here, we consider the first two binding steps, as the third one corresponds to the decomposition of the assemblies. This master-plot reveals a linear dependency of the nano-assemblies' size (hydrodynamic radius) on the binding enthalpy. Stronger enthalpic interactions correlate with larger assemblies. As it is especially true for loading ratios l > 2.0, a clear excess of photoacids is essential. In other words, induced secondary mutual interactions of the photoacids play an important role in defining the size.

Furthermore, also the shape of assemblies can be determined thermodynamically: previously, we have shown that the interplay between enthalpy and entropy assists in predicting the assembly shape in the electrostatic self-assembly of a different (exothermic, π–π interacting) system.[16] After adding the data of the dendrimer-photoacid assembly obtained herein (red symbols), all points fall onto one master curve (Fig. 8b). The existence of this cross-system shape-determining enthalpy–entropy relation represents a remarkable and new finding.

This cross-system enthalpy–entropy relation clearly differs from the one observed for other systems. Mostly, the temperature or the salt concentration within the same system was varied, and in any case a single set of systems has been considered only – and, in particular, no relation to a nanoscale particle shape or alike has been made.[72–75] Possibly, a decreasing freedom of the molecules – *i.e.* a more expressed decrease in entropy – is caused by the more negative enthalpy changes due to the stronger interactions. This is consistent with previous hypotheses, which, however, did not vary the building blocks.[76–79] Lately, it was shown that the strength of dye–dye π–π interactions stemming from ionic binding to the polyelectrolyte determines whether spherical or more anisotropic aggregates are formed.[16] Correspondingly, in this case, photoacid–photoacid interactions are weaker and isotropic structures are built. Yet, complex many body effects in a multicomponent

Published on 13 December 2023. Downloaded by Universitat Erlangen Nurnberg on 1/11/2026 10:32:27 PM.

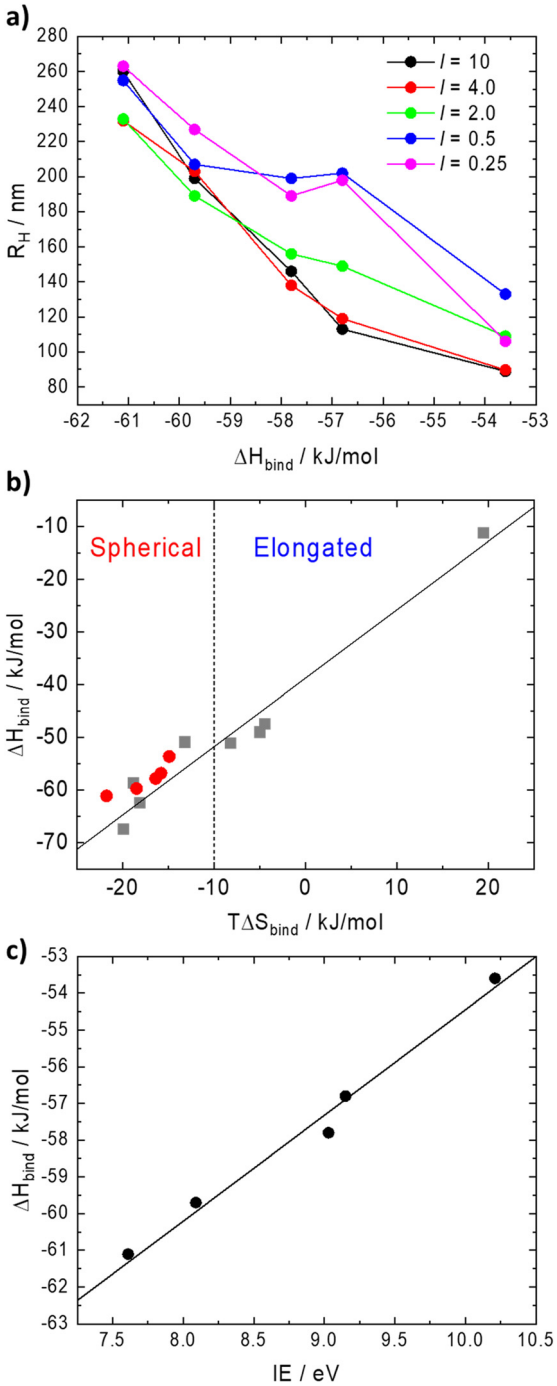


Fig. 8 Thermodynamic control on the nanostructure of the photoacid-macroion nano-objects: (a) dependency of assembly size (hydrodynamic radius R_H) on the binding enthalpy ΔH_{bind} at different charge ratios (different colours); (b) enthalpy–entropy relation for electrostatic self-assembly at the same temperature with the different building blocks: photoacid-macroion assembly (this study, red symbols) and results from previous studies on dendrimer–dye assembly based on a very different interaction scenario with π–π interaction and exothermic binding steps only (grey symbols);[16] (c) analysis of secondary interaction of photoacid-macroion assemblies: Dependency of the association enthalpy on the ionization energy of the hydroxyl group calculated by DFT.

polyelectrolyte systems including electrostatic effects, hydration effects, hydrogen bonding and dynamics of course occur, which is yet to be fundamentally elucidated.

As mentioned before, in previous macroion- π–π interacting dye studies, the PSA encoded the size and shape.[16] In the current case, it is crucial to emphasize that the PSA does not represent a determining parameter, even though the structure of the molecules are similar. This discrepancy arises from the different mutual photoacid interaction, notably the absence of any π–π interactions and the presence of hydrogen bonds. A critical factor in influencing the strength of hydrogen bonds is the electronegativity. For a quantitative comparison, the related ionization potentials were considered. The influence of a possible mesomeric stabilization of the proton-dissociated structure is also included. Ionization potentials often have been used to consider chemical reactions and determine the strength of binding such as in hydrogen bonds.[80–83] Fig. 8c gives the dependency of the association enthalpy from the ITC on the ionization energy (IE) of the OH-hydrogen determined by DFT calculation. The absolute value of the association enthalpy decreases with increasing ionization energy. As such, weaker hydrogen bonds consequence a less exothermic binding of the photoacid. In contrast, the dipole moment does not exhibit any clear dependency (Fig. S15†).

Hence, we conclude that likely, the ionization energy of the hydrogen encodes mutual photoacid–photoacid interactions and it is strongly dependent on the positioning of the functional groups. Thus, it is evident that thermodynamics encodes the assemblies' nanoscale structure, while the molecular structure encodes the thermodynamics of the binding. Thermodynamics is essential to relate molecular structure and nanoscale structure.

G. Relating nanoscale structure with molecular parameters

It is now of interest to draw a relation between the determining molecular parameter and the nanoscale structure. Therefore, we have plotted the hydrodynamic radius as a function of IE in Fig. 9a. It becomes evident that IE also controls the size of the assemblies, especially at an excess of photoacids. This may not be unexpected, as the influence of the hydrogen bond increases due to the excess of photoacids. But, at an excess of positive charges, its influence should be weakened. In contrast to the previous study,[60] again the PSA does not show any clear dependency. Overall, the different techniques provide a good understanding of assembly formation and switching thereof. The formation of the assemblies strongly hinges on the photoacids, which direct the ionization energy and photoacidity. Before photo-irradiation, the molecular parameter IE encodes the association enthalpy and, thus, the size of the assemblies by correlation to the strength of the hydrogen bonds in-between photoacids that are induced when the photoacids electrostatically bind to the dendrimer macroions and are thereby brought into proximity. Stronger hydrogen bonds lead to larger nano-assemblies. This accounts for the larger size of assemblies comprising the 2-OH isomers in comparison to the 1-OH isomers, owing to the greater strength of their hydrogen bonds.

This journal is © The Royal Society of Chemistry 2024

Published on 13 December 2023. Downloaded by Universitat Erlangen Nurnberg on 1/11/2026 10:32:27 PM.

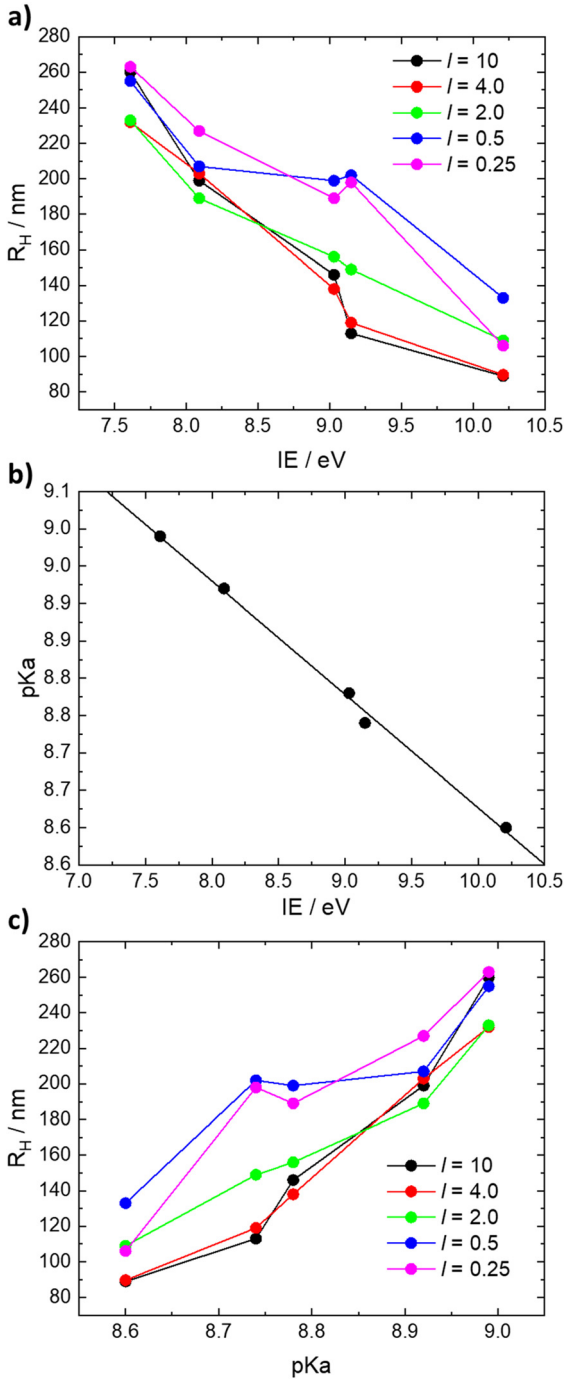


Fig. 9 (a) Dependency of the ionization energy of the hydroxyl group (not the complete molecule) on the size of the assemblies at different charge ratios (different colours). Dependency of (b) the pK_a-value on the ionization energy and (c) of the hydrodynamic radius of the assemblies on the pK_a-value.

Fig. 9b illustrates that the pK_a depends linearly on the ionization energy. As IE increases, the pK_a decreases, and stronger hydrogen bonds accompany a hindered hydrogen release. This renders it feasible to correlate the pK_a directly with the size of the assemblies as given in Fig. 9c.

Thus, once the underlying thermodynamics have been understood, nanoscale features (R_H) are directly correlated with molecular features (pK_a). This almost certainly enables the prediction of aggregate sizes prior to any assembly formation simply by determining the pK_a-value of the photoacid. This is not possible after irradiation. As the photoacid is deprotonated upon irradiation, the secondary interaction in form of hydrogen bonds are not formed anymore. Thus, there is no analogous correlation between R_H and the pK_a^* after irradiation.

As compared to previously investigated dendrimer-azo dye systems, not many nano-assemblies are present before photo-irradiation since secondary interactions here are weaker than in the π–π interactions in the previous systems. ITC measurements herein showed that the assembly formation occurs due to an entropy gain. At the same time, the shape of the assemblies strongly depends on the nano-object size and the association enthalpy. For this reason, the thermodynamics of the assembly formation also differ, which, in this case, leads to a weaker interactions between the building blocks and a smaller number of assemblies. Though the differences in binding type and assembly characteristics are this extreme, both systems still follow the same master curve regarding the enthalpy–entropy relation.

H. Thermodynamic understanding after irradiation

As it is impossible to perform the same analysis after photo-irradiation due to the short excited state lifetime of the photoacid, we complemented our investigations with the study of a pH-independent polymer, namely poly(diallyldimethylammonium chloride) (PDADMAC) in combination with 1N36S. In this case, the photoacid can be deprotonated through changing the pH. First, the changes after photo-irradiation are compared with changes upon deprotonating the photoacid with NaOH. Changing the pH and photo-irradiating the assembly leads to the same results in terms of assembly size (R_H = 215 nm *vs.* R_H = 209 nm). The comparable behavior of the PDADMAC system without the need of photo-irradiation motivated ITC measurements of this system at different pHs. For pH 7.0, we found a behavior similar to that with the dendrimer macroion. This confirms that the assembly principle is general and applies to any binding independent of the polyelectrolyte.

For the measurement at pH 10, three binding steps occur Interestingly, the first step is exothermic ($\Delta H_{PDADMAC,1}$ = −33 kJ mol^{-1}; $\Delta S_{PDADMAC,1}$ = −0.11 kJ mol^{-1} K^{-1}; $K_{PDADMAC,1}$ = 4.2 × 10^4 mol^{-1}), followed by an endothermic one ($\Delta H_{PDADMAC,2}$ = 92 kJ mol^{-1}; $\Delta S_{PDADMAC,2}$ = 0.31 kJ mol^{-1} K^{-1}; $K_{PDADMAC,2}$ = 2.2 × 10^5 mol^{-1}), and again an exothermic one ($\Delta H_{PDADMAC,3}$ = −100 kJ mol^{-1}; $\Delta S_{PDADMAC,3}$ = −0.33 kJ mol^{-1} K^{-1}; $K_{PDADMAC,3}$ = 6.0 × 10^5 mol^{-1}, Fig. S16†).

Molecularly, the only difference between both pHs is the deprotonated photoacid. Thus, the first exothermic step represents the electrostatic interaction of the deprotonated hydroxyl group of the photoacid with the cationic polyelectrolyte. At the same time, the hydration characteristics of the

Published on 13 December 2023. Downloaded by Universitat Erlangen Nurnberg on 1/11/2026 10:32:27 PM.

molecule undergo discernible changes in its deprotonated state relative to its protonated state. This can be observed at the negative $\Delta S_{PDADMAC,1}$, which may also stem from a change in hydration, which thus may be a plausible contributing factor. However, given the notably negative $\Delta H_{PDADMAC,1}$, it is evident that this cannot constitute the primary origin in the overall process. In a subsequent step, the release of the counterions from the sulfonate groups of the photoacid and the electrostatic interactions occur. A possible cause of the stronger interactions with the deprotonated hydroxide group rather than the sulfonate group is its stronger affinity to opposite-charged ions. This is understandable when viewing the association tendency of an anionic group with a polycation in analogy to its basicity. Arguably, sulfonic acids and phenols are close to the structure of the photoacids' structure. Since sulfonic acids are stronger acids than phenols, the conjugate base of a sulfonic acid displays weaker interactions with a proton in comparison to the conjugate base of a phenol. If the affinity of the anionic group to the cationic proton is utilized as an approximation to its affinity to cationic species in general, the behavior after irradiation is well understood.

Changes after photo-irradiation compared to before irradiation strongly depend on the strength of the photoacidity and, thus, the molecular structure of the photoacids, namely the proximity of the functional groups. Fig. 10a displays how the size of the assemblies increases upon photo-irradiation as long as a sulfonate group is spatially not too close to the hydroxyl group. In the case of 1N38S and 1N48S, the close proximity of the anionic sulfonate group and deprotonated hydroxyl group leads to a reduced nano-object size. This difference of the photoacids is especially the case for an excess of photoacid at $l > 1.0$. Furthermore, the number of assemblies increases upon photo-irradiation caused by the increase in the number of charges and the stronger interaction with the deprotonated hydroxyl group as compared to the one with the sulfonate groups. Thus, the photoacid molecules, which were free in solution before irradiation, now interact with the dendrimer and build new assemblies. After photo-irradiation, the secondary interactions do not play a significant role. Instead, the sizes of the assemblies are determined by electrostatic interactions and the molecular structure of the photoacid.

Compared to that the changes upon irradiation in the structure of the nano-assemblies are strongly dependent on the charge density (Table S3†). As the deprotonated hydroxyl group of the photoacids is pivotal for the changes after irradiation, the structural change should be strongly dependent on the photoacidity, which can be seen by plotting the change of the R_G/R_H value against the difference in pK_a ($(\Delta pK_a = pK_a - pK_a^*)$ (Fig. 10b). The stronger the photoacid and the larger the change in pK_a upon irradiation, the larger is the increase of R_G/R_H. This can probably be understood as the strength of the photoacid (ΔpK_a) determines the amount of deprotonated photoacid molecules and with that also to the charge density. Consequently, a more expressed change in pK_a causes an increase in charge density leading to a structural change of a core–shell structure to a spherical one: due to the irradiation

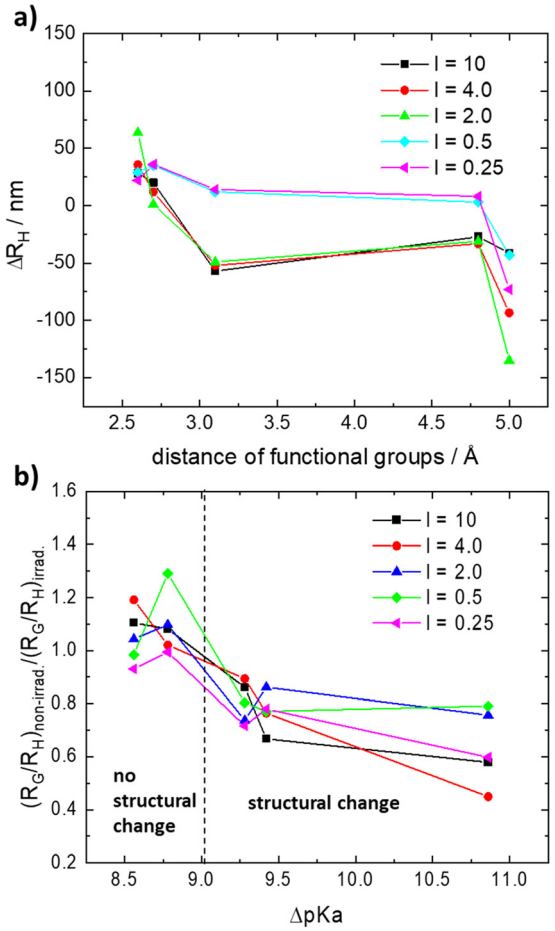


Fig. 10 Dependency of (a) the hydrodynamic radius of the assemblies after irradiation on the distance of the hydroxide group to the closest sulfonate group and (b) ratio of R_G/R_H before irradiation to R_G/R_H after irradiation on the difference of the pK_a value of the ground and excited state.

of the photoacid and subsequent deprotonation, more charges are present, which leads to a stronger interconnection between the building blocks so that a homogeneous sphere structure is formed. Thus, it is possible to predict the structural changes after irradiation by considering the difference in photoacidity between the ground and excited state.

General discussion

For a set of related photoacids with their functional groups at different positions and thus different acidity constants, we have investigated their assembly with dendrimer macroions: the photoacid-macroion nano-objects' sizes before and after irradiation in dependence on loading ratio underscore the importance of the photoacid connectors' functional group positioning. The structure of the photoacids influences the ionization energy of the hydroxyl group and thus the strength of the possible hydrogen bonds. In general, the 2-OH isomers show stronger hydrogen bonds and thus larger nano-assemblies before irradiation. Next to the particle size, the charge

This journal is © The Royal Society of Chemistry 2024

Published on 13 December 2023. Downloaded by Universitat Erlangen Nurnberg on 1/11/2026 10:32:27 PM.

characteristics were determined, elucidating the decisive role of the effective charge density for the particle size and structure. Further, assembly thermodynamics as studied by isothermal titration calorimetry have revealed association mechanisms and interaction forces including a dominant role of a first entropy-driven step due to counterion release and water rearrangement. The structure formation first is controlled by relatively weak electrostatic interactions between macroion and photoacid molecules, and then, thereby induced, secondary hydrogen bonds in-between photoacid molecules bound to the dendrimer macroion. This thermodynamic study allowed us to correlate thermodynamic parameters like the binding enthalpy to molecular properties like the ionization energy of the hydroxyl-group. The outcome contradicts previous results, where the PSA was found to have a structure-directing effect with regard to the size of the nano-assemblies in electrostatic self-assembly. This can likely be understood by the different secondary interactions: while the photoacid molecules in this study undergo mutual hydrogen bonds, the building blocks in the other study were ionic dye molecules which were shown to perform mutual π–π interaction. In summary, the relationship between ionization energy (IE) and the size of these assemblies presumably provides a predictive tool for estimating the dimensions of assemblies made of macroions and similar photoacid molecules as used herein. Beyond size prediction, we have also established a connection between thermodynamics and the structure of photoacid-macroion assemblies in form of the enthalpy–entropy relation. Interestingly, this principle seems to be independent of the specific type of secondary interaction among the interconnecting counterion molecules. Previously, experimental research had demonstrated that dye–dye π–π interactions, in combination with electrostatic self-assembly, produced either spherosymmetric or – also well-defined – anisotropic structures depending on the mutual dye–dye interaction strength.[16] Hence, results indicate that utilizing the enthalpy–entropy relation, one can anticipate the shape of nano-assemblies formed through electrostatic self-assembly.

UV-light photo-irradiation induces alterations in both the size and structure of the particles, with the extent of these changes strongly contingent upon the photoacidity and the molecular structure of the photoacids. The increase in size is attributed to an excited-state dissociation of the photoacidic hydroxyl group, resulting in enhanced electrostatic interactions with the cationic macroion and increased interconnections, consequently leading to the formation of more nano-objects. Simultaneously, the absence of hydrogen bonds arises as the OH-group undergoes deprotonation. For instance, in the case of 1N38S and 1N48S, irradiation causes a reduction in size, a consequence of two concurrent effects. The absence of hydrogen bonds is coupled with the close proximity of the sulfonate group to the now deprotonated OH-group, preventing further interconnection. This results in the disappearance of the hydrogen bond and the absence of additional interactions stemming from electrostatic forces. In general, the proximity of the deprotonated OH-group to the nearest sulfonate group plays a pivotal role in influencing size changes, given the fundamental basis of electrostatic interaction. The substitution of the hydrogen bond with another electrostatic interaction also leads to an increase in the number of particles. This phenomenon is underscored in thermodynamic studies, which demonstrate that binding to the $-O^-$ group is notably stronger and primarily enthalpically driven as compared to the sulfonate groups. Conversely, the structural alterations in the nano-assemblies upon irradiation likely are dependent on the difference between the pK_a in the excited and in the ground state ΔpK_a. A more pronounced change in pK_a values upon irradiation results in a more significant transformation in the assembly's structure characterized by a higher degree of deprotonation and consequently elevated charge density. Consequently, this structural transition shifts from a core–shell sphere to a simpler spherical configuration.

Several points of the results here are most striking, also as a basis for the theory of complex self-assembly and polyelectrolytes. First of all the formation of well-defined nano-objects with a certain size and structure: a general analogy may be seen with the calculated stabilization of nanoscale biomacromolecule bundles through a net charge caused by secondary effects — in that case finite size counterions as opposed to point-like counterions — as considered by Pincus *et al.* and Holm *et al.*[84,85] As for our previous electrostatics-plus π–π-interacting systems,[24] results herein may be seen as in accordance with calculations by Douglas *et al.* where the interplay of two types of interaction forces with differing directionality and range was shown to be a key to defined supramolecular particles.[86,87] Yet, those involved only one kind of building block and cannot explain the more complex scenario found here. Overall, also for polyelectrolyte solutions itself, due to the involvement of multiple interplaying and many-body effects, theoretical developments are challenging and so far no theory can describe all aspects. Even more so, for the type of electrostatic self-assembly established by us that combines ionic interaction with another type of secondary interactions – yielding remarkably well-defined nano-objects the size and shape of which can be fine-tuned *via* the subtle non-covalent interaction effects – no full theoretical approach exists yet. This is not really surprising, not only given these mutually interplaying effects, but also because this principle of electrostatic self-assembly has just emerged in the last couple of years, as opposed to, for example, the traditional use of amphiphiles. Hence, it is most significant to provide comprehensive experimental data and master plots on the relationship of molecular scale forces, association thermodynamics and nanoscale structure and response, as presented here, as these phenomenological data may then inspire theoretical scientists in the area of self-assembly, next to setting a basis for a targeted design for applications.

3. Conclusion

In conclusion, we have gained a deeper understanding of electrostatically self-assembled nanostructures from ionic

Published on 13 December 2023. Downloaded by Universitat Erlangen Nurnberg on 1/11/2026 10:32:27 PM.

photoacids and macroions, whose size and structure are controlled by photo-irradiation with UV-light. Particle structures and charge characteristics were determined uncovering the significance of hydrogen bonds as a secondary interaction. Following that, we established the ionization energy of the hydroxyl group as a parameter encoding the thermodynamics and, consequently impacting particle size. The enthalpy-entropy relation across various systems plays a major role in the structure of photoacid-macroion assembly. UV-light photo-irradiation causes a change in the size and structure of the particles which strongly depends on the molecular structure of the photoacids and the photoacidity. Significantly, this research provides a foundation for the development of a predictive framework applicable to molecules sharing a similar structure and type of secondary interactions. By knowing photoacids' molecular structure and determining the thermodynamic parameters, interactions and re-structuring upon irradiation can be predicted. This, in turn, bears profound implications for the advancement of photo-responsive carrier systems and photocatalysis, offering a novel approach hinged on molecular insights and thermodynamics. In essence, this foundational research holds pivotal significance in governing the size and shape of nano-objects, for example, for a targeted cell uptake in drug delivery.

Author contributions

The manuscript was written through contributions of all authors. All authors have given approval to the final version of the manuscript.

Conflicts of interest

There are no conflicts to declare.

Acknowledgements

We gratefully acknowledge the German Science Foundation (DFG) and the Institut Laue-Langevin (ILL) for funding. SANS was performed at the D11 instrument at the Institut Laue-Langevin (ILL), Grenoble, France (proposal 9-11-2039; DOI: 10.5291/ILL-DATA.9-11-2039). This work benefited from the use of the SasView application (**https://www.sasview.org**), originally developed under NSF award DMR-0520547. F. Gröhn, M. Agarwal, R. Schweins, A. Zika, *Light-Triggerable Photoacid Nano-Assemblies*, Institut Laue-Langevin (ILL), 2021.

References

1 P. Majumder, S. Bhunia and A. Chaudhuri, A lipid-based cell penetrating nano-assembly for RNAi-mediated anti-angiogenic cancer therapy, *Chem. Commun.*, 2018, **54**(12), 1489–1492, DOI: **10.1039/c7cc08517f**.

2 L. Kai, X. Ruirui, Z. Qianli, M. Guanghui, M. Helmuth and Y. Xuehai, Simple Peptide-Tuned Self-Assembly of Photosensitizers towards Anticancer Photodynamic Therapy, *Angew. Chem., Int. Ed.*, 2016, **55**(9), 3036–3039, Verfügbar unter: **https://onlinelibrary.wiley.com/doi/10.1002/anie.201509810**.

3 X. Wang, J. Wang, J. Wang, Y. Zhong, L. Han, J. Yan, *et al.*, Noncovalent Self-Assembled Smart Gold(III) Porphyrin Nanodrug for Synergistic Chemo-Photothermal Therapy, *Nano Lett.*, 2021, **21**(8), 3418–3425, DOI: **10.1021/acs.nanolett.0c04915**.

4 G. Zhang, N. Wang, H. Sun, X. Fu, S. Zhai and J. Cui, Self-adjuvanting photosensitizer nanoparticles for combination photodynamic immunotherapy, *Biomater. Sci.*, 2021, **9**(20), 6940–6949, DOI: **10.1039/d1bm01139a**.

5 L. Jianhui, B. Sander, S. JvdM, D. Sandra, W. H. Alexander, S. Christian, *et al.*, Ordered nanoparticle arrays interconnected by molecular linkers: electronic and optoelectronic properties, *Chem. Soc. Rev.*, 2015, **44**(4), 999–1014, Verfügbar unter: **https://pubs.rsc.org/en/content/articlelanding/2015/cs/c4cs00225c**.

6 J. S. Kamatchi, K. Srinivasu, S. Balakrishnan, H. Ping-Yen, C. Huang-Chin, L. Keh-Chyang, *et al.*, Gold nanoparticle–ultrananocrystalline diamond hybrid structured materials for high-performance optoelectronic device applications, *Nanoscale*, 2015, **7**(10), 4377–4385, Verfügbar unter: **https://pubs.rsc.org/en/content/articlehtml/2015/nr/c4nr07030e?casa_token=_l_5JI4ZrKYAAAAA:bpKRLCNHalOyRmRbOdaxQ90J-R6NE8h22tAN2hwme1Gem-uuOGbpSujsU3YiDeUC0rBg8IHv7bppQQ**.

7 H. B. Lee, W.–G. Kim, M. Lee, J.–M. Lee, S. He, N. Kumar, *et al.*, Gap Plasmon of Virus–Templated Biohybrid Nanostructures Uplifting the Performance of Organic Optoelectronic Devices, *Adv. Opt. Mater.*, 2020, **8**(11), 1902080, DOI: **10.1002/adom.201902080**.

8 H. Fang, J. Zhou and P. Jena, Super-alkalis as building blocks of one-dimensional hierarchical electrides, *Nanoscale*, 2018, **10**(48), 22963–22969, DOI: **10.1039/c8nr07609j**.

9 D.–D. Zhang, J.–L. Xu and H.–B. Sun, Toward High Efficiency Organic Light–Emitting Diodes: Role of Nanoparticles, *Adv. Opt. Mater.*, 2021, **9**(6), 2001710, DOI: **10.1002/adom.202001710**.

10 O. M. Wani, H. Zeng and A. Priimagi, A light-driven artificial flytrap, *Nat. Commun.*, 2017, **8**(1), 1–7, Verfügbar unter: **https://www.nature.com/articles/ncomms15546**.

11 P. Yan, D. Jiang, Y. Tian, L. Xu, J. Qian, H. Li, *et al.*, A sensitive signal-on photoelectrochemical sensor for tetracycline determination using visible-light-driven flower-like CN/BiOBr composites, *Biosens. Bioelectron.*, 2018, **111**, 74–81, Verfügbar unter: **https://www.sciencedirect.com/science/article/pii/S0956566318302380**.

12 J. S. Sidhu, A. Singh, N. Garg, N. Kaur and N. Singh, Gold conjugated carbon dots nano assembly: FRET paired fluorescence probe for cysteine recognition, *Sens. Actuators, B*, 2019, **282**, 515–522, Verfügbar unter: **https://www.sciencedirect.com/science/article/pii/S0925400518320628**.

 This journal is © The Royal Society of Chemistry 2024

Published on 13 December 2023. Downloaded by Universitat Erlangen Nurnberg on 1/11/2026 10:32:27 PM.

13 K.-Y. Hwa and T. S. K. Sharma, Nano assembly of NiFe spheres anchored on f-MWCNT for electrocatalytic reduction and sensing of nitrofurantoin in biological samples, *Sci. Rep.*, 2020, **10**(1), 12256, DOI: **10.1038/s41598-020-69125-5**.

14 I. Willerich and F. Gröhn, Photoswitchable Nanoassemblies by Electrostatic Self-Assembly, *Angew. Chem., Int. Ed.*, 2010, **49**(44), 8104–8108, Verfügbar unter: **https://onlinelibrary.wiley.com/doi/full/10.1002/anie.201003271**.

15 I. Willerich and F. Gröhn, Switchable nanoassemblies from macroions and multivalent dye counterions, *Chemistry*, 2008, **14**(30), 9112–9116, DOI: **10.1002/chem.200801167**.

16 G. Mariani, D. Moldenhauer, R. Schweins and F. Gröhn, Elucidating Electrostatic Self-Assembly: Molecular Parameters as Key to Thermodynamics and Nanoparticle Shape, *J. Am. Chem. Soc.*, 2016, **138**(4), 1280–1293, DOI: **10.1021/jacs.5b11497**.

17 G. Mariani, A. Kutz, Z. Di, R. Schweins and F. Gröhn, Inducing Hetero-aggregation of Different Azo Dyes through Electrostatic Self-Assembly, *Chem. – Eur. J.*, 2017, **23**(26), 6249–6254, Verfügbar unter: **https://chemistry-europe.onlinelibrary.wiley.com/doi/full/10.1002/chem.201605194**.

18 G. Mariani, R. Schweins and F. Gröhn, Electrostatic Self-Assembly of Dendrimer Macroions and Multivalent Dye Counterions: The Role of Solution Ionic Strength, *Macromolecules*, 2016, **49**(22), 8661–8671, DOI: **10.1021/acs.macromol.6b00565**.

19 A. Kutz, G. Mariani, R. Schweins, C. Streb and F. Gröhn, Self-assembled polyoxometalate-dendrimer structures for selective photocatalysis, *Nanoscale*, 2018, **10**(3), 914–920, DOI: **10.1039/c7nr07097g**.

20 Y. Upadhyay, R. Kumar and S. K. Sahoo, Developing a Cost-Effective Bioassay to Detect Alkaline Phosphatase Activity and Generating White Light Emission from a Single Nano-Assembly by Conjugating Vitamin B 6 Cofactors with Lysozyme-Stabilized Fluorescent Gold Nanoclusters, *ACS Sustainable Chem. Eng.*, 2020, **8**(10), 4107–4113, DOI: **10.1021/acssuschemeng.9b06563**.

21 A. Krieger, A. Zika and F. Gröhn, Functional Nano-Objects by Electrostatic Self-Assembly: Structure, Switching, and Photocatalysis, *Front. Chem.*, 2021, **9**, 779360, DOI: **10.3389/fchem.2021.779360**.

22 F. Gröhn, K. Klein and S. Brand, Facile route to supramolecular structures: self-assembly of dendrimers and naphthalene dicarboxylic acids, *Chem. – Eur. J.*, 2008, **14**(23), 6866–6869, DOI: **10.1002/chem.200800650**.

23 S. Frühbeißer and F. Gröhn, Porphyrin–Polyelectrolyte Nanoassemblies: The Role of Charge and Building Block Architecture in Self-Assembly, *Macromol. Chem. Phys.*, 2017, **218**(17), 1600526, Verfügbar unter: **https://onlinelibrary.wiley.com/doi/full/10.1002/macp.201600526**.

24 I. Willerich and F. Gröhn, Molecular Structure Encodes Nanoscale Assemblies: Understanding Driving Forces in Electrostatic Self-Assembly, *J. Am. Chem. Soc.*, 2011, **133**(50), 20341–20356, DOI: **10.1021/ja207565m**.

25 M. Chetia, S. Debnath, S. Chowdhury and S. Chatterjee, Self-assembly and multifunctionality of peptide organogels: oil spill recovery, dye absorption and synthesis of conducting biomaterials, *RSC Adv.*, 2020, **10**(9), 5220–5233, Verfügbar unter: **https://pubs.rsc.org/fa/content/articlehtml/2020/ra/c9ra10395c**.

26 X. Guo, M. Baumgarten and K. Müllen, Designing π-conjugated polymers for organic electronics, *Prog. Polym. Sci.*, 2013, **38**(12), 1832–1908, Verfügbar unter: **https://www.sciencedirect.com/science/article/pii/S0079670013001196**.

27 F. Li, D. Liu, T. Wang, J. Hu, F. Meng, H. Sun, *et al.*, J-aggregation in porphyrin nanoparticles induced by diphenylalanine, *J. Solid State Chem.*, 2017, **252**, 86–92, Verfügbar unter: **https://www.sciencedirect.com/science/article/pii/S0022459617301536**.

28 M. Marcia, A. Hirsch and F. Hauke, Perylene-based non-covalent functionalization of 2D materials, *FlatChem*, 2017, **1**, 89–103, DOI: **10.1016/j.flatc.2017.01.001**.

29 S. Mishra, D. Beyer, K. Eimre, J. Liu, R. Berger, O. Gröning, *et al.*, Synthesis and Characterization of π-Extended Triangulene, *J. Am. Chem. Soc.*, 2019, **141**(27), 10621–10625, DOI: **10.1021/jacs.9b05319**.

30 S. J. Grabowski, Hydrogen bonding strength—measures based on geometric and topological parameters, *J. Phys. Org. Chem.*, 2004, **17**(1), 18–31, DOI: **10.1002/poc.685**.

31 J. Guilleme, M. J. Mayoral, J. Calbo, J. Aragó, P. M. Viruela, E. Ortí, *et al.*, Non-centrosymmetric homochiral supramolecular polymers of tetrahedral subphthalocyanine molecules, *Angew. Chem., Int. Ed.*, 2015, **54**(8), 2543–2547, Verfügbar unter: **https://onlinelibrary.wiley.com/doi/full/10.1002/anie.201411272**.

32 M. Li, W. Zajaczkowski, G. Velpula, D. Jänsch, R. Graf, T. Marszalek, *et al.*, Transformation from helical to layered supramolecular organization of asymmetric perylene diimides via multiple intermolecular hydrogen bonding, *Chem. Sci.*, 2020, **11**(19), 4960–4968, Verfügbar unter: **https://pubs.rsc.org/ko/content/articlehtml/2020/sc/d0sc01911a**.

33 D. Mazzier, S. De, B. Wicher, V. Maurizot and I. Huc, Parallel Homochiral and Anti-Parallel Heterochiral Hydrogen-Bonding Interfaces in Multi-Helical Abiotic Foldamers, *Angew. Chem., Int. Ed.*, 2020, **59**(4), 1606–1610, Verfügbar unter: **https://onlinelibrary.wiley.com/doi/full/10.1002/anie.201912805**.

34 Y. Wang, M. Liu and J. Gao, Enhanced receptor binding of SARS-CoV-2 through networks of hydrogen-bonding and hydrophobic interactions, *Proc. Natl. Acad. Sci. U. S. A.*, 2020, **117**(25), 13967–13974, Verfügbar unter: **https://www.pnas.org/content/117/25/13967.short**.

35 C. Ruthard, M. Maskos, U. Kolb and F. Gröhn, Polystyrene Sulfonate–Porphyrin Assemblies: Influence of Polyelectrolyte and Porphyrin Structure, *J. Phys. Chem. B*, 2011, **115**(19), 5716–5729, DOI: **10.1021/jp1078357**.

36 C.-V. Martín, C. Miguel, B.-S. Ana, G. Nélida and M. R. Blanca, Towards supramolecular nanostructured materials: control of the self-assembly of ionic bent-core

Published on 13 December 2023. Downloaded by Universitat Erlangen Nurnberg on 1/11/2026 10:32:27 PM.

amphiphiles, *J. Mater. Chem. C*, 2020, **8**(6), 1998–2007, Verfügbar unter: https://pubs.rsc.org/en/content/articlelanding/2020/Kc/c9tc06002b.

37 B. Fehér, K. Zhu, B. Nyström, I. Varga and J. S. Pedersen, Effect of Temperature and Ionic Strength on Micellar Aggregates of Oppositely Charged Thermoresponsive Block Copolymer Polyelectrolytes, *Langmuir*, 2019, **35**(42), 13614–13623, DOI: 10.1021/acs.langmuir.9b01896.

38 L. Feng, L. Xu, S. Dong and J. Hao, Thermo-reversible capture and release of DNA by zwitterionic surfactants, *Soft Matter*, 2016, **12**(36), 7495–7504, DOI: 10.1039/c6sm00704j.

39 B. Jing, X. Chen, Y. Zhao, X. Wang, F. Ma and X. Yue, Ionic self-assembled solid-like vesicles and their temperature-induced transformation, *J. Mater. Chem.*, 2009, **19**(14), 2037, DOI: 10.1039/b818006g.

40 T. Xu, Y. Ma, J. Huang, H. Lai, D. Yuan, X. Tang, *et al.*, Self-organized thermo-responsive poly (lactic-co-glycolic acid)-graft-pullulan nanoparticles for synergistic thermo-chemo-therapy of tumor, *Carbohydr. Polym.*, 2020, **237**, 116104, DOI: 10.1016/j.carbpol.2020.116104.

41 N. Carl, W. Müller, R. Schweins and K. Huber, Controlling Self-Assembly with Light and Temperature, *Langmuir*, 2020, **36**(1), 223–231, DOI: 10.1021/acs.langmuir.9b03040.

42 D. Moldenhauer, J. P. Fuenzalida Werner, C. A. Strassert and F. Gröhn, Light-Responsive Size of Self-Assembled Spiropyran-Lysozyme Nanoparticles with Enzymatic Function, *Biomacromolecules*, 2019, **20**(2), 979–991, DOI: 10.1021/acs.biomac.8b01605.

43 K. Surjith, A. Jean-Francois, M. Denis, L. D. Yves, L. Martin and Z. Yue, Near-infrared light sensitive polypeptide block copolymer micelles for drug delivery, *J. Mater. Chem.*, 2012, **22**(15), 7252–7259, Verfügbar unter: https://pubs.rsc.org/en/content/articlelanding/2012/JM/c2jm16380b.

44 S. A. Eghtesadi, M. A. Kashfipour, X. Sun, W. Zhang, R. S. Lillard, S. Z. D. Cheng, *et al.*, Hierarchical self-assembly of zwitterionic dendrimer-anionic surfactant complexes into multiple stimuli-responsive dynamic nanotubes, *Nanoscale*, 2018, **10**(3), 1411–1419, DOI: 10.1039/c7nr07950h.

45 M. Fathalla and L. Sinatra, pH-Responsive porphyrin-silica nanoparticles conjugate via ionic self-assembly, *J. Porous Mater.*, 2021, **28**(1), 183–189, Verfügbar unter: https://link.springer.com/article/10.1007/s10934-020-00976-z.

46 G. Mariani, R. Schweins and F. Gröhn, Structure Tuning of Electrostatically Self-Assembled Nanoparticles through pH, *J. Phys. Chem. B*, 2016, **120**(7), 1380–1389, DOI: 10.1021/acs.jpcb.5b10966.

47 C. Ruthard, S. Manfred and F. Gröhn, Porphyrin–Polymer Networks, Worms, and Nanorods: pH-triggerable Hierarchical Self-assembly, *Macromol. Rapid Commun.*, 2011, **32**(9–10), 706–711, Verfügbar unter: https://onlinelibrary.wiley.com/doi/full/10.1002/marc.201100097.

48 J. Shen, Z. Wang, D. Sun, C. Xia, S. Yuan, P. Sun, *et al.*, pH-Responsive Nanovesicles with Enhanced Emission Co-Assembled by Ag(I) Nanoclusters and Polyethyleneimine as a Superior Sensor for Al3, *ACS Appl. Mater. Interfaces*, 2018, **10**(4), 3955–3963, DOI: 10.1021/acsami.7b16316.

49 D. Chong, J. Tan, J. Zhang, Y. Zhou, X. Wan and J. Zhang, Dual electrical switching permeability of vesicles via redox-responsive self-assembly of amphiphilic block copolymers and polyoxometalates, *Chem. Commun.*, 2018, **54**(56), 7838–7841, DOI: 10.1039/c8cc03749c.

50 S. E. Herrera, M. L. Agazzi, M. L. Cortez, W. A. Marmisollé, M. Tagliazucchi and O. Azzaroni, Redox-active polyamine-salt aggregates as multistimuli-responsive soft nanoparticles, *Phys. Chem. Chem. Phys.*, 2020, **22**(14), 7440–7450, DOI: 10.1039/d0cp00077a.

51 H. Liu, L. Wang, X. Wang, Y. Hu, L. Feng, S. Dong, *et al.*, Vesicle transition of catanionic redox-switchable surfactants controlled by DNA with different chain lengths, *J. Colloid Interface Sci.*, 2019, **549**, 89–97, DOI: 10.1016/j.jcis.2019.04.048.

52 Z. Özdemir, M. Yang, G. Kim, U. Bildziukevich, D. Šaman, X. Li, *et al.*, Redox-responsive nanoparticles self-assembled from porphyrin-betulinic acid conjugates for chemo- and photodynamic therapy, *Dyes Pigm.*, 2021, **190**, 109307, Verfügbar unter: https://www.sciencedirect.com/science/article/pii/S0143720821001741.

53 D. Moldenhauer and F. Gröhn, Nanoassemblies with light-responsive size and density from linear flexible polyelectrolytes, *J. Polym. Sci., Part B: Polym. Phys.*, 2013, **51**(10), 802–816, Verfügbar unter: https://onlinelibrary.wiley.com/doi/full/10.1002/polb.23276.

54 X. Xie, L. Wang, X. Liu, Z. Du, Y. Li, B. Li, *et al.*, Light-powered and transient peptide two-dimensional assembly driven by trans-to-cis isomerization of azobenzene side chains, *Chem. Commun.*, 2020, **56**(12), 1867–1870, DOI: 10.1039/c9cc09448b.

55 I. Willerich and F. Gröhn, Thermodynamics of Photoresponsive Polyelectrolyte–Dye Assemblies with Irradiation Wavelength Triggered Particle Size, *Macromolecules*, 2011, **44**(11), 4452–4461, DOI: 10.1021/ma200538e.

56 G. Mariani, A. Krieger, D. Moldenhauer, R. Schweins and F. Gröhn, Light-Responsive Shape: From Micrometer-Long Nanocylinders to Compact Particles in Electrostatic Self-Assembly, *Macromol. Rapid Commun.*, 2018, **39**(17), e1700860, DOI: 10.1002/marc.201700860.

57 D. Moldenhauer and F. Gröhn, Water-Soluble Spiropyrans with Inverse Photochromism and Their Photoresponsive Electrostatic Self-Assembly, *Chem. – Eur. J.*, 2017, **23**(16), 3966–3978, DOI: 10.1002/chem.201605621.

58 B. Razavi, A. Abdollahi, H. Roghani-Mamaqani and M. Salami-Kalajahi, Light-, temperature-, and pH-responsive micellar assemblies of spiropyran-initiated amphiphilic block copolymers: Kinetics of photochromism, responsiveness, and smart drug delivery, *Mater. Sci. Eng.*, 2020, **109**, 110524, Verfügbar unter: https://www.sciencedirect.com/science/article/pii/S0928493119323859.

59 C. Cardenas-Daw and F. Gröhn, Photo-Induced Assembly of Nanostructures Triggered by Short-Lived Proton Transfers

 This journal is © The Royal Society of Chemistry 2024

Published on 13 December 2023. Downloaded by Universitat Erlangen Nurnberg on 1/11/2026 10:32:27 PM.

in the Excited-State, *J. Am. Chem. Soc.*, 2015, **137**(27), 8660–8663, DOI: 10.1021/jacs.5b01357.

60 A. Zika, S. Bernhardt and F. Gröhn, Photoresponsive Photoacid-Macroion Nano-Assemblies, *Polymers*, 2020, **12**(8), 1746–1763, DOI: 10.3390/polym12081746.

61 A. Zika and F. Gröhn, Multiswitchable photoacid-hydroxyflavylium-polyelectrolyte nano-assemblies, *Beilstein J. Org. Chem.*, 2021, **17**, 166–185, DOI: 10.3762/bjoc.17.17.

62 I. Willerich, Y. Li and F. Gröhn, Influencing particle size and stability of ionic dendrimer–dye assemblies, *J. Phys. Chem. B*, 2010, **114**(47), 15466–15476, DOI: 10.1021/jp107358q.

63 J. T. Prosa, B. J. Bauer, E. J. Amis, D. A. Tomalia and R. Scherrenberg, A SAXS study of the internal structure of dendritic polymer systems, *J. Polym. Sci., Part B: Polym. Phys.*, 1997, **35**(17), 2913–2924, DOI: 10.1002/(SICI)1099-0488(199712)35:17<2913::AID-POLB14>3.0.CO;2-A.

64 F. Gröhn, B. J. Bauer, Y. A. Akpalu, C. L. Jackson and E. J. Amis, Dendrimer Templates for the Formation of Gold Nanoclusters, *Macromolecules*, 2000, **33**(16), 6042–6050, DOI: 10.1021/ma000149v.

65 M. Schmidt, D. Nerger and W. Burchard, Quasi-elastic light scattering from branched polymers: 1. Polyvinylacetate and polyvinylacetate—microgels prepared by emulsion polymerization, *Polymer*, 1979, **20**(5), 582–588, DOI: 10.1016/0032-3861(79)90169-1.

66 A. Krieger, J. P. Fuenzalida Werner, G. Mariani and F. Gröhn, Functional Supramolecular Porphyrin–Dendrimer Assemblies for Light Harvesting and Photocatalysis, *Macromolecules*, 2017, **50**(9), 3464–3475, DOI: 10.1021/acs.macromol.6b02435.

67 F. Vargas-Lara, F. W. Starr and J. F. Douglas, Solution properties of spherical gold nanoparticles with grafted DNA chains from simulation and theory, *Nanoscale Adv.*, 2022, **4**(19), 4144–4161, DOI: 10.1039/d2na00377e.

68 C. G. Sinn, R. Dimova and M. Antonietti, Isothermal Titration Calorimetry of the Polyelectrolyte/Water Interaction and Binding of Ca^{2+}: Effects Determining the Quality of Polymeric Scale Inhibitors, *Macromolecules*, 2004, **37**(9), 3444–3450, DOI: 10.1021/ma030550s.

69 Z. Ou and M. Muthukumur, Entropy and enthalpy of polyelectrolyte complexation: Langevin dynamics simulations, *J. Chem. Phys.*, 2006, **124**, 154902, DOI: 10.1063/1.2178803.

70 I. Willerich, H. Ritter and F. Gröhn, Structure and thermodynamics of ionic dendrimer-dye assemblies, *J. Phys. Chem. B*, 2009, **113**(11), 3339–3354, DOI: 10.1021/jp8096605.

71 I. Willerich, T. Schindler and F. Gröhn, Effect of polyelectrolyte architecture and size on macroion-dye assemblies, *J. Phys. Chem. B*, 2011, **115**(32), 9710–9719, DOI: 10.1021/jp204368t.

72 M. Zhao, H. He, C. Dai, X. Wu, Y. Zhang, Y. Huang, *et al.*, Micelle formation by amine-based CO2-responsive surfactant of imidazoline type in an aqueous solution, *J. Mol. Liq.*, 2018, **268**, 875–881, DOI: 10.1016/j.molliq.2018.08.010.

73 Z. Wu, C. Zhao, Y. Huang, F. Ye and G. Zhao, Molecular mechanism underlying the effects of temperature and pH on the size and surface charge of octenylsuccinated oat β-glucan aggregates, *Carbohydr. Polym.*, 2020, **237**, 116115, DOI: 10.1016/j.carbpol.2020.116115.

74 H. Qiu, X. Chen, X. Wei, J. Liang, D. Zhou, W. Tang, *et al.*, A green resin acid ester surfactant from colophony and xylitol: Synthesis, self–assembly in nonaqueous solvents, and thermodynamics, *J. Appl. Polym. Sci.*, 2021, **138**(6), 49808, DOI: 10.1002/app.49808.

75 K. Achazi, R. Haag, M. Ballauff, J. Dernedde, J. N. Kizhakkedathu, D. Maysinger, *et al.*, Understanding the Interaction of Polyelectrolyte Architectures with Proteins and Biosystems, *Angew. Chem., Int. Ed.*, 2021, **60**(8), 3882–3904, DOI: 10.1002/anie.202006457.

76 F. Vargas-Lara, F. W. Starr and J. F. Douglas, Molecular rigidity and enthalpy-entropy compensation in DNA melting, *Soft Matter*, 2017, **13**(44), 8309–8330, DOI: 10.1039/c7sm01220a.

77 J. Dudowicz, J. F. Douglas and K. F. Freed, Lattice theory of competitive binding: Influence of van der Waals interactions on molecular binding and adsorption to a solid substrate from binary liquid mixtures, *J. Chem. Phys.*, 2018, **149**(4), 44704, DOI: 10.1063/1.5040105.

78 T. Haino and T. Hirao, Supramolecular Polymerization and Functions of Isoxazole Ring Monomers, *Chem. Lett.*, 2020, **49**(5), 574–584, DOI: 10.1246/cl.200031.

79 G. Yu, M. Walker and M. R. Wilson, Atomistic simulation studies of ionic cyanine dyes: self-assembly and aggregate formation in aqueous solution, *Phys. Chem. Chem. Phys.*, 2021, **23**(11), 6408–6421, DOI: 10.1039/D0CP06205G.

80 A. Demeter and T. Bérces, Hydrogen-bond formation between isoindolo2,1-aindol-6-one and aliphatic alcohols in n-hexane, *J. Phys. Chem. A*, 2005, **109**(10), 2043–2049, DOI: 10.1021/jp045495j.

81 R. Janciene, Z. Stumbreviciute, A. Vektariene, L. Kosychova, A. Klimavicius, A. Palaima, *et al.*, Synthesis of novel annelated systems based on the interaction and reactivity estimation of amino-1,5-benzodiazepin-2-ones with dimethyl-2-oxoglutaconate, *J. Heterocycl. Chem.*, 2009, **46**(6), 1339–1345, DOI: 10.1002/jhet.226.

82 K. Wendler, J. Thar, S. Zahn and B. Kirchner, Estimating the hydrogen bond energy, *J. Phys. Chem. A*, 2010, **114**(35), 9529–9536, DOI: 10.1021/jp103470e.

83 C. Bun, M. Damian, J. E. Christopher and R. Leo, Impact of Hydrogen Bonding on the Susceptibility of Peptides to Oxidation, *Chem. – Asian J.*, 2017, **12**(13), 1485–1489, Verfügbar unter: https://onlinelibrary.wiley.com/doi/full/10.1002/asia.201700492.

84 M. L. Henle and P. A. Pincus, Equilibrium bundle size of rodlike polyelectrolytes with counterion-induced attractive interactions, *Phys. Rev. E: Stat., Nonlinear, Soft Matter Phys.*, 2005, **71**, 060801, DOI: 10.1103/PhysRevE.71.060801.

85 M. Sayar and C. Holm, Finite-size polyelectrolyte bundles at thermodynamic equilibrium, *Europhys. Lett.*, 2007, **77**, 16001, DOI: 10.1209/0295-5075/77/16001.

86 K. Van Workum and J. F. Douglas, Symmetry, equivalence, and molecular self-assembly, *Phys. Rev. E: Stat., Nonlinear, Soft Matter Phys.*, 2006, **73**, 031502, DOI: **10.1103/PhysRevE.73.031502**.

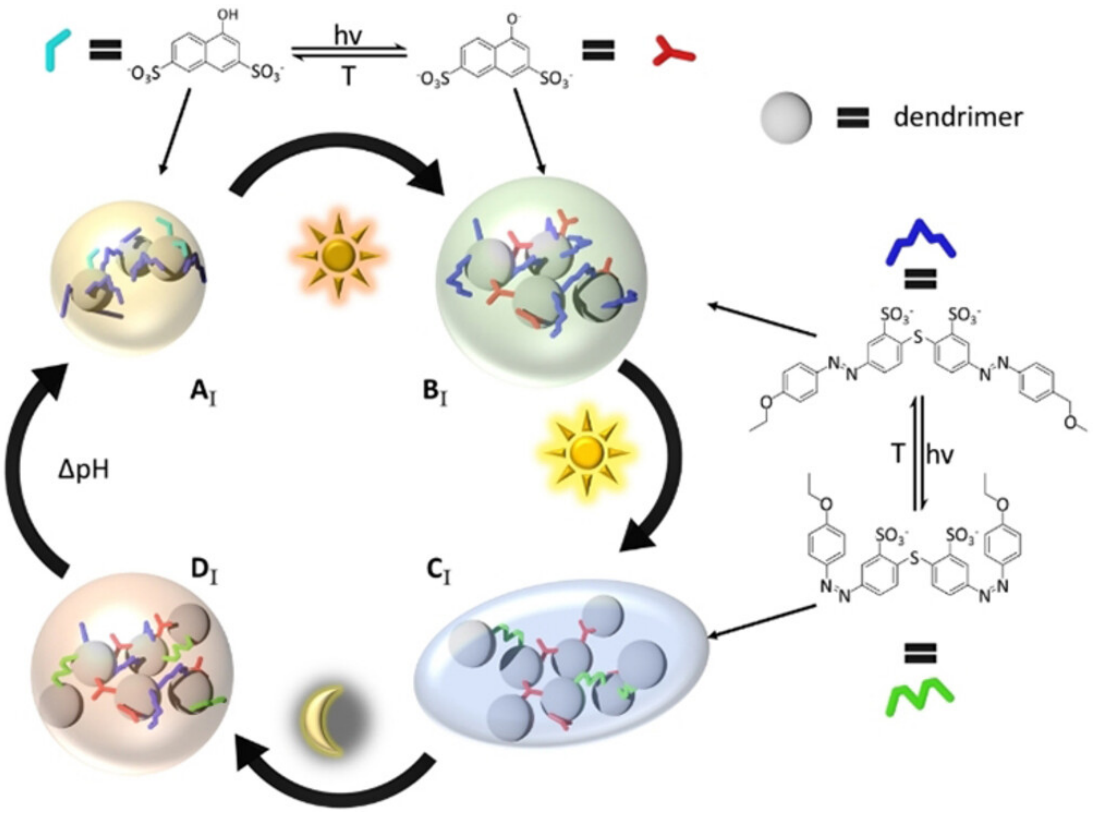
87 S. Srebnik and J. F. Douglas, Self-assembly of Charged Particles on Nanotubes and the Emergence of Particle Rings, Chains, Ribbons and Chiral Sheets, *Soft Matter*, 2011, **7**, 6897, DOI: **10.1039/c1sm05168g**.

Published on 13 December 2023. Downloaded by Universitat Erlangen Nurnberg on 1/11/2026 10:32:27 PM.

This journal is © The Royal Society of Chemistry 2024

7.2.6. Joining Two Switches in One Nano-Object: Photoacidity and Photoisomerization in Electrostatic Self-Assembly

Alexander Zika, **Mohit Agarwal**, Ralf Schweins, Franziska Gröhn; *Chem. Eur. J.,* **2022**, e202203373.



Check for updates

Chemistry–A European Journal

Research Article
doi.org/10.1002/chem.202203373

Chemistry Europe
European Chemical Societies Publishing

www.chemeurj.org

Joining Two Switches in One Nano-Object: Photoacidity and Photoisomerization in Electrostatic Self-Assembly

Alexander Zika,[a] Mohit Agarwal,[a, b] Ralf Schweins,[b] and Franziska Gröhn*[a]

Abstract: Multi-switchable supramolecular nano-objects that respond to irradiation of different wavelengths with changes in size and shape have been built from two different water-soluble molecular switches, joined by attachment to the same polyelectrolyte. Accordingly, two wavelength-specific reactions, namely the excited-state proton dissociation of a photoacid and the *cis–trans* isomerization of an azo dye, are combined in one supramolecular nano-object that is stable in aqueous solution. The concept has potential in the fields of sensors, molecular motors, and transport.

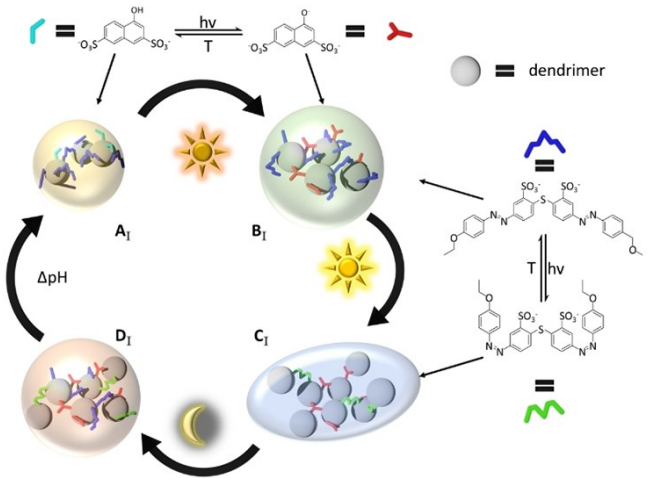
Introduction

Functional supramolecular nanoparticles that respond to an external trigger[1–4] denote an emerging field due to their great potential as carrier systems,[5–7] sensors,[8,9] and optoelectronics.[10,11] Recently, supramolecular nano-assemblies that respond to more than one trigger have elicited a growing amount of scholarly attention.[12–20] When it comes to multi-switchable assemblies in solution, the classical usage of amphiphiles is predominant, while only most recently singular examples of using different non-covalent interactions have been described.[21,22] In solid materials, one system responding to different wavelength irradiation has been reported.[23] Yet, no nano-assemblies combining two switches and responding to irradiation at different wavelengths in aqueous solution are known at all, even though this would be highly desirable, for example, for complex, triggerable drug delivery.

It is possible to effectively create supramolecular assemblies through self-assembly, using π-π interactions,[24–27] amphiphilicity,[28–31] or ionic interactions.[32–35] In recent years, we have demonstrated that electrostatic self-assembly of polyelectrolytes and multivalent oppositely charged aromatic ions can lead to nano-objects of various shapes in solution, where the combination of ionic and π-π interactions (between counterions) directs the assembly formation: in particular the total Gibbs free energy $\triangle G$, resulting from the sum of the electrostatic along with the π-π contribution, controls the aggregation number, while the $\triangle H/\triangle S$ balance encodes the aspect ratio.[36,37]

Supramolecular structures have the advantage that they can be triggered by changes in pH[37–40] and temperature.[41–44] Light-responsive systems are of particular interest due to the noninvasiveness of the trigger.[45–51] Electrostatic self-assembly allowed to address the size of nano-objects in solution.[50] In the recent past, we have utilized the special property of photoacids, an excited-state proton dissociation, to trigger both, nano-object formation and size.[51–53]

Herein, we present a multi-responsive system of electrostatically self-assembled particles with double-light and pH responsiveness. The model system (Scheme 1) comprises a fourth-generation poly(amidoamine) dendrimer (G4), which is a 4 nm-sized flexible branched hydrophilic molecule carrying 62 tertiary and 64 primary protonatable amine groups as a cationic model macroion, together with the divalent anionic photoacid sodium 1-naphthol-3,6-disulfonate (1 N36S), and the photo-isomerizable di-anionic azo dye acid yellow 38 (AY38). Following excitation, the photoacid undergoes an increase in acidity of the hydroxy



Scheme 1. Schematic representation of photoacid–dye–dendrimer assemblies in different states.

[a] *A. Zika, M. Agarwal, Prof. Dr. F. Gröhn*
Department of Chemistry and Pharmacy &
Interdisciplinary Center for Molecular Materials
Friedrich-Alexander Universität Erlangen–Nürnberg
Egerlandstraße 3, 91058 Erlangen (Germany)
E-mail: Franziska.groehn@fau.de

[b] *M. Agarwal, Dr. R. Schweins*
DS / LSS, Institut Laue–Langevin
71 Avenue des Martyrs, CS 20 156, 38042 Grenoble Cedex 9 (France)

Supporting information for this article is available on the WWW under https://doi.org/10.1002/chem.202203373

© 2022 The Authors. Chemistry - A European Journal published by Wiley-VCH GmbH. This is an open access article under the terms of the Creative Commons Attribution License, which permits use, distribution and reproduction in any medium, provided the original work is properly cited.

© 2022 The Authors. Chemistry - A European Journal published by Wiley-VCH GmbH

proton, whereas pH responsiveness originates from the pH-dependent protonation of the photoacid and the dendrimer.

Results and Discussion

Assemblies are formed by mixing aqueous solutions of the building blocks set to pH 7.0 where the dendrimer's primary amine groups are protonated. Hence, the cationic polyelectrolyte associates with the anionic photoacid and azo dye. To investigate these assemblies, we vary the loading ratio *l*, defined as the total molar concentration of negative charges, that is, photoacid and azo dye charges, divided by the molar concentration of the cationic polyelectrolyte charges, and the molar ratio *k*, defined as the molar concentration ratio of photoacid to azo dye.

Atomic force microscopy (AFM) was performed to gain a first view on assembly sizes and size-triggering upon irradiation. Figure 1 illustrates that the irradiation with $\lambda = 300$ nm leads to an increase in assembly size from $d = (36 \pm 5)$ nm (state $\mathbf{A_I}$) to $d = (79 \pm 16)$ nm (state $\mathbf{B_I}$) and subsequently isomerization of AY38 (state $\mathbf{C_I}$) causes a size change to $d = (257 \pm 54)$ nm. In the last two steps, the size decreases to $d = (198 \pm 33)$ nm (state $\mathbf{D_I}$) after light exclusion, and changing to pH 7 chemically results in particles with $d = (64 \pm 13)$ nm (state **F**). In this manner, electrostatically self-assembled particles of a certain size are formed, which can be addressed by the different triggers. The latter switching also demonstrates a reversibility. At the same time, due to structural changes upon deposition onto the surface and drying, AFM can give only a first impression, and solution characterization methods are needed in conjunction.

Dynamic light scattering (DLS) was performed to characterize the assembly sizes in the solution. Figure 2a shows the results at different irradiation steps (loading ratio $l = 5.0$, molar ratio $k = 2.0$). Directly after the nano-assemblies are formed (state $\mathbf{A_I}$), the hydrodynamic radius is $R_H = 20$ nm ($\sigma = 0.08$). After irradiation with $\lambda = 300$ nm (state $\mathbf{B_I}$), the size slightly increases to $R_H = 24$ nm ($\sigma = 0.07$). This is attributed to both the more highly charged photoacid and the higher protonation of the dendrimer as the pH value decreased to 4.3 through photoacid dissociation. Subsequent irradiation at $\lambda = 380 \pm 20$ nm (affecting the azo dye) to state $\mathbf{C_I}$ an increase to $R_H = 134$ nm ($\sigma = 0.07$). This can be understood with the isomerization to the *cis* state of the azo dye, in which the dye–dye interaction is much weaker than in the *trans* state,[50] leading to less stabilization and thus growth of the nano-assemblies. Keeping the solution in the dark (state $\mathbf{D_I}$), notably, the size of the assemblies does not revert completely and decreases only slightly to $R_H = 124$ nm ($\sigma = 0.06$) due to a photoprotective effect (to be discussed below). Changing back to pH 7.0 completes the cycle (state $\mathbf{F_I}$). Relative size changes correspond to each other in DLS and AFM, whereas the structures in AFM are substantially smaller due to the shrinking upon drying during the AFM sample preparation (Table S1 in the Supporting

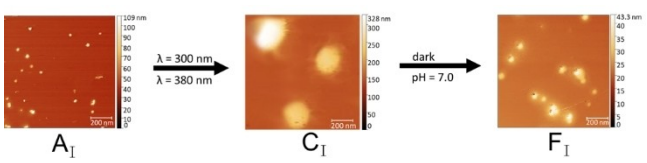


Figure 1. Irradiation-dependent AFM of photoacid–dye–dendrimer assemblies at $l = 5.0$ and $k = 2.0$ after deposition onto a mica surface.

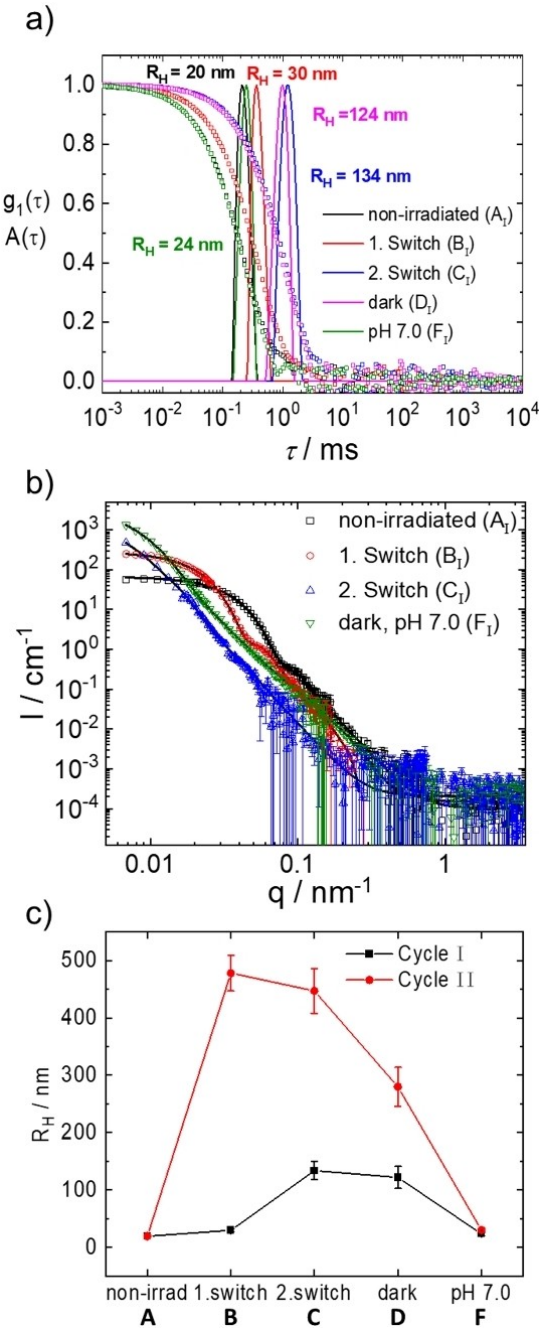


Figure 2. a) Multi-switching of photoacid–dye–dendrimer assemblies: a) DLS, electric field autocorrelation functions $g_1(\tau)$, and distributions of relaxation times $A(\tau)$ at a scattering angle of $\theta = 90°$ for Cycle I. b) SLS-SANS, scattering curves and structural fits for Cycle I. c) DLS, R_H of the Cycle I and II depending on the different states.

© 2022 The Authors. Chemistry - A European Journal published by Wiley-VCH GmbH

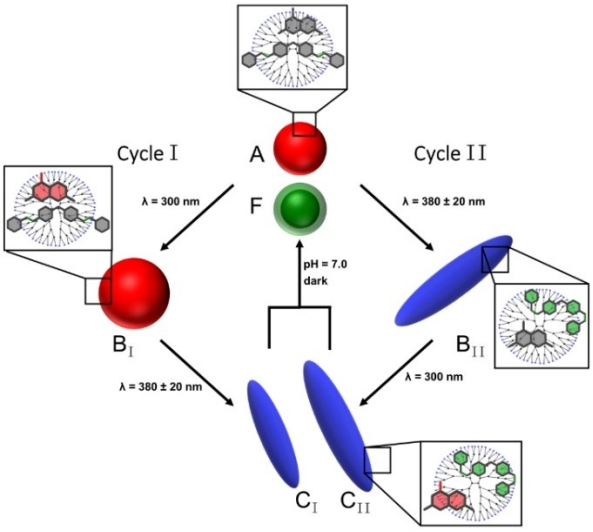
15213765, 2023, 10, Downloaded from https://chemistry-europe.onlinelibrary.wiley.com/doi/10.1002/chem.202203373, Wiley Online Library on [11/01/2026]. See the Terms and Conditions (https://onlinelibrary.wiley.com/terms-and-conditions) on Wiley Online Library for rules of use; OA articles are governed by the applicable Creative Commons License

Information). Next to the reversibility, DLS also showed, that this cycle can be repeated at least three times (Figure S1a).

Small-angle neutron-scattering (SANS, using D11@ ILL) and static light scattering (SLS) were combined to understand how the assemblies' shape and structure are influenced by the switching of the two molecules (Figure 2b). In the non-irradiated status, the resulting nanoparticles are spheres with a size of 100 nm (state $\mathbf{A}_{\mathrm{I}}$). Excitation of the photoacid (state $\mathbf{B}_{\mathrm{I}}$) again reveals a spherical geometry with an increased size of 180 nm. Subsequent isomerization of the azo dye (state $\mathbf{C}_{\mathrm{I}}$) changes the nanoparticle shape to an ellipsoid with a length of 800 nm (major axis) and a diameter of 240 nm (minor axis). By keeping the particles in the dark and changing back to pH 7.0 chemically, the shape changes to the core-shell sphere with a total size of 280 nm and a shell thickness of 26 nm (state $\mathbf{F}_{\mathrm{I}}$). The size does not reach 100 nm of the starting point because the azo dye transformation is not completed (see below), due to the photoprotective effect, where the electrostatic interaction with the dendrimer hinders the isomerization.[50]

Combining two light switchable molecules allows for another cycle: For Cycle II, the irradiation order of photoacid and azo dye is reversed (Scheme 2). Isomerization of the azo dye leads to particles with $R_{\mathrm{H}}=478$ nm ($\sigma=0.07$) at state $\mathbf{B}_{\mathrm{II}}$. This is nearly twice as large as the corresponding state in Cycle I, that is, the non-irradiated photoacid does not stabilize the particles as well. Subsequent excitation of the photoacid (state $\mathbf{C}_{\mathrm{II}}$) results in a size decline to $R_{\mathrm{H}}=447$ nm ($\sigma=0.07$). The first irradiation changes the shape from the sphere to an ellipsoid with a length of 830 nm (major axis) and diameter of 270 nm (minor axis). After the second irradiation, a significant difference between both cycles can be found: In Cycle II, subsequent irradiation of the photoacid does not lead to a shape change, although the size decreases (to 780 nm (major axis) and 220 nm (minor axis)). Changing back to state $\mathbf{F}_{\mathrm{II}}$ leads to the same shape and size as in Cycle I. These shape changes are also confirmed by considering the radius of gyration determined by SLS: The shape sensitive parameter $R_{\mathrm{G}}/R_{\mathrm{H}}$ shows that the assemblies are more elongated after irradiation of the azo dye in both cycles (Figure S3), while the irradiation of the photoacid does not lead to any differences. The reversibility is also confirmed by SLS.

To understand the size control and inner structure of the assemblies, ζ-potential, UV-Vis spectroscopy and isothermal titration calorimetry (ITC) were performed (Figures 3 and S4). Overall, assemblies are negatively charged and electrostatically stabilized in solution, as evidenced by the negative ζ-potential (Figure 3a). The anionic charge is caused by an overstoichiometric binding of azo dye molecules. Together with the self-assembly thermodynamics elucidated by ITC of the ternary and, for comparison, the corresponding binary systems, it can be surmised that AY38 binds electrostatically to the dendrimer and undergoes mutual π-π interaction, while the photoacid binds electrostatically and less strongly. The photoacid itself has two binding steps: The first is endothermic and entropically driven, corresponding to the release of the initial counterions of the sulfonate groups. The second binding step is exothermic and in combination with IR spectroscopy reveals that photoacids undergo mutual hydrogen bonding. The last binding step,



Scheme 2. Scheme of the different shapes depending on the irradiation steps according to SANS.

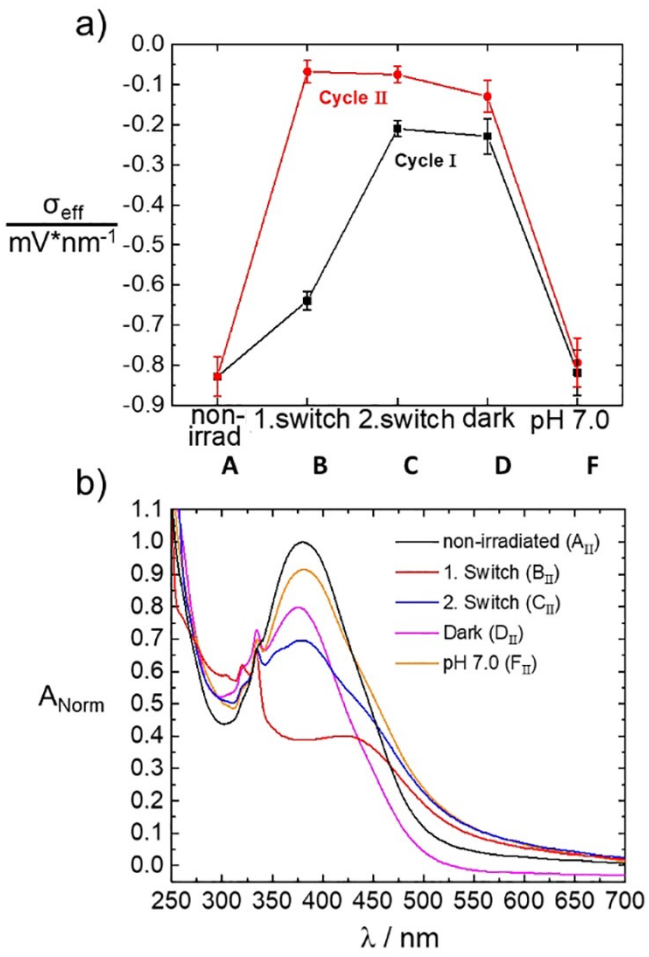


Figure 3. a) Effective surface charge density σ_{eff} depending on the different switching steps for Cycles I and II. b) UV/Vis spectroscopy of Cycle II.

© 2022 The Authors. Chemistry - A European Journal published by Wiley-VCH GmbH

15213765, 2023, 10, Downloaded from https://chemistry-europe.onlinelibrary.wiley.com/doi/10.1002/chem.202203373, Wiley Online Library on [11/01/2026]. See the Terms and Conditions (https://onlinelibrary.wiley.com/terms-and-conditions) on Wiley Online Library for rules of use; OA articles are governed by the applicable Creative Commons License

15213765, 2023, 10, Downloaded from https://chemistry-europe.onlinelibrary.wiley.com/doi/10.1002/chem.202203373, Wiley Online Library on [11/01/2026]. See the Terms and Conditions (https://onlinelibrary.wiley.com/terms-and-conditions) on Wiley Online Library for rules of use; OA articles are governed by the applicable Creative Commons License

again an endothermic one, can be understood by the increased dendrimer concentration leading to inter-cationic dendrimer repulsion, subsequent disassembly and decrease in assembly size. The difference in binding between both anionic building blocks with the cationic dendrimer is due to the different secondary interactions and their strength.

Figure 3a considers the effective charge density derived from the ζ-potential as a function of the switching step. The dependency corresponds to the size dependency (Figure 2b); the more negative the charge density, the more total surface can be stabilized, that is, the smaller the particles, similar to the behavior of the assemblies without photoacid.[50] In the first step of Cycle I, irradiation at $\lambda = 300$ nm leads to an increase in the negative surface charge density (a decrease in its absolute value, state $\mathbf{B_I}$): Next to the formation of the more highly charged photoacid molecule, the excitation also leads to a pH decrease to pH 4.3, where the dendrimer is further protonated with a degree of ionization close to 90%, corresponding to 113 positive charges per G4 dendrimer.[54] Subsequent irradiation with $\lambda = 380 \pm 20$ nm (state $\mathbf{C_I}$) leads to a further increase in surface charge density to a value close to zero, which is indicative of reduced electrostatic stabilization and, as a consequence, aggregation and growth in correspondence with the increased particle size. Upon keeping the samples in the dark and changing to pH 7.0 (state **F**), the surface charge density decreases back to the starting point, demonstrating the reversibility and thus, the thermodynamic control of the triggered equilibrium self-assembly. Regarding Cycle II, the direct isomerization of the azo dye (state $\mathbf{B_{II}}$) leads to an increase in the surface charge density to an even higher value (a negative surface charge density with a smaller absolute value) than in Cycle I. This difference is caused by the photoacid which has only two negative charges in Cycle II, providing less electrostatic stabilization than in Cycle I. Next, the excitation of the photoacid (state $\mathbf{C_{II}}$) yields a slight further decrease in surface charge density. Further, Cycle II corresponds to Cycle I.

UV-Vis absorption spectra given in Figure 3b elucidate the underlying molecular changes of the nano-assemblies. In Cycle II, irradiation at $\lambda = 380 \pm 20$ nm (state $\mathbf{B_{II}}$) shows a large influence on the isomerization, as evidenced by the appearance of two bands at $\lambda = 322$ and 445 nm. Table 1 summarizes the azo dye's degrees of isomerization in the nano-assemblies. The amount of *cis* conformation is 91%, while dark storage and subsequent pH change (state $\mathbf{F_{II}}$) lead to back-isomerization to *trans* with a degree of 85%. Thus, following the completion of Cycle II, the spectra resemble those prior to irradiation. Comparing Cycle I (state $\mathbf{C_I}$) and Cycle II (state $\mathbf{B_{II}}$), the isomerization in Cycle I takes place to a higher degree. Due to the lower affinity of the *cis* dye to the dendrimer in comparison to the *trans* isomer, there is less repulsion for the photoacid to interact with the dendrimer. Interestingly, a more expressed change is observed in Cycle I for the isomerization to the *trans* configuration in the dark, which happens less for Cycle I (state $\mathbf{D_I}$ and $\mathbf{D_{II}}$). This is attributed to the photoprotective effect, where the azo dye is kept in its state due to electrostatic interaction with the dendrimer.

Table 1. Degree of dye isomerization from *trans* to *cis* and from *cis* to *trans* as derived from UV-Vis spectroscopy.

Head 1[a]	trans→cis	cis→trans
Cycle I	92%	87%
Cycle II	85%	91%

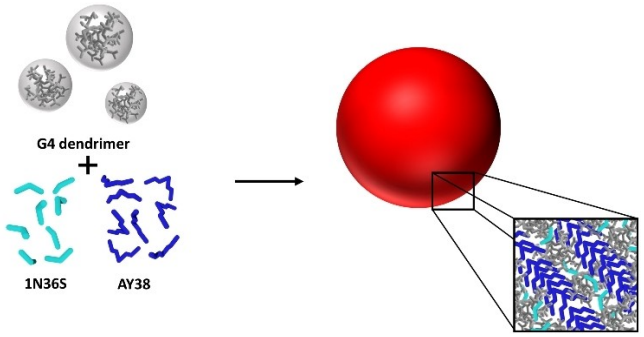
Further, it is necessary to develop a fundamental understanding of the size and shape changes. Table 2 summarizes the enthalpies for the ternary system investigated herein as well as for the binary systems and dye dilution experiments to determine the π-π interaction, obtained by ITC. ITC of the ternary system revealed (Figure S4a) that the azo dye binds exothermically and overstoichiometrically through electrostatic and π-π interactions with the dendrimer, in analogy to the binary dendrimer–Ay38 system (Figure S4c, and measured earlier[50,55]). By contrast, the photoacid binds less strongly and electrostatically only (with some H-bonding contribution, Figure S4a and b and Scheme 3). Compared to the binary systems, the binding enthalpies are less negative for both the anionic building blocks attaching to the dendrimer, which, in turn, is attributed to the electrostatic repulsion with the third building block.

Thus, understanding the size changes qualitatively is quite straight forward: ITC and ζ-potential show that the *cis* dye binds to the dendrimer less strongly and to a lesser extent than the *trans* dye (in the ternary system here in analogy to binary systems measured earlier[50,55]), while the photoacid increases its valency upon irradiation and subsequently attaches more strongly. Accordingly, the charge of the assembly changes, which leads to an adjustment in the size of the electrostatically stabilized particles. Put differently, the aggregation number is controlled thermodynamically in analogy to a previous study on

Table 2. Binding enthalpies measured by ITC for AY38-1 N36S–G4 assemblies and comparison systems.

System	Process	ΔH [kJ mol^{-1}]	Interaction
G4-AY38-1 N36S dark and irradiated	1 N36S binding to G4	−11.8	total (electrostatic + H bonding)
	trans-AY38 binding to G4	−37.3	total (electrostatic + π-π)
	cis-AY38 binding to G4	−20.0	total (electrostatic + π-π)
G4-AY38 dark and irradiated	*trans*-AY83 binding to G4	−42.5	total (electrostatic + π-π)
	cis-AY38 binding to G4	−26.2	total (electrostatic + π-π)
G4-1 N36S	1 N36S binding to G4	−53.9	total (electrostatic + H bonding)
AY38 into water (comparison for π-π interaction) dark and irradiated	*trans*-AY38 self-stacking	−29.3	π-π *trans*-AY38
	cis-AY38 self-stacking	−2.0	π-π *cis*-AY38
G4-AY38-1 N36S (calcd)	*trans*-AY38 binding to G4 electrostatic contribution	−8.0	*trans*-AY38-G4 electrostatic
	cis-AY38 binding to G4 electrostatic contribution	−18.0	*cis*-AY38-G4 electrostatic

© 2022 The Authors. Chemistry - A European Journal published by Wiley-VCH GmbH



Scheme 3. Schematic overview on assembly formation and internal structure (state **A**).

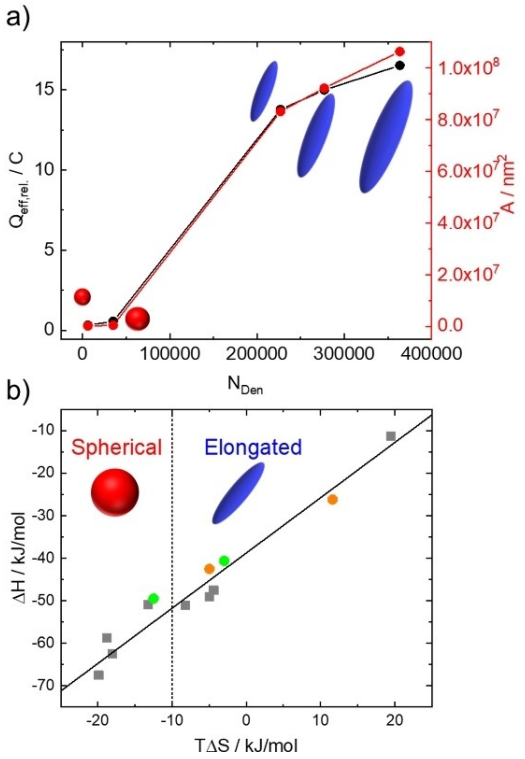


Figure 4. a) Particle charge Q_{eff} (measured from the ζ-potential) and particle surface A (measured by SANS) as function of aggregation number (measured by SANS). b) Enthalpy–entropy compensation plot for light-switchable binary and ternary systems; orange circles: AY38-G4 dendrimer, green triangles: AY38-1 N36S–G4, gray squares: various azo dyes from previous studies.[36]

non-switchable systems of ours.[36] This is further substantiated by the fact that mixing the uncharged building blocks at pH 10 and changing the pH to 7.0 afterwards, that is charging the building blocks and initiating the assembly, results in the same nano-objects (Figure S6).

In stark contrast, previous structure-directing effects do not hold for the particle shape. The strong alteration from spherical to elongated ellipsoids upon isomerization of the AY38 is especially significant. Against this backdrop, it is remarkable that the ΔH of the *cis*-AY38 π-π interaction ($\Delta H = -2.0$ kJ mol^{-1}) is much weaker than for the *trans*-AY38 π-π interaction ($\Delta H = -29.3$ kJ mol^{-1}). In fact, the *cis* isomer shows nearly no π-π interaction, which most likely is due to steric hindrance in the *cis* form. Thus this is in contrast to the previous finding where stronger π-π interaction (a more negative $\Delta H_{dye\text{-}dye}$) promoted anisotropy on the nanoscale.[36] In this case, the anisotropic shape of the assemblies herein is not controlled by secondary π-π interactions. Instead, it must be ionic effects that encode the shape.

Figure 3a makes it evident that the effective surface charge density (here related to a sphere with the radius R_H) assumes significance and smaller particles need a higher charge density to be stabilized. On the one hand, in analogy to classical colloid and nanoparticle science (though we study hydrophilic assemblies from water-soluble building blocks here), the energy needed to create a surface is proportional to this surface, that is, here to the particle surface. On the other hand, the Poisson–Boltzmann equation and Debye–Hückel approximation suggest that for smaller particles, the electrostatic potential can be approximated to scale with the charge. For this reason, Figure 4a plots both the particle surface (obtained from SANS) and the effective particle charge (derived from the ζ-potential) as a function of the aggregation number (from SANS), in conjunction with the shapes of the particles identified. It is also noteworthy that both curves overlay almost exactly, thus ascertaining the importance of the charge-surface relation (rather than with the ζ-potential or the surface charge density).

It is evident that an increase of surface required for the purpose of stabilization with charge occurs steeply; for higher aggregation numbers it is no longer possible to increase the size of a sphere only, but particles must adopt a geometry with a larger surface and ellipsoids with a higher surface per aggregation number (particle volume) form. Here, the aggregation number is determined thermodynamically. At the same time, the thermodynamically encoded aggregation number must geometrically fit in terms of surface/volume ratio, that is, in terms of particle shape.

From a molecular point of view, the thermodynamic binding equilibria of the connecting ions to the macroion, based on all the molecular effects – ionic binding, π-π interaction, geometric effects – cause a certain aggregation number and a certain net charge. Thus, upon irradiation and subsequent isomerization from *trans* to *cis*, the increase in size and change from a spherical to an ellipsoidal shape is due to the "missing" π-π interactions.

Furthermore, Figure 4b pictures the enthalpy-entropy master plot defining regions of isotropic and anisotropic nano-objects, in analogy to the one that was previously introduced by us (with prior data points shown in gray).[36] It pictures the enthalpic versus the entropic contribution to the free energy change for the binding of one small molecule to the macroion. Evidently, despite a totally different molecular and nanoscale mechanism for particle shape control, this master plot still holds for the system herein. Self-assembly with a large gain in enthalpy but a negative change in entropy leads to spherical particles, while self-assembly with smaller enthalpy gain and larger entropy gain (i.e., smaller entropy loss or entropy gain)

© 2022 The Authors. Chemistry - A European Journal published by Wiley-VCH GmbH

15213765, 2023, 10, Downloaded from https://chemistry-europe.onlinelibrary.wiley.com/doi/10.1002/chem.202203373, Wiley Online Library on [11/01/2026]. See the Terms and Conditions (https://onlinelibrary.wiley.com/terms-and-conditions) on Wiley Online Library for rules of use; OA articles are governed by the applicable Creative Commons License

leads to the formation of elongated, anisotropic particles. While there is some lack of clarity with regard to the details of this scenario, this might point to a very general connection of nanoscale particle shape with interaction thermodynamics, which might be widely applied to understand the shape of self-assembled nanoparticles.

Conclusions

In conclusion, we have demonstrated in this study that the ternary electrostatic self-assembly of a photoacid, an azo dye, and a cationic dendrimer leads to a novel multi-switchable system in aqueous solution. By joining two different ionic molecular switches through a polyelectrolyte, the resulting nano-objects can respond to changes in pH and different irradiation wavelengths with changes in size and shape. The supramolecular assemblies exhibit a size between $R_H = 20$ and 134 nm and shapes ranging from spheres via core–shell spheres to ellipsoids. Nanoscale size and shape changes are caused by excitation-dependent photoacid dissociation and azo dye isomerization. Particle sizes can be understood according to the extent of overstoichiometrically π-π bound dye molecules. Importantly, it is the particle surface required to accommodate a certain (particle) charge and volume that determines particle shapes. Thermodynamic data reveal an enthalpy–entropy master plot with spherical and elongated structures falling into different regions that, in turn, may be widely valid for shapes of supramolecular nano-objects. This new type of electrostatically self-assembled multi-switchable nanoparticles could pave the way for new sensors and molecular transport.

Experimental Section

Essential experimental procedures/data, a comparison of AFM and DLS, reversibility and UV/Vis of cycle I and autocorrelation function and SANS of cycle II, SLS results of both cycles, ITC measurements, and a comparison of different synthesis procedure can all be found in the Supporting Information[z1] .

Acknowledgements

We gratefully acknowledge the German Science Foundation (DFG) for funding, the Institut Laue-Langevin (ILL), France, for the beamtime, and the Partnership for Soft Condensed Matter (PSCM) for providing us with light scattering instrument support. This work benefited from the use of the SasView application (www.sasview.org), originally developed under NSF award DMR-0520547. The DOI for the beamtime on D11 at the ILL is: 10.5291/ILL–DATA.9-11-2077. Open Access funding enabled and organized by Projekt DEAL.

Conflict of Interest

The authors declare no conflict of interest.

Keywords: azo dyes · electrostatic self-assembly · light responsiveness · multi-switchable nano-objects · shape change

[1] G. Gröger, W. Meyer-Zaika, C. Böttcher, F. Gröhn, C. Ruthard, C. Schmuck, *J. Am. Chem. Soc.* **2011**, *133*, 8961.
[2] P. Akcora, H. Liu, S. K. Kumar, J. Moll, Y. Li, B. C. Benicewicz, L. S. Schadler, D. Acehan, A. Z. Panagiotopoulos, V. Pryamitsyn, V. Ganesan, J. Ilavsky, P. Thiyagarajan, R. H. Colby, J. F. Douglas, *Nat. Mater.* **2009**, *8*, 354.
[3] J. F. Reuther, D. A. Siriwardane, R. Campos, B. M. Novak, *Macromolecules* **2015**, *48*, 6890.
[4] S. Zhang, J. Zou, F. Zhang, M. Elsabahy, S. E. Felder, J. Zhu, D. J. Pochan, K. L. Wooley, *J. Am. Chem. Soc.* **2012**, *134*, 18467.
[5] O. M. Wani, H. Zeng, A. Priimagi, *Nat. Commun.* **2017**, *8*, 1.
[6] P. Yan, D. Jiang, Y. Tian, L. Xu, J. Qian, H. Li, J. Xia, H. Li, *Biosens. Bioelectron.* **2018**, *111*, 74.
[7] T. Jingqi, C. Ningyan, L. Qian, X. Wei, S. Xuping, *Angew. Chem. Int. Ed.* **2015**, *127*, 5583.
[8] K. Liu, R. Xing, Q. Zou, G. Ma, H. Möhwald, X. Yan, *Angew. Chem. Int. Ed.* **2016**, *55*, 3036.
[9] F. Yin, C. Yang, Q. Wang, S. Zeng, R. Hu, G. Lin, J. Tian, S. Hu, R. F. Lan, H. S. Yoon, F. Lu, K. Wang, K.-T. Yong, *Theranostics* **2015**, *5*, 818.
[10] X. Cheng, R. Sun, L. Yin, Z. Chai, H. Shi, M. Gao, *Adv. Mater.* **2017**, *29*, 1604894.
[11] G. Konstantatos, I. Howard, A. Fischer, S. Hoogland, J. Clifford, E. Klem, L. Levina, E. H. Sargent, *Nature* **2006**, *442*, 180.
[12] D. J. Callahan, W. Liu, X. Li, M. R. Dreher, W. Hassouneh, M. Kim, P. Marszalek, A. Chilkoti, *Nano Lett.* **2012**, *12*, 2165.
[13] S. Carmen, V. Jens, J. Pascal, H. Jurriaan, *Angew. Chem. Int. Ed.* **2014**, *53*, 3400.
[14] X. Chi, X. Ji, D. Xia, F. Huang, *J. Am. Chem. Soc.* **2015**, *137*, 1440.
[15] C. Shuo, J. Fengjuan, C. Ziquan, W. Guojie, D. Zhi-Min, *Chem. Commun.* **2015**, *51*, 12633.
[16] H. Xiao-Yu, J. Keke, C. Yu, L. Yan, Q. Shan, Z. Fan, L. Chen, Z. Dongmei, W. Leyong, *Eur. J. Chem.* **2015**, *21*, 1208.
[17] P. G. Falireas, M. Vamvakaki, *Macromolecules* **2018**, *51*, 6848.
[18] A. A. Foster, C. T. Greco, M. D. Green, T. H. Epps, M. O. Sullivan, *Adv. Healthcare Mater.* **2015**, *4*, 760.
[19] S.-J. Jeon, A. W. Hauser, R. C. Hayward, *Acc. Chem. Res.* **2017**, *50*, 161.
[20] N. Lei, D. Shen, X. Chen, *Soft Matter* **2019**, *15*.
[21] Z. Xiaomin, Z. Jian, M. Cheng, L. Siyu, Z. Youliang, *Polym. Chem.* **2020**, *11*, 3003.
[22] Y. Huajie, S. Pengliang, G. Shujin, C. Xiujie, L. Qiuhong, L. Aixiang, S. Xia, *Nano Select* **2021**, *2*, 2176.
[23] J. Lee, W. Lee, D. Kim, M. Kim, J. Kim, *Sci. Rep.* **2019**, *9*, 12458.
[24] L. Zang, Y. Che, J. S. Moore, *Acc. Chem. Res.* **2008**, *41*, 1596.
[25] K. Adrien, Albertus, P. H. J. Schenning, *Adv. Mater.* **2010**, *22*, 2985.
[26] X. Feng, W. Pisula, T. Kudernac, D. Wu, L. Zhi, S. de Feyter, K. Müllen, *J. Am. Chem. Soc.* **2009**, *131*, 4439.
[27] V. Percec, B. C. Won, M. Peterca, P. A. Heiney, *J. Am. Chem. Soc.* **2007**, *129*, 11265.
[28] H. Qiu, Z. M. Hudson, M. A. Winnik, I. Manners, *Science* **2015**, *347*, 1329.
[29] T. G. Barclay, K. Constantopoulos, J. Matisons, *Chem. Rev.* **2014**, *114*, 10217.
[30] Z. Tan, Y. Jiang, M. S. Ganewatta, R. Kumar, A. Keith, K. Twaroski, T. Pengo, J. Tolar, T. P. Lodge, T. M. Reineke, *Macromolecules* **2019**, *52*, 8197.
[31] C. Fürst, P. Zhang, S. V. Roth, M. Drechsler, S. Förster, *Polymer* **2016**, *107*, 434.
[32] G. Mariani, R. Schweins, F. Gröhn, *Macromolecules* **2016**, *49*, 8661.
[33] A. Krieger, J. P. Fuenzalida Werner, G. Mariani, F. Gröhn, *Macromolecules* **2017**, *50*, 3464.
[34] J. Düring, B. Butz, E. Spiecker, F. Gröhn, *Macromolecules* **2015**, *48*, 8399.
[35] D. Yi, C. Meng, C. Zhigang, H. Leilei, W. Lei, L. Xinhua, C. Yuanli, *Angew. Chem. Int. Ed.* **2018**, *57*, 1053.
[36] G. Mariani, D. Moldenhauer, R. Schweins, F. Gröhn, *J. Am. Chem. Soc.* **2016**, *138*, 1280.
[37] I. Willerich, Y. Li, F. Gröhn, *J. Phys. Chem. B* **2010**, *114*, 15466.
[38] S. P. Nunes, A. R. Behzad, B. Hooghan, R. Sougrat, M. Karunakaran, N. Pradeep, U. Vainio, K.-V. Peinemann, *ACS Nano* **2011**, *5*, 3516.
[39] Y. Li, L. Song, B. Wang, J. He, Y. Li, Z. Deng, C. Mao, *Angew. Chem. Int. Ed.* **2018**, *57*, 6892.

© 2022 The Authors. Chemistry - A European Journal published by Wiley-VCH GmbH

15213765, 2023, 10, Downloaded from https://chemistry-europe.onlinelibrary.wiley.com/doi/10.1002/chem.202203373, Wiley Online Library on [11/01/2026]. See the Terms and Conditions (https://onlinelibrary.wiley.com/terms-and-conditions) on Wiley Online Library for rules of use; OA articles are governed by the applicable Creative Commons License

[40] I. Martín-Fabiani, A. Fortini, J. Lesage de la Haye, M. L. Koh, S. E. Taylor, E. Bourgeat-Lami, M. Lansalot, F. D'Agosto, R. P. Sear, J. L. Keddie, *ACS Appl. Mater. Interfaces* **2016**, *8*, 34755.
[41] Y. Hu, A. Cecconello, A. Idili, F. Ricci, I. Willner, *Angew. Chem. Int. Ed.* **2017**, *56*, 15210.
[42] A. J. Simnick, C. A. Valencia, R. Liu, A. Chilkoti, *ACS Nano* **2010**, *4*, 2217.
[43] W. Lewandowski, M. Fruhnert, J. Mieczkowski, C. Rockstuhl, E. Górecka, *Nat. Commun.* **2015**, *6*, 1.
[44] X. Fan, Q. Long, L. Minghua, *Chem. Commun.* **2016**, *52*, 930.
[45] V. I. Michailova, D. B. Momekova, H. A. Velichkova, E. H. Ivanov, R. K. Kotsilkova, D. B. Karashanova, E. D. Mileva, I. V. Dimitrov, S. M. Rangelov, *J. Phys. Chem. B* **2018**, *122*, 6072.
[46] X. Yao, T. Li, J. Wang, X. Ma, H. Tian, *Adv. Opt. Mater.* **2016**, *4*, 1322.
[47] X. Wang, J. Hu, G. Liu, J. Tian, H. Wang, M. Gong, S. Liu, *J. Am. Chem. Soc.* **2015**, *137*, 15262.
[48] X. Li, C.-y. Kim, S. Lee, D. Lee, H.-M. Chung, G. Kim, S.-H. Heo, C. Kim, K.-S. Hong, J. Yoon, *J. Am. Chem. Soc.* **2017**, *139*, 10880.
[49] H. Jiang, Y. Jiang, J. Han, L. Zhang, M. Liu, *Angew. Chem. Int. Ed.* **2019**, *58*, 785.
[50] I. Willerich, F. Gröhn, *Angew. Chem. Int. Ed.* **2010**, *49*, 8104.
[51] C. Cardenas-Daw, F. Gröhn, *J. Am. Chem. Soc.* **2015**, *137*, 8660.
[52] A. Zika, S. Bernhardt, F. Gröhn, *Polymer* **2020**, *12*, 1746.
[53] A. Zika, F. Gröhn, *Beilstein J. Org. Chem.* **2021**, *17*, 166.
[54] I. Willerich, H. Ritter, F. Gröhn, *J. Phys. Chem. B* **2009**, *113*, 3339.
[55] I. Willerich, F. Gröhn, *Macromolecules* **2011**, *44*, 4452.

Manuscript received: October 31, 2022
Accepted manuscript online: November 6, 2022
Version of record online: December 27, 2022

© 2022 The Authors. Chemistry - A European Journal published by Wiley-VCH GmbH

15213765, 2023, 10, Downloaded from https://chemistry-europe.onlinelibrary.wiley.com/doi/10.1002/chem.202203373, Wiley Online Library on [11/01/2026]. See the Terms and Conditions (https://onlinelibrary.wiley.com/terms-and-conditions) on Wiley Online Library for rules of use; OA articles are governed by the applicable Creative Commons License

8. Conference Contributions

8.1. Presented a poster on “Spontaneous and time-controlled aggregation of nanoparticles in electrostatic self-assembly” at the 35th ECIS conference in Athens, Greece, from 3rd – 8th September 2021.

8.2. Delivered an oral presentation on “Light Tunable Structures by Self-Assembly: In-situ SANS under Irradiation” at the 12th ICNS conference in Buenos Aires, Argentina, from 21st – 25th August 2022.

8.3. Delivered an oral presentation on “Light Tunable Structures by Self-Assembly: In-situ SANS under Irradiation” at the 18th SAS conference in Campinas, Brazil, from 11th – 16th September 202

9. Methods

9.1. Light Scattering

In a typical light scattering experiment, light is scattered when interacting with matter, and an appropriate detector detects the signal. In the mid-19th century, John Tyndall analyzed scattering from colloidal suspensions, where the wavelength of incident light was smaller than the particle size [1]. In contrast, Rayleigh described light scattering, where the incident wavelength of light is larger than the particles, by providing an example of a blue-colored sky in daylight. Mie used the elastic scattering of light by particles of a similar size to the light wavelength [2]. Later, major developments were implemented by Einstein [3], Debye [4], and Zimm based on Brownian theory.

Light scattering has emerged as a highly suitable technique for characterizing polyelectrolytes in solution, including dynamic and static light scattering. Both static and dynamic light scattering (SLS/DLS) techniques are used throughout this thesis as primary tools for characterizing aqueous self-assembled nano-objects. DLS provides rapid access to hydrodynamic size, size distributions, and time-dependent structural evolution (e.g., equilibration, pathway effects, irradiation-induced restructuring). SLS provides radius of gyration, molecular weight, and interaction parameters (when concentration series are measured), and topology-sensitive information via the angular dependence of the time-averaged scattered intensity.

Light scattering is treated here as a multi-angle method with built-in internal consistency checks across different scattering angles rather than a single "mean size" measurement. In particular, q-dependence, concentration dependence, and consistency between R_H, R_G, and $\rho = R_G/R_H$ are used as quality and interpretability criteria to ensure that extracted parameters reflect intrinsic single-object properties rather than collective or instrumental artifacts.

The length scale probed in a light scattering experiment is described in reciprocal space by the magnitude of the scattering vector q. For scattering in a medium of refractive index n, using laser wavelength λ in the medium and scattering angle θ, q is defined as:

$$q = \left(\frac{4\pi n}{\lambda}\right) \cdot sin\left(\frac{\theta}{2}\right) \quad (1)$$

This is essential for extracting angular form-factor information in SLS and for testing q-dependence and enabling $q \rightarrow 0$ extrapolations in DLS.

A goniometer-based multi-angle configuration is used to measure both:

- SLS: time-averaged intensity $I(q)$ (or Rayleigh ratio $R(q)$) as a function of angle.
- DLS: time-dependent intensity $I(q,t)$ followed by correlation analysis.

The principal methodological advantage is that SLS and DLS are performed on identical samples under identical optical geometry, enabling direct comparison of R_H and R_G and calculation of $\rho = R_G/R_H$. Multi-angle acquisition is emphasized because the systems studied in this thesis may exhibit pathway dependence, coexistence of populations, weak aggregation, and interaction-induced concentration effects.

Light scattering is highly sensitive to rare large contaminants such as dust, lint, or microbubbles. Because the scattered intensity increases strongly with particle size, approximately with the sixth power of the size (scattering intensity $\propto$ size^6), even a very small number of large impurities can dominate the signal and distort both DLS size distributions and the low-q slope in SLS. For this reason, cleanliness and sample handling are treated as integral parts of the method. Measurements are therefore carried out using clean, dust-free cuvettes and carefully rinsed or filtered solvents where compatible with the sample chemistry, while avoiding bubbles and convection in the cell. Samples are allowed to reach thermal equilibrium before acquisition, and their history, including mixing pathway, equilibration time, and irradiation history, is defined and kept constant whenever comparisons are made.

For DLS, R_H depends on temperature and viscosity; therefore solvent/buffer viscosity η must correspond to the actual composition and temperature. For SLS, optical contrast is governed by the refractive index increment dn/dc; uncertainty in dn/dc propagates directly into Zimm analysis. Temperature stability is therefore critical for both quantitative sizing and meaningful comparisons across conditions.

9.1.1. Dynamic Light Scattering

Dynamic light scattering (DLS) is an effective technique for probing the diffusive behavior of colloids and polymers (macromolecules) in solution. Over the past few years, advances in instrumentation and analysis have substantially expanded its range of applications by addressing earlier technical limitations, including reduced performance in turbid samples and limited accuracy in size determination. In DLS, the translational diffusion coefficient, D, is extracted from the time-dependent scattering signal and is directly related to particle size.

The method is based on quasi-elastic light scattering and exploits temporal fluctuations in the scattered intensity generated by coherent laser illumination. As particles undergo translational Brownian motion,

their positions change continuously, causing the scattered electric field to decorrelate as a function of the delay time, τ. The resulting decay rate of the correlation function is directly linked to the translational diffusion coefficient.

The measured quantity is the normalized intensity autocorrelation function $g_2(q,\tau)$:

$$g_2(q,\tau) = \frac{\langle I(q,t)I(q,t+\tau)\rangle}{\langle I(q,t)\rangle^2} \tag{2}$$

The above function describes the correlation between the scattering intensity at time $t = 0$ and time $t + \tau$, where q is the momentum transfer and τ is the shift in time. For homodyne detection, $g_2(q,\tau)$is related to the electric field autocorrelation function $g_1(q,\tau)$ by the Siegert relation:

$$g_2(q,\tau) = 1 + \beta[g_1(q,\tau)]^2 \tag{3}$$

where β is the coherence factor (intercept). In practice, β is a useful diagnostic: unusually low intercepts can indicate misalignment, increased background, detector artifacts, or multiple scattering.

For a monodisperse population undergoing purely translational diffusion:

$$g_1(q,\tau) = exp(-\Gamma\tau) \tag{4}$$

with relaxation rate:

$$\Gamma = Dq^2 \tag{5}$$

where D is the translational diffusion coefficient. The proportionality $\Gamma \propto q^2$ is used throughout this thesis as a key internal check for diffusive behavior.

For polydisperse or multimodal systems, $g_1(q,\tau)$ can be analyzed by a regularized inverse Laplace transformation using the CONTIN algorithm by S. Provencher [5,6] to obtain the relaxation times distribution and is represented as a superposition of exponentials:

$$g_1(q,\tau) = \int_0^\infty A(\Gamma)exp(-\Gamma\tau)d\Gamma \tag{6}$$

where $A(\Gamma)$ is the distribution of relaxation rates. Regularized inversion (CONTIN) is used to obtain stable distributions. Distributions are interpreted with explicit consideration that DLS is inherently intensity-weighted, and multimodality is reported explicitly rather than being reduced to a single mean size.

When the decay is close to single-mode, cumulant analysis provides a compact parameterization of g_1:

$$ln[g_1(q,\tau)] = -\Gamma_1\tau + \left(\frac{\mu_2}{2!}\right)\tau^2 - \left(\frac{\mu_3}{3!}\right)\tau^3 + \cdots \quad (7)$$

where Γ_1 is the first cumulant (mean relaxation rate) and μ_2 is related to the variance (polydispersity). This approach is used only when justified by near-unimodal decay behavior.

From a characteristic relaxation time τ, an apparent diffusion coefficient, D_{app} is obtained using the relation:

$$D_{app} = q^{-2}\tau^{-1} \quad (8)$$

Interparticle interactions, collective diffusion, weak multiple scattering, or anisotropy can introduce q-dependence of $D_{app}(q)$. Therefore, D_{app} is evaluated across angles. When systematic q-dependence is observed, $D_{app}(q)$ is extrapolated to $q \rightarrow 0$ to obtain the self-diffusion coefficient D_0. When D_{app} is q-independent within uncertainty, the angular average is used as D_0.

The hydrodynamic radius R_H is calculated from D_0 using:

$$D(q^2 \rightarrow 0) = \frac{kT}{6\pi\eta R_H} \quad (9)$$

Where k is the Boltzmann constant, T is the absolute temperature in Kelvin, and η is the solvent viscosity.

9.1.2. Static Light Scattering (SLS)

Instead of X-rays or neutrons, one can also use visible light as a characterization probe for particles in solution. This technique is called static light scattering (SLS). In an SLS experiment, the macroscopic scattering cross-section $\frac{d\Sigma}{d\Omega}(q)$ is measured and is commonly denoted as the Rayleigh ratio ΔR_θ:

$$\frac{d\Sigma}{d\Omega}(q) = \Delta R_\theta = KcM_wP(q)S(q) \quad (10)$$

where K is the optical constant, c the mass concentration, M_w the weight-average molar mass, $P(q)$ the single-particle form factor, and $S(q)$ the structure factor capturing interparticle correlations.

The optical constant groups physical constants and optical contrast:

$$K = \frac{4\pi^2}{\lambda_0^4 N_A}\left(n_{std}\frac{dn}{dc}\right)^2 \quad (11)$$

with λ_0 being the wavelength of the incoming light, N_A the Avogadro constant, n_{std} the refractive index of the standard solution used for calibration of absolute intensity, and dn/dc being the refractive index

increment and also equivalent to scattering length density $\Delta\rho$ used in SANS experiments.

The form factor at low q can be described by either the Guinier approximation:

$$P(q) \approx exp\left(\frac{-q^2 R_G^2}{3}\right) \tag{12}$$

Taking the logarithm yields a linearized Guinier form:

$$ln[R(q)] = ln[R(0)] - \frac{q^2 R_G^2}{3} \tag{13}$$

Or by Zimm equation:

$$\frac{Kc}{\Delta R_\theta} = \frac{1}{M_w}\left(1 + \frac{1}{3}q^2\langle R_G^2\rangle\right) + 2A_2C \tag{14}$$

with R_G the radius of gyration and A_2 the second osmotic virial coefficient.

Guinier and Zimm analyses are applied only within the low-q regime. The practical criterion used in this thesis is:

$$qR_G \leq 1.2 \tag{15}$$

9.1.3. Combined SLS/DLS Interpretation

When both R_G (SLS) and R_H (DLS) are obtained for the same sample state, their ratio is defined as:

$$\rho = \frac{R_G}{R_H} \tag{16}$$

The ratio of R_G/R_H, also known as the ρ-ratio, assists in determining the nanoparticles' topology, especially in a small nano range (10 – 100 nm), where a detailed analysis of particle form factor is not possible due to the limited length scale of light scattering. Combined light scattering techniques give only primary hints about the particle shape. Theoretically calculated values of ρ-ratios are summarized in Table 7.1.

Table 7.1. ρ-ratio for the most common particle morphologies [7].

Nanostructures Topology	ρ-ratio
Sphere	0.775
Cylinder of length *l* and diameter *d*	$\frac{1}{\sqrt{3}}.\ln(\frac{l}{d} - 0.5)$
Ellipsoid	0.775-4

Hollow Sphere	1
Random Polymer Coil	1.505

Measurements were carried out using an ALV CGS3 goniometer with an ALV 5004 correlator (ALV Germany) equipped with a HeNe laser with a wavelength of λ = 632.8 nm and a maximum output power of 23 mW.

9.2. Small-Angle Neutron Scattering

Small-angle neutron scattering (SANS) is a widely used technique to probe the structure of almost any material, ranging from polymers, colloids, micelles, and biomolecules [8–13] to glasses [14], liquid crystals [15], concrete [16], including chocolates, and even cheese [17] and shampoo manufacturing [18,19]. SANS is a sophisticated and cutting-edge technique that harnesses neutrons' unique properties and unveils intricate structures by exploiting their sensitivity to interact with atomic nuclei. The wave-like nature of neutrons and their low intrinsic interactions with matter make SANS a non-destructive technique for studying materials in their native environment. SANS provides invaluable insights into deciphering the fundamental mechanisms governing the functionality and performance of the studied materials. SANS has an advantage over SAXS (small-angle X-ray scattering) due to its sensitivity towards isotopes while studying organic macroions or polyelectrolytes. In general, hydrogen has a very different scattering length compared to deuterium, which contributes more to the scattering length density (SLD) and results in a stronger scattering signal or higher noise. Therefore, using deuterated compounds or solvents is advantageous for better contrast, which cannot be obtained using SAXS.

Small-angle neutron scattering (SANS) is a central structural tool in this thesis for resolving the size and shape of electrostatically self-assembled nano-objects in aqueous solution. In contrast to light scattering, which yields highly accessible hydrodynamic and topology descriptors (e.g., R_G, ρ = R_G/R_H), SANS provides a model-based, q-resolved structural fingerprint over length scales typically spanning from a few nanometers to several hundred nanometers.

SANS measurements were performed at beamline D11 at the Institut Laue Langevin (ILL), Grenoble, France, and at the SINQ facility at the Paul Scherrer Institute (PSI), Villigen, Switzerland.

In SANS, the structural signal arises primarily from coherent elastic scattering, while incoherent and inelastic contributions contribute to the background and are treated during data correction. In a small-angle experiment, the measurable structural information is expressed as a

function of the scattering vector magnitude q, defined by the neutron wavelength λ and the scattering angle θ as shown in Eq. 1.

SANS is a reciprocal-space technique; the dominant real-space length scale d associated with a given q-range is commonly estimated as:

$$d = \frac{2\pi}{q} \tag{17}$$

Thus, decreasing q extends the probed length scale toward larger objects and long-range correlations, while increasing q provides sensitivity to smaller cross-sectional dimensions and internal interfaces.

The key physical quantity governing neutron contrast is the coherent scattering length density (SLD), which depends on the nuclear scattering lengths b_i of the atoms and their number density within a volume, V:

$$\rho_{SLD} = \frac{\sum_{i=1}^{n} b_i}{V_m} \tag{18}$$

The measurable contrast between a particle and the solvent is the SLD difference:

$$\Delta\rho_{SLD} = \rho_{SLD,particle} - \rho_{SLD,solvent} \tag{19}$$

Because hydrogen and deuterium have significantly different coherent and incoherent scattering properties, using D_2O-based solvents typically (i) increases coherent contrast for organic soft matter and (ii) reduces incoherent background from hydrogen. In this thesis, SANS samples are therefore predominantly prepared in D_2O (and, where necessary, using deuterated auxiliary reagents), both to improve signal quality and to enable reliable background subtraction and absolute-scale analysis.

Data were put on an absolute scale via the attenuated direct beam intensity, measured per instrument configuration. Azimuthally averaged scattering curves were then used to subtract the solvent scattering and incoherent background.

The SANS intensity after data correction is:

$$I(q) = \emptyset V_{NP} (\Delta\rho_{SLD})^2 P(q) S(q) \tag{20}$$

Where $\emptyset$ is the volume fraction, V_{NP} the particle volume, $\Delta\rho_{SLD}$ is the difference in scattering length densities between solute and the solvent, and $P(q)$ the particle form factor corresponds to the particle shape. The structure factor $S(q)$ represents the interparticle correlations considered equal to 1, as the samples have been diluted. No evidence of interparticle interactions is observed within the investigated q-range.

For soft-matter nano-objects, the primary structural parameters (radii, lengths, shell thicknesses, polydispersities) are obtained by fitting $I(q)$ using physically motivated models. The form factor is related to the scattering amplitude $F(q)$ by:

$$P(q) = |F(q)|^2 \tag{21}$$

Below are the principal amplitude expressions used repeatedly in the attached studies and adopted as standard models in this thesis.

(a) Homogeneous sphere (radius R)

For a sphere with radius R, the scattering amplitude $F(q)$ is [20];

$$F(q) = 3\frac{sinqR - qRcosqR}{(qR)^3} \tag{10}$$

(b) Circular cylinder (radius R, length L)

For a cylinder with length L and radius R, $P(q)$ is [21,22];

$$P(q,\alpha) = \frac{scale}{V}F^2(q,\alpha).sin(\alpha) + background \tag{11}$$

Where,

$$F(\mathrm{q},\alpha) = 2(\Delta\rho)V\frac{sin\left(\frac{1}{2}qLcos\alpha\right)}{\frac{1}{2}qLcos\alpha}\frac{J_1(qRsin\alpha)}{qRsin\alpha} \tag{12}$$

Where α is the angle between the axis of the cylinder, $V = \pi R^2 L$ is the volume of the cylinder, $\Delta\rho$ (contrast) is the scattering length density difference between the scatterer and the solvent, and J_1 is the first-order Bessel function.

(c) Ellipsoid (equatorial radius R_e, polar radius R_p)

For an ellipsoid, the scattering amplitude $F(q)$ is:

$$F(q,\alpha) = \Delta\rho V\frac{3(sin\,qr - qr\,cos\,qr)}{(qr)^3} \tag{13}$$

where,

$$r = \left[R_e^2 sin^2\alpha + R_p^2 cos\alpha\right]^{\frac{1}{2}} \tag{14}$$

α is the angle between the axis of the ellipsoid and $V = (4/3)\pi R_p R_e^2$ is the volume of the ellipsoid, R_p is the polar radius along the rotational axis of the ellipsoid, and R_e is the equatorial radius perpendicular to the rotational axis of the ellipsoid.

(d) Polydispersity

Soft assemblies are rarely perfectly monodisperse. In model fitting, polydispersity is implemented by averaging the form factor over an assumed parameter distribution (commonly Gaussian or log-normal for size parameters). The practical outcome is (i) improved fit quality and (ii) a physically realistic uncertainty envelope on extracted dimensions.

SasView 4.2.2 fit the scattering data using various model form factors. The quality of fitting the SANS data can be determined by χ^2 value.

Raw two-dimensional detector data require several corrections before quantitative modelling. Across the studies included in this thesis, data reduction followed a consistent workflow comprising electronic background subtraction, correction for detector efficiency and non-uniformity, and masking of defective pixels or shadowed detector regions. Detector normalization was commonly performed using a standard sample, for example a thin H_2O sample.

The measured intensities were further corrected for sample transmission in order to account for attenuation by the sample and the cell and to ensure normalization across different measurements. In addition, empty-cell scattering was measured separately and subtracted, followed by subtraction of solvent scattering and the incoherent background from the sample signal.

To enable quantitative comparison between samples and instrument configurations, the data were placed on an absolute intensity scale using an attenuated direct-beam measurement and, where appropriate, calibrated standards. Assuming isotropic scattering in solution, the corrected two-dimensional detector patterns were then azimuthally averaged to obtain one-dimensional scattering curves, (q).

The software packages used for data reduction and averaging in the work included in this thesis comprised Mantid, particularly for datasets measured at D11, and instrument-specific tools such as BerSANS for SANS-I. Subsequent model fitting and structural analysis were carried out using SasView.

A substantial fraction of SANS measurements in this thesis were performed at the D11 instrument at the Institut Laue–Langevin (ILL, Grenoble). At D11, the employed neutron beam was 15 mm in diameter. At neutron wavelength λ = 6.0 Å (FWHM 9%), three different sample-detector distances (1.7, 8, and 38 m) were used with collimation distances of 4, 8, and 40.5 m. A total scattering vector range of 0.016 $nm^{-1} \leq q \leq 4.9\ nm^{-1}$ was investigated, extending in the low-q region by 0.0046 $nm^{-1} \leq q \leq 0.025\ nm^{-1}$ using SLS data. Scattered neutrons were detected using a 96 x 96 cm^2 CERCA ^{3}He multi-detector mounted on a moveable

trolley in an evacuated detector tube. 2D Data were corrected for empty cell scattering, electronic background, detector uniformity via measuring 1 mm H_2O scattering, and transmissions using the LAMP software. Later, in 2021, a new detector was installed at D11, using a multitube array of ^3He gas consisting of three detector panels: a central one with 192 horizontally oriented tubes and a left and a right-side panel of 32 vertically oriented tubes. Each tube is 1 m long with a pixel size of 4 mm along the tube, with the inner tube diameter being 8 mm. The detector is therefore composed of 256×256 pixels. Here, the data were corrected using the above procedure with the help of the new Mantid software package (developed by ISIS Rutherford Appleton Laboratory UKRI, NScD Oak Ridge National Laboratory, European Spallation Source, Institut Laue - Langevin & CSNS, Institute of High Energy Physics, CAS) [23].

A different SANS beamline, SANS-I, at PSI (Paul Scherrer Institute), was used to measure samples. In this beamline, three different sample-detector distances (1.6, 6, and 18m) were used with the collimation distances of 6, 6, and 18m, respectively, at 6.0 Å neutron wavelength. BerSANS (2002) software was used for the data reduction. Later, the SANS data was combined with the SLS data to extend the *q*-range.

Throughout the thesis, samples are routinely measured in short path-length quartz cells, for example, Hellma 404-QX cells with a typical path length of 2 mm, in order to reduce multiple scattering. D_2O-based solutions are used as a solvent to reduce the incoherent background and improve scattering contrast.

For very large aggregates, conventional SANS configurations may not fully access the ultra-low-*q* regime required to constrain the global particle dimensions. In such cases, SLS data (measured on the identical sample) are merged with SANS to extend the low-*q* region, yielding a combined dataset that stabilizes shape assignment and reduces ambiguity in model fits.

A major methodological contribution in this thesis is the development and application of SANS under controlled in-situ UV irradiation, enabling direct observation of irradiation-driven restructuring in electrostatic assemblies.

Continuous irradiation during scattering is experimentally non-trivial because the sample must simultaneously provide stable neutron transmission and scattering intensity, uniform optical irradiation of the volume intersected by the neutron beam, effective exclusion of unintended ambient light, and minimal heating or convection artefacts. At the same time, the experimental setup must maintain sufficient neutron flux for time-resolved slicing without compromising *q*-resolution.

A dedicated irradiation setup as shown in Figure 1 is used in which:

A UV light source (typically λ = 365 nm) was used to irradiate the sample during SANS measurements. The beam was directed onto the sample cell at a fixed angle relative to the neutron beam, and the lamp position was kept constant for all experiments to ensure reproducible illumination conditions. A convex lens was placed between the lamp and the sample to adjust the working distance and to obtain a homogeneous illumination of the neutron-probed volume. The sample environment was enclosed with a light-tight cover to suppress ambient light and to prevent unintended pre-irradiation during handling. The irradiation geometry (lamp to sample distance, incidence angle, and illuminated area) was maintained unchanged across measurements to allow direct comparison between datasets.

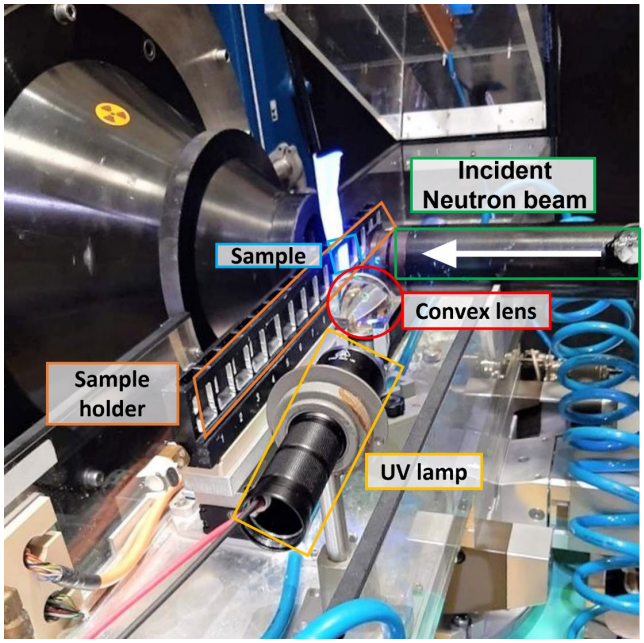


Figure 1 Photograph of the in-situ UV irradiation setup used during SANS measurements. The UV lamp is positioned to ensure full illumination of the cuvette region intersected by the neutron beam (the irradiation geometry was kept fixed for all in-situ experiments and thus does not substantially influence the outcome, as maximum irradiation is assured).

Time-resolved SANS is performed by repeating short acquisitions during irradiation and tracking the evolution of $I(q,t)$ within a selected q-window, or across the full accessible q-range where feasible. Two experimental regimes are used depending on the characteristic timescale of the structural evolution. For fast kinetics, the sample-detector distance is kept short, typically around 16.5 m, in order to maximize neutron flux. Under these conditions, a representative q-range of about 0.038 nm^{-1} to 0.58 nm^{-1} is accessible, and short time slices are recorded, for example 10 s scans during the first minutes, followed by longer slices such as 60 s as the evolution slows down. For slow kinetics,

longer sample-detector distances, for example 28 m or 38 m with matching collimation, are employed to access lower *q*-values. In this configuration, a representative q-range of about 0.018 nm^{-1} to 0.22 nm^{-1} is covered, and the time slices are adapted to the slower structural evolution, typically ranging from several minutes to tens of minutes depending on the flux and setup. This approach makes it possible to resolve the frequently observed two-step restructuring, consisting of a rapid initial change, often associated with fast photoisomerization or excited-state proton-transfer events, followed by a slower relaxation or reorganization toward a new steady-state morphology.

9.3. UV-Vis Spectroscopy

UV-vis spectroscopy is a fundamental and widely used technique that plays a pivotal role in unraveling the chemical composition and electronic structure by providing the absorption and transmission spectra of a molecule in the ultraviolet (UV) and visible (vis) regions of the electromagnetic spectrum. Kinetic UV–vis measurements enable monitoring of temporal changes in the spectrum under defined conditions. An increase in baseline absorbance (turbidity) and band broadening may indicate aggregation or the formation of larger scattering objects.

In dye dendrimer assemblies, the absorption spectrum provides information about the electronic transitions and the conformation of the dye molecules. This information can be used to understand the electrostatic interactions between the dye molecules and the counterions and to study the formation of self-assembled structures. This technique also analyzes the change in dye confirmation over time that causes structural rearrangement. Centrifugation was also used as a complementary method with UV-Vis to calculate the amount of dye in the assemblies and the solution. Absorption spectra were recorded on a JASCO V-630 spectrometer using 1 mm pathlength quartz cuvettes. Room temperature was used for each measurement. UV-Vis measurements were also performed to calculate the amount of *trans* and *cis* isomers in the solution and in the assemblies. The fraction of the bound dye molecules was calculated by the following formula:

$$Fraction\ of\ bound\ Cis\ dye = \frac{quantity\ of\ Cis\ dye\ in\ the\ assemblies}{total\ quantity\ of\ dye\ in\ the\ assemblies}$$

$$= \frac{Cis\ area(before\ centr.) - Cis\ area(supernat.)}{\left(Cis\ area(before\ centr.) - Cis\ area(supernat.)\right) + \left(Trans\ area(before\ centr.) - Trans\ area(supernat.)\right)}$$

The value obtained from the above formula was multiplied by 100 to find the bound *cis* % in the assemblies. The area of the isomers was calculated using the Gaussian model in Origin 9.0 software as follows:

$$y = y_0 + (A/(w\sqrt{\pi/2}))e^{(-2((x-xc)/w^2))}$$

where *y* is the Gaussian function, y_0 is the offset, *xc* is the center of the peak, *w* is the width, and *A* is the area of the peak.

9.4. Isothermal Titration Calorimetry (ITC)

Isothermal titration calorimetry (ITC) is a versatile technique for studying molecular interactions and thermodynamics by measuring the heat changes during a chemical reaction or binding event. It allows the determination of thermodynamic parameters, such as enthalpy (*ΔH*) and equilibrium constant (*K*), for the reaction or binding during a controlled titration process. A precisely calibrated microcalorimeter monitors the temperature changes and quantifies the heat transfer due to molecular interactions occurring in the sample solution.

In a typical ITC experiment, a sample is placed in a calorimeter cell, and a titrant is added in small aliquots. As the titrant is added, it reacts with the sample solution, causing a heat flow. The calorimeter monitors the heat change (releasing or absorbing) to determine the thermodynamics of the reaction or binding.

ITC offers a profound understanding of thermodynamics involved in molecular interactions in complex biological processes, and it can also be applied in the area of designing novel therapeutic agents.

In the ITC instrument, two identical spherical cells, a reference, and a sample cell with a 1.442 mL volume are enclosed in an adiabatic jacket. The solvent is filled in the reference cell, and the sample solution is filled in the working cell. The titrant injection contains a total volume of 288 μL.

In a constantly stirring working cell with the speed of 351rpm, the titrant is successively injected in small aliquots (typically 2-10 μL). The timespan between each injection was 300s. All the measurements were performed at a constant temperature of 25 °C. The first injection is usually set to a small volume of 2 μL due to the possible dilution during the equilibration time. Therefore, the first injection is normally ignored in the data analysis. The data reduction was performed with their respective titrant–solvent reference measurements. Origin 7.0 software, provided by MicroCal, was used to analyze and fit the data. The data were fitted with the two-site model. Gibbs free energy (*ΔG*) was calculated using the formula:

$$\Delta G = \Delta H - T\Delta S = -RTlnK$$

This work was performed on a VP-ITC microcalorimeter at the Grenoble Instruct-ERIC center (ISBG; UAR 3518 CNRS-CEA-UGA-EMBL)

within the Grenoble Partnership for Structural Biology (PSB), supported by FRISBI (ANR-10-INBS-0005-02) and GRAL, financed within the University Grenoble Alpes graduate school (Ecoles Universitaires de Recherche) CBH-EUR-GS (ANR-17-EURE-0003).

9.5. ζ-potential

The behavior of electrostatic assemblies dispersed in aqueous solutions strongly depends on the nature of the particle-liquid interface. ζ-potential is a parameter that measures the potential difference between the electrical double layer (EDL) at the particle-liquid interface and the dispersion medium. The EDL is a thin layer of ions that surrounds the particle surface and is responsible for the electrostatic properties of the particle. The ζ-potential has thus become a fundamental parameter to determine particle stability. The term stability in aqueous dispersions is related to the resistance to change of the dispersion with time. The magnitude of the ζ-potential also determines the strength of the electrostatic interactions. The greater the magnitude of the ζ-potential, the stronger the interactions will be.

In the early 20th century, Marian Smoluchowski developed a theoretical framework [24], still the most well-known and widely used method for calculating ζ-potential using electrophoretic mobility. The ζ-potential instrument measures the electrophoretic mobility, μ of charged particles while the external electric field is applied. The ζ-potential could be calculated experimentally using the Smoluchowski equation:

$$\zeta = (\mu * \eta)/\varepsilon \qquad (15)$$

Where η is the viscosity of the solution and ε is the dielectric constant of the dispersive medium. The ζ-potential is expressed in units of volts (V) or millivolts (mV). Positive values indicate a positively charged surface, while negative values indicate a negatively charged surface.

The ζ-potential measurements and analysis have various real-world applications in biomedical research, material science, and colloid science, including the usage in water purification treatment and aqueous waste products.

The ζ-potential measurements were performed on a Zetasizer Nano ZS analyzer with an integrated 4 mW HeNe laser λ = 633 nm (Malvern Instruments Ltd., UK).

9.6. References

1. J. Tyndall On the Blue Colour of the Sky, and the Polarization of Light. *Proc. R. Soc. London,* **1868**, *17*, 223–233, doi:10.1098/rspl.1868.0033.
2. Mie, G. Beiträge Zur Optik Trüber Medien, Speziell Kolloidaler Metallösungen. *Ann. Phys.* **1908**, *330*, 377–445, doi:10.1002/andp.19083300302.
3. Einstein, A. Zur Theorie Der Brownschen Bewegung. *Ann. Phys.,* **1906**, *324*, 371–381, doi:10.1002/andp.19063240208.
4. Debye, P. Zerstreuung von Röntgenstrahlen. *Ann. Phys.,* **1915**, *351*, 809–823, doi:10.1002/andp.19153510606.
5. Provencher, S.W. A Constrained Regularization Method for Inverting Data Represented by Linear Algebraic or Integral Equations. *Comput. Phys. Commun.,* **1982**, *27*, 213–227, doi:10.1016/0010-4655(82)90173-4.
6. Provencher, S.W. Inverse Problems in Polymer Characterization: Direct Analysis of Polydispersity with Photon Correlation Spectroscopy. *Makromol. Chem.,* **1979**, *180*, 201–209, doi:10.1002/macp.1979.021800119.
7. Schärtl, W. Light Scattering from Polymer Solutions and Nanoparticle Dispersions. In *Springer Berlin, Heidelberg*; **2007**; pp. 1–24 ISBN 9783540719519.
8. Mariani, G.; Moldenhauer, D.; Schweins, R.; Gröhn, F. Elucidating Electrostatic Self-Assembly: Molecular Parameters as Key to Thermodynamics and Nanoparticle Shape. *J. Am. Chem. Soc.,* **2016**, *138*, 1280–1293, doi:10.1021/jacs.5b11497.
9. Karg, M.; Prévost, S.; Brandt, A.; Wallacher, D.; Klitzing, R. Von; Hellweg, T. Intelligent Hydrogels. *Intell. Hydrogels,* **2013**, doi:10.1007/978-3-319-01683-2.
10. Kutz, A.; Mariani, G.; Gröhn, F. Ionic Dye–Surfactant Nanoassemblies: Interplay of Electrostatics, Hydrophobic Effect, and π–π Stacking. *Colloid Polym. Sci.,* **2016**, *294*, 591–606, doi:10.1007/s00396-015-3814-2.
11. Akamatsu, M.; Kobayashi, K.; Iwase, H.; Sakaguchi, Y.; Tanaka, R.; Sakai, K.; Sakai, H. Rapid Controlled Release by Photo-Irradiation Using Morphological Changes in Micelles Formed by Amphiphilic Lophine Dimers. *Sci. Rep.,* **2021**, *11*, 1–10, doi:10.1038/s41598-021-90097-7.
12. Jeffries, C.M.; Ilavsky, J.; Martel, A.; Hinrichs, S.; Meyer, A.; Pedersen, J.S.; Sokolova, A. V.; Svergun, D.I. *Small-Angle X-Ray and Neutron Scattering*; Springer US, **2021**; Vol. 1; ISBN 0123456789.
13. Carl, N.; Müller, W.; Schweins, R.; Huber, K. Controlling Self-Assembly with Light and Temperature. *Langmuir,* **2020**, *36*, 223–231, doi:10.1021/acs.langmuir.9b03040.
14. Kim, M.H.; Suh, J.Y.; Fleury, E.; Han, S.G.; Hong, K.T. Structural Homogeneity and Mass Density of Bulk Metallic Glasses Revealed by Their Rough Surfaces and Ultra-Small Angle Neutron Scattering (USANS). *Sci. Rep.,* **2018**, *8*, 1–13, doi:10.1038/s41598-018-30333-9.
15. Fan, Y.; Wang, Y. Applications of Small-Angle X-Ray Scattering/Small-Angle Neutron Scattering and Cryogenic Transmission Electron Microscopy to Understand Self-Assembly of Surfactants. *Curr. Opin. Colloid Interface Sci.,* **2019**, *42*, 1–16, doi:10.1016/j.cocis.2019.02.011.
16. Allen, A.J.; Thomas, J.J. Analysis of C-S-H Gel and Cement Paste by Small-Angle Neutron Scattering. *Cem. Concr. Res.,* **2007**, *37*, 319–324, doi:10.1016/j.cemconres.2006.09.002.
17. Adams, C.P.; Callaghan-Patrachar, N.; Peyronel, F.; Barker, J.; Pink, D.A.; Marangoni, A.G. Small and Ultra-Small Angle Neutron Scattering Studies of Commercial Milk. *Food Struct.* **2019**, *21*, 100120, doi:10.1016/j.foostr.2019.100120.
18. Müller, W.; Schweins, R.; Nöcker, B.; Kohlbrecher, J.; Smales, G.J.; Huber, K. Comparative Study of

the Co-Assembly Behaviour of 3-Chloro-4-Hydroxy-Phenylazo Dyes with DTAB. *Soft Matter,* **2023**, *19*, 4588–4598, doi:10.1039/d3sm00501a.

19. Müller, W.; Schweins, R.; Nöcker, B.; Egold, H.; Huber, K. Comparative Study of the Self-Assembly Behaviour of 3-Chloro-4-Hydroxy-Phenylazo Dyes. *Soft Matter,* **2023**, *19*, 4579–4587, doi:10.1039/d3sm00500c.
20. Guinier, A.; Fouret, G. Small-Angle Scattering of X-Rays. *New York John Wiley Sons, Inc.,* **1955**, *18*, 5–78, doi:10.1016/0146-3535(89)90023-3.
21. Onsager, L. The Effects of Shape on the Interaction of Colloidal Particles. *Ann. N. Y. Acad. Sci.,* **1949**, *51*, 627–659, doi:10.1111/j.1749-6632.1949.tb27296.x.
22. Pedersen, J.S. Analysis of Small-Angle Scattering Data from Colloids and Polymer Solutions: Modeling and Least-Squares Fitting. *Adv. Colloid Interface Sci.,* **1997**, *70*, 171–210, doi:10.1016/S0001-8686(97)00312-6.
23. Arnold, O.; Bilheux, J.C.; Borreguero, J.M.; Buts, A.; Campbell, S.I.; Chapon, L.; Doucet, M.; Draper, N.; Ferraz Leal, R.; Gigg, M.A.; et al. Mantid - Data Analysis and Visualization Package for Neutron Scattering and μ SR Experiments. *Nucl. Instruments Methods Phys. Res. Sect. A Accel. Spectrometers, Detect. Assoc. Equip.,* **2014**, *764*, 156–166, doi:10.1016/j.nima.2014.07.029.
24. Smoluchowski., M. v. Molekular-Kinetische Theorie Der Opaleszenz von Gasen Im Kritischen Zustande, Sowie Einiger Verwandter Erscheinungen. *Ann. Phys.,* **1908**, *330*, 205–226, doi:10.1002/andp.19083300203.